Ludwig-Maximilians-Universität München

CRITICAL KINETIC PLASMA PROCESSES IN RELATIVISTIC ASTROPHYSICS

Dissertation
der Fakultät für Physik
der Ludwig-Maximilians-Universität
München

vorgelegt von
Claus H. Jaroschek
aus Würzburg

München, März 2005

1. Gutachter: Prof. Dr. Harald Lesch
2. Gutachter: Prof. Dr. Rudolf A. Treumann

Tag der mündlichen Prüfung: 20. Juli 2005

In the universe, there are things that are known,
and things that are unknown,
and in between, there are doors ...
If the doors of perception were cleansed,
everything would appear to man as it is, infinite.

William Blake, 1790

Ich widme diese Arbeit

all' diesen Menschen, die mir nahestehen
und immer noch zu mir halten
obschon ich Ihnen bis jetzt nie die Zeit schenken konnte, die Ihnen zusteht ...

Abstract

Plasma astrophysics deals with collective plasma processes in astrophysical scenarios. As observational astronomy pushes towards unprecedented resolutions in space and time, the focus of theoretical research necessarily ventures towards a description of the plasma microphysics. On microphysical scales the plasma is pervasively collisionless and the magnetohydrodynamic approximation breaks down. Consequently theoretical concepts rely on a kinetic plasma description as the most sophisticated plasma model. The present work discusses some fundamental kinetic plasma processes in relativistic astrophysics: Fast Magnetic Reconnection (FMR) associated with discontinuities in the magnetic field topology, and the Coupled Two-Stream-Weibel instability (CTW) in the wake of collisionless shocks. Both processes are ubiquitous in astrophysical sites, prevail over competing plasma modes because of dominant growth rates, experience significant relativistic modifications, and develop essential features solely in the highly non-linear regime. The computational representation invokes the entire 6D phase space. These characteristics distinguish FMR and the CTW as distinctively *critical* processes.

FMR and the CTW are studied here in the framework of self-consistent, relativistic and fully electromagnetic Particle-In-Cell (PIC) simulations. Typical scenarios comprise ensembles of 10^9 particles and endure for several 10^4 time steps. The computational task is challenging and completely in the realm of the massively parallelized architectures of state-of-the-art supercomputers.

We present the first self-consistent 3D simulations of FMR in relativistic pair plasma. Focusing on the mechanism of particle acceleration we show that the highly dynamic evolution of the current sheet in the non-linear regime is the essential stage. Therein non-stationary acceleration zones arise in the superposition of the relativistic tearing and the relativistic drift kink mode as competing current sheet instabilities. Though the topology of electromagnetic fields is highly turbulent, the FMR process shows the remarkable quality to generate smooth and stable power-laws $\mathrm{f}(\gamma)\mathrm{d}\gamma \propto \gamma^{\mathrm{s}}\mathrm{d}\gamma$ in the particle distribution function (PDF) out of an initial Maxwellian. The upper PDF cut-off in relativistic energy γ is determined by the ratio of light to Alfvén velocity $\mathrm{c}/\mathrm{v}_{\mathrm{A}}$. The power-law index assumes $\mathrm{s} \simeq -1$ within the reconnection X-zone irrespective of parameter variations. Intriguingly the power-law index appears as the universal characteristic of the source process. The associated synchrotron spectra provide a valid description of the extremely hard spectra and rapid variabilities of 'Flat Spectrum Radio Quasars'.

Conceptual γ-ray burst (GRB) synchrotron emission models depend on a plasma process which ensures efficient magnetic field generation. The CTW converts bulk-kinetic energy of counter-streaming plasma shells into Weibel magnetic fields. Pivoted by the linear analysis of the CTW, the PIC simulations confirm the correspondence between saturation magnetic fields and bulk-kinetic energy. Plasma shell collisions in GRBs are either associated with internal or external shocks. As direct consequence of the energy dependence the CTW evolves from a complex 3D topology in internal collisions towards quasi-2D, Weibel-dominated conformalizations at the higher external shock energies. The PIC results prove that the Weibel fields are sufficiently strong to sustain synchrotron emission scenarios, particularly in external shocks. By determining the first lifetime limits we show that Weibel fields are also sufficiently long-lived with respect to typical synchrotron cooling times. We further identify the stability-limiting diffusion process as of 'Bohm'-type, i.e. the diffusion coefficient exhibits the $\propto \mathrm{T}/\mathrm{B}$-dependence and herewith represents a conservative stability criterion. The CTW generates stable power-law spectra in the magnetic fields implying power-law shaped PDFs as self-similar solutions for diffusive particle scattering. This suggests a universal power-law index as the characteristic of the CTW process.

Imposing a magnetic guide field of well-defined strength suppresses the Weibel contributions of the CTW in favour of the electrostatic Two-Stream instability (TSI). The pulsar magnetosphere is the paradigmatic scenario in which we discuss the mechanism of Coherent Collisionless Bremsstrahlung (CCB) triggered by the TSI. The PIC simulations show that the CCB mechanism provides a valid description of the phenomenon of 'Giant Radio Pulses' as recently observed from the Crab pulsar.

Contents

1 Introduction **1**
1.1 Motivation - Self-Consistent Modelling of Critical Plasma Processes in Astrophysical Scenarios 1
1.2 Magnetic Reconnection - Topical Problems of a Long-Discussed Process 4
1.3 The Weibel Mechanism - Microphysical Origin of Astrophysical Magnetic Fields 15
1.4 The Weibel-Two-Stream-Connection - The Plasma Microphysics of Jets and Pulsars 20

2 The Computational Method of Choice: Particle-In-Cell **23**

3 Collisionless Magnetic Reconnection **33**
3.1 The Relativistic Harris Equilibrium 33
3.2 Relativistic Particles in Electromagnetic Fields 38
3.3 The Mechanism of Relativistic Particle Acceleration 40
3.3.1 Abstract 40
3.3.2 Introduction 40
3.3.3 Simulation Description 42
3.3.4 Simulation Results 44
General Time Evolution of Reconnection in a Pair Plasma 44
Initial Plasma Parameter / Acceleration Efficiency Correspondence . 50
Characteristics of the 3D Configuration 53
Detailed Analysis of the Acceleration Mechanism 54
3.3.5 Discussion 59
Particle Acceleration in Electron-Proton Plasma Reconnection 59
Comparison with Previous Results on 2D Scenarios 60
Concluding Remarks on Particle Acceleration in FMR 60
3.4 Synchrotron Signatures of the Self-Consistent Model 62
3.4.1 Abstract 62
3.4.2 Introduction 62
3.4.3 Simulation Model 63
3.4.4 Numerical Results and Physical Picture 64
Non-thermal Particle Generation in the Late-time Evolution 64

Synchrotron Emission . . . 65
3.4.5 Summary and Conclusions . . . 69

4 Magnetic Fields in 3D Weibel Scenarios 71
4.1 Magnetic Fields in γ-Ray Burst Models - Generation, Topology and Lifetime . . . 71
4.2 Ultra-Relativistic Plasma Shell Collisions - The Magnetic Equipartition Ratio . . . 84
4.2.1 Abstract . . . 84
4.2.2 Introduction . . . 84
4.2.3 Simulation Description . . . 86
4.2.4 Dimensional Effects in Relativistic Plasma Shell Collisions . . . 87
Linear Progenitors of the Preeminent Plasma Instability Modes . . . 87
Effects of a Finite Thermal Spread: Kinetic Modifications . . . 91
4.2.5 The Saturated and Steady-State Final Magnetic Fields . . . 96
4.2.6 Summary and Perspectives . . . 104
4.3 Topology and Lifetime - A Critical Test for Synchrotron Emission Models 106
4.3.1 Abstract . . . 106
4.3.2 Introduction . . . 106
4.3.3 Simulation Description . . . 108
4.3.4 Diffusion Limited Lifetime of Magnetic Fields . . . 110
Diffusion Coefficients Obtained by the PIC Simulation . . . 110
Diffusion is Identified as ‘Bohm’-type . . . 115
4.3.5 Consequences for Synchrotron Emission . . . 116
4.4 Self-Consistent Synchrotron Cascades . . . 119

5 The Weibel-Two-Stream Connection 125
5.1 The Electromagnetic Counterstreaming Instability with Magnetic Guide Field . . . 125
5.2 The Connection to Pulsar Physics - Stimulation of Collisionless Bremsstrahlung . . . 135

6 Final Remarks 151
6.1 Achievements . . . 151
6.2 Perspectives . . . 157

A Dimensionless Representation of Physical Quantities 159

B Linear Theory of the 2D EM Counterstreaming Instability 163

List of Publications 177

Acknowledgements 179

Curriculum Vitae 181

Chapter 1

Introduction

1.1 Motivation - Self-consistent Modelling of Critical Plasma Processes in Astrophysical Scenarios

During the recent decades the observational techniques of modern astronomy have reached an unprecedented degree of sophistication. The radiative signatures of astrophysical phenomena are resolved on progressively refined scales in space and time. The wealth of new discoveries challenges the theorist to provide a viable explanation. Plasma physics plays a key role in the solution to the puzzles which have been posed by the recent observational data. Paradigms are the σ-problem of the Crab pulsar wind (section 1.2), the discovery of γ-ray bursts (GRBs) (section 1.3) and the observation of extremely intense pulsar radio outbursts on nanosecond time scales (section 1.4). At a superficial glance diversity proliferates in the observational characteristics of these phenomena: Wavelengths encompass the entire range from γ-rays in GRBs to the radio regime in pulsars. Time scales span from nanoseconds in pulsar radio outbursts to seconds for the 'synchrotron wisps' associated with pulsar winds.

However, a closer look unveils that these observed features are all deeply connected to two fundamental plasma processes: Collisionless magnetic reconnection and collisionless shocks. The quantitative differences in the observations arise solely due to the variety in the plasma parameters of the specific source. Both processes are central problems of plasma-physical research for more than 40 years. So what makes them so special to continuously keep up the minds of theoreticians? The unifying element common to both processes is that they are connected to discontinuities. Magnetic reconnection takes place at a discontinuity in the magnetic field topology. The free energy of shocks is stored in a discontinuity in phase space. Within the realm of classical physics, discontinuities are a mathematical idealization and generally point out critical assumptions in non-selfconsistent physical models.

The crucial point is the combination with collisionless conditions. The plasma in astrophysical sites is usually highly rarefied in density. As the direct consequence, the mean free path of an individual particle becomes large compared to the typical dynamic length scales introduced by kinetic plasma processes. The particles are not anymore scattered in

Coulomb collisions between nearest neighbours, but merely in the collective electromagnetic fields of plasma modes. Coulomb collisions isotropize and thermalize the particle distribution function (PDF) in phase space towards the Maxwellian equilibrium. In the absence of Coulomb collisions the PDF is potentially highly non-thermal.

Theoretical models of the plasma state observe a hierarchical structure of sophistication (cf. chapter 2): The crudest approach is realized in the magnetohydrodynamic (MHD) plasma model. The MHD description is based on the first order moment of the PDF assuming Maxwellian conditions. Consequently the MHD approach is valid only on the macroscopic scales on which the Maxwellian approximation of the PDF is justified. The basic MHD model is successively refined by taking into account higher order moments of the PDF. The trend to reduce the restrictive idealizations culminates in the kinetic plasma description. The kinetic approach considers the complete PDF. In the kinetic model time scales are unambiguously linked to the particle gyro motion and length scales to the plasma inertial length, respectively. Consequently the kinetic model is completely self-consistent. The crucial point is that the kinetic approach is also the most complicated. The numerical treatment is utmostly costly with respect to computational expenses. The dawn of massively parallel supercomputer architectures in the recent years has given a new quality to kinetic plasma modelling. As one freak of nature, the discontinuities associated with collisionless reconnection and collisionless shocks test the microphysical scales. As observational techniques advance to successively higher resolutions, the global MHD description breaks down and microphysics makes a kinetic treatment of plasma processes indispensable.

Plasma astrophysics currently performs a metamorphosis equivalent to the one space plasma physics has been confronted with 30 years ago as satellites paved the way towards *in-situ* measurements in the earth's magnetosphere. The presented work is dedicated to the self-consistent, kinetic modelling of plasma processes critical in the context of astrophysical research. Explicitly, these processes are collisionless kinetic reconnection and the Coupled Two-Stream-Weibel (CTW) instability. The CTW is the electromagnetic instability mode which proceeds in the wake of collisionless shocks.

Which characteristics distinguish these plasma processes as distinctively *critical*?

- Both processes are of fundamental nature, i.e. are ubiquitous in astrophysical plasmas. The reason is obvious: Magnetic discontinuities and plasma entities with significant relative bulk drift appear necessarily at the boundaries of different source environments. Reconnection and the CTW mode are kinetic instabilities and therefore fast by definition. The inherent growth rates supersede the growth of competing modes. Consequently both prevail as the dominant processes.

- Essential features appear in the highly dynamic phase during the late-time evolution. Since plasma dynamic scales are short compared to astrophysical time scales, the non-linear saturation at late times is the prevalent state in astrophysical sites. This instability regime is entirely in the domain of numerical simulations.

- The physics of both processes crucially depends on microscopic plasma scales.

Therefore the simulation demands a self-consistent, kinetic plasma model. We convened on the Particle-In-Cell (PIC) approach and employed a fully electromagnetic, relativistic, massively parallelized code.

- A dimensional reduction to simplify the numerical treatment is impossible. Both processes require the complete representation of all 6 phase space dimensions. Dimensional reduction in previous studies has implied non-physical artifacts.

- Both processes show significant relativistic modifications, i.e. obtain a new quality in the inherently relativistic regime of pair plasma dominance. In such plasma environments the equipartition Alfvén velocity becomes comparable to the speed of light $\mathrm{v_A} \sim \mathrm{c}$. Then plasma dynamic scales are equivalent to electromagnetic scales.

- Self-consistent numerical modelling is computationally utmostly expensive. Kinetic simulations of 3D scenarios comprise about 10^9 particles and endure for several 10^4 time steps. This corresponds to roughly 150 GByte main memory and 50000 CPhs computing time. Such hardware requirements are only accessible by the massively parallel architectures of high performance supercomputing facilities.

- Finally, the term *critical* pays homage to Roald Sagdeev's *The 1976 Oppenheimer lectures: Critical problems in plasma astrophysics* [Sagdeev, 1979a;b] in which the reconnection and shock problem assume a central issue.

The present work is structured in the following fashion: The foundations and potentials of the Particle-In-Cell approach as self-consistent kinetic plasma model are discussed in chapter 2. In section 1.2 we introduce on the topical problems of collisionless reconnection. In chapter 3 follow pioneering simulations on particle acceleration in Fast Magnetic Reconnection (FMR) of relativistic pair plasmas. This is the first self-consistent treatment of relativistic reconnection and associated synchrotron signatures in 3D scenarios. In section 1.3 we give a primer on the importance of the CTW mode in the context of generic GRB synchrotron shock models. The corresponding PIC simulations of GRB internal and external shocks are subject to chapter 4. We provide fundamental insights into the self-consistent generation and diffusion-limited lifetimes of CTW magnetic fields. In section 1.4 we generalize the potential importance of the CTW in the context of jet and pulsar physics. In chapter 5 we present the detailed linear analysis of the CTW mode and the effects of a magnetic guide component on the respective mode degeneracy. This provides the framework for the PIC simulation study of Coherent Collisionless Bremsstrahlung (CCB) as a possible explanation of pulsar radio outbursts. We conclude in chapter 6 with a final account of achievements and a brief comment on future perspectives.

1.2 Magnetic Reconnection - Topical Problems of a Long-Discussed Process

The process of *magnetic reconnection* or *field line merging* is one of the most extensively studied phenomena in plasma physics. The term *reconnection* originally refers to a theoretical scenario describing the interaction of the interplanetary magnetic field carried by the solar wind and the field of the earth's magnetosphere (Fig. 1.1). Since the interplanetary and the earth's dipolar field have roughly opposite orientation, a region of antiparallel magnetic field lines results at the dayside magnetospheric boundary (cf. field line 1 in Fig. 1.1a). In principle the interplanetary field lines 'frozen in' the solar wind plasma can laterally pass towards the nightside without further interaction with the earth's dipolar field. However, the magnetospheric plasma abundance points towards a vivid interaction with the solar wind. Furthermore observations indicate that field line convective motion takes place azimuthally across the polar regions towards the nightside. Antiparallel field lines in close proximity represent an energetically metastable configuration. Parker [1957] therefore proposed a scenario in which antiparallel field

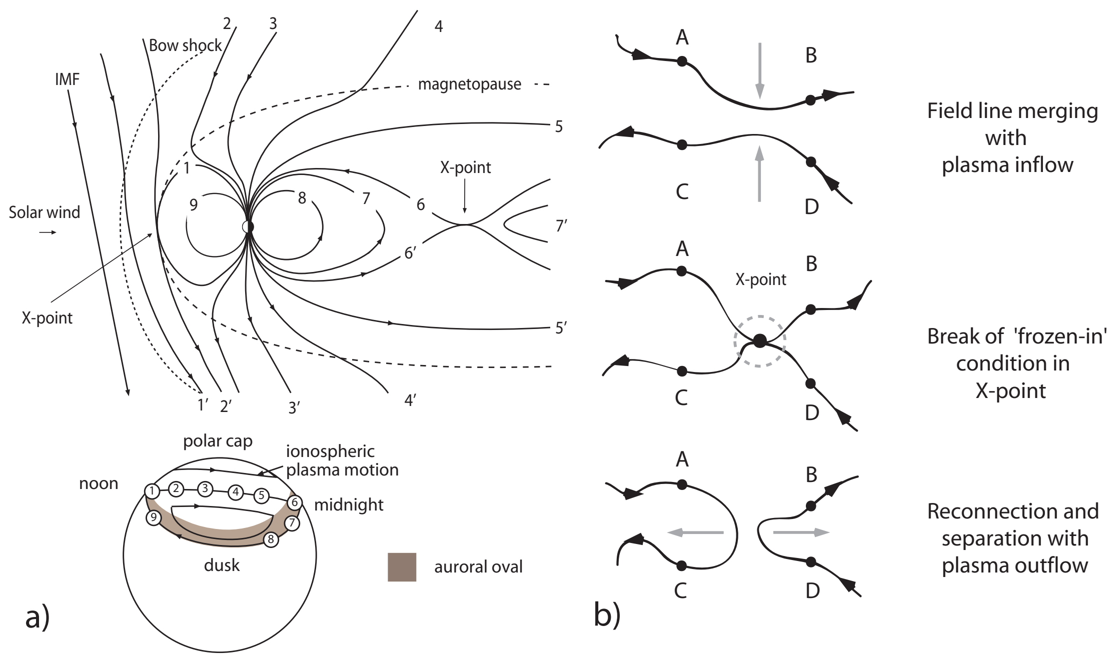
IMF
Bow shock
2
3
4
magnetopause
5
1
X-point
9
8
7
6
Solar wind
→
7′
6′
X-point
5′
1′
2′
3′
4′
polar cap
ionospheric
plasma motion
noon
①
②
③
④
⑤
⑥
midnight
⑨
⑦
⑧
dusk
auroral oval
a)
A
B
Field line merging
with
plasma inflow
C
D
A
X-point
B
Break of 'frozen-in'
condition in
X-point
C
D
A
B
Reconnection and
separation with
plasma outflow
C
D
b)

Fig. 1.1: Historical definition of magnetic reconnection (a): Magnetic field lines of the earth's dipolar field break up in the dayside X-point (line 1) and *reconnect* on the nightside (line 6). In a schematic description (b) magnetic reconnection defines the process of field line merging, the restructuring of magnetic topology around the X-point and final disentanglement.

lines merge towards an X-shaped configuration. The field lines break up in this X-point and connect to the respective field lines of the solar wind plasma on the dayside, pass over the polar regions and *reconnect* again on the nightside (cf. the evolution of lines 1-8 in Fig. 1.1a). The fundamental processes at the dayside and nightside X-points are equivalent. Therefore deviating from the historical introduction the term *magnetic reconnection* generally refers to the schematic process which is outlined in Fig. 1.1b: Magnetic field lines are connected to the plasma inflow into the reconnection zone and merge towards each other. In close proximity to the X-point the *frozen-in* condition is violated. In this region the field lines decouple from the plasma motion, i.e. the field lines 'break up' and *reconnect*. The phenomenon of magnetic reconnection is unique in plasma physics because it is the only process which is in the position to change the magnetic field topology. This has profound implications on the plasma transport in the respective area: Before the reconnection event plasma particles which are appendant to different field lines (cf. points A and C in Fig. 1.1b) interact only on diffusive time scales. After reconnection took place the particles are interchanged with thermal velocities between the points A and C. Since collisionless cross-field diffusion is generally much slower than any thermal motion, magnetic reconnection is the key process to understand the plasma flows and plasma mixing. Finally the reconnected field lines disperse with the plasma flow out of the reconnection zone. The free energy of the process is stored in the initial magnetic field configuration. During magnetic reconnection the magnetic tension is relaxed and the free energy is converted into particle kinetic energy.

Such an elementary definition implies that magnetic reconnection is ubiquitous in plasma scenarios of any kind. Magnetic reconnection plays a key role in the plasma laboratory on earth (for instance Baum & Bratenahl [1980]; Stenzel [1982]; Yamada [1997]), in the eponymous solar-terrestrial plasma interconnection [Øieroset et al., 2001; Treumann & Scholer, 2002], furtheron in planetary and stellar magnetospheres [Schaefer et al., 2000] like during magnetic substorms [Slavin et al., 2002] and flares [Priest, 2001], in plasma turbulence in the interstellar medium, and in magnetic topologies of expanding supernova shells [Aharonian et al., 2004], active galactic nuclei [Lesch & Reich, 1992; Lesch & Birk, 1997; Jaroschek, Lesch, & Treumann, 2004a] and extragalactic jets [Lesch & Birk, 1998]. Already foreshading its fundamental nature, the survey of phenomena in which magnetic reconnection is expected to be present spans from human adapted meter-scale, over solar system typical astronomical-unit-(AU)-extensions, up to extragalactic mega-parsec-scale-sizes. Magnetic reconnection is involved in all scenarios in which plasma entities with individually homogeneous magnetic field structure are confronted and thereby form boundary layers with critical discontinuities [Sagdeev, 1979a;b; Bulanov et al., 2002]. Consequently magnetic reconnection appears to be omnipresent in plasma physics.

Likewise abundant is the variety of theoretical concepts attempting to attack the various facets of the reconnection problem. Such efforts differ in the sophistication of the plasma model, the initial configuration and the invoked dimensional degrees of freedom. The applied plasma models range from elementary hydrodynamic flux equilibria, successively refined by compressible, magnetokinematic and -dynamic effects, up to kinetic Maxwell-Vlasov approaches. Initial setups start with rudimentary ad-hoc discontinuities of anti-parallel fields, continue with hyperbolic magnetic configurations around a central X-point, include neo-classical modifications and end with self-consistent kinetic quasi-equilibria like the Harris solution. The accumulated literature is vast. A detailed compendium on such concepts is found in Biskamp [2000].

More than 40 years of research have passed since the original idea of the reconnection mechanism was introduced. Still a cumbersome number of unanswered questions remain. This, in combination with the ubiquity in plasma scenarios, makes magnetic reconnection a critical process by definition. In the present work we focus on the topical issues of the reconnection problem. Despite of the simple definition, the reconnection process turns out to be very complex in detail. This is due to the following characteristics:

- Magnetic reconnection is a microphysical and inherently kinetic phenomenon. Therefore the self-consistent treatment requires a kinetic plasma model.
- The magnetic field/plasma motion topologies are three dimensional, i.e. a dimensional reduction to simplify the analytic treatment or to reduce the computational effort is impossible.
- The evolution of reconnection is chaotic in the sense that the process depends critically on the choice of initial conditions.
- During the reconnection process magnetic field components of opposite orientation annihilate, i.e. physical quantities change on a scale height comparable to its absolute magnitude. Consequently reconnection is a highly non-linear phenomenon.
- Self-consistent kinetic plasma simulations are utmostly expensive with respect to computational costs. Three dimensional reconnection scenarios require massively parallel architectures and tens of thousand CPUhs of computing time on contemporary top-level supercomputers.

Magnetic reconnection is not only an interesting subject of fundamental plasma research. Beyond the pure academic objectives reconnection represents one of the key processes in astrophysical scenarios. As already mentioned earlier, in astrophysical sites the plasma is pervasively collisionless. Since *in-situ*-measurements are impossible, the radiative features are the unique probe to astrophysical plasma conditions. In the collisionless case thermal emission processes and non-thermal Bremsstrahlung become insignificant. Pulsar winds and extragalactic jets are paradigms for plasmas which are density-rarefied to an extent that Comptonization is also negligible. In such cases synchrotron emission remains as the dominant process. Typical synchrotron cooling times are long compared to reconnection time scales. Therefore the radiative signatures of synchrotron emission are characterized by the dynamic evolution of magnetic field topologies and continuous *in-situ* reacceleration of particles. In both processes magnetic reconnection plays a key role. A quantitative understanding of the reconnection problem from first principles is therefore indispensable. The topical issues in contemporary reconnection research are addressed below.

The mechanism of fast magnetic reconnection

The fundamental reconnection models proposed by Parker [1957] and Sweet [1958] are based on a magnetohydrodynamic (MHD) description of the plasma (cf. chapter 2 for details on the differences between the MHD and the kinetic plasma description). Therein the reconnection zone assumes the shape of a magnetic nozzle (Fig. 1.2). Within the MHD description the nozzle remains macroscopic in length L, whereas the width δ is resistivity-dependent [Biskamp, 1986; Biskamp & Bremer, 1993]. The plasma outflow is mediated by Alfvén waves and, hence, the maximum outflow speed is limited to the Alfvén velocity $\mathrm{v_A}$. In the collisionless case the resistive diffusion becomes very small and therefore the nozzle width tends to $\delta \rightarrow 0$. The plasma inflow into the reconnection zone is severely limited by the simple flux conservation argument $\mathrm{v_{in}} \sim (\delta/\mathrm{L})\,\mathrm{v_A} \ll \mathrm{v_A}$. The plasma inflow determines the reconnection rate. The slow reconnection rates predicted in the framework of the Sweet-Parker model fail to describe the explosive reconnection events observed in solar flares or magnetospheric substorms by several orders of magnitude. Petschek [1964] attempted to overcome the resistive limitations in bypassing the diffusion zone. In Petschek's scenario the gross yield of the reconnection flux is mediated by four standing shock waves which are laterally attached to the nozzle outflow area. However, the systematic problem of nozzle throttled slow reconnection remains.
In the recent years the process of fast magnetic reconnection (FMR) in electron-proton plasma has been subject to intense scrutinities in the framework of the Geophysical Environment Modelling (GEM) Challenge [Birn et al., 2001]. The essential results subsume to the following: Magnetic reconnection is a multi-scale process [Sonnerup, 1979]. Be-

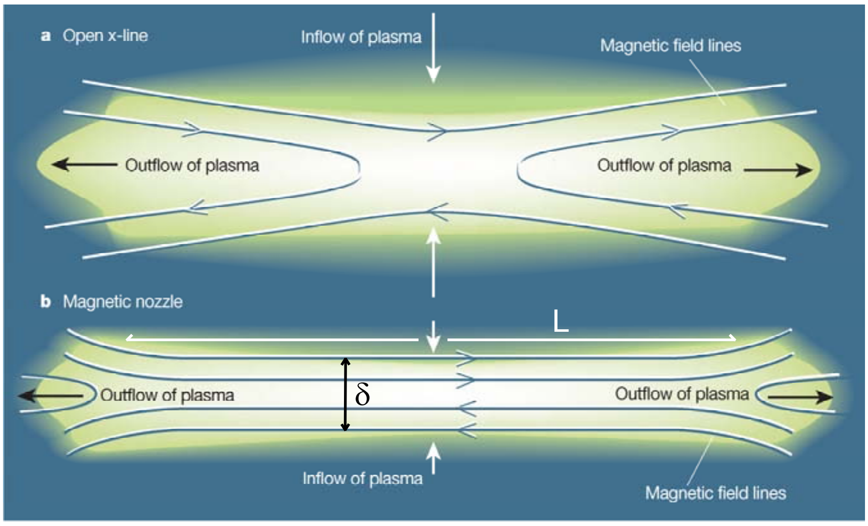

Fig. 1.2: The mechanism of Fast Magnetic Reconnection favors the open X-line configuration to overcome the restrictions of nozzle throttling of the Sweet-Parker model. (Source: Drake [2001])

yond the ion inertial length scale $c/\omega_{\mathrm{pi}} = c(m_i/4\pi e^2 n)^{1/2}$ the MHD description is valid. Below c/ω_{pi} the ions demagnetize whereas the electrons remain coupled to the magnetic field down to $c/\omega_{\mathrm{pe}} \ll c/\omega_{\mathrm{pi}}$. The different behaviour of electrons and protons in this transition region gives rise to in-plane Hall currents [Terasawa, 1983]. All plasma models incorporating a Hall term show comparable gross reconnection rates [Shay et al., 2001]. Below electron inertial scales c/ω_{pe} the electrons also decouple from the magnetic field. Most remarkable: The electron dissipation region L_e remains microscopic in length. Consequently, the plasma inflow is Alfvénic $v_{\mathrm{in}} \sim \delta_e/L_e \simeq c/\omega_{\mathrm{pe}}L_e \sim v_A$ and, hence, magnetic reconnection is fast by definition. In the diffusion zone FMR is mediated by whistler waves [Shay & Drake, 1998; Shay et al., 1999; 2001; Drake, 2001]. Whistler waves show the characteristic of quadratic dispersion $\omega \propto k^2$, i.e. the whistler phase velocity $v_{\mathrm{ph}} = \omega/k \propto k$ is proportional to the wavenumber. This dispersive behaviour is responsible for the name 'whistler', since high frequencies travel faster and reach radio interceptors first, announcing a falling tone. The flux of outflowing plasma $\sim \delta_e v_{\mathrm{ph}}$ remains finite even at microscopic widths of the outflow region because $v_{\mathrm{ph}} \propto k \sim 1/\delta_e$ holds.

In the case of an electron-proton plasma the FMR rates are ultimately limited by ion inertia. On the larger ion inertial scales the flux conservation $v_{\mathrm{in}} \sim \delta_i/L$ allows near-Alfvénic inflow and Alfvén wave mediated outflow. In Rogers et al. [2001] FMR is associated with whistler / kinetic Alfvén dynamics appendant to an open X-line configuration as illustrated in Fig. 1.2. In conclusion, the distinct characteristics of fast magnetic reconnection (FMR) are that the plasma inflow is Alfvénic and the reconnection rate is independent of the scale size of electron demagnetization.

In chapter 3 we study FMR in relativistic electron-positron plasmas. Since both species have equal masses, reconnection proceeds solely on the electron scale and the reconnection rate is not limited by ion inertia. As shown below, the Hall term is absent in pair plasmas. Nevertheless reconnection is fast with Alfvénic inflow. The current sheet thickness of the relativistic Harris solution (cf. section 3.1) corresponds to the demagnetization scale size. The reconnection is independent of the current sheet thickness. Consequently, the essentials of the FMR mechanism are retained in the case of astrophysical pair plasma reconnection.

Collisionless resistive diffusion in the reconnection zone

In an ideally conducting plasma the field lines are 'frozen-in', i.e. the plasma motion is directly coupled to the magnetic field. Reconnection takes place in an area in which some non-ideality decouples particles and field. This localized region in space is generally referred to as the *diffusion region*. Especially in pair plasma reconnection the electron dynamics in the diffusion zone are ultimately important. Outside of the diffusion region the plasma observes the ideality condition

$$\mathbf{E} + \mathbf{v}/c \times \mathbf{B} = 0,$$

i.e. the MHD description of the plasma is valid. On entering the diffusion zone the electrons decouple from the magnetic field owing to their finite thermal velocity [Laval et al., 1966] or their convective motion [Dungey, 1988; Burkhart et al., 1990]. In a more formal fashion the various types of non-idealities are included in the generalized Ohm's Law [Krall und Trivelpiece, 1986] for two species (ions s=i and electrons s=e) with $\mathbf{V}$ the center-of-mass (cms) velocity:

$$
\begin{array}{rl}
\frac{\partial \mathbf{J}}{\partial t} + \nabla \cdot (\mathbf{VJ} + \mathbf{JV} - \mathbf{VV} e(n_i - n_e)) = & \text{current density rate of change} \\
e^2 \left(\frac{n_i}{m_i} + \frac{n_e}{m_e}\right) \mathbf{E} & \\
 & \text{Lorentz force / MHD description} \\
+ \left(\frac{e^2}{m_e c} + \frac{e^2}{m_i c}\right) \left(\frac{n_e m_e + n_i m_i}{m_e + m_i}\right) \mathbf{V} \times \mathbf{B} & \\
- \frac{e}{c} \left(\frac{m_i}{m_e} - \frac{m_e}{m_i}\right) \frac{1}{m_e + m_i} \mathbf{J} \times \mathbf{B} & \text{Hall term} \\
- \frac{e}{m_e} \nabla \cdot (P_i \frac{m_e}{m_i} - P_e) & \text{pressure gradient} \\
+ \sum_{s=i,e} \int q_s n_{0,s} \mathbf{v} \, \frac{\partial f_s}{\partial t}|_{coll} \, d\mathbf{v} & \text{Coulomb collision term}
\end{array}
$$

In the collision-dominated case the collision term is linearly approximated by $-\nu \mathbf{J}$. Then we retain in the case of negligible magnetic field the familiar version of Ohm's Law $\mathbf{E} = \eta \mathbf{J}$ with the resistivity $\eta = \nu \mathrm{m_e}/\mathrm{n_e e^2}$ determined by the collision frequency ν. However, in collisionless astrophysical plasmas the contributions from the collision term become insignificant. Then we are in the realm of collisionless resistivity. Several plasma microinstabilities are potential candidates to generate collisionless resistivity, though the definite answer to the origin of resistivity is still to be found (for a detailed discussion see Treumann [2001]). Sagdeev [1979a] considered ion acoustic turbulence as the preeminent contribution to collisionless resistivity. The ion acoustic modes are triggered beyond a minimum threshold current density $\mathrm{j_c}$. Therefore non-self-consistent plasma models (for instance resistive MHD simulations) include a current-dependent resistivity $\sim \eta(\mathrm{j} - \mathrm{j_c})$ which sets in above the critical threshold.

Self-consistent kinetic plasma models like the Particle-In-Cell approach (cf. chapter 2 for details on the simulation model) take into account all contributing terms of the generalized Ohm's Law. Astrophysical plasmas are inherently quasi-neutral ($\mathrm{n_i} = \mathrm{n_e}$). Consequently, electron demagnetization is reflected in the current inertial terms and/or in non-gyrotropic components [Hesse et al., 1999; Pritchett, 2001] of the pressure tensor (indicated in red). These terms then balance the reconnection electric field which is absent in the MHD description (indicated in blue). Obviously, the Hall term is generally absent in pair plasmas. This is physically intuitive, since the Hall term results from a multi-scale diffusion region as the consequence of plasma components with large mass differences.

From a purely plasma-theoretical point of view the identification of terms contributing to collisionless resistivity is interesting. However, to understand the importance of magnetic reconnection in astrophysical sites the detailed diagnostics of collisionless resistivity is irrelevant. This follows from two important insights. First, PIC simulations are completely self-consistent and all terms of the generalized Ohm's Law are included. Second and most important: On astrophysical time scales reconnection proceeds in highly non-linear phases. In the non-linear regime reconnection rates are independent of the mechanism that breaks the ‘frozen-in’ condition [Biskamp et al., 1997; Shay & Drake, 1998; Hesse et al., 1999; Pritchett, 2001]. Therefore we focus, in the framework of the present work, on the consequences of FMR and current sheet instabilities with respect to particle acceleration in relativistic pair plasmas.

Instabilities of thin current sheets

Magnetic reconnection takes place at discontinuities in the magnetic topology. The field gradient associated with the discontinuity drives a balancing current along the separatrix. In order to start from a well-defined initial configuration the PIC simulations are initialized with the Harris solution for a plane-parallel discontinuity between exactly anti-parallel fields. The Harris configuration is the only analytical solution for anti-parallel fields that is consistent with the Maxwell-Vlasov set of plasma equations. Details on the relativistic generalization of the Harris solution for pair plasmas are found in section 3.1.

The instabilities of thin current sheets divide into a class propagating parallel to the current (i.e. perpendicular to the magnetic fields) and another class with propagation perpendicular to the current. The current-parallel instabilities cause macroscopic current sheet deformations which are either symmetric (i.e. of sausage-type) or anti-symmetric (i.e. of kink-type). These macroscopic deformations are caused by microscopic plasma instabilities. On long time scales and with significant plasma background on the current sheet outskirts the fluid-type Kelvin-Helmholtz-Instability (KHI) triggers current-sheet-kinking [Daughton, 1999]. However, the KHI growth rate is small compared to kinetic instabilities, and contributions for rarefied background (as is the case in the presented PIC simulations) are insignificant. In the case of an electron-proton plasma the electric field of the Lower-Hybrid-Drift-Instability (LHDI) triggers the sheet deformation [Yoon et al., 2002; Scholer et al., 2003; Shinohara et al., 2001]. The Relativistic-Drift-Kink-Instability (RDKI) is the analogon for pair plasma current sheets. The RDKI is identified as the dominant current-parallel instability mode in 2D [Zenitani & Hoshino, 2005] and realistic 3D [Jaroschek et al., 2004] self-consistent PIC simulations.

In current-perpendicular (i.e. magnetic field-aligned) direction impinges the tearing-mode-instability (TMI) [Syrovatskii, 1971; Jaroschek et al., 2004]. The TMI is an aperiodic standing and purely electromagnetic instability. Consequently the TMI remains unaffected by the electrostatic fields introduced by the drift modes. In sections 3.3 and 3.4 the instabilities of thin pair-plasma current sheets are studied for the first time self-consistently in 3D scenarios. Three dimensions are essential because TMI and RDKI proceed in respectively perpendicular planes. The electromagnetic TMI and electrostatic RDKI compete because, in a leptonic plasma, the Alfvén velocity is comparable to the speed of light $\mathrm{v_A} \sim \mathrm{c}$. Furthermore, for the thin sheets under consideration, the relative drift of charge species is sufficiently high to drive the Relativistic-Two-Stream-Instability (RTSI). The RTSI then serves as the trigger mechanism for the RDKI. The simulations show that RDKI and TMI exhibit comparable growth and only a photo-finish can decide which instability disrupts the current sheet in the first place. Certainly, this result has profound implications for the particle acceleration associated with thin current sheet reconnection.

3D topologies and particle acceleration

Understanding the particle dynamics is the key towards an explanation of the physics in astrophysical sites. Since *in-situ* measurements are impossible, the radiative signatures of energetic charged particles in magnetic fields represent the unique probe for the physical conditions in collisionless plasmas. A plasma state under equilibrium conditions is initially thermalized, i.e. of Maxwellian nature. The spectral analysis of a variety of astrophysical objects ranging from γ-ray bursts, over pulsar nebulae, to quasars and relativistic jets shows prominent power-law synchrotron features in wavelength regimes specific for these sources. For pitch-angle isotropized particle distribution functions (PDFs) a power-law shaped synchrotron spectrum directly translates into a power-law in the PDF (cf. section 4.4 for characteristics of the synchrotron emission process). Consequently the essential issue boils down to a few very simple questions:

- Which plasma process generates self-consistently a power-law shaped particle distribution $\mathrm{f}(\gamma) \propto \gamma^{\mathrm{s}}$ in relativistic energy?
- What is the particle acceleration mechanism?
- Is there a characteristic power-law spectral index s associated with a specific source process?

These questions are the central motivation to the simulations of FMR in relativistic pair plasmas in section 3.3. For the first time the mechanism of pair plasma FMR is studied self-consistently in 3D configurations. The previous discussion of current sheet instabilities already pointed out that FMR is an inherently 3D process. Especially the mechanism of particle acceleration is inextricably connected to the 3D topology of electric and magnetic fields. Therefore the full resolution of three spatial dimensions is indispensable in this context:

The efficiency of particle acceleration depends crucially on the electric potential gain in the reconnection zone $\Delta\Phi \simeq \mathrm{E}_{\mathrm{acc}}\Delta\mathrm{x}$, i.e. the average acceleration electric field $\mathrm{E}_{\mathrm{acc}}$ and the extension $\Delta\mathrm{x}$ perpendicular (!) to the 2D plane in which the TMI / reconnection plasma inflow take place. In 2D configurations [Zenitani & Hoshino, 2001] the acceleration potential is infinite and the acceleration step is terminated by the deflection of the respective particle out of the reconnection zone by the newly reconnected magnetic field lines. Solely 3D self-consistent kinetic plasma simulations provide a definite answer to the particle acceleration efficiency during reconnection (as discussed in chapter 2 the study of test particles in 3D MHD field configurations is inadequate, since the MHD acceleration potential remains freely scalable).

The simulated volume is comprised by more than 10^9 particles and large enough to advance towards the late time evolution. FMR proceeds on in a quasi-stationary single

X-point at early times and turns into highly dynamic 3D scenario at late times which is governed by the current sheet instabilities. We resolve the finite extension Δx of the reconnection zone. Furthermore we identify the various acceleration mechanisms via trace particles. Most remarkable: FMR generates self-consistently a power-law-shaped PDF of relativistic particles out of an initial Maxwellian. The power-law index assumes $\mathrm{s} = -1$ within the reconnection zone and $\mathrm{s} = -3$ for a larger volume in which TMI (reconnection) and RDKI are competing current sheet instabilities. The power-law indices are stable throughout the quasi-stationary regime at early times as well as the dynamic regime of reconnection at late-times. We conclude that the respective power-law index is of universal nature and is unambiguously connected to the process of FMR in relativistic pair plasmas.

To exploit the consequences for astrophysical studies, we calculate synchrotron spectra, polarizations and total power dissipations for the first time from self-consistent PIC data in section 3.3. As FMR proceeds towards the turbulent regime at late times the pitch angle distribution is isotropized. As a direct consequence thereof, extremely hard synchrotron spectral indices of $\mathrm{s} = -0.17$ within the inner X-zone and $\mathrm{s} = -1.36$ for the entire configuration are reached. The hard spectra are accompanied by strong polarization. We applied the simulation data to typical environment conditions expected in extragalactic radio sources. The obtained synchrotron features in combination with the specific temporal and spatial characteristics of the FMR process provide a valid scenario for intra-day variabilities, spectral features and extreme power outputs which are observed from such sources.

Hot issues for pair plasma reconnection in astrophysical sites

As has been pointed out magnetic reconnection is an ubiquitous phenomenon in plasma astrophysics. However, there are some examples of peculiar interest in astrophysical research which are puzzling theoreticians for decades and are deeply related to FMR in pair plasmas.

The striped magnetic wind of the Crab pulsar is one of such conundrums. The pulsed radiation emission comprises only a tiny fraction of the pulsar's spin-down energy. The preeminent power outflow is constituted by the Poynting-flux-dominated pulsar wind [Rees & Gunn, 1974; Michel, 1982; Arons, 1983; Hibschmann & Arons, 2001]. The outflow is Poynting-flux-driven when the magnetic energy density dominates the kinetic energy density which is quantitatively reflected in the ratio $\sigma = \mathrm{B}^2/8\pi(\gamma - 1)\mathrm{nmc}^2 \geq 1$. In non-axisymmetric pulsar models [Gunn & Ostriker, 1969] the magnetic field assumes an oblique dipole. Then the pulsar wind forms toroidal 'stripes' of opposite magnetic polarity in the equatorial plane (Fig. 1.3d-f). The σ-problem of the Crab pulsar wind is posed by the termination shock of the striped wind, i.e. the diffusely defined transition of the pulsar wind into the surrounding pulsar wind nebula (PWN).

Recently, the transition region has found an impressive observational confirmation in a joint effort of the Chandra X-ray observatory and the Hubble space telescope (Fig. 1.3a-c). Both orbiting scopes teamed up to show the termination shock of the pulsar wind in correlated X-ray and optical events. The Chandra X-ray data (Fig. 1.3a) discloses

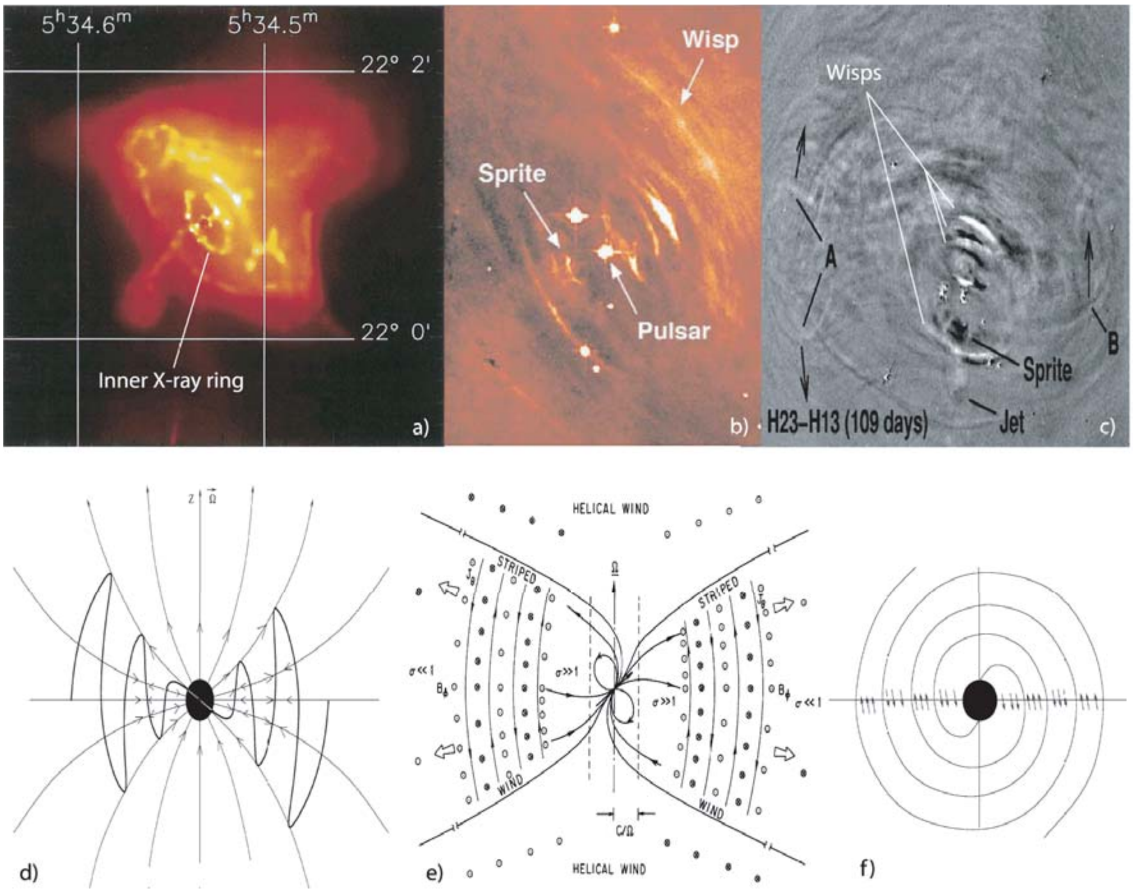
5h34.6m
5h34.5m
22° 2'
22° 0'
Inner X-ray ring
a)
Wisp
Sprite
Pulsar
b)
Wisps
A
B
Sprite
H23–H13 (109 days)
Jet
c)
z Ω
d)
HELICAL WIND
STRIPED
WIND
Ω
σ<<1
B_φ
σ>>1
J_θ
C/Ω
HELICAL WIND
e)
f)

Fig. 1.3: Fast Magnetic Reconnection (FMR) as the possible solution to the σ-problem of the Crab pulsar wind: Chandra resolves the inner X-ray ring marking the transition of the Poynting-flux-dominated pulsar wind into pulsar wind nebula [Weisskopf et al., 2000]. The nebula upstream of the termination shock is dominated by particle-born kinetic energy and the associated synchrotron burn-off illuminates the entire X-ray torus (a). Emerging wisps indicate the dynamic structure of the striped pulsar wind. The wisps appear exactly correlated (b,c) in the optical passbands of the Hubble Space Telescope [Hester et al., 2002]. The observations give credit to the model of a striped magnetic wind which is nourished in the mind of theoreticians for more than 20 years. Poynting-flux-driven winds emerge in the equatorial plane of an oblique rotator (d). Force-free conditions imply that the oscillating magnetic field stripes are separated by current sheets (e,f). Self-consistent PIC simulations of FMR serve to understand the microphysics of the transition from Poynting-flux-dominated flow conditions ($\sigma \geq 1$) to particle-born kinetic energy ($\sigma \ll 1$) as has been first proposed by Coroniti [1990](e).

the inner X-ray ring as the inner edge of the PWN torus. The ring marks the transition of the pulsar wind Poynting-flux into particle-born-flux and the successive synchrotron burn-off of the most energetic particles. According to the spectral analysis [Mori et al., 2004] the synchrotron spectral index assumes $s = -0.9$ over the entire torus independent of the surface brightness, and gradually softens to $s \sim 2$ towards the outskirts. Crisp, narrowly defined arcs emerge intermittently from the ring and remain confined to the equatorial plane. Such 'wisps' show correlated signatures in the optical Hubble data (Fig. 1.3b,c). The wisps are prominent indications of the striped wind model. Apparently the events at the termination shock are restricted to the most energetic particles, because presently there is no correlated pendant to the wisps found in the radio regime [Bietenholz et al., 2004].

The pulsar wind nebula is freely expanding. In order to reconcile with the observed expansion speed the theoretical wind models end up with an extremely low magnetization $\sigma \sim 10^{-2}$-10^{-3} [Coroniti, 1990; Michel, 1994; Shibata et al., 2003; Mori et al., 2004] just upstream of the shock front. Consequently the σ-problem translates to the simple question: Is there a plasma process providing a valid explanation for such an extremely efficient conversion of Poynting-flux into particle-born-flux ?

The demagnetization of ideal MHD flows is far to slow [Lyubarski & Eichler, 2001; Lyubarski, 2002] for the observed expansion rates. The same argument kills the concept of MHD shock fronts [Lyubarski, 2003]. Furthermore, assuming an ideal MHD flow for the striped wind incorporates a systematic weakness. During radial expansion the density of the charge carriers attenuates faster than the oscillating component of the magnetic field. At some point the drift speed of the current carriers approaches the speed of light and the force-free equilibrium condition breaks down [Melatos & Melrose, 1996].

Alternatively, the concept of magnetic reconnection as the pervasive Poynting-flux dissipation mechanism is extremely promising [Kennel & Coroniti, 1984; Coroniti, 1990; Michel, 1994; Lyubarski & Kirk, 2001; Kirk & Skjæraasen, 2003]. The current sheets at the discontinuities of the magnetic stripes are unstable to magnetic reconnection. Granted that the reconnection rate is sufficiently high, there are solutions which are consistent with the Poynting-flux dissipation rate and the stability of the striped pulsar wind scenario. The critical assumptions in such concepts concern the microphysics of FMR. The PIC simulation studies in chapter 3 provide the first insights into how FMR proceeds self-consistently in relativistic pair plasma. In conclusion, the obtained dissipation efficiencies provide the first reliable foundation to attack the σ-problem from first principles.

1.3 The Weibel Mechanism - Microphysical Origin of Astrophysical Magnetic Fields

Another fundamental scenario in astrophysics is the interaction of counterstreaming plasma flows. Under collisionless conditions plasma entities with different bulk motion (= plasma shells) interpenetrate deeply. The resulting counterstreaming motion triggers the Electromagnetic Counterstreaming Instability (EMCSI) or Coupled Two-Stream-Weibel (CTW) mode. Particles are scattered off the collective electromagnetic fields of the instability. The EMCSI is a coupled instability mode comprised by an electrostatic, parallel mode and an electromagnetic mode, which proceeds entirely perpendicular to the bulk motion. The electromagnetic component is plainly described by the Weibel mechanism [Weibel, 1959]. The physical nature of the Weibel process is intuitively understandable: Like charges comoving with an individual plasma shell represent parallel currents. Parallel currents are mutually attractive. Incipient current filaments are confined by a toroidal magnetic field. The magnetic field self-pinches its generating current, thereby closing the instability feedback loop. Due to the coalescing currents the Weibel mode is also referred to as electromagnetic filamentation instability. In the previous section magnetic reconnection is introduced as the process which converts magnetic field energy into particle kinetic energy. The Weibel mechanism facilitates the complementary scenario of magnetic field generation driven by the relative plasma bulk motion. We regard the generation of magnetic fields by the EMCSI as a critical process for several reasons:

- Magnetic field generation via Weibel filamentation is a fundamental process. This is because plasma flows with relative bulk drifts are ubiquitous in astrophysical sites and the Weibel process is fast, i.e. takes place on plasma inertial time scales.

- Weibel filamentation is inherently kinetic and the EMCSI proceeds in the non-linear regime in 3D. Consequently a dimensional reduction is impossible. The simulations require a fully electromagnetic, kinetic plasma model.

- The Weibel mechanism evolves to full strength in the relativistic regime. The original work by Weibel [1959] considered anisotropic Maxwellians of non-relativistic temperature. In this case the magnetic field generation ranges around $\epsilon_{\mathrm{B}} \sim 10^{-5}$. The equipartition value $\epsilon_{\mathrm{B}} = \int \mathrm{dV}\, \mathrm{B}^2 / \int \mathrm{dV}\, 8\pi(\gamma - 1)\mathrm{mnc}^2$ is the dimensionless quantity characterizing the efficiency of magnetic field generation (cf. the magnetization parameter σ in the reconnection scenario).
  Relativistic counterstreaming plasma flows represent an extreme temperature / momentum anisotropy. In this case the Weibel mechanism assumes an entirely different quality and the magnetization advances up to $\epsilon_{\mathrm{B}} \sim 0.1$, i.e. 10 % of equipartition [Silva et al., 2003; Jaroschek, Lesch & Treumann, 2004c].

Recently [Medvedev & Loeb, 1999] proposed the Weibel mechanism for the conversion of the kinetic energy stored in ultra-relativistic particle flows into Poynting flux. Such mechanisms are essential to circumvent the *compactness problem* in extreme outbursts of high energy radiation. Γ-ray bursts (GRBs) are the paradigm for such events. In the wake of [Medvedev & Loeb, 1999]'s advance the community of theoretical astrophysics shares growing interest in the Weibel mechanism in the context of the GRB fireball and of conceptual GRB synchrotron emission models. Before continuing with the physics of relativistic 3D Weibel scenarios, we intermittently introduce on the phenomenon of γ-ray bursts.

A concise primer on γ-ray bursts

GRBs have remained a riddle to theoreticians since their accidental discovery by the Vela satellites in the late sixties [Klebesadel et al., 1973]. The Vela satellites were part of a military surveillance operation monitoring the compliance of the 'Outer Space Treaty' - the ban on nuclear tests in the earth's magnetosphere. The γ-ray sensitive detectors monitored an unexpectedly high number of events which turned out to be not of human, but rather astrophysical origin. GRBs are outbursts of high energy photons with $\mathrm{E_{ph}} > 100\,\mathrm{keV}$, accompanied by X-ray to optical transients and successively followed by radio afterglows [Piran, 2003]. Up to now space-born telescopes have gathered a tremendous amount of data on GRBs. The observational key features subsume to the following: GRBs are observed at a rate of about 1 per day corresponding to 1 burst per 10^6 years per galaxy. Therefore GRBs are comparatively rare events, i.e. roughly by a factor 1/500 more deficient than supernovae. This is straightforwardly explained by the assumption that GRBs are highly collimated and geometrically inobservable in most cases. GRBs form a bimodal distribution with the characteristic of short burst time ($< 3\,\mathrm{s}$)/hard spectra and of long burst time ($> 3\,\mathrm{s}$)/soft spectra/associated afterglow [van Paradijs et al., 2000]. The distinction between both classes is currently not understood.

According to the BATSE (Burst And Transient Source Experiment) all-sky survey GRBs are isotropically distributed [Meegan et al., 1992]. In combination with the redshift measurements in afterglow absorption lines (first observed for GRB970508 by Metzger et al. [1997]) the cosmological origin of GRBs is established. Further, the long-standing 'no-host-problem' is resolved by the detection of redshifted emission lines of associated galaxies [Kulkarni et al., 1998].

The cosmological distance measure implies that GRBs are the electromagnetically most luminous objects in the universe, releasing 10^{51}-10^{54} ergs in a few seconds. The detection of iron lines in GRB spectra disseminated the idea of supernovae (SN) as likely culprits. In individual cases there exists positive evidence since spectra appear SN-like [Uemura et al., 2003; Price et al., 2003; Hjorth et al., 2003; Mészáros, 2003]. However, the SN hypothesis is far from commonly accepted. In general the GRB spectra follow a phenomenological fit introduced by [Band et al., 1993] which consists of two power-laws joined smoothly at some break energy. Though not self-consistently motivated, the break energy is associated with a sideways dispersion of the collimated GRB outflow.

The concept of a variable collimated outflow is essential to the fireball model of GRB (see Piran [1999]; Mészáros [2002] for reviews on the theoretical GRB models with special emphasis on the fireball scenario). In such models of GRB the relativistic outflow from the generating source is the central hypothesis. This is also the decisive discrimi-

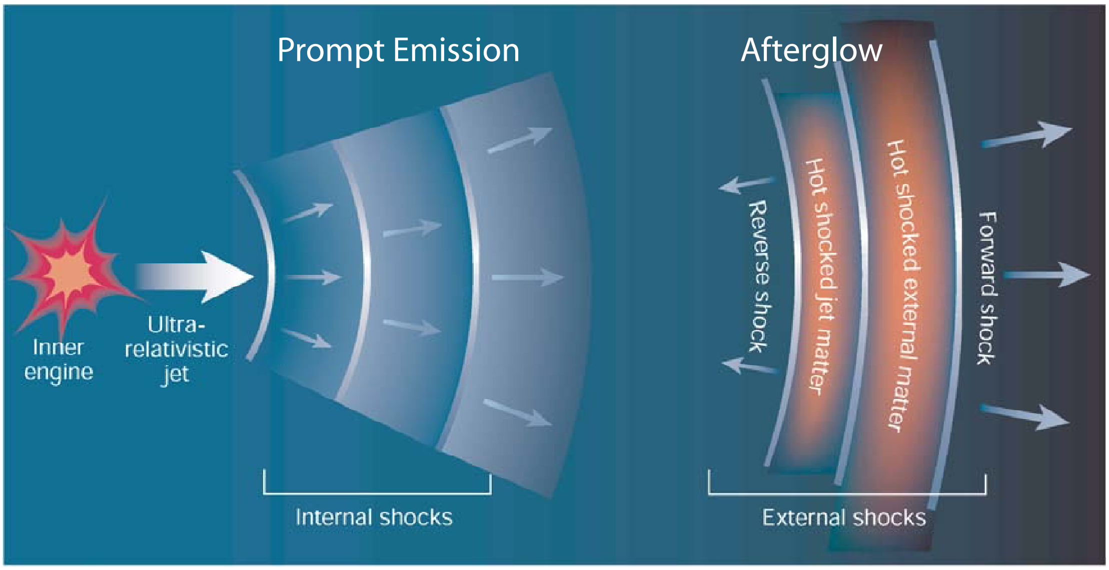

Fig. 1.4: Conceptual GRB fireball scenario: The central engine (some unspecified cataclysmic event) ejects ultra-relativistic fireball shells. Internal collisions of optically thin plasma shells are responsible for prompt Γ-emission as well as X-ray/optical transients. The long-enduring afterglow is associated with external shocks as the shells run into the ambient medium. Synchrotron emission in combination with Weibel magnetic fields proofs to be a valid mechanism for the conversion of particle-born flux to radiation. The EMCSI is the pervasive instability mode in the collisionless plasmas of the post-shock regions.

nation to SN explosions. During SN explosions the expanding shell contains a few $M_\odot$ (solar masses) and the expansion speed remains non-relativistic. The high mass ejection implies a quasi-Newtonian flow. Complementarily, the initial mass ejection in GRBs is only $\sim 10^{-5}\,M_\odot$ enforcing relativistic flow conditions for an emission power of roughly $10^{50}\,\mathrm{erg\,s^{-1}}$. In short, the GRB fireball scenario includes four stages (Fig. 1.4):

1. **Ejection from the central engine.** The central engine is a cataclysmic event which disseminates extreme energies in form of Poynting flux, leptons and probably a small amount of baryons. GRB progenitors are the realm of wild speculations spanning from black hole - neutron star merging towards *failed* SN scenarios. All concepts limit the central engine to an extension of roughly $r \sim 10^7$-10^8 cm.

2. **Fireballs accelerate to ultra-relativistic flow.** The extreme energy densities close to the central engine pose the famous *Compactness Problem*. The apparent γ-photon densities result in tremendous pair production. The fireball is the unavoidable dynamic thermal equilibrium of γ-photons and electron-positron pairs. The fireball is initially radiation-dominated, i.e. the opacity introduced by the lepton pairs yields a high optical thickness. Consequently the fireball is inescapable to radiation in this stage of *high compactness*. Goodman [1986] and

Paczyński [1986] showed that the fireball necessarily cools to matter-dominated phase, thereby translating the initial energy into a highly-relativistic bulk flow. The relativistic motion is the ultimate solution to the *Compactness Problem* via relativistic collimation of radiation and Doppler-shifted emission. The short observed variability time scales of GRB ($< 10^{-2}\,\mathrm{s}$) are simply resolved by assuming variabilities in the flow, i.e. plasma shells.

3. **Internal conversion of kinetic energy into GRB prompt emission.** The power-law-shape of observed spectra [Band et al., 1993] indicates the clearly non-thermal origin of radiation. Consequently the radiation does not appear from a thermalized fireball. Most promising are synchrotron mechanisms with successive inverse Compton upscattering [Medvedev & Loeb, 1999; Medvedev, 2000]. The radiative energy stems from the relativistic bulk motion of colliding plasma shells. Internal collisions arise from source variabilities. Such collisions are expected to take place at $\mathrm{r} \sim 10^{12}$-$10^{14}\,\mathrm{cm}$ from the central engine and to be responsible for GRB prompt emission.

4. **Afterglow in external shocks**. Finally the plasma shells encounter the ambient interstellar medium at $\mathrm{r} \sim 10^{16}\,\mathrm{cm}$. The interactions are not restricted to variability time scales anymore and appear as long-enduring ($10^4\,\mathrm{s}$) optical/radio GRB afterglow.

The essential problem of the fireball scenario involves the conversion of the kinetic energy of the plasma shells into radiation via the Weibel process. This problem is the central issue of chapter 4 of the present work. In the following we introduce the scenario of relativistic plasma shell collisions.

PIC simulations of relativistic plasma shell collisions

The efficient magnetic field generation is the crucial point in synchrotron emission models. The critical quantity is the equipartition ratio ϵ_{B}. Theoretical modelling of GRB light curves and afterglow spectra determines the magnetization to $\epsilon_{\mathrm{B}} \simeq 10^{-1}$-$10^{-3}$ varying with the initial assumptions [Waxman, 1997; Panaitescu & Kumar, 2000; 2002]. Consequently the validation of the synchrotron emission model is indebted to the identification of the source process for the magnetic fields.
Dipolar fields decay $\propto \mathrm{r}^{-3}$ with distance r from the central engine. Even for the most strongly magnetized objects (magnetars, neutron stars) with $\mathrm{B} \lesssim 10^{16}\,\mathrm{G}$, the magnetization ϵ_{B} becomes negligible in distances reconciling with the minimum imposed by the compactness problem [Mészáros & Rees, 1993]. Another potential candidate is the amplification of the ambient magnetic field by shock compression. Analytical estimates predict only poor magnetizations $\epsilon_{\mathrm{B}} \simeq 10^{-11}$ [Sari et al., 1996]. Though self-consistent 2D PIC simulations of shock compression show near-equipartition magnetization, the magnetic fields decay rapidly downstream of the shock front [Gruzinov, 2001]. Most promising is currently the magnetic field generation via the Weibel mechanism in the

wake of the EMCSI as suggested by Medvedev & Loeb [1999]. The scenario is closely related to 3D collisionless shocks. However, the essential physics is not taking place in the shock front, but in the counterstreaming plasmas trailing the shock front.

The EMCSI is studied in self-consistent PIC simulations in the pioneering work of Kazimura et al. [1998] and Silva et al. [2003]. Therein the generation of near-equipartition magnetic fields is established in 2D [Kazimura et al., 1998] and confirmed in 3D [Silva et al., 2003] for weakly ($\gamma = 1.17$) and moderately ($\gamma = 10$) relativistic collision energies. In chapter 4 we address the questions which arise as the immediate consequence: How do the equipartition ratio and the magnetic field spectrum scale with the collision energy of the plasma shells? Is the stability of the generated Weibel fields sufficiently long with respect to synchrotron cooling times?

Written in a formal fashion, the EMCSI is composed of the 1D Two-Stream (TSI) and 1D Weibel (WBI) modes

$$\mathrm{EMCSI} = \mathrm{TSI} \cdot \mathrm{CT} + \mathrm{WBI},$$

which are connected via a coupling term (CT). From the detailed linear analysis of the EMCSI in section 4.1 and Appendix B we identify the energy-dependence in the relative contributions of WBI and TSI. WBI and TSI are competing modes and their relative weight determines the physical nature of the EMCSI. We investigate for the first time the distinct features of the EMCSI for internal and external GRB shocks. The analytical prediction is then elaborated in the self-consistent PIC simulations of ultra-relativistic plasma shell collisions in section 4.2. The analysis covers the highly-nonlinear regime and the impact of significant thermal contributions.

The PIC simulations establish the Weibel mechanism as viable process to generate magnetic fields with sufficient strengths. The critical question is whether the Weibel fields survive on time scales reconciling with synchrotron cooling. In section 4.3 we identify cross-field diffusion as the lifetime-limiting microphysical process for the magnetic fields. We characterize the diffusion as of ‘Bohm’-type and provide the first self-consistent diffusive lifetime-limits for Weibel fields in GRB shocks. In section 4.4 we discuss magnetic field spectra in the context of self-similarity and take first steps towards ‘kinetic turbulence’. We infer the evolution of particle spectra in GRB shocks and conclude with the characteristics of synchrotron spectra of Weibel fields.

Finally, is there any observational evidence in favor of the synchrotron mechanism besides the power-law shape of the spectra? If the Weibel scenario is valid, the synchrotron emission in GRBs is radially polarized. Though the net polarization vanishes for circularly symmetric sources, the interaction with the galactic interstellar medium diffracts the source image. Such polarization scintillations are indicative for the synchrotron source proceeds and have recently been observed for prompt emission [Coburn & Boggs, 2003] as well as afterglows [Greiner et al., 2003].

1.4 The Weibel-Two-Stream-Connection - The Plasma Microphysics of Jets and Pulsars

The EMCSI is the dominant instability mode in ultra-relativistic plasma shell collisions. The EMCSI is a composite of 1D modes (therefore we equivocally use the term Coupled-Two-Stream-Weibel (CTW) mode). Though the EMCSI is an individual mode, the physical nature of the instability is clearly determined by the relative weight of the 1D constituents. The formal characteristics of the 1D TSI are bulk-parallel electrostatic fields associated with particle heating and phase space-mixing. Complementarily, the 1D WBI evolves to pervasively transversal, quasi-static magnetic fields. During non-linear saturation the particle distribution function (PDF) retains a residual anisotropy and particles travel close to 'force-free' within magnetically confined current filaments. In conclusion the TSI is responsible for the dissipation of the kinetic energy in the particle flow. The WBI establishes efficient particle transport, only limited by cross-field diffusion.

The critical question is whether there is a physical constraint which breaks the degen-

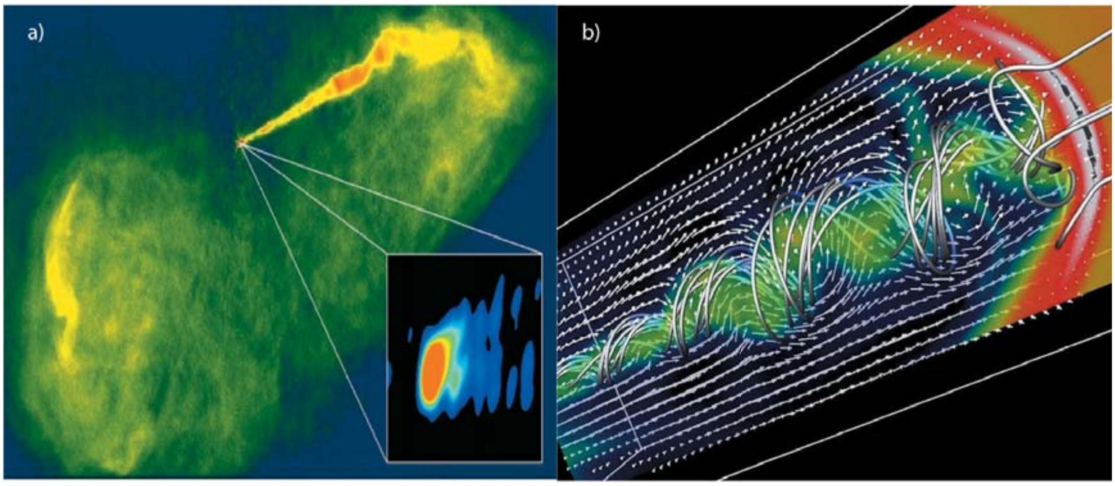

Fig. 1.5: Relativistic jets are the paradigm for critical plasma processes. Efficient particle transport is established over kiloparsec distances in filamented, self-stabilized Weibel pinches (a). In regions of pronounced magnetic guide topologies the Two-Stream component of the EMCSI gains in importance and the bulk kinetic energy is dissipated in so-called 'hot spots'. Particle transport takes place over several synchrotron cooling lengths. The current filamentation in jets implies complex magnetic field topologies (b). Consequently fast magnetic reconnection is expected to be omnipresent along the jet and is the most promising candidate for continuous in-situ reacceleration of synchrotron-cooled particles.

eracy of the EMCSI and forces the 1D constituents to proceed individually. In section 5.1 and Appendix B we show that a magnetic guide field B_G breaks the degeneracy. The guide field is imposed parallel to the bulk motion and the strength of B_G determines whether the TSI or the WBI prevails. At small guide fields the WBI is dominant up to critical threshold B_G^{ths}. In section 5.1 we calculate the critical energy dependence of B_G^{ths} and discuss the implications for astrophysical jets and pulsar magnetospheres.

Jets are paradigms for the interplay of TSI and WBI in relativistic plasma flows (Fig. 1.5). Particles are transported over vast distances in current-carrying filaments - in individual cases over hundreds of kiloparsec. Consequently the transport mechanism is necessarily efficient and synchrotron cooling is the dominant dissipation mechanism. In certain 'hot spots' the dissipation of particle kinetic energy is tremendously increased. The transition from WBI to TSI dominance appears here as a promising explanation of the microphysics. Our results apply strictly only to relativistic pair-dominated plasma scenarios. However, there is ample evidence for the existence of 'light' jets [Wardle et al., 1998; Hirotani et al., 2000; Lobanov & Zensus, 2001] with significant pair content. However, the plasma filamentation as discussed in chapters 4 and 5 is valid also on ion inertial scales as shown in PIC simulations of electron-proton plasma by Nishikawa et al. [2003] and Frederiksen et al. [2004].

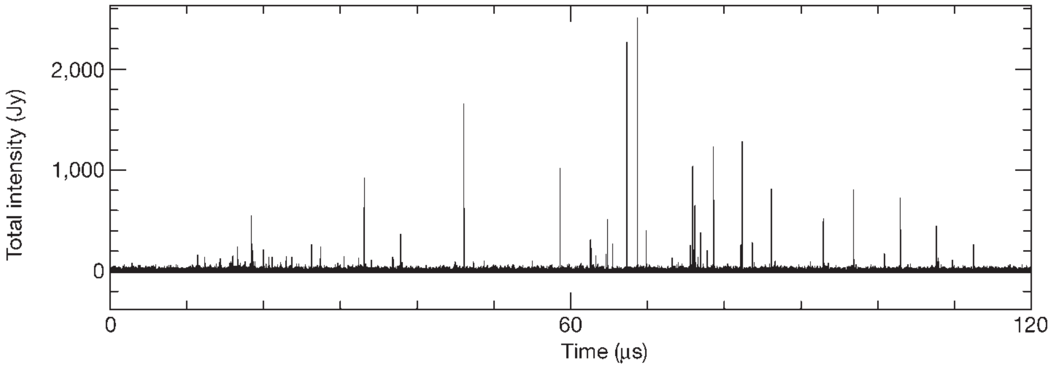

Fig. 1.6: Radio outbursts ($\nu = 5.5\,\text{GHz}$) with the extreme spectral intensity of $S \sim 1000\,\text{Jy}$ observed by Hankins et al. [2003] serve as an impressive probe of the microphysics of the Crab pulsar magnetosphere. The 'power spikes' endure typically $\sim 2\,\text{ns}$ restricting the size of the emission region to somewhat less than 100 cm. The inferred brightness temperatures of $T_B \sim 10^{37}\,\text{K}$ clearly indicate a non-thermal emission process. We performed pioneering PIC simulations of Coherent Collisionless Bremsstrahlung suggesting a viable explanation for the involved time scales and power output.

The pulsar magnetosphere represents another scenario in which the Weibel-Two-Stream connection is of utmost importance. In this case the magnetic guide field is of such extreme strength that the WBI mode is suppressed up to the so called emission height. The TSI introduces strong electrostatic fluctuations (Langmuir turbulence) in the plasma shells moving outwards from the polar caps of the pulsar. The electrostatic fluctuations trigger the process of Collisionless Coherent Bremsstrahlung (CCB). We discuss the generation of CCB in relativistic plasma shell collisions in section 5.2. We start with a primer on the physics of the pulsar magnetosphere with special emphasis on Giant Radio Pulses (GRPs). On the basis of fundamental considerations we infer the plasma conditions at typical GRP emission heights. The emission mechanism and non-linear dynamics of CCB are studied self-consistently in PIC simulations. Applying the PIC results to the derived plasma conditions, we conclude that the time scales and total power output of the CCB process provide a consistent explanation for the recently observed Nanosecond Radio Bursts of the Crab pulsar (Hankins et al. [2003], Fig. 1.6).

Chapter 2

The Computational Method of Choice: Particle-In-Cell

The present work is motivated by critical problems in astrophysical plasma scenarios. In the introduction we elaborated on the aspects which determine whether plasma processes are critical in the context of contemporary research. 'Critical effects' arise in plasma configurations which are intrinsically relativistic, highly non-linear and non-thermal. The success of all efforts to resolve such critical problems relies on the choice of appropriate methods. On astrophysical timescales the non-linear saturation is the pervasive stationary plasma state. Saturated plasma states are beyond the scope of linear analytical treatment and are only accessible in direct numerical simulations. The Particle-In-Cell (PIC) approach is our simulation method of choice. Every simulation model comes along with pros and cons. In the following we provide answers to the questions which arise as the immediate consequence of our choice:

Why is the self-consistent PIC model the most suitable choice ?

The detailed representation of a physical process in the framework of a numerical simulation involves three formal levels of abstraction as illustrated in Fig. 2.1. On the top level is the appropriate choice of the physical model. Different plasma models strongly vary in the degree of sophistication. Each plasma description involves certain assumptions and idealizations. The plasma description determines the nature of physical processes which can be observed within the model constraints. The more restrictive the prescribed assumptions are, the more selective is the model on the number of possible physical processes. The problem is that such a selection is an artefact of the theoretical description. It is the physicist's commitment to ensure that the applied model reflects the 'true' image of nature. The results of a simulation are 'true' in this sense, if the processes which appear dominant within certain model constraints would appear in the same fashion under relaxed idealization. Some processes do not allow for any idealizations, i.e. demand complete self-consistency.

Plasma physics is the science of charged particles in electromagnetic fields. The challenge is the self-consistent treatment of individual particle orbits in the collective fields,

since the charged particles serve as the field generators as part of the feedback loop. Potential simplifications are either to average over particle motion, as it is realized in the magnetohydrodynamic (MHD) approach, or to study particle trajectories in prescribed static field configurations, as is done in test-particle schemes. Both approaches break the feedback loop and, hence, bypass self-consistency. The advantage is that the numerical effort is tremendously cheaper. So why are MHD and test-particle models insufficient to study the critical plasma processes which are the subject of this work?
The MHD model is a fluid description of the plasma in which the particle motion is reduced to density n, bulk velocity $\mathbf{v}_\mathrm{b}$ and pressure/temperature T

$$n = \int f(\mathbf{x},\mathbf{p},t)d^3p \qquad \gamma(v_b)\, n\, \mathbf{v}_b = \int \mathbf{p} m^{-1} f(\mathbf{x},\mathbf{p},t)d^3p \qquad n\, T_{mn} = \int p_m v_n f(\mathbf{x},\mathbf{p},t)d^3p$$

as the respective 0th, 1st and 2nd order moments of the particle distribution function (PDF) $\mathrm{f}(\mathbf{x},\mathbf{p},\mathrm{t})$. Since the PDF itself is not represented in the MHD model, the 2nd order moment (i.e. the connection between pressure and density) is usually substituted

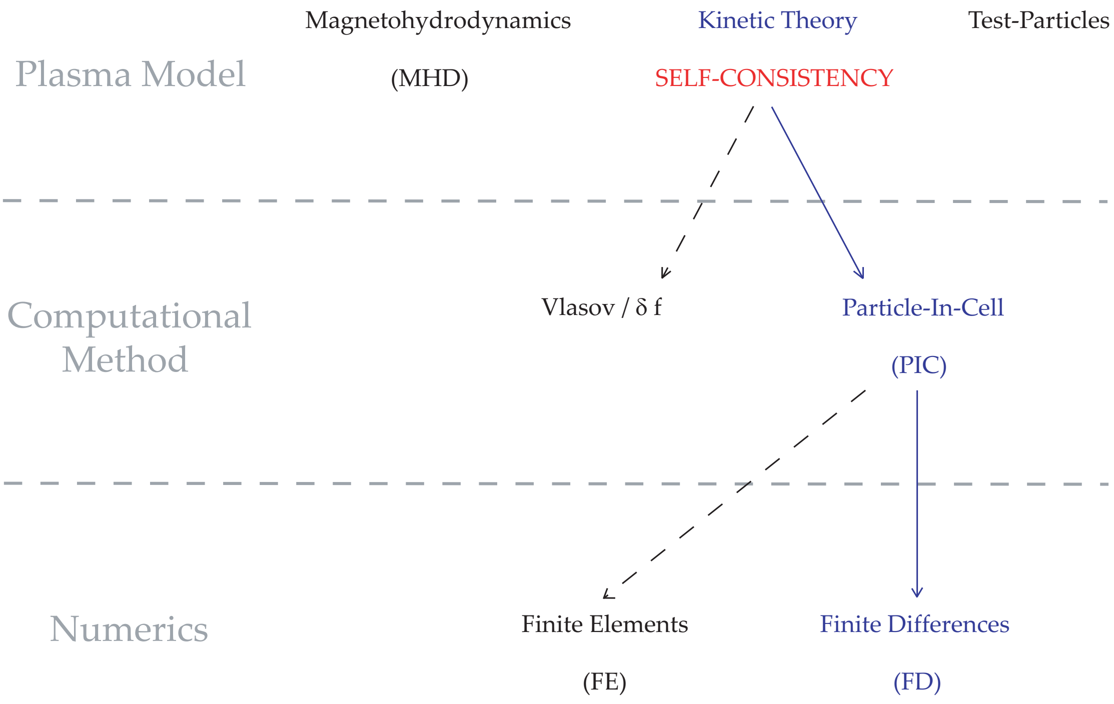
Magnetohydrodynamics
(MHD)
Kinetic Theory
SELF-CONSISTENCY
Test-Particles
Plasma Model
Computational Method
Vlasov / δ f
Particle-In-Cell
(PIC)
Numerics
Finite Elements
(FE)
Finite Differences
(FD)

Fig. 2.1: Translation of plasma physical scenarios into the framework of a numerical simulation formally divides into three levels: (1) The plasma physical model, (2) the computational method, and (3) the numerical paradigm. Solely kinetic plasma models allow for a self-consistent plasma description.

by an ad-hoc assumption on the thermal equation of state $\mathrm{P}(\mathrm{n},\mathrm{T})$ and the simplification to isothermal or adiabatic conditions. These additional assumptions represent severe restrictions because the PDF is reduced to the isotropic thermal equilibrium, i.e. $\mathrm{f}(\mathbf{x},\mathbf{p},\mathrm{t})$ is reduced to Maxwellian. One outstanding purpose of the present work is to study particle acceleration and the self-consistent generation of non-thermal (power-law shaped) and, hence, highly non-Maxwellian PDFs. This is possible in kinetic approaches because these are based on the explicit representation of the PDF. Furthermore, the MHD model assumes Ohm's resistivity as constant or linearly dependent on the current density. This is critical particularly in the context of particle acceleration during magnetic reconnection, since the reconnection rate / inductive electric field are determined by the ad-hoc definition of resistivity. Again this is not an issue in kinetic models which implement resistivity as self-consistent microphysical particle-field-scattering events. Finally, MHD models neglect Maxwell's displacement current $\mathrm{c}^{-1}\partial_\mathrm{t}\mathbf{E}$ which generally excludes the study of electromagnetic radiation emission.

The fluid approach simplifies the treatment of particle motion. The other extreme case is realized in test-particle studies. Therein the trajectories of a limited number of particles are calculated in a time-stationary field configuration. The field configuration is conveniently obtained as a selected point in the time evolution of a MHD simulation. The test-particle approach completely neglects the feedback of particles on the field configuration. Therefore also the test-particle description is not self-consistent. Test-particle studies allow for non-thermal contributions to the PDF, however, the shape of the PDF is strongly dependent on the model parameters. The MHD fields are scalable to arbitrary spatial extensions, because the interaction with the particle motion is not included. As a consequence thereof particle acceleration depends critically on the parameterization of a specific scenario: The efficiency of particle acceleration during magnetic reconnection is essentially determined by the acceleration potential $\Delta\Phi_\mathrm{acc} = \mathrm{E}_\mathrm{ind}\Delta\mathrm{l}$. The MHD inductive electric field E_ind is tuned by the choice of the resistivity, and $\Delta\mathrm{l}$ is tuned by the system scale size, respectively. Furthermore, as long as the temperature definition is not based on the relativistic energy-momentum tensor, the MHD fields are non-relativistic, even though in some scenarios test-particles reach ultra-relativistic energies.

Solely the kinetic plasma description fulfills the ultimate demand of complete self-consistency. Kinetic models are not in need of any of the previously introduced idealizations. Electromagnetic fields are self-consistently generated from the charged particles. Individual particle trajectories are calculated in the respective field topology. Consequently, the smallest length scale is not relegated to an arbitrary choice, rather it is set on a physical foundation, i.e. the typical particle gyro radius or inertial length. Finally, the self-consistency loop is closed by accounting for the feedback of the variations in particle phase space on the field configuration. Since the field topology is self-consistently coupled to the particle motion the field length scales are also physical.

It is important to stress the distinctive meaning of self-consistency and scale invariance of the dimensionless representation. In a self-consistent plasma simulation the lengths, times, velocities, field energy and relativistic particle energy result as the consequence of the physical nature of the plasma process under study. The result is independent of ad-hoc defined tuning parameters. In the dimensionless representation times are normalized to the particle gyration time $\omega_{\rm c0}^{-1} = {\rm mc/eB_0}$ and lengths to the electron inertial length ${\rm c}/\omega_{\rm p0} = {\rm c(m/4\pi e^2 n_0)^{1/2}}$. In Gaussian-cgs units the definition of equivalents for length and time is sufficient for the dimensionless representation of all simulation quantities. The dimensionless representation of physical quantities in a simulation is of utmost importance, since it immediately concerns the interpretation of simulation results. A sophisticated dimensionless representation comes along with two eminent advantages: First, one simulation is applicable to an entire class of physical environments. This does not imply a contradiction with self-consistency. The dimensionless values are obtained self-consistently for the simulated plasma process. Then the dimensional values are calculated with the reference values for $\rm B_0$ and $\rm n_0$, which are typical for a specific physical environment. In this way, a single self-consistent simulation of magnetic reconnection applies equally well to the earth's magnetosphere and core regions of active galactic nuclei. This characteristic of dimensionless simulations is extremely powerful because the physical nature of the process is in the focus. And second, the numerical performance is optimal for quantities of comparable magnitudes, which is ensured by an adapted normalization. The detailed description of the dimensionless representation is rather technical and therefore deferred to Appendix A.

The vital motivation of the present work is the study of plasma processes which represent critical problems in relativistic astrophysics. To be concise we finally list the most important arguments why a kinetic plasma description is essential to the study of such plasma processes:

- The efficiency of particle acceleration in collisionless magnetic reconnection is determined by the acceleration electric potential $\Phi_{\rm acc}$. As a consequence thereof reliable results on the 3D extensions of the reconnection region and the inherent anomalous resistivity are indispensable. Solely the self-consistent kinetic description is in the position to provide a definite answer.

- The Weibel instability is an inherently kinetic and electromagnetic instability. The temperature anisotropy of the initial configuration represents the reservoir of free energy. Solely the highly non-linear saturated state is of importance in astrophysical scenarios. Therein a finite residual phase space anisotropy is characteristic. This corresponds to a PDF consisting of thermalized and highly non-thermal contributions.

- The two-stream instability is accompanied by complete phase space mixing with significant non-thermal effects. The saturated state of strong Langmuir turbulence crucially depends on the interplay of thermalization and non-thermal particle generation. In addition, the study of radiation emission in collisionless Bremsstrahlung is entirely in the realm of fully electromagnetic plasma models.

Finally, with the necessity of a kinetic plasma description granted, we need to convene on the computational implementation (Fig. 2.1). There exist two options: On the one side stands the Vlasov approach which implicitly represents the PDF in 6D phase space. On the other side is the PIC model which explicitly represents the PDF in form of (quasi-)particles in configuration and momentum space.

What are the characteristics of the PIC model ?

The time evolution of collisionless plasmas is described by the Vlasov equation

$$\frac{d\,f(t,\mathbf{x},\mathbf{p})}{dt} = \frac{\partial f}{\partial t} + \dot{\mathbf{x}}\cdot\frac{\partial f}{\partial \mathbf{x}} + \dot{\mathbf{p}}\cdot\frac{\partial f}{\partial \mathbf{p}} = \frac{\partial f}{\partial t} + \mathbf{v}\cdot\frac{\partial f}{\partial \mathbf{x}} + (\mathbf{E} + \frac{\mathbf{v}}{c}\times\mathbf{B})\cdot\frac{\partial f}{\partial \mathbf{p}} = 0$$

which results from the Boltzmann transport equation in the limit of negligible Coulomb collisions. The PDF evolves under the influence of the Lorentz force $\mathbf{F}_\mathrm{L} = \mathbf{E} + \mathbf{v}/\mathrm{c} \times \mathbf{B}$ in the electric and magnetic fields which are generated by collective plasma instabilities. In principle the computational task of kinetic plasma simulation is straightforwardly defined, i.e. to calculate the collective electromagnetic fields at each particle position as the superposition of all contributing ensemble particles. This approach is generally referred to as the Molecular Dynamics (MD) concept [Hockney & Eastwood, 1988]. For an ensemble of $\mathrm{N_p}$ particles the MD model accounts for the contributions of $(\mathrm{N_p} - 1)$ particles in order to calculate the Lorentz force term for each particle (Fig. 2.2, upper right). Therefore, the computational effort behaves like $\epsilon_\mathrm{ce} \propto \mathrm{N_p}(\mathrm{N_p} - 1) \sim \mathrm{N_p^2}$. Contemporary supercomputing facilities allow for the simulation of MD ensembles consisting of $\sim 10^6$ particles. Granted that the MD concept comes along with idealizations like distance

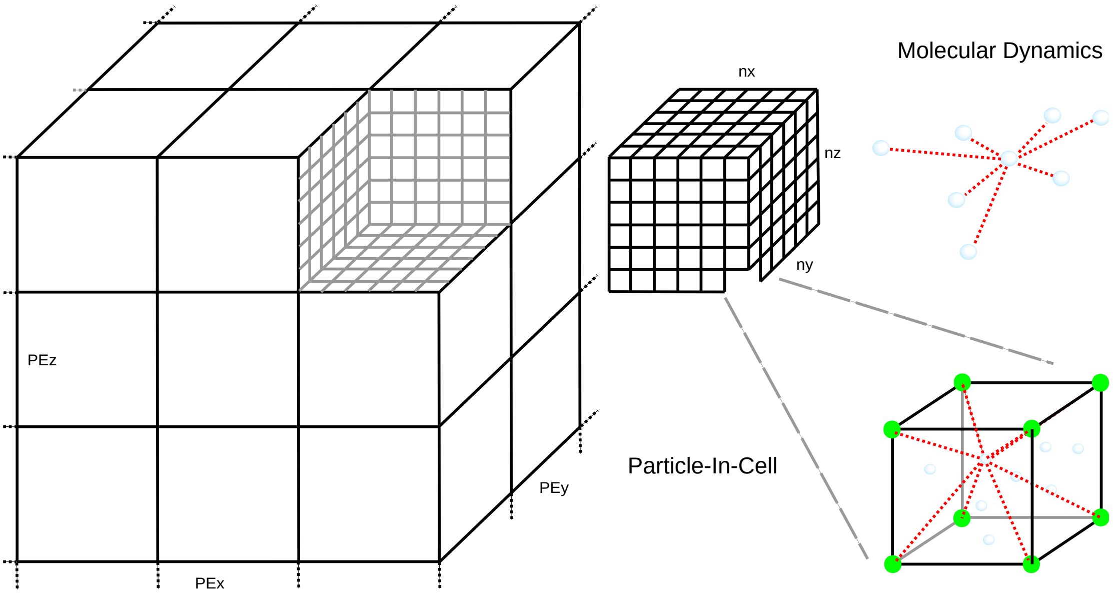

Fig. 2.2: The idea behind the Particle-In-Cell (PIC) model is the grid representation of the fields. The physical foundation of the approach is based on the ‘collective behaviour’ of plasma particles as the characteristic of the collisionless plasma state. With respect to the overall computational effort, the PIC model is superior to the Molecular Dynamics (MD) concept.

restrictions on the contributing ensemble members one might gain another factor of 10. However, this is simply not enough to simulate the necessarily three dimensional scenarios of critical plasma processes! An adequate representation of 3D plasma scenarios employs somewhat like 10^9 individual particles.

The solution relies on harnessing a physical characteristic of the plasma state: The feature of collective behaviour. Each particle is surrounded by a cloud of charge opposites, i.e. the electric field arising from each charge is effectively screened. Therefore each volume element with a typical extension larger than a characteristic minimum length appears quasi-neutral. This temperature-dependent minimum extension is called the Debye length $\lambda_\mathrm{D} = (\mathrm{T}/4\pi \mathrm{e}^2\mathrm{n})^{1/2}$. Sufficient resolution of the Debye length is indispensable in PIC simulations in order to avoid artificial self-heating of the system. This restriction determines the minimum resolved length scale in the simulation. Beyond the Debye sphere rule the electric and magnetic fields originating from collective plasma instabilities. Such collective fields are adequately represented on a numerical grid mesh of sufficient refinement. The field values on the respective closest grid points are interpolated to the particle position (Fig. 2.2). The interpolation is either linear or uses some low order spline. The mesh representation incorporates tremendous alleviations in the computational effort. Computational costs now scale like $\epsilon_\mathrm{ce} = \alpha \mathrm{N_p} + \beta \mathrm{N_m^3} \log(\mathrm{N_m}) \sim \mathrm{N_p}$. Therein α and β are constants determined by the individual simulation setup, and $\mathrm{N_m} \ll \mathrm{N_p}$ is the number of mesh points in each dimension which is by definition much less than the overall particle number $\mathrm{N_p}$. Decisive is the linear growth with the ensemble size. This allows the simulation of systems with $\mathrm{N_p} \sim 10^9$ on contemporary supercomputers. For the first time we are in the position to study critical plasma processes in realistic 3D scenarios. However, even in the PIC model it is impossible to translate a plasma configuration from the appearance in nature to the simulation by a one-to-one assignment of particles. Therefore each particle in the simulation is some kind of ‘super’-particle or ‘quasi’-particle which represents a collection of particles in the real life scenario. The cardinal number $\mathrm{N_C}$ of each quasi-particle describes the ratio of simulation particles to physical particles. $\mathrm{N_C}$ is a function of the reference density $\mathrm{n_0}$ and scales like $\mathrm{N_C} \propto \mathrm{n}_0^{-1/2}$.

A competing approach to the PIC method is the Vlasov simulation model (Fig. 2.1). In the Vlasov description the grid mesh representation is pushed to the limits, since the entire 6D phase space is mapped onto a numerical mesh. In this approach the PDF is not explicitly represented by particles, but implicitly with the grid mesh points as sampling points. The study of critical plasma processes in the present work is performed with the PIC model. To be concise and complete, we list the major arguments decisive for this choice with respect to the alternative Vlasov model:

- The Vlasov model employs a fixed number of sampling points for the representation of the PDF in momentum space. The analysis of particle acceleration involves distinct non-thermal features in the PDF. Such features are in some cases subtle and extend towards unexpectedly high momenta (see for instance the evolution of the PDF high-energy tail in the reconnection scenario in Fig. 3.3). The grid representation of the PDF in the Vlasov approach comes along with a certain degree of refinement and predefined upper limit. Consequently the momentum representation of the PDF is biased by the choice of the sampling points. In this case critical features are possibly not detectable. This problem is resolved in the PIC approach with the explicit representation via particles.

- The microscopic analysis of the acceleration mechanism requires the diagnostics of trace particle trajectories and cross-correlation with field topology. This form of analysis is solely in the realm of the PIC model.
- An equivalent argumentation also holds for the determination of diffusion mechanisms and diffusive transport coefficients. On the microphysical level such processes represent particle scattering events with fields off collective plasma instabilities. Again particle motion / field topology correlations are essential.

Finally, after the issue of the computational method is settled, two options remain for the numerical implementation of the time scheme (Fig. 2.1). The numerical setup is either based on a Finite Element (FE) or Finite Difference (FD) method. We convened on the alternative of a time-centered FD scheme.
After initialization the entire time evolution of the system is governed by the dynamic Maxwell equations in the fields

$$\frac{1}{c}\frac{\partial \mathbf{B}}{\partial t} = -\nabla \times \mathbf{E} \qquad\qquad \frac{1}{c}\frac{\partial \mathbf{E}}{\partial t} = \nabla \times \mathbf{B} - \frac{4\pi}{\mathrm{c}}\mathbf{j},$$

and the Lorentz force with respect to particle motion. In a very generic fashion the integration scheme consists of a first integration half-time step, during which new field values are calculated in accordance with the dynamic Maxwell equations. In a consecutive second half-time step particles are stepped using the Boris algorithm [Boris, 1970] according to the updated fields. Half-time steps indicate that the scheme is time-centered. Self-consistency in PIC simulations is ensured by intermediate updating of the fields with respect to particle motion by means of the current density $\mathbf{j} = (\Sigma \mathrm{q_i} \mathbf{v}_\mathrm{i})_\mathrm{cell}/\mathrm{ppg}$. The current density $\mathbf{j}$ is directly calculated in each grid cell from particles with charge q moving with velocity $\mathbf{v}$, i.e. representing the feedback of particles on the fields. ppg is the amount of particles per grid cell which refers to the dimensional reference density $\mathrm{n_0}$. A systematic problem in the PIC approximation is the secular violation of Poisson's equation. Consequently, to ensure code stability during extremely long runs up to 40000 time steps, we have to solve Poisson's equation and correct discrepancies arising from the particle stepping. The method of choice is a multigrid algorithm [McCormick, 1988]. Typically we use a Gauss-Seidel scheme for the restriction/prolongation steps and enforce a residual of $\leq 10^{-12}$. The code is written in Fortran 90, parallelization is realized with the Message-Passing-Interface (MPI).

Which limits are imposed by contemporary supercomputers ?

The demand of complete self-consistency is computationally utmostly expensive. Kinetic plasma simulations represent an ultimate challenge to contemporary high performance computing. In the following we introduce into the hardware-critical points of N-body problems in simulations. There are two criteria for the quality of a simulation with respect to computational limitations: The total system extension and the required computation time, i.e. the memory requirement and the number of time steps.

We first address the issue of computer memory. The necessary amount of memory in plasma simulations $\mathrm{M_{tot}} = \mathrm{M_{fld}} + \mathrm{M_{prt}}$ is composed of the field data on the grid mesh $\mathrm{M_{fld}}$ and the particle contributions $\mathrm{M_{prt}}$. The amount $\mathrm{M_{fld}}$ is comparable for MHD, test-particle and kinetic simulation models. Typical scenarios employ a grid mesh with $\mathrm{N_m^3} = 256^3$ sampling points. Varying with the implementation of the numerical scheme about 15-20 quantities need to be represented on the grid mesh which subsumes to a memory consumption

$$\mathrm{M_{fld}} \simeq 8\,\mathrm{Byte} \times 256^3 \times 20 = 2.5\,\mathrm{GByte}.$$

For MHD and test-particle approaches this is the end of the story. For the self-consistent PIC approach the field data only contributes a few (negligible!) percent to the total amount of memory. The limiting constraint is imposed by the particle data. Well resolved PIC simulations employ 50-100 particles per grid cell (ppg). Then the 6 phase space components of each particle specie consume in total

$$\mathrm{M_{prt}} \simeq 8\,\mathrm{Byte} \times 256^3 \times 12 \times 100 = 150\,\mathrm{GByte}.$$

In principle this amount of data is produced in every time step. In this work we study critical plasma processes during magnetic reconnection and relativistic plasma shell collisions. The simulations comprise up to 60000 time steps. Currently no supercomputing facility (at least for civilian use) is capable to provide such data storage potentials. Furthermore the data transfer bandwidth for input/output is limited. It takes roughly 15 minutes to write 150 GB to hard disk. To cut the story short: Every simulation involves an individual setup and the data output indispensable to comply with the scientific objectives are to be defined previously to the actual run.

The other constraint is the total computation time. The amount of data directly corresponds to the number of computations required to produce and modify this data. In individual cases the simulations of this work required up to 70000 CPUhs of computation time. Such CPU time and memory requirements are completely in the realm of massively parallel supercomputing architectures. To comply with this demand the code is MPI-parallelized with a domain decomposition to individual processing elements (PE) as indicated in Fig. 2.2. The simulations were performed on the IBM p690 REGATTA system of the Max-Planck-Society Computing Center (RZG) in Garching and the HITACHI SR8000-F1 supercomputer of the Leibniz Computing Center (LRZ) in Munich.

Up to this point we reported on what was accomplished with the currently available high performance computing systems. In some final words we shortly point out the prospective scientific progress expectable from near-future hardware developments. The empirical Moore's Law states that the speed of microprocessors doubles about every 18 months. The benchmark results of the world's top supercomputers increased by a factor of ~ 67 in the past 7 years. The increase in supercomputer performance runs out Moore's Law by roughly a factor of 2.5 which is the result of turning towards massively parallel architectures. Parallelization is the logical consequence of the faster growth of memory capacities which gained a factor of $\sim 10^3$ in the comparable time interval. In conclusion the trend in conventional (i.e. semi-conductor based) hardware points towards performance gains by roughly a factor of 10^2-10^3 within the next decade. This is enough to address questions which arise in the aftermath of the insights obtained during the present work. These are for instance:

- The study of several likewisely anti-parallel relativistic Harris sheets. Such a configuration corresponds to the combined reconnection-shock problem. This is the paradigm for the transition of a Poynting-flux-driven towards a kinetically dominated plasma wind. An astrophysical paradigm for this problem is the σ-problem of the Crab pulsar wind.
- Currently all 3D self-consistent simulations of collisionless reconnection are restricted to thin current sheets. The phenomenon of fast reconnection is observed for thin sheets. An interesting theoretical question is the evolution of the kinetic reconnection process towards broader sheets. Currently the maximum sheet width in the reconnection problem is limited by the maximum number of simulated particles.
- Higher performance also allows for smaller time steps and relaxes the problems with numerical accuracy. This is essential to push towards higher relativistic energies in the EMCSI scenario (cf. chapter 4).
- Reduced computation times would also open up the possibility to study the Weibel-Two-Stream connection in the fully evolved, three dimensional configuration after non-linear saturation (cf. section 5.1).

However, the performance gain is still by far not sufficient to change to a different computational paradigm like the MD method or the explicit resolution of synchrotron radiation (as is accomplished in section 3.3 with helps of an implicit approach). For such revolutionary modifications, an increase in computational power by at least a factor of $\sim 10^8$ would be necessary. However, we write the year 2004. Maybe in 10 years things look completely different.

Chapter 3

Collisionless Magnetic Reconnection

3.1 The Relativistic Harris Equilibrium

In order to study magnetic reconnection as an individual process one needs to set up an initial force-free solution of antiparallel field lines. Harris [1962] found a one-dimensional analytical quasi-equilibrium for antiparallel magnetic fields generated by a central plane-parallel current sheet. The quasi-neutral 'Harris sheet' consists of two Maxwellians with oppositely directed drifts. In the following we derive the relativistic generalization of the Harris equilibrium and retain the original solution in the non-relativistic limit $\gamma \to 0$. Under collisionless conditions the particle distribution function $\mathrm{f}(\mathbf{x}, \mathbf{p}, \mathrm{t})$ of each plasma specie obeys the Vlasov equation

$$\frac{df}{dt} \equiv \frac{\partial f}{\partial t} + \mathbf{v} \cdot \frac{\partial f}{\partial \mathbf{x}} + \dot{\mathbf{p}} \cdot \frac{\partial f}{\partial \mathbf{p}} = 0.$$

We deliberately choose the 1D spatial dependence of quantities in y-direction. Then the solution of the Vlasov equation is a combination of the following constants of motion (total energy and generalized momenta):

$$\begin{aligned} E &= \left(1 + \left(\frac{p}{mc}\right)^2\right)^{1/2} mc^2 \\ P_x &= p_x + \frac{q}{c} A_x(y) = p_x \\ P_z &= p_z + \frac{q}{c} A_z(y). \end{aligned}$$

We further restrict to the case $\mathrm{A_x} = 0$, though in general the Harris solution remains unaffected by the superposition of a constant magnetic guide field $\mathrm{B_z} = \mathrm{const}$, $\mathrm{A_x} = -\mathrm{y}\mathrm{B_z}$. In the PIC simulations magnetic reconnection is studied in a Cartesian box with extensions $\{\mathrm{L_x}, \mathrm{L_y}, \mathrm{L_z}\}$. The additional constraint $\partial_\mathrm{y} \mathrm{A_z}(\mathrm{y}{=}\mathrm{L_y}/2){=}0$ localizes the current sheet in the (x, z)-plane through the simulation box center. The direction of the diamagnetic current is determined to $\mathbf{j} = \{0, 0, -\mathrm{j_z}\}$ by the convenient choice $\partial_\mathrm{yy} \mathrm{A_z} = \partial_\mathrm{y} \mathrm{B_x} > 0$ for all y-values.

The original Harris solution $\mathrm{f}_{\mathrm{H}}^{\pm}(\mathbf{x},\mathbf{p}) = \mathrm{f}_{\mathrm{H}}^{\pm}(\mathrm{y},\mathbf{p}) = \mathrm{f}_{\mathrm{M}}^{\pm}(\mathbf{p}) \cdot \mathrm{f}_{\mathrm{v}}(\mathrm{y})$ is constructed by a drifting Maxwellian f_{M} and a spatial dependence in accordance with the magnetic vector potential f_{v}. In pair plasma the particle drift is of equal magnitude but opposite direction for each specie. In the following we denote positrons with $+$ and electrons with $-$, respectively.
Generalization to the relativistic regime is straightforward if we efficiently use the transformations/invariances:

- **Lorentz transformations**
  relate 4-vector components $\mathrm{x}^{\nu'} = \Lambda_{\mu}^{\nu'}\,\mathrm{x}^{\mu}$ represented in two inertial frames K, K' moving with arbitrary relative velocity $\beta_{\mathrm{k}} = \mathrm{v}_{\mathrm{k}}/\mathrm{c} = \beta \cdot \{\mathrm{n}_1, \mathrm{n}_2, \mathrm{n}_3\}$,

$$\begin{pmatrix} x^{0'} \\ x^{1'} \\ x^{2'} \\ x^{3'} \end{pmatrix} = \begin{pmatrix} \gamma & -\beta\gamma n^1 & -\beta\gamma n^2 & -\beta\gamma n^3 \\ -\beta\gamma n^1 & (\gamma-1)n^1n^1+1 & (\gamma-1)n^1n^2 & (\gamma-1)n^1n^3 \\ -\beta\gamma n^2 & (\gamma-1)n^2n^1 & (\gamma-1)n^2n^2+1 & (\gamma-1)n^2n^3 \\ -\beta\gamma n^3 & (\gamma-1)n^3n^1 & (\gamma-1)n^3n^2 & (\gamma-1)n^3n^3+1 \end{pmatrix} \begin{pmatrix} x^0 \\ x^1 \\ x^2 \\ x^3 \end{pmatrix}.$$

  For the relativistic Harris solution the relation of momentum 4-vectors $\mathrm{p}^{\mu} = \{\mathrm{E}, \mathbf{p}\mathrm{c}\}$ in the current comoving system and the lab frame (in the exposed geometry positrons move in -z !) reduces to

$$\begin{pmatrix} E' \\ p'_z c \end{pmatrix} = \begin{pmatrix} \gamma_0 & \frac{q}{e}\gamma_0\beta_{z0} \\ \frac{q}{e}\gamma_0\beta_{z0} & \gamma_0 \end{pmatrix} \begin{pmatrix} E \\ p_z c \end{pmatrix} \qquad \text{with } \gamma_0 = (1-\beta_{z0}^2)^{-1/2}$$

- **Lorentz invariance**
  applies to the phase space density f and the entity $\mathrm{d}^3\mathrm{p}/\mathrm{E}$. $\mathrm{d}^3\mathrm{p}/\mathrm{E}$ is a Lorentz invariant because it characterizes the elementary solid angle in momentum 4-space. Momentum 4-space is only one representative of Minkowskian 4-spaces (spacetime for instance is another). Therein momentum 4-vectors p^{μ} define the pseudo sphere of given invariant mass $\mathrm{p}^{\mu}\mathrm{p}_{\mu} = -(\mathrm{mc}^2)^2$, as is evident from the Jüttner/Synge transformations [Synge, 1956; 1965]:

$$\begin{aligned} \gamma\beta = p/mc &= \sinh\tau \\ \gamma = E/mc^2 &= \cosh\tau \\ \beta &= \tanh\tau \end{aligned}$$

$$\begin{aligned} E/c &= mc\cosh\tau \\ p_x &= mc\sinh\tau\sin\theta\cos\phi \\ p_y &= mc\sinh\tau\sin\theta\sin\phi \\ p_z &= mc\sinh\tau\cos\theta \end{aligned}$$

The pseudo sphere describes all momenta/energies accessible to a particle with rest mass m. In any given Lorentz frame the elementary volume element of momentum 3-space $\mathrm{d^3p = (mc)^3 \sinh^2\tau \cosh\tau\, d\tau d\theta d\phi}$ is a surface element of the pseudo sphere. The normal vector of the surface element is parallel to the energy component $\mathrm{p^0 = E/c = (mc)\cosh\tau}$. Consequently, $\mathrm{d^3p/E = (mc)^2 \sinh^2\tau\, d\tau d\theta d\phi = d\omega}$ is the elementary solid angle of momentum 4-space. Observing the transformation characteristics $\mathrm{dp'_x dp'_y dp'_z = \gamma dp_x dp_y dp_z}$ and $\mathrm{\gamma = E'/E}$ the ratio $\mathrm{d^3p/E}$ is identified as Lorentz scalar. An analogous argumentation yields the Lorentz invariance of $\mathrm{E'd^3x' = Ed^3x}$.
The Lorentz invariance of phase space density $\mathrm{f(\mathbf{p},\mathbf{x},t)}$ ensues from the conservation of the total particle number per phase space volume for any given time t $\mathrm{f(\mathbf{p},\mathbf{x})\,d^3p\,d^3x = f'(\mathbf{p}',\mathbf{x}')\,d^3p'\,d^3x'}$. Employing the Lorentz scalars $\mathrm{Ed^3x}$ and $\mathrm{d^3p/E}$ the identity $\mathrm{f(\mathbf{x},\mathbf{p}) = f'(\mathbf{x}',\mathbf{p}')}$ is straightforwardly obtained.

- **Relativistic Maxwell-Jüttner distributions**
  are the relativistic generalization $\mathrm{f_J = C\,Exp[-E/T]}$ of the thermal Maxwellian. The normalization C is readily obtained applying the Jüttner transformations [Jüttner, 1911; 1928]

$$\begin{aligned} N &= \int C\,\mathrm{Exp}[-E/T]\,d^3p \\ N &= C\,4\pi(mc)^3 \int_0^\infty \mathrm{Exp}[-a\,\cosh\tau]\sinh^2\tau\cosh\tau d\tau, \end{aligned}$$

with the substitution $\mathrm{a = mc^2/T}$. Using the relations for the modified Bessel-K functions of integer order ν

$$\begin{aligned} K_\nu(a) &= a^\nu/(2\nu-1)! \int_0^\infty \mathrm{Exp}[-a\,\cosh\tau]\sinh^{2\nu}\tau\,d\tau \\ K_{\nu+1}(a) &= -K'_\nu(a) + \nu/a\ K_\nu(a) \\ \longrightarrow K_2(a) &= -K'_1(a) + 1/a\ K_1(a) = a\int_0^\infty \mathrm{Exp}[-a\,\cosh\tau]\sinh^2\tau\cosh\tau d\tau, \end{aligned}$$

we finally derive

$$C = aN/4\pi(mc)^3 K_2(a).$$

Now equipped with the basic tools we proceed to derive the relativistic Harris equilibrium. Preserving the formal structure of the original Harris solution we translate to the relativistic regime

$$f^\pm_{RH} = f'_J = \frac{n'a'}{4\pi(mc)^3K_2(a')}\,\mathrm{Exp}[-\gamma'(p')a'],$$

with $\mathrm{a' = mc^2/T'}$ and $\mathrm{n'}$ the particle number density. Primed quantities refer to the current comoving frame of the respective particle specie. Obviously $\mathrm{f_{RH}}$ is a function of the constants of motion $\mathrm{E}' = \gamma'(\mathrm{p}')\mathrm{mc}^2$ and P'_z. Transformation to the simulation/lab frame yields

$$f^{\pm}_{RH} = f_J \cdot f_v = \frac{\gamma_0 n \bar{a}}{4\pi (mc)^3 K_2(\bar{a})} \mathrm{Exp}\left[-\frac{\gamma_0(\gamma(p)mc^2 + (q/e)\beta_{z0} p_z c + q\beta_{z0} A_z)}{\bar{T}} \right],$$

in which $\bar{\mathrm{T}}, \bar{\mathrm{a}}$ represent a scalar temperature. In general the kinetic temperature in the relativistic regime is defined with the relativistic energy-momentum tensor. Details of the relativistic definition of kinetic temperature are discussed in section 4.2.4. Assuming an isotropic distribution (i.e. scalar temperature T') in the current comoving frame implies a temperature anisotropy in the lab frame. Nevertheless we define a scalar $\bar{\mathrm{T}} = \mathrm{T}'$ in the lab frame and motivate in the end the relativistic Harris solution just by a redefinition of the scalar temperature.

Then the current density ensues to

$$j_z = \int e(p_z c^2/E)(f^{+}_{RH} + f^{-}_{RH}) d^3p,$$

and using the invariance of $\mathrm{d}^3\mathrm{p}/\mathrm{E}$ conveniently simplifies to

$$\begin{aligned} j_z = 2 f_v ec \int (d^3p'/E')\gamma_0(-\beta_{z0}E' + p'_{z0}c) f_j &= -e\gamma_0\beta_{z0}c(n^{+'} + n^{-'}) f_v \\ &= -e\beta_{z0}c(n^{+} + n^{-}) f_v. \end{aligned}$$

In the following we assume quasi-neutrality $\mathrm{n}^+ = \mathrm{n}^- = \mathrm{n}$, and the rest of the derivation continues for a total plasma density $2\,\mathrm{n}$. As is shown below the shape of the current sheet is independent of the particle specie, just the direction of the drift is opposite for the respective charges. In the chosen geometry the positrons drift with $-\beta_{\mathrm{z0}}$ and the electrons with β_{z0}. With Ampere's Law $(4\pi/\mathrm{c})\,\mathrm{j_z} = -\partial_\mathrm{y}\mathrm{B_x}$ we obtain the final differential equation

$$\partial_{yy} A_z(y) = 8\pi e \beta_{z0} n\, \mathrm{Exp}\left[\frac{e\gamma_0\beta_{z0}A_z(y)}{\bar{T}} \right].$$

If we then identify the scalar temperature in the lab frame with $T = \bar{T}/\gamma_0$ the differential equation coincides with the original Harris problem. With the condition $\mathrm{A_z}(\mathrm{y{=}L_y/2}) = 0$ we obtain the solution

$$A_z(y) = -\frac{T}{e\beta_{z0}} \ln[\mathrm{sech}^2 \left(\frac{y - L_y/2}{w_0} \right)].$$

Therein we defined the width of the current sheet $\mathrm{w_0} = \Lambda_\mathrm{D}/\beta_\mathrm{z0}$ via the Debye length $\lambda_\mathrm{D} = \beta_\mathrm{th}\mathrm{c}/\omega_\mathrm{p0} = (\mathrm{T}/4\pi\mathrm{e}^2\mathrm{n})^{1/2}$ of the plasma. Consequently the magnetic field structure constitutes in the functional form

$$B_x(y) = B_0 \tanh\left(\frac{y - L_y/2}{w_0} \right).$$

The asymptotic magnetic field value is defined by $\mathrm{B}_0^2/8\pi = 2\mathrm{nT}$, which precisely represents the force balance between magnetic and plasma kinetic energy density. Finally we calculate with Ampere's Law the current sheet density profile to

$$n(y) = n\,\mathrm{sech}^2\left(\frac{y - L_y/2}{w_0}\right).$$

The PIC simulations are performed with physical quantities in dimensionless representation. A thorough discussion of the dimensionless representation is found in Appendix A. The dimensionless formulation of the force balance condition ensues to $\hat{\mathrm{B}}_0^2 = 2\hat{\mathrm{n}}(\hat{\mathrm{T}}^+ + \hat{\mathrm{T}}^-)$. In the PIC simulation we choose $\hat{\mathrm{B}}_0 = 1$ for convenience, and then adapt the density $\hat{\mathrm{n}} = \hat{\mathrm{n}}_0/(2(\hat{\mathrm{T}}^+ + \hat{\mathrm{T}}^-))$ according to the temperature $\hat{\mathrm{T}}$ realized in the specific scenario. In the derivation we assumed the lab frame coincides with the center-of-mass (cms) frame and the respective drift of current constituents is of equal absolute value though oppositely directed. This implies equal temperatures for both species $\hat{\mathrm{T}}^+ = \hat{\mathrm{T}}^- = \hat{\mathrm{T}}$, since quasi-neutrality enforces equal sheet widths $\hat{\mathrm{w}}_0$ for the distributions in configuration space. If we initialize a current sheet of width $\hat{\mathrm{w}}_0$, the Harris equilibrium is established with particle drifts $\beta_{\mathrm{z0}}^- = -\beta_{\mathrm{z0}}^+ = \hat{\lambda}_{\mathrm{D}}(\hat{\mathrm{T}})/\hat{\mathrm{w}}_0 = \lambda_{\mathrm{D}}(\mathrm{T})/\mathrm{w}_0$. Intriguingly, within the constraints of the 1D approach quasi-neutrality enforces $\mathrm{w}_0 > \lambda_{\mathrm{D}}$ observing $|\beta_{\mathrm{z0}}| < 1$.

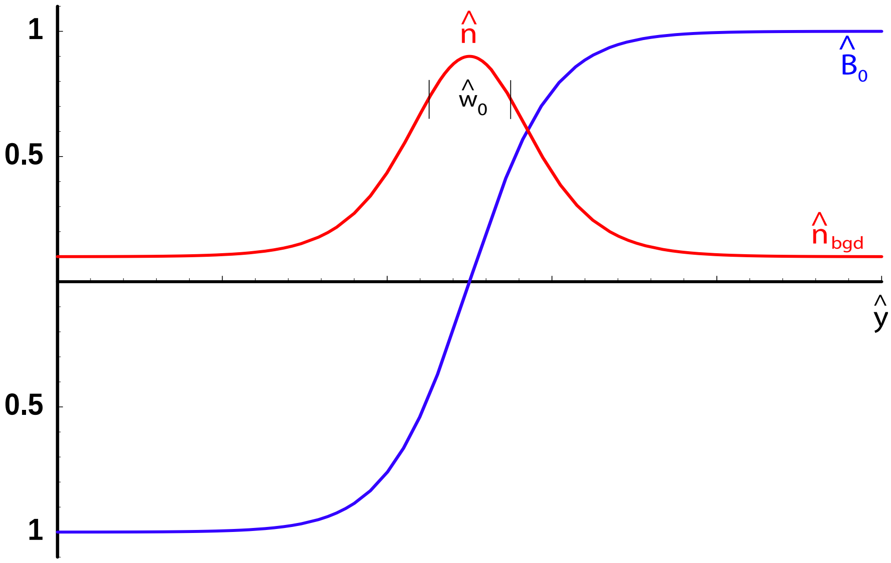

Fig. 3.1: Magnetic field (blue) and current sheet profile (red) for the 1D Harris solution. Asymptotic magnetic field $\hat{\mathrm{B}}_0$ and current sheet central density $\hat{\mathrm{n}}$ are determined according to the force balance condition for a given temperature. In order to increase the stability of the Harris equilibrium an optional homogeneous background $\hat{\mathrm{n}}_{\mathrm{bgd}}$ of particles at rest is introduced in certain scenarios.

3.2 Relativistic Particles in Electromagnetic Fields

In the consecutive sections we study the mechanism of particle acceleration during collisionless magnetic reconnection in the relativistic regime. It is instructive to place in advance some very general remarks on the problem of relativistic particle acceleration in electromagnetic fields. The relativistic particle dynamics in time-dependent electric $\mathbf{E}$ and magnetic fields $\mathbf{B}$ are non-trivial and are addressed in the numerical simulation. On introduction we restrict to the special case of a stationary field configuration, in which $\mathbf{E}$ and $\mathbf{B}$ have exactly transversal orientations. The reasons for this choice are straightforward: First, the scalar produce $\mathbf{E}\cdot\mathbf{B}$ is a Lorentz invariant. Therefore only in configurations with $\mathbf{E}\perp\mathbf{B}$ it is in principle possible to remove either $\mathbf{E}$ or $\mathbf{B}$ contributions by transforming into a distinguished Lorentz frame. And second, in a very rough approximation the magnetic field topology starting from the initial Harris equilibrium evolves during the initial stages of reconnection within the (x,y)-plane. Then the inductive electric field $\mathrm{c}^{-1}\partial_{\mathrm{t}}\mathrm{E}_{\mathrm{z}} = -(\partial_{\mathrm{x}}\mathrm{B}_{\mathrm{y}} - \partial_{\mathrm{y}}\mathrm{B}_{\mathrm{x}})$ points exactly perpendicular to the magnetic field.

Hence, we consider an inertial frame K in which $\mathbf{E}\cdot\mathbf{B} = 0$ is valid. Then two alternatives remain: For $\mathrm{E} < \mathrm{B}$ we transform into the so-called de Hoffmann-Teller-frame. This is a Lorentz frame K' moving with velocity

$$\boldsymbol{\beta}_{HT} = \frac{\mathbf{u}_{HT}}{c} = \frac{\mathbf{E}\times\mathbf{B}}{B^2}$$

with respect to K. The relativistic field transformations are derived to

$$\begin{aligned}
\mathbf{E}' &= \gamma(\mathbf{E} + \boldsymbol{\beta}\times\mathbf{B}) - \frac{\gamma^2}{\gamma+1}\boldsymbol{\beta}(\boldsymbol{\beta}\cdot\mathbf{E}) \\
\mathbf{B}' &= \gamma(\mathbf{B} + \boldsymbol{\beta}\times\mathbf{E}) - \frac{\gamma^2}{\gamma+1}\boldsymbol{\beta}(\boldsymbol{\beta}\cdot\mathbf{B})
\end{aligned}$$

from the Lorentz transformations of the field strength tensor $\mathrm{F}^{\mu'\nu'} = \Lambda^{\mu'}_{\ \sigma}\mathrm{F}^{\sigma\tau}\Lambda_{\tau}^{\ \nu'}$ with $\mathrm{F}^{\mu\nu} = \partial^{\mu}\mathrm{A}^{\nu} - \partial^{\nu}\mathrm{A}^{\mu}$ and $\mathrm{A}^{\mu} = \{\Phi, \mathbf{A}\}$. Applied to the transition $\mathrm{K}\rightarrow\mathrm{K}'$ the fields in the de Hoffmann-Teller-frame ensue to

$$\begin{aligned}
\mathbf{E}'_{\|} &= 0 & \qquad\qquad \mathbf{E}'_{\perp} &= 0 \\
\mathbf{B}'_{\|} &= 0 & \qquad\qquad \mathbf{B}'_{\perp} &= \gamma_{HT}^{-1}\mathbf{B}
\end{aligned}$$

As a consequence thereof, the electric field vanishes in the de Hoffmann-Teller-frame K' and the particle motion is reduced to a simple gyration in the perpendicular (with respect to $\mathbf{u}/\mathrm{c}$) magnetic field $\mathbf{B}'_{\perp}$. For an observer in K the particle trajectory is composed by the superposition of a gyration (with charge-dependent orientation) and a charge-independent drift motion $\mathbf{u}$ perpendicular to the $\mathbf{E}$ and $\mathbf{B}$ fields.

Alternatively, for $\mathrm{E} > \mathrm{B}$ we transform into a different frame K' moving with

$$\boldsymbol{\beta} = \frac{\mathbf{u}}{c} = \frac{\mathbf{E}\times\mathbf{B}}{E^2}$$

in which

$$\begin{aligned} \mathbf{E}'_{\|} &= 0 & \qquad \mathbf{E}'_{\perp} &= \gamma^{-1}\mathbf{E} \\ \mathbf{B}'_{\|} &= 0 & \qquad \mathbf{B}'_{\perp} &= 0 \end{aligned}$$

holds. In this regime particle acceleration by the electric field dominates over the gyro motion. In the frame K' only a finite electric field contribution remains. In the lab frame K the trajectory is described as the superposition of a continuous drift $\mathbf{u}$ and a continuous acceleration parallel to $\mathbf{E}$. In all configurations with $\mathbf{E} \perp \mathbf{B}$ the gyro radius scales as $\mathrm{r_L} \propto \gamma$. For the case $\mathrm{E} > \mathrm{B}$ the particle trajectory can be understood as a gyro motion, in which the relativistic growth of $\mathrm{r_L}$ supersedes the magnetic deflection. The case $\mathbf{E} \perp \mathbf{B}$ is pervasive in reconnection scenarios.

For completeness we consider the other extreme case $\mathbf{E} \| \mathbf{B}$, in which the electric field acceleration takes place always perpendicular to the gyro motion. In this case the motion is continuously accelerated in z and approaches asymptotically the speed of light. The gyro radius remains constant, i.e. $\mathrm{p}_\perp$ is a cyclic variable and $\mathrm{p}_\perp/\mathrm{B}$ is a so-called *adiabatic invariant*.

Finally, what can we infer from these simple considerations? For stationary reconnection (i.e. for a reconnection scenario, in which the X-point remains localized to a fixed position $(\mathrm{x_0}, \mathrm{y_0}, \mathrm{z_0})$) the ratio of inductive electric field to magnetic field is always $\mathrm{E_z}/\mathrm{B_0} \lesssim 1$. Consequently, a transformation to the de Hoffmann-Teller frame is always possible. In the next sections we analyze the particle acceleration in relativistic collisionless reconnection. For the thin current sheets under consideration, the reconnection zone evolves from stationarity in the early stages to highly dynamic configurations in the late time evolution. Remarkably, during late times the accelerating electric field $|\mathbf{E}_{\mathrm{acc}}| = |\mathbf{E}_{\mathrm{ind}} + \mathbf{E}_{\mathrm{com}}| > \mathrm{B_0}$ supersedes the Harris equilibrium field. This is because $\mathbf{E}_{\mathrm{acc}}$ can be understood as the superposition of a reconnection inductive component $\mathbf{E}_{\mathrm{ind}}$ and an additional field contribution $\mathbf{E}_{\mathrm{com}} = -\mathbf{v}/\mathrm{c} \times \mathbf{B}$ from the comotion of the reconnection zone with the dynamically evolving current sheet filaments. In a formal way of argumentation the transformation to the de Hoffmann-Teller-frame $\mathbf{E}_{\mathrm{acc}} = -\mathbf{u}_{\mathrm{HT}}/\mathrm{c} \times \mathbf{B}_0$ would imply a ‘superluminal’ particle comotion $\mathrm{c} \lesssim \mathrm{u_{HT}}$. This formal reasoning proceeds in analogy to the argumentation in the context of particle acceleration during ‘superluminal’ collisionless shocks. Intriguingly, such ‘superluminal’ effects are essential to explain the transition from Poynting-flux-driven flows to kinetically-dominated flows - the most famous paradigm for this transition being the σ-problem of the Crab pulsar wind [Lyubarski & Kirk, 2001; Kirk & Skjæraasen, 2003].

3.3 The Mechanism of Relativistic Particle Acceleration

The following section is published as

'Fast reconnection in relativistic pair plasmas:
Analysis of particle acceleration in self-consistent full particle simulations'

C.H. Jaroschek, R.A. Treumann, H. Lesch, and M. Scholer
Physics of Plasmas, 11(3), 1151-1163, 2004

3.3.1 Abstract

Particle acceleration in collisionless magnetic reconnection is studied in the relativistic regime of an electron-positron plasma. For the first time, the highly dynamic late-time evolution of reconnection is simulated in 2D and the finite size of the acceleration region is resolved in 3D applying a fully electromagnetic relativistic Particle-In-Cell (PIC) code. The late-time evolution is extremely important with respect to particle acceleration, because thin current sheets show a highly dynamic late-time phase with instabilities evolving in the Alfvén velocity $\mathrm{v_{A0}}$ regime. Consequently, since $\mathrm{c} \sim \mathrm{v_{A0}}$ is valid as a peculiarity of pair plasmas, $\mathbf{v} \times \mathbf{B}$-contributions become dominant in the accelerating electric field. Most remarkable: Though acceleration regions are highly variable at late times, the power-law shape of the particle energy distribution is smoothed compared to quasi-static reconnection configurations at early times [Zenitani & Hoshino, 2001]. Spectral power indices of $\mathrm{s} \sim -3$ for the complete simulation box, $\mathrm{s} \sim -1$ within the X-zone are preserved at late times and appear as a characteristic of pair plasma reconnection of thin current sheets! The spectral high-energy cut-off depends on the sheet width at late times and is most efficiently tuned by the ratio $\mathrm{c/v_{A0}}$. In 3D, sheet instabilities limit the acceleration potential of a single X-zone, but current driven instabilities like the relativistic drift kink mode can also significantly contribute to particle acceleration. Via the analysis of particle trajectories, the consequences of a finite 3D acceleration zone are resolved and efficient acceleration mechanisms in the context of dynamic X-points are identified.

3.3.2 Introduction

Magnetic reconnection is the key process for changes in the magnetic field topology [Parker, 1979]. Plasmas in solar-terrestrial as well as astrophysical sites are usually rarefied, as a consequence reconnection takes place in a collisionless environment [Sagdeev, 1979b]. Pair dominance is observed in the plasma of relativistic extragalactic jets [Wardle et al., 1998; Jones, 1998; Lobanov & Zensus, 2001; Hirotani et al., 2000], pulsar outflows like the Crab Nebula [Coroniti, 1990] and core regions of active galactic nuclei (AGN) as the respective jet origin. Magnetic reconnection efficiently transforms magnetic energy into particle kinetic energy [Parker, 1979; Sagdeev, 1979b]. Therefore relativistic magnetic reconnection is proposed as the solution to the σ-problem of the Crab pulsar wind [Coroniti, 1990; Lyubarski & Kirk, 2001; Kirk & Skjæraasen, 2003], as the source of perpetual in situ particle acceleration to compensate for radiative losses in radio jets [Coroniti & Eviatar, 1977; Romanova & Lovelace, 1992; Birk et al., 2001], to provide the lepton injection function for shock acceleration [Sikora et al., 2002], and as the source process for intra-day variability within intrinsic AGN variability models [Reeves et al., 2002; Di Matteo, 1998]. Relativistic pair plasma reconnection of thin current sheets has been studied before analytically [Blackman & Field, 1994], and in 2D Particle-In-Cell (PIC) simulations [Zenitani & Hoshino, 2001]. In Zenitani & Hoshino [2001] a double Harris sheet [Harris, 1962] configuration is applied, which improves current sheet stability and plasma inflow into the initialized X-points. For the total simulation time / spatial extension the particle acceleration region (AR) remains quasi-static, the time and length scales are linear functions of the current sheet width. The relativistic mass gain inhibits particle deflection out of the AR by the reconnected magnetic field yielding an optimized acceleration efficiency. In 2D reconnection configurations the retention time $\mathrm{t_R}$ within the AR solely determines the effective energy gain. In Zenitani & Hoshino [2001] for the regime of quasi-static AR at early times a power-law shaped particle distribution function (PDF) with spectral index $\mathrm{s} \sim -1$ within the X-zone and $\mathrm{s} \sim -3$ for the complete simulation box is obtained. In the present article we investigate in extension to Zenitani & Hoshino [2001] the particle acceleration in the late-time evolution of pair plasma reconnection in 2D PIC simulations and study the influence of the finite AR electric potential associated with current sheet instabilities in real 3D PIC configurations. The late-time evolution is most important with respect to particle acceleration. It is the preeminent condition in the context of astrophysical scenarios. Furthermore, thin currents sheets show a violent dynamic phase at late times with self-consistent reconnection onset in several X-points. The ARs associated to X-points exhibit a dynamic evolution that results in significant $\mathbf{v} \times \mathbf{B}$-contributions to the inductive electric field $\mathbf{E}$, which is the source of particle acceleration. $\mathbf{v} \times \mathbf{B}$-contributions increase $\mathbf{E}$ by one power of ten in the late evolution. Significant $\mathbf{v} \times \mathbf{B}$-contributions are a peculiarity of pair plasmas, because the sheet instabilities evolve roughly with $\mathrm{v_{A0}}$, and only in pair plasmas the Alfvén velocity is comparable to the speed of light $\mathrm{v_{A0}} \sim \mathrm{c}$ for high plasma $\beta \sim 1$ environments with no magnetic guide component. We use the term fast magnetic reconnection (FMR) to distinguish kinetic pair plasma reconnection from conventional Sweet-Parker/Petschek reconnection of electron-proton plasma [Parker, 1957; Sweet, 1958; Petschek, 1964], because FMR takes place on electron inertial scales and the plasma outflow velocity is comparable to $\mathrm{v_{A0}}$. The present article is structured in the following fashion: We introduce the 2D and 3D simulation configurations in section 3.3.3 and the general time scheme observed in all runs in section 3.3.4. The time scheme encloses three phases, within the intermediate phase the reconnection system evolves from a quasi-static X-zone/AR structure into a highly non-linear dynamic configuration predominant at late times. A parametric study in section 3.3.4 shows the connection between initial plasma parameters and PDF. At late times pair plasma reconnection is not anymore independent of the sheet width, and the high energy cut-off is most efficiently tuned by $\mathrm{c/v_{A0}}$. Most remarkable: The power-law tail in the PDF is preserved and even smoothed during the late-time evolution, though dynamic ARs and several X-points contribute to particle acceleration. Furthermore, even though the high energy cut-off shows parameter dependence, the spectral index s ~ -3 appears as a characteristic of the FMR process in pair plasmas. Section 3.3.4 deals with the particle acceleration in a real 3D reconnection configuration. 3D is essential, because the AR is finite in the direction perpendicular to the 2D simulation plane and the finite extension is caused both by instabilities effective within as well as perpendicular to the current sheet plane ! The particle acceleration mechanism is resolved with trace particles in section 3.3.4. Most energetic particles generated in a single acceleration step are an artefact of the 2D configuration, and we give examples of particles accelerated in several consecutive acceleration steps. The FMR mechanism has been intensely studied for an electron-proton plasma [Birn et al., 2001; Shay et al., 1999; Rogers et al., 2001; Hesse et al., 1999; Shay et al., 2001; Pritchett, 2001; Shay & Drake, 1998; Drake, 2001; Zeiler et al., 2002; Hesse & Kuznetsova, 2001; Shinohara et al., 2001; Drake et al., 2003]. A detailed comparison between the particle acceleration via reconnection reported in this article with the electron-proton case is done in section 3.3.5 and with Zenitani & Hoshino [2001] in 3.3.5. In 3.3.5 we summarize our basic findings and give an outlook on possible improvements of the particle energization efficiency.

3.3.3 Simulation Description

The simulations are performed with a fully electromagnetic relativistic Particle-In-Cell (PIC) code. Particles are treated within a real space grid according to a time-centered finite difference scheme [Hockney & Eastwood, 1988; Birdsall & Langdon, 2000]. Particles are moved according to the Boris algorithm [Boris, 1970]. Poisson‘s equation is solved to correct accumulating numerical errors in the electric field. The correction in the electric field is obtained via a multigrid algorithm [Birdsall & Langdon, 2000], which allows to implement non-periodic boundary conditions. Since the symmetric pair plasma case is studied, time and length scales are determined by the electron inertial mass m. Time is normalized to the inverse gyro frequency $\omega_{\mathrm{c0}}^{-1} = (\mathrm{mc/eB_0})$. Lengths are measured in electron inertial lengths $\mathrm{d_0} = \mathrm{c}/\omega_{\mathrm{p0}}$, with plasma frequency $\omega_{\mathrm{p0}} = (4\pi \mathrm{e^2 n_0/m})^{1/2}$. Consequently, velocities refer to the typical Alfvén velocity $\mathrm{v_{A0}} = \mathrm{B_0}/(4\pi \mathrm{mn_0})^{1/2}$ of the system. Dimensional quantities for length and time are restored with the magnetic field $\mathrm{B_0}$ and density $\mathrm{n_0}$ at reference conditions. The ratio of light to Alfvén velocity $\mathrm{c/v_{A0}}$ needs to be adapted to the physical context at hand - and therefore places an additional constraint on the ratio of $\mathrm{B_0/n_0}$ to which the simulation results are applicable in nature. In all our simulation runs $\mathrm{v_{A0}}$ has been chosen on the order of the speed of light, however, the acceleration process turns out to be extremely sensitive to the exact value of $\mathrm{c/v_{A0}}$ (see section 3.3.4). Dimensionless, the Lorentz force

$$\partial_t(\gamma m \mathbf{v}) = \mathbf{E} + \mathbf{v} \times \mathbf{B}$$

and Maxwell‘s equations

$$\nabla \cdot \mathbf{E} = (c/v_{A0})^2 n \qquad \Bigg| \qquad \nabla \times \mathbf{E} = -\partial_t \mathbf{B}$$

$$\nabla \cdot \mathbf{E} \;=\; (c/v_{A0})^2 n \qquad\qquad \Big| \qquad\qquad \nabla \times \mathbf{E} \;=\; -\partial_t \mathbf{B}$$

appear in this fashion. The connection to the equilibrium state is introduced via the initial thermodynamic particle distribution function. We initialize the system with the relativistic Maxwell-Juettner distribution

$$f(p) \propto p^2 \,\mathrm{Exp}[-\gamma(p)\, mc^2/T_s].$$

p is the particle momentum, γ the Lorentz factor, and $\mathrm{T_s}$ the temperature of the specie s ($\mathrm{s = i, e}$ for positrons and electrons). A 1D Harris configuration with sheet width $\mathrm{w_0}$ is set up as initial configuration in the magnetic field and density in the $\mathrm{(x, y)}$-simulation plane,

$$\begin{aligned} B_x(y) &= B_0 \tanh[(y - L_y/2)/w_0] \\ n(y) &= n_0/(2(T_i + T_e))\ \mathrm{sech}^2[(y - L_y/2)/w_0], \end{aligned}$$

respectively. $\mathrm{L_y}$ is the total extension in y-direction, in which the system is confined by conducting walls. Periodic boundary conditions are applied to the corresponding perpendicular directions.

In this article the results of five $2\frac{1}{2}$-D simulations and one 3D simulation are presented. In the 2D configuration particles are moved according to all three momentum components, but quantities are translationally invariant in the z-direction. Typical system size for the 2D configuration is $\mathrm{L_x = 408.0}$ and $\mathrm{L_y = 51.0}$. The computational grid is designed to $\mathrm{nx \times ny = 2048 \times 256}$ and resolves the Debye length more than twice. The 3D run has a spatial extension of $\mathrm{L_x = 102.0}$, $\mathrm{L_y = 51.0}$, $\mathrm{L_z = 25.5}$ and applies $\mathrm{nx = 512}$, $\mathrm{ny = 256}$ and $\mathrm{nz = 128}$ grid points. The key quantities characterizing the initial conditions for the individual runs are listed in Table 3.1. A typical load per cell is 910 pairs in the current sheet and about 8-9 background pairs outside in the lobe, respectively. One purpose is to

Table 3.1: Characteristic Initial Parameters for the Individual Simulations

RUN_ID	$\mathrm{w_0/d_0}$	$\mathrm{c/v_{A0}}$	$\mathrm{T_s/mc^2}$	Nmb. of particles in 10^8
2D_a	1.0	$\sqrt{2}$	0.2	0.51
2D_b	1.7	$\sqrt{2}$	0.2	0.81
2D_c	2.0	$\sqrt{2}$	0.2	0.94
2D_d	1.0	$\sqrt{2}$	0.125	0.51
2D_e	1.0	1	0.25	0.51
3D	1.0	$\sqrt{2}$	0.125	16.4

analyze individual particle trajectories, so the time step is reduced to resolve $\sim \gamma \cdot 600$ points on each gyro orbit. For 15000 time steps, energy conservation is maintained within 10^{-4} in the 2D runs and about 10^{-3} in the 3D run. The applied finite difference scheme is momentum conserving (locally, not for the entire system due to the application of conducting wall boundaries in y) and, hence, by design not energy conserving on the microscopic level [Birdsall & Langdon, 2000]. The deviations occur in wave-particle interactions at small wavelengths. The overall energy stability of the simulation points out that the transformation of field energy into particle kinetic energy is not caused by field fluctuations comparable or beneath the grid resolution. This is a surprise in the first place, because the synchrotron power output of the accelerated fraction of particles is expected to be significant. The solution relies on the fact that typical synchrotron cooling times are $10^8 \mathrm{t_{tot}} \lesssim \mathrm{t_{sc}}$ of the total simulated time $\mathrm{t_{tot}}$. Several tests of the evolution of the initial Harris equilibrium revealed that in systems with $\mathrm{w_0} \sim 1.0$ the current sheet is very fragile and and reconnection sets on spontaneously in multiple X-points in the case of absent initial disturbance. This article focuses on the particle acceleration mechanism during collisionless reconnection. To save computing time and fix the initial X-point to the center of the simulation box, an initial disturbance in the magnetic field is introduced. We neglect quantum effects like Comptonization and pair annihilation/creation. The PIC code is massively parallelized and the 3D configuration requires several thousand CPUh of runtime on an IBM p690 POWER 4 system.

3.3.4 Simulation Results

General Time Evolution of Reconnection in a Pair Plasma

The temporal evolution of the system is divided into three phases. During onset phase $0 \leq \mathrm{t} \leq \mathrm{t_{on}}$ the reconnection starts in a single X-point. The second phase $\mathrm{t_{on}} \leq \mathrm{t} \leq \mathrm{t_{coa}}$, in which the first X-point evolves is the important physical phase. Due to the fragility of the thin current sheet, secondary X-points develop and the system evolves into a collisionless tearing configuration. In the final phase starting at $\mathrm{t} \sim \mathrm{t_{coa}}$ the various tearing islands begin to coalesce. The second phase is subdivided into three subphases by time

Table 3.2: 2D Characteristic Timescales and Reconnection Field Quantities

RUN_ID	$\mathrm{t_{on}}\,\omega_{c0}$	$\mathrm{E_z^{on}/B_0}$	$\mathrm{B_y^{on}\,w_0/B_0\,d_0}$	$\mathrm{t_{sep}}\,\omega_{c0}$	$\mathrm{t_{equ}}\,\omega_{c0}$	$\mathrm{E_z^{equ}/B_0}$	$\mathrm{t_{coa}}\,\omega_{c0}$
2D_a	20.	-0.18	0.6	25.	60.	-2.1	70.
2D_b	40.	-0.18	0.6	55.	75.	-1.8	140.
2D_c	45.	-0.18	0.6	65.	90.	-1.5	/
2D_d	20.-25.	-0.15	0.5	30.-35.	65.	-2.1	85.
2D_e	30.	-0.24	0.75	40.	75.	-2.5	100.

marks $\mathrm{t_{sep}}$ and $\mathrm{t_{equ}}$. The reconnection X-point separates at $t \sim t_{sep}$ and disperses into ±x-direction. This corresponds to the dynamic evolution of the first X-point and marks the time from which on the plasma configuration fundamentally deviates from the system studied in Zenitani & Hoshino [2001]. The separation speed is progressive, until at $\mathrm{t \sim t_{equ}}$ a dynamic equilibrium is reached as soon as the rigidity of the current sheet compensates for the separative forces. The division into these phases is common for all runs. Just the quantitative values for the time scales and the reconnection electric and magnetic fields vary according to the individual parameter set. In Table 3.2 characteristic quantities are listed for each individual run. These values are used below in the detailed description of phases.

Onset phase

During onset phase the artificial disturbance in the magnetic field seeds field line merging at a fixed location in the center of the simulation box. The onset time $\mathrm{t_{on}}$ is the typical time period until a single X-point region is established. The strength of the initial non-ideality is equal for all runs, its spatial extension scales with the sheet width. Therefore, the onset time and the typical time periods of consecutive phases reflect the influence of critical parameters and should be independent from the initialization in the relative comparison of different runs. Figs. 3.2(a) and (b), respectively show the initial X-point in magnetic field lines and inductive electric field $\mathrm{E_z}$. Reconnection is static and centered in the $\mathrm{(x, y)}$-plane, particle inflow starts from the background particle reservoir. The line close to the initial Maxwellian in Fig. 3.3(a) corresponds to the single X-point configuration at $\mathrm{t \sim t_{on} \sim t_1}$. Acceleration of particles by $\mathrm{E_z}$ gradually generates non-thermal contributions.

Single X-point Phase

The runs 2D_a,b,c reflect the influence of the sheet width $\mathrm{w_0}$ (Table 3.1) on the reconnection rate in the quasi-static phase $\mathrm{t_{on} \leq t \leq t_{sep}}$. For the special case of the pair plasma the sheet width $\mathrm{w_0}$ is the demagnetization scale size, since no ion inertial length is involved. The reconnection rate is constant for all three runs as indicated in the inductive electric field $\mathrm{E_z^{on}/(B_0) \sim 0.3}$ and reconnected current $\mathrm{B_y^{on}\, w_0/(B_0\, d_0) \sim 0.6}$. This is in accordance with results obtained elsewhere for the electron dissipation region in an electron-proton plasma X-point configuration [Shay et al., 1999; 2001; Pritchett, 2001; Shay & Drake, 1998]. The particle inflow takes place perpendicular to the current sheet [Fig. 3.4(c)]. Up to $\mathrm{t_{sep}}$ the physics is comparable to the configuration discussed in Zenitani & Hoshino [2001]. After $\mathrm{t_{sep}}$ the current sheet evolution becomes extremely dynamic. The background particle reservoir is limited, and as a consequence the current sheet as well as the inflow region around the initial X-point thin out in density [Fig. 3.4(b)]. The system evades under the premise of optimum particle inflow, splitting the inflow stream from transversal into an X-like shape [Fig. 3.4(d)]. The x-contiguity of the current sheet is disrupted. Consequently the acceleration region (AR) connected to the initial X-point divides as well, and recedes into ±x-direction, each part attached

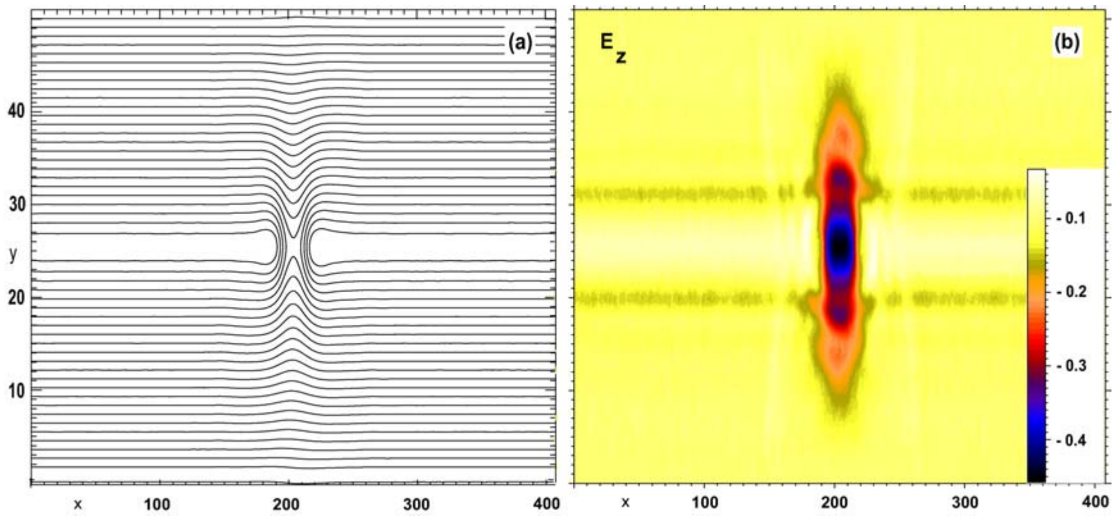

Fig. 3.2: Contour plot of the magnetic vector potential A_z (a) and the inductive electric field E_z (b) in the (x, y)-plane for run 2D_b after reconnection onset at $t_{on} = 40$. E_z constitutes a single contiguous quasi-static acceleration region (AR).

to another current sheet end [Fig. 3.4(a)]. We define an AR as the region, in which E_z exceeds the local B_{tot}, assuring the accelerating force component dominates the deflecting component in every Lorentz frame. In section 3.3.4 we show that the inductive reconnection field E_z is the predominant acceleration force. Hence, in the following we use AR and regions with substantial E_z contributions synonymously. The separation speed is progressive until at $t = t_{equ}$ a dynamic equilibrium stage is reached. During $t_{sep} \leqq t \leqq t_{equ}$, the absolute value of the accelerating field E_z increases dramatically by one order of magnitude (Table 3.2). A significant number of non-thermal particles is generated. Particles traversing ARs connected to each sheet end form a “bump” on the particle distribution function at high energies as indicated in Fig. 3.3. At t_{equ} the separation speed as well as E_z saturate. The reconnection rate in this dynamic equilibrium is limited by the current sheet rigidity ($= w_0$), since imported magnetic flux via plasma inflow competes with separation velocity. As both sheet ends retreat in $\pm x$, the plasma piles up in the transverse direction along the reconnected B_y-component. Each sheet end evolves into T-like shape [Fig. 3.5(c)]. The AR extends many sheet widths in $\pm y$. The magnetic field follows this shape, with the B_y^{equ}-components on both sides of the transverse extension being oppositely aligned [Fig. 3.5(b)]. After t_{equ} each of the T-shaped configurations recedes with $\mathbf{v}_{equ}$ towards the edges of the simulation plane. The resulting electric field $\mathbf{E}_z^{equ} = -\mathbf{v}_{equ} \times \mathbf{B}_y^{equ}$ is also oppositely directed on each side of the T-shaped sheet ends [Fig. 3.5(a)]. This highly dynamic late-time evolution is most important for the particle acceleration process as seen in Fig. 3.3(a) for $t = t_{2,3}$. AR formation and time evolution of the particle distribution function (PDF) correspond directly [Fig. 3.3(b)]: Dynamic $-\mathbf{v}_{equ} \times \mathbf{B}_y$-contributions shift the high energy bump

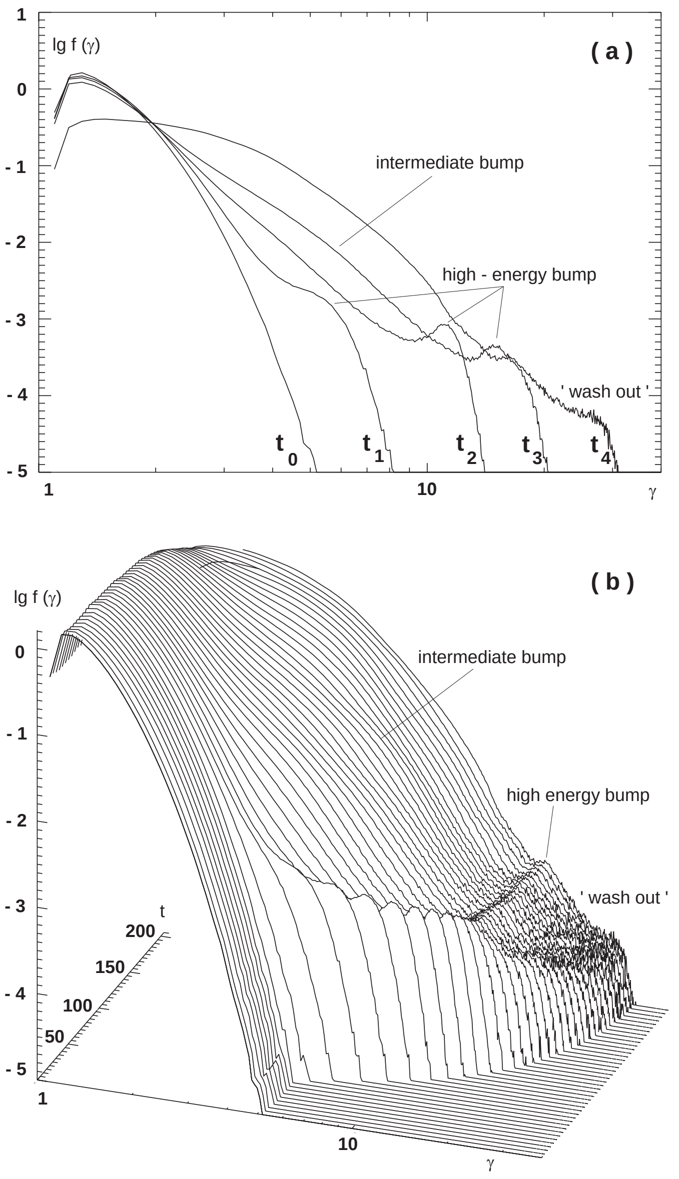

Fig. 3.3: Normalized PDFs $f(\gamma)d\gamma$ for selected times $t_{0,1,2,3,4}\,\omega_{c0}$=0,45,85,105,205 (a) and as time stack plot (b) of run 2D_b for the complete simulation box. Time points show non-thermal contributions in the quasi-static phase ($t_{on} \leq t_1 \leq t_{sep}$) and after current sheet separation ($t_2 \geq t_{sep}$), intermediate bump formation ($t_3 \sim t_{equ}$), and "wash out" of the high-energy bump ($t_{coa} \lesssim t_4$).

upwards, a new bump forms at intermediate energies, generated by particles traversing one of the ARs surrounding each T-shaped current sheet end. Finally the high energy bump is dispersed by particles receiving individual energy boosts from each of these

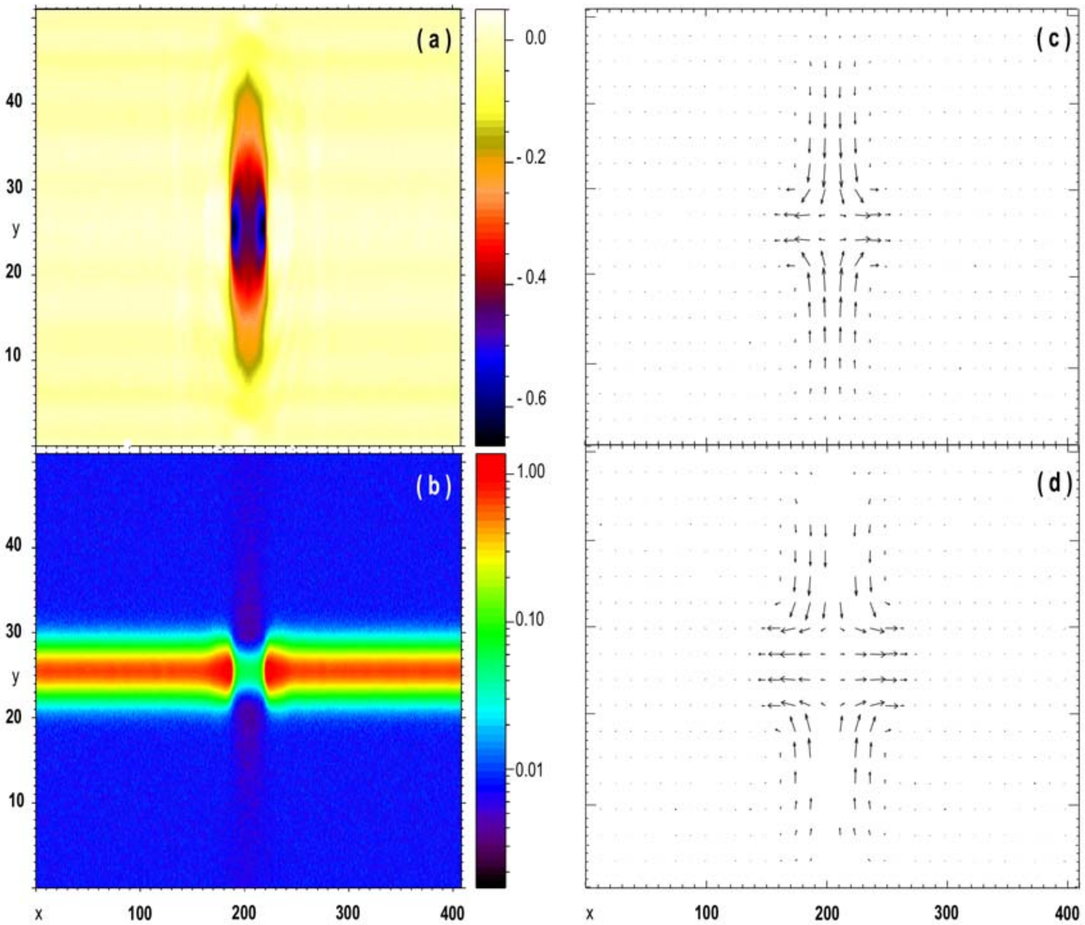

Fig. 3.4: E_z (a) and logarithmic particle density lg(n) (b) in the (x, y)-plane shortly after t_{sep} for run 2D_b. The depletion of the background plasma in the inflow region of the first X-point can be clearly identified in (b). As a consequence thereof, the current sheet (b) and the quasi-static AR (a) separate. Vector field plots show the bulk velocity within the (x, y) -plane for run 2D_b immediately before (c) and shortly after t_{sep} (c). The particle inflow restructures from transversal to the current sheet (c) into assuming an X-shape with each lateral connected to the AR of the respective current sheet end.

ARs. This “wash out” effect is charactistic for the final phase, in which the T-shaped sheet end transforms into an island, and the current sheet disrupts into several filaments.

Island Coalescence Phase

In the third and final phase the current sheet breakes up into several X-points. The magnetic field reconfigures into a collisionless tearing configuration [see the contours of A_z in Fig. 3.5(e)]. It is obvious from the complex structure of E_z in Fig. 3.5(f) that each

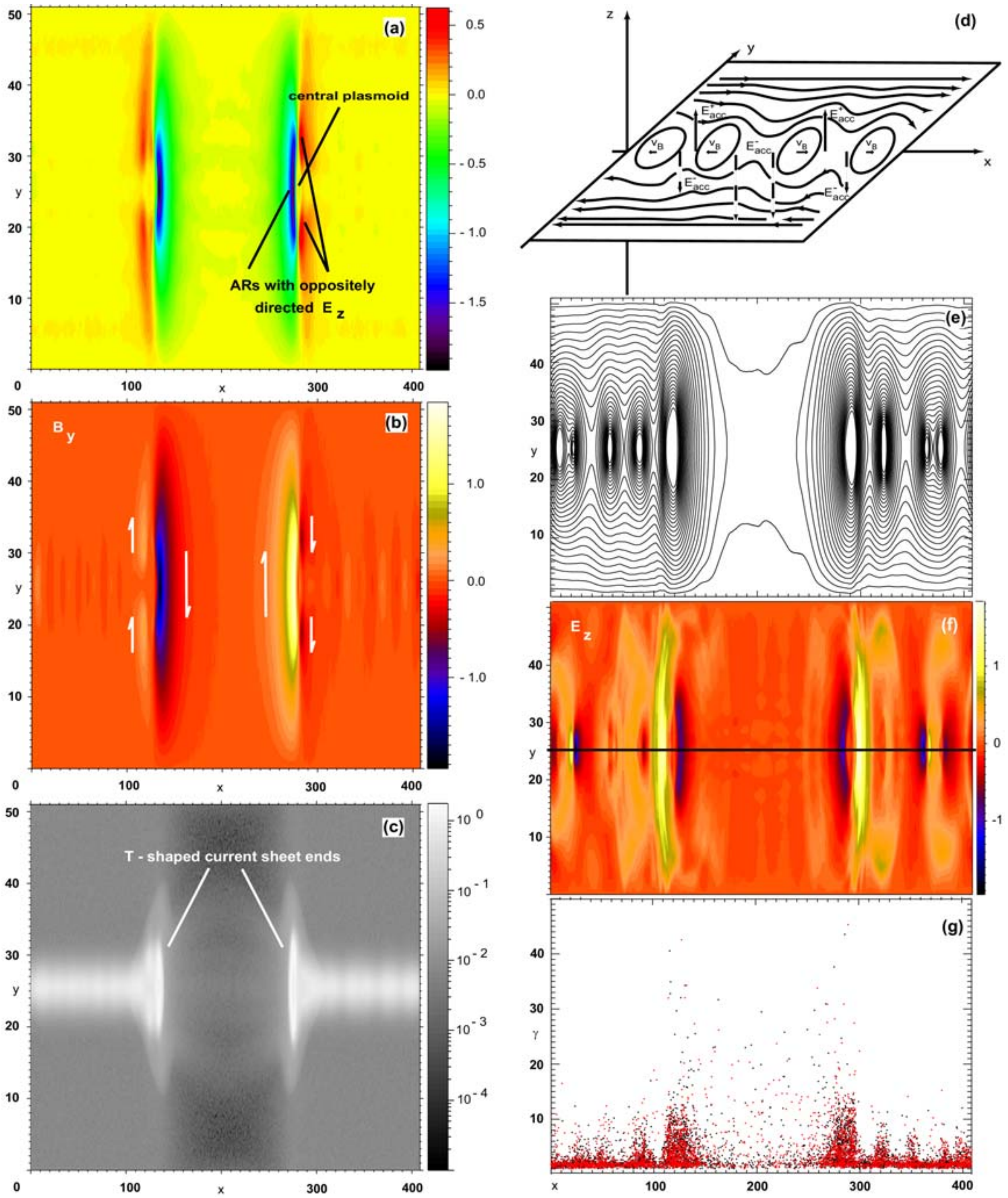

Fig. 3.5: Accelerating field E_z (a), reconnected magnetic field B_y (b) and logarithmic density lg(n) (c) in the (x, y)-plane for run 2D_b at $t_{sep} < t\,\omega_{c0} = 105 < t_{coa}$. The plasma piles up in the outflow direction and forms at each current sheet end into T-like shape (c). B_y starts to line out plasmoid islands at each sheet end (b). The $\mathbf{v} \times \mathbf{B}$-motion of the island structure results in oppositely directed AR zones embracing each island (a). Schematic view of the field topology within the (x, y)-plane for the island coalescence phase $t > t_{coa}$ (d). Several tearing islands evolve and coalesce due to the attraction of parallel $\mathbf{j}_z$ current filaments. Dynamic E_z contributions arise from the $\mathbf{v}_{equ} \times \mathbf{B}$ island motion. Direct correspondence to simulated magnetic field lines (e) and E_z (f) at $t_{coa} \lesssim t$ (exemplaric from run 2D_b at $t\,\omega_{c0} = 165$). Particle energization (g) along the white line drawn in (f) shows the relation between dynamic ARs and PDF bump structure for positrons (red) and electrons (black).

X-point forms a new set of ARs. Neighbouring islands start to coalesce at $\mathrm{t} = \mathrm{t}_{\mathrm{coa}}$. This coalescence is caused by the attraction of parallel current j_{z} filaments and affects the E_{z} structure in a stochastic manner since, in the nonlinear regime, the X-points appear at random positions.

Figs. 3.5(d) represents a schematic view of the field configuration. The magnitude of E_{z} is constrained by the bulk velocities $\mathbf{v}_{\mathrm{B}}$ of the islands. The process of multiple acceleration becomes increasingly more important with decreasing spatial separation of X-points and hence with decreasing width of the current sheet. The final particle distribution function in Fig. 3.3(b) for $\mathrm{t} \sim \mathrm{t}_{\mathrm{fin}} = \mathrm{t}_4$ reflects the contributions of several ARs in several bumpy structures at various energies, “washed out” out due to particles traversing more than one AR. Surprisingly, despite of the highly turbulent spatial and temporal appearance of ARs, the PDF maintains a power-law shape !

Fig. 3.5(g) shows the Lorentz factor γ as function of x-position for particles located along the center of the current sheet. Particles are depleted in the region where the current sheet breaks up. Maximum energy gain occurs in the zones of high inductive electric fields at each end of the separating sheet parts. These particles constitute the “washed out” first bump (Fig. 3.3). At other positions along the current sheet the energy gain is less than in the first X-point. It is sufficient, though, to generate an intermediate bump on the smooth power-law tail. This new bump appears at a position in γ up to which an individual new AR is capable to contribute.

Initial Plasma Parameter / Acceleration Efficiency Correspondence

The key initial parameters are current sheet width w_0, Maxwellian temperature T_{s}, and the ratio $\mathrm{c}/\mathrm{v}_{\mathrm{A0}}$. A set of five 2D simulations has been performed, in which for a subsample of two to three runs each just a single parameter is varied to allow direct comparison (Table 3.1). Compared are time scales of the time scheme introduced in 3.3.4, reconnection rates in the quasi-static phase ($\mathrm{E}_{\mathrm{z}}^{\mathrm{on}}, \mathrm{B}_{\mathrm{y}}^{\mathrm{on}}\,\mathrm{w}_0$) and in the late-time evolution ($\mathrm{E}_{\mathrm{z}}^{\mathrm{equ}}$) (Table 3.2). According to Runs 2D_a,b,c, onset times t_{on} roughly scale linearly, whice $\mathrm{t}_{\mathrm{sep}}, \mathrm{t}_{\mathrm{equ}}, \mathrm{t}_{\mathrm{coa}}$ scale logarithmically with w_0. In the quasi-static phase reconnection rates are independent of sheet width, whereas sheet rigidity ($=\mathrm{w}_0$) determines the maximum $\mathrm{E}_{\mathrm{z}}^{\mathrm{equ}}$ at late times. Broader sheets have less $-\mathbf{v}_{\mathrm{equ}} \times \mathbf{B}_{\mathrm{y}}$-contributions due to slower plasmoid coalescence. T_{s} speeds up the time evolution and makes the quasi-static phase more violent, but is unimportant for $\mathrm{E}_{\mathrm{z}}^{\mathrm{equ}}$ at late times (Runs 2D_a,d). Decisive for the reconnection rates/acceleration efficiency at all times is $\mathrm{c}/\mathrm{v}_{\mathrm{A0}}$ (Runs 2D_d,e). Maximum $\mathrm{E}_{\mathrm{z}}^{\mathrm{equ}}$ values are reached for $\mathrm{c} = \mathrm{v}_{\mathrm{A0}}$. The correspondence between reconnection rates and particle acceleration efficiency is demonstrated in the PDF time evolution of the respective simulations (Fig. 3.6). All spectra are power-law shaped and show a high-energy spectral cut-off. Both, high-energy cut-off as well as spectral index s indicate the acceleration efficiency. In the 2D reconnection configuration the acceleration potential is not finite along the separatrix. The energy gain $\Delta\mathrm{E}_{\mathrm{2D}}=\mathrm{e}\,\Delta\phi_{\mathrm{2D}} \sim \mathrm{e}\,\mathrm{c}\,\mathrm{t}_{\mathrm{R}}\,\mathrm{E}_{\mathrm{z}}$ is determined by the particle’s retention time t_{R} within the AR. For the quasi-static reconnection configuration established until $\mathrm{t}=\mathrm{t}_{\mathrm{sep}}$ (situation studied in Zenitani & Hoshino [2001]), t_{R} is directly related to the AR geometry:E_{z} is independent of w_0, the deflecting

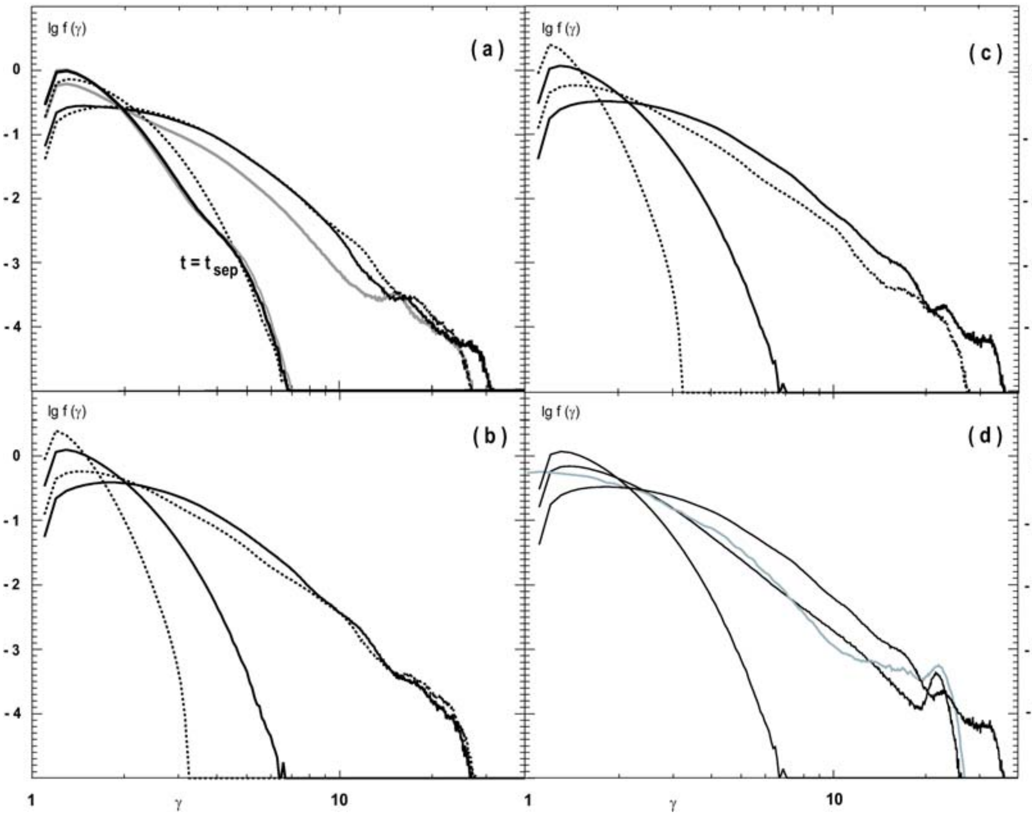

Fig. 3.6: Comparison of $f(\gamma)d\gamma$ for different sheet widths (a) $w_0 = 1, 1.7, 2$ (dotted,solid,grey) at the end of the quasi-static ($t \lesssim t_{sep}$) and dynamic phase. Influence of Maxwellian temperature (b) for $T_s = 64\,keV$ (2D_d dotted) and $T_s = 102\,keV$ (2D_a solid), as well as the ratio of light to Alfvén velocity (c) $c/v_{A0} = \sqrt{2}, 1$ (dotted, solid) for initial and final state. In (d) the PDF of run 2D_e (black) is plotted for $t_0 = 0$, $t_1 = 90\,\omega_{c0}^{-1} < t_{coa}$ and the final state at $t_3 = 165\,\omega_{c0}^{-1}$. Up to t_1 the first X-point dominates and the PDF is compared to the result published in Zenitani & Hoshino [2001].

force is $\propto 1/w_0$. In the quasi-static phase the AR location is fixed in the (x, y)-plane, the particle performs some fraction of a gyro-orbit in the (x, z)-plane. $t_R = w_0/\langle v_x^{esc}\rangle$, because $\langle v_x^{esc}\rangle \propto c\,B_y/E_z$ defines an average sidewards escape velocity from the AR. Consequently, t_R and ΔE_{2D} are independent of sheet width, and the runs 2D_a,b,c show comparable non-thermal cut-offs at $t = t_{sep}$ [Fig. 3.6(a)]. In the late-time evolution AR geometry and location evolve dynamically. t_R is usually prolonged, since $\langle \mathbf{v}^{esc}\rangle$ always has a component parallel to the AR velocity $\mathbf{v}_{equ}$. The AR size in the (x, y)-plane is some monotonic function of w_0. On the contrary, the essential $-\mathbf{v}_{equ} \times \mathbf{B}_y$-contributions to $\mathbf{E}_z$ decrease with w_0. Consequently, the run 2D_b with intermediate sheet width shows the best trade-off in the t_R/E_z-competition and the highest final energy cut-off at $\gamma \sim 30$ in Fig. 3.6(a).

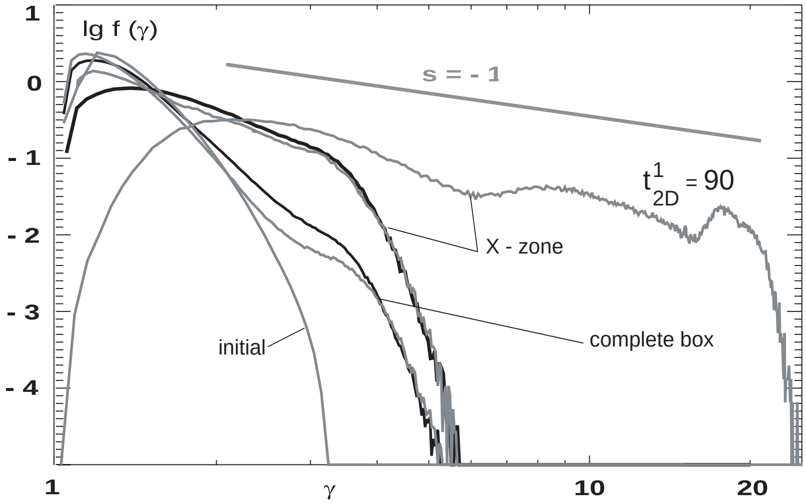

Fig. 3.7: PDF comparison $f(\gamma)d\gamma$ for the runs 2D_d (grey) and 3D (black), which accord in initial parameters. X-zone selections extended in $0.39 \le x/L_x \le 0.61$, $0.41 \le y/L_y \le 0.59$, $0.24 \le z/L_z \le 0.82$ at $t_{3D}\,\omega_{c0} = 55$ for the 3D case, for the 2D cases in $0.47 \le x/L_x \le 0.54$, $0.40 \le y/L_y \le 0.59$ at $t^0_{2D}\,\omega_{c0} = 35$, and $0.37 \le x/L_x \le 0.63$, $0.37 \le y/L_y \le 0.63$ at $t^1_{2D}\,\omega_{c0} = 90$, respectively. t_{3D}, t^0_{2D} correspond to t_{sep}, t^1_{2D} is the time compared with Zenitani & Hoshino [2001] for the complete box in Fig. 3.6(d)

Fig. 3.6(b) illustrates the weak temperature dependence of the acceleration process. Compared are runs with initial $T_s = 64\,\mathrm{keV}$ and $102\,\mathrm{keV}$. Although the initial PDFs differ significantly, the power-law cut-off of the final PDFs appears at comparable energies.The number of plasmoid islands formed during $t_{sep} \lesssim t \lesssim t_{coa}$ increases with T_s. The islands coalesce and the number of X-points is reflected in the number of newly created secondary bumps. For the lower T_s in Fig. 3.6(b) three distinct bumps can be identified. For higher T_s the number of secondary bumps is too large to be resolved individually. More X-points that are less stable and less geometrically extended result in a zero net effect on the acceleration efficiency.

Fig. 3.6(c) finally shows that the acceleration efficiency in non-driven reconnection of thin current layers is most efficiently tuned with c/v_{A0}. For $c = v_{A0}$ the spectral cut-off appears at $\gamma \sim 38$, with spectral index $s \sim -2.8$. It is important to note, that the spectral cut-off depends on the size of the simulation box. We have performed another run with $L_x \times L_y = 816\,d_0 \times 102\,d_0$, in which the spectral cut-off extends up to $\gamma \sim 70$. In such a case consecutive acceleration in several ARs becomes more important (see section 3.3.4). Another critical parameter is the fractional background density n_{bgd}/n_0. Accordinging to Fig. 3.4, the background plasma is rapidly depleted. Higher fractional background density stabilizes the system and feeds the first X-point with plasma. This prolongs the quasi-static phase and pronounces the bump in the PDF at the high energy cut-off. Throughout the simulations presented in this article $\mathrm{n_{bgd}/n_0} = 0.95\%$ to ensure a violent late-time evolution. For all the five runs, for the PDF of the complete simulation box the final spectral cut-off varies between $25 < \gamma < 38$ and the spectral index between $-2.8 > \mathrm{s} > -3.5$.

Two results of the parametric study are especially remarkable: First, the energy spectrum remains power-law, regardless of the number of X-points contributing, and of the lifetime / geometric extension of ARs - despite of the fact that $\mathrm{w_0, c/v_{A0}, T_s}$ dramatically influence these characteristics in the late evolution. Second, remarkably flat spectral indices $\mathrm{s} \sim -1$ are obtained within the reconnection zone of the first single X-point configuration for all runs (Fig. 3.7). The selection criterion for the spectrum is the time up to which the AR of the first single X-point evolves individually, i.e. essentially $\mathrm{t} \sim \mathrm{t_{coa}}$. In Fig. 3.7 the PDF appears divided into two steps and the final bump, which is due to geometrical effects, because the shape and spatial extension of the AR vary rapidly after $\mathrm{t_{sep}}$. Within an individual X-point as well as for the complete simulation box the spectral index s does not show significant parameter dependence, whereas the high energy cut-off does. In fact, s appears as a characteristic of the reconnection process of thin current layers in the quasi-static as well as in the dynamic phase!

Characteristics of the 3D Configuration

Finite size of 3D acceleration potential

Particle acceleration in magnetic reconnection is a real 3D problem, if the AR extension $\Delta \mathrm{z_{AR}}$ perpendicular to the $(\mathrm{x, y})$-simulation plane of the 2D configuration limits $\mathrm{t_R}$. In fact, $\mathrm{t_R^{3D}} = \Delta \mathrm{z_{AR}/c} \leq \mathrm{t_R^{2D}}$. Consequently, the finite 3D AR size determines the particle acceleration in pair plasma reconnection of thin current sheets. Figs. 3.8(a)-(c) show that the AR forming from the initialized X-point extends roughly $\Delta \mathrm{z/d_0} \sim 20$, $\Delta \mathrm{y/d_0} \sim 10$, $\Delta \mathrm{x/d_0} \sim 25$, which limits the energy gain per AR encounter to $\Delta\gamma \sim 30$ (see section 3.3.4 for details on the acceleration mechanism). The AR separates into ±x-direction analogous to the 2D case [Figs. 3.8(b),(c),(e)]. The system enters the dynamic phase at $\mathrm{t} = \mathrm{t_{sep}} \sim 50\,\omega_{c0}^{-1}$ slightly later than the respective 2D simulation 2D_d. Again, the reason is the rapid depletion of background plasma and particle inflow from ±x along the $\mathrm{B_x}$ Harris lobe-field.

Instabilities Effective Parallel to the Diamagnetic Current

In 3D, instabilities are effective in addition parallel to the diamagnetic Harris current. For very thin sheets possible instability modes in a pair plasma are the relativistic two-stream instability (RTSI), and the relativistic drift kink instability (RDKI), i.e. the relativistic generalization of the DKI [Pritchett et al., 1996; Daughton, 1998]. Due to the low fractional background density, contributions from the Kelvin-Helmholtz instability are not expected. The parallel instability mode sets on very early at $t\,\omega_{c0} \sim 18$, presumably by the electrostatic, current-driven (=Buneman-type) RTSI, which strongly heats up the plasma and serves as the trigger mechanism of the RDKI. The RTSI is unimportant at late times. In Fig. 3.8 the RDKI dominates: Within the (x,z)-plane, (d) shows the crossings of the kinked current sheet, (b) the alternating zones of the Harris B_x shifted in from opposite lobes, and (c) alternating zones of $E_z/B_0 = -0.3$ and $E_z/B_0 = +0.1$. Characteristic "trapping" structures arise from the RDKI in $(z, v_z/c)$-phasespace (f). The extended thermal spread around the positron bulk drift in (f) indicates the strong plasma heating. If the heating is suppressed by a magnetic guide component, characteristic lepton phase space holes [Drake et al., 2003] should become visible. We note that broader sheets are not anymore unstable with respect to the RTSI. If the non-linear evolution of the current sheet is not electrostatically triggered by the RTSI, the evolution of the RDKI mode appears to be strongly inhibited in time, though the final state is comparable [Zenitani & Hoshino, 2003]. Concluding, we observe instabilities within the (x,z)-plane effective both parallel to the initial Harris current as well as perpendicular. As a consequence, current sheet instabilities are also a real 3D problem.

3D Consequences on the Particle Acceleration Efficiency

In the present article we treat current sheet instabilities solely with respect to particle acceleration efficiency. A comparison of the 2D and 3D PDFs between runs with comparable parameter set (Fig. 3.7) provides two important insights : First, instabilities driven by the Harris current significantly contribute to particle acceleration. The 3D PDF for the complete simulation box contains about two times more non-thermal particles than the 2D pendant in which the RDKI is suppressed. Second, within the initialized X-zone 2D and 3D PDFs are comparable. Consequently, the importance of $\mathbf{v} \times \mathbf{B}$-contributions in the dynamic phase effective within the (x,y)-plane as discussed in 2D is valid also in the 3D case. The consequences for the acceleration mechanism are discussed in the following section.

Detailed Analysis of the Acceleration Mechanism

In every 2D run a representative sample of 8192 particle trajectories was analyzed and correlated with the field data at every time step. We identified three classes of acceleration scenarios : In Class 1 particles traverse only a single AR and are accelerated within a single step. In Class 2 particles experience consecutive energy boosts in both ARs surrounding an evolving plasmoid island. Finally, Class 3 contains all particles accelerated in ARs of several X-points. Two general remarks hold for all classes : First, particle energization is most efficient during the highly dynamic late-time phase ($t_{sep} \lesssim t$) of reconnection. Second, E_z is the solely accelerating, B_y the predominant deflecting component acting on the particle trajectory.
Class 1 is illustrated in Fig. 3.10 (dotted lines). The time mark introduced at $t_0\,\omega_{c0} = 85$ corresponds to the E_z, B_y contours in Figs. 3.9(a),(b), on which the particle trajectory for $0 < t \leq t_0$ is superimposed. At early times one sees the cyclic (p_y, p_z) gyro-motion

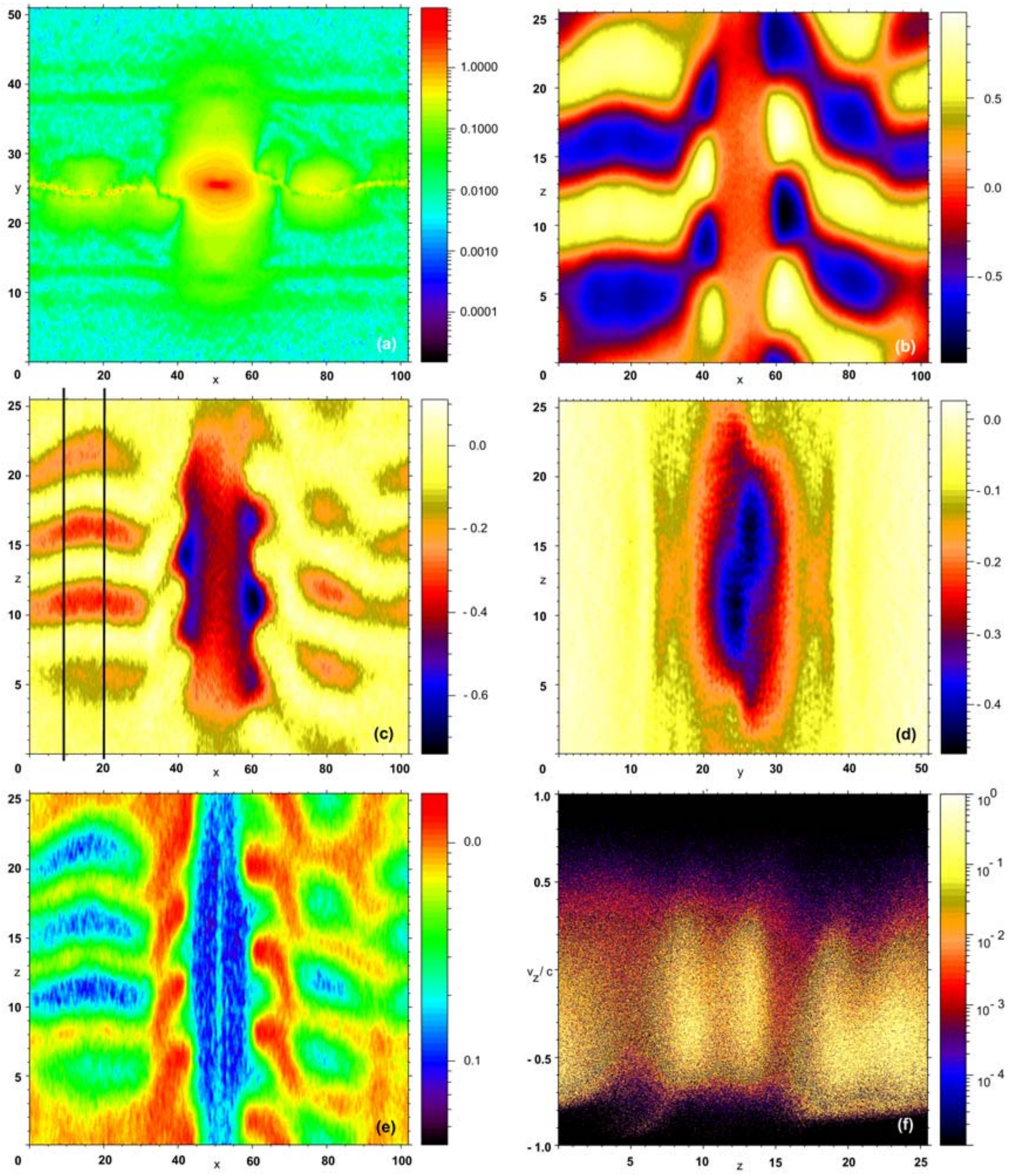

Fig. 3.8: 3D data shortly after the start of the dynamic phase $t_{sep} \lesssim t\,\omega_{c0} \sim 55$. Contours in (x, y) of the AR size $\lg(E_z/B_{tot})$ (a), in (x, z) of B_x/B_0 (b), in (x, z) of E_z/B_0 (c), in (y, z) of E_z/B_0 (d), in (x, z) of $\lg(n/n_0)$, and in $(z, v_c/c)$ of the positron phasespace density (e). All spatial contour planes include the simulation box center. Spatial selection in (x, z) for the phase space plot (f) are the black lines indicated in (c) and the sheet width in y.

in the initial Harris $\mathrm{B_x}$-field and its projection onto the $(\mathrm{p_x}, \mathrm{p_z})$-plane [straight line in Fig. 3.10(d)]. The particle is drawn with the inflowing plasma into the reconnection region. Significant growth of relativistic energy [Fig. 3.10(c)] is coincident with the particle's entrance into the stationary AR of the quasi-static reconnection phase. From this point on the trajectory is determined by $\mathrm{B_y}$ and $\mathrm{E_z}$. The temporal behaviour of $\mathrm{E_z}, \mathrm{B_y}$ [Fig. 3.10(a),(b)] is paradigmatic for Class 1 positrons (for Class 1 electrons just the sign is reversed): The positron enters the reconnection region where $\mathbf{E}_\mathrm{z}$ accelerates it in $-$z-direction, thereby gaining $-\mathrm{p_z}$-momentum. The initial gyro-motion in the $(\mathrm{p_y}, \mathrm{p_z})$-plane is progressively transferred into a $(\mathrm{p_x}, \mathrm{p_z})$-motion as long as $\mathbf{B}_\mathrm{y}$ deflects the particle out of the AR. $\mathbf{v}^\mathrm{esc} \sim \mathbf{p}_\mathrm{x}/\gamma$ is the particle's AR escape velocity. At $\mathrm{t} \geq \mathrm{t_{sep}} \sim 60\,\omega_\mathrm{c0}^{-1}$ reconnection enters the dynamic phase. The maxima in the accelerating electric field recede with the current sheet ends towards ±x-direction. The AR moves with $\mathbf{v}_\mathrm{equ}$ out of the particle's trajectory. This is the reason for the $\mathrm{E_z}, \mathrm{B_y}$ values to saturate at $\mathrm{t}\,\omega_\mathrm{c0} \sim 60$. But $\mathbf{v}^\mathrm{esc}$ always has significant parallel components to $\mathbf{v}_\mathrm{equ}$. During this stage $\mathrm{v_{equ}}$ is some fraction of $\mathrm{v_{A0}}$. The positron velocity is close to c. It is progressively deflected into $-$x and, with its higher velocity, runs out the receding center of the AR until it reenters the zone of maximum $\mathrm{E_z}$ [Fig. 3.9(a),(b)]. In addition, $\mathrm{E_z}$ increases significantly during this dynamic phase. The deflection continues until all the particle momentum is converted into $-$x-direction and the positron moves faster than the AR. The acceleration process stops when the particle has crossed the entire AR. The particle performs just half an extended gyro orbit in the reconnected field $\mathrm{B_y}$ during acceleration [Fig. 3.10(d)]. During the acceleration step the particle advances about $\Delta \mathrm{z} \sim 70\,\mathrm{d_0}$. The total energy gain is ~ 45 times the rest mass, 65% of the energy gain takes place in the dynamic late-time evolution. Concluding, there are two reasons for the increased acceleration efficiency : First, the relativistic mass gain inhibits the deflection out of the quasi-static AR ($\dot{\mathbf{v}}^\mathrm{esc} \propto 1/\gamma$) [Zenitani & Hoshino, 2001]. Second, in the dynamic phase, $\mathbf{v}^\mathrm{esc}$ has always significant parallel components to the AR motion $\mathbf{v}_\mathrm{equ}$, so that particles can comove with AR dynamics.

Within Class 2, particles are grouped which traverse ARs that surround an evolving plasmoid island. An exemplaric case is illustrated in Figs. 3.9(c)-(f) and Fig. 3.10 (grey line). The initial position of the particle is located further away from the current sheet. It passes the first AR when the system is already in its dynamic phase $\mathrm{t_{sep}} \lesssim \mathrm{t_1}$ and the effect of the deflecting field $\mathrm{B_y}$ is already significant [Figs. 3.9(c),(d)]. The particle receives a first velocity boost, is deflected from $-$z into +x, and closes in towards the second AR. In the second AR both accelerating and deflecting field quantities change sign. Around $\mathrm{t_2}$ the positron is accelerated into +z and afterwards is again deflected into +x [Figs. 3.9(e),(f)]. In the second acceleration step the particle gains an amount in energy that is comparable to the first AR encounter [Fig. 3.10(c)], both acceleration steps take place in the late-time configuration.

Class 3 particles are found only for current sheets with $\mathrm{w_0} = 1.0$ for the simulation box sizes at hand. X-point separations are related to $\mathrm{w_0}, \mathrm{T_s}$, and $\mathrm{c/v_{A0}}$. For thin sheets and high $\mathrm{c/v_{A0}}, \mathrm{T_s}$ the typical separation distance decreases. Exemplaric field and energy time dependence for a Class 3 particle that consecutively traverses two X-points are displayed in Fig. 3.10 (black line). The selected positron is effectively deflected into $-$x

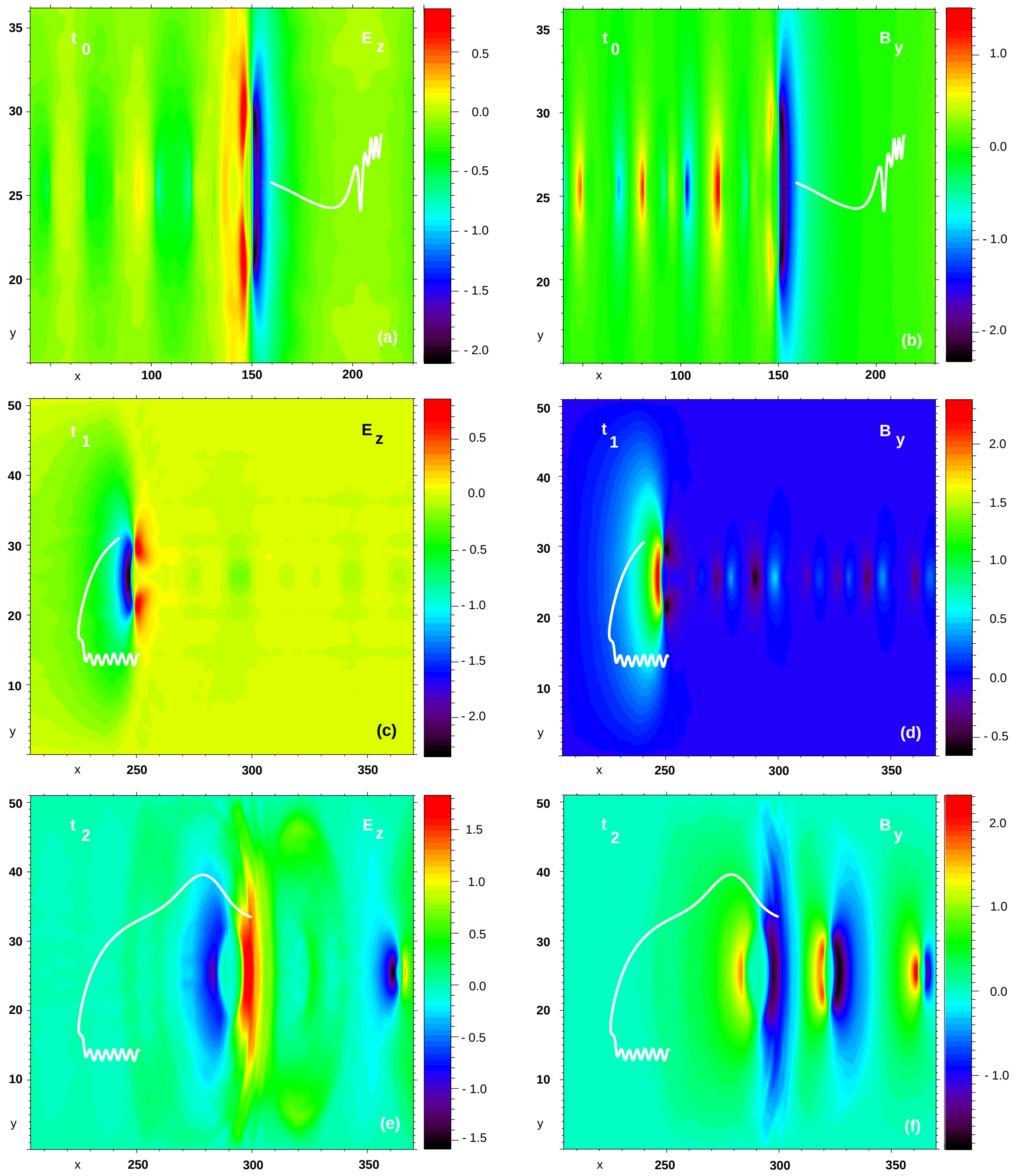

Fig. 3.9: Contours of accelerating E_z (left column) and deflecting field B_y (right column) for run 2D_a. (a),(b) show a Class 1 positron comoving with the dynamic AR at $t_0\,\omega_{c0} = 85$. X-point position during the quasi-static phase has been $x_{qs} = 204, y_{qs} = 25.5$. A Class 2 positron during the first acceleration step at $t\,\omega_{c0} = 80$ is illustrated in (c),(d), and during reentry into the second AR around the same plasmoid island at $t\,\omega_{c0} = 120$ in (e),(f).

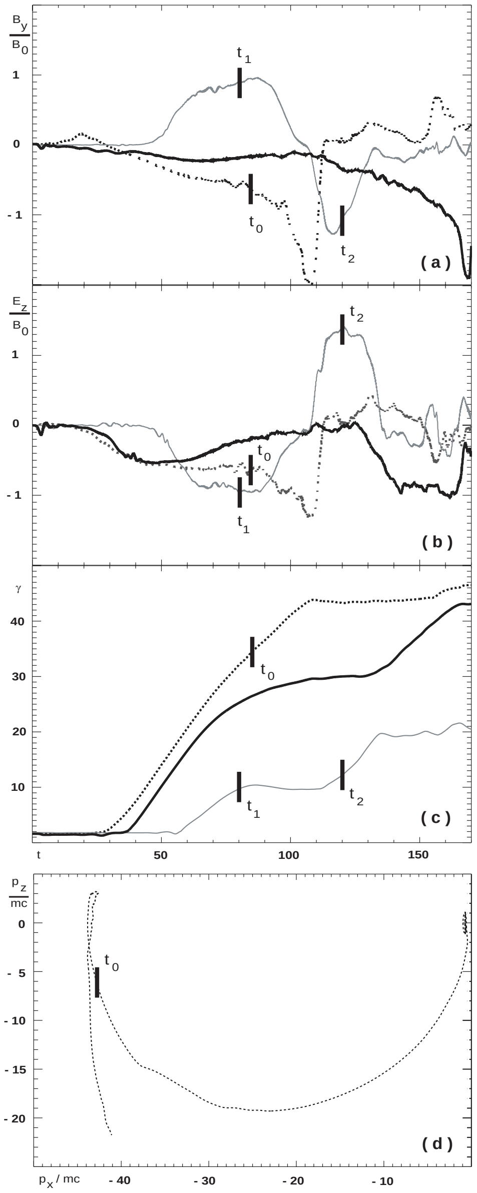

Fig. 3.10: Time evolution of $\mathrm{E_z}$ (a), $\mathrm{B_y}$ (b), γ (c) along exemplaric particle trajectories for Class 1 (dotted), Class 2 (grey), Class 3 (solid) scenario. Time mark $\mathrm{t_0}\,\omega = 80$ corresponds to field contours in Figs. 3.9(a),(b), $\mathrm{t_{1,2}}\,\omega_{\mathrm{c0}} = 80, 120$ to Figs. 3.9(c)-(f). (d) is the Class 1 trajectory in the $(\mathrm{p_x}, \mathrm{p_z})$-phase space plane. The gyro radius $\mathrm{r_L}$ is extended by relativistic mass gain $\mathrm{r_L} \propto \gamma$, the particle advances $\sim 70\,\mathrm{d_0}$ in $-\mathrm{z}$ and comoves with the dynamic AR!

in the first X-point. It manages to outrun the recessing second X-point and experiences a significant second energy boost. The number of consecutive acceleration steps is primarily restricted by the spatial extension of the simulation box.

There is one pitfall for 2D reconnection acceleration scenarios: As shown in 3.3.4, in the 3D configuration the AR has a finite extension of $\Delta \mathrm{z} \sim 20\,\mathrm{d}_0$ at $\mathrm{t} \sim \mathrm{t}_{\mathrm{sep}}$. The z-contiguity of the AR in later stages is an even more problematic issue due to the instabilities effective in the transverse direction. The finite potential difference is $\Delta\phi_{3\mathrm{D}} \sim 15$ MV, which corresponds to an energy gain $\Delta\gamma \sim 30$ for electrons. The only possibility to acchieve a higher energy gain is the consecutive acceleration in several ARs. Consequently, the most energetic Class 1 particles are an artefact of the 2D simulation configuration. Only Class 2 and Class 3 acceleration processes are possible in a real 3D scenario with finite acceleration potential ! Class 2 and Class 3 processes are not present in a quasi-static reconnection configuration, but take place in the highly dynamic late-time phases.

3.3.5 Discussion

Particle Acceleration in Electron-Proton Plasma Reconnection

For the comparison of particle energization efficiency in lepton and electron-proton plasmas we discuss three essential points of the acceleration process: The ratio $\mathrm{c}/\mathrm{v}_{\mathrm{A0}}$, the acceleration mechanism, and the size/lifetime of ARs.

$\mathrm{c}/\mathrm{v}_{\mathrm{A0}}$ determines the inductive electric field in the quasi-static $\mathrm{E}_{\mathrm{z}}^{\mathrm{on}}$ as well as in the dynamic phase $\mathrm{E}_{\mathrm{z}}^{\mathrm{equ}}$. In PIC reconnection simulations of electron-proton plasma $\mathrm{E}_{\mathrm{z}}/\mathrm{B}_0 \sim 0.012$ for $\mathrm{c}/\mathrm{v}_{\mathrm{A0}} = 20$ is obtained [Pritchett, 2001], so $(\mathrm{E}_{\mathrm{z}}/\mathrm{B}_0)(\mathrm{c}/\mathrm{v}_{\mathrm{A0}})$ is comparable to the results for $(\mathrm{E}_{\mathrm{z}}^{\mathrm{on}}/\mathrm{B}_0)(\mathrm{c}/\mathrm{v}_{\mathrm{A0}})$ presented in this article (Table 3.2). In the dynamic phase $\mathrm{v}_{\mathrm{equ}}$ is comparable to v_{A0}. Consequently, significant $\mathbf{v} \times \mathbf{B}$-contributions arise only in case $\mathrm{c} \sim \mathrm{v}_{\mathrm{A0}}$, which requires an extremely low-density and, hence, presumably sub-equipartitioned electron-proton plasma with magnetic guide field component.

The acceleration mechanism is inevitably connected via the inductive field to the mechanism of fast magnetic reconnection (FMR), which proceeds on electron inertial scales. In the electron-proton case, mass asymmetry introduces two inertial scales. Conventional Sweet-Parker/Petschek reconnection [Parker, 1957; Sweet, 1958; Petschek, 1964] proceeds on ion scales, and provides the framework with respect to flow conditions for FMR on the electron demagnetization scale. The difference between ion and electron dynamics in the diffusion region gives rise to (x, y)-plane Hall currents which produce an out-of-plane quadrupolar B_{z} field [Sonnerup, 1979; Terasawa, 1983]. The importance of the Hall term for FMR rates has been studied in the GEM reconnection challenge (see [Birn et al., 2001] and references therein). It cannot be important for FMR in pair plasmas, because Hall contributions are absent. Nevertheless for the quasi-static phase in pair plasma reconnection, FMR rates are independent from the scale size of electron demagnetization. This statement is essential in the electron-proton case and there is associated with the inverse phase velocity/wavelength characteristic of whistler/kinetic Alfvén (KA) waves [Rogers et al., 2001; Drake, 2001], and hence, ion inertia ultimately limits the FRM rate [Shay & Drake, 1998]. Whistler/KA dynamics break down in the face

of absent Hall term and negligible background plasma [Pritchett, 2001]. Consequently, the observed pair plasma FMR rates correspond to rather vacuum type reconnection, which is only limited by electron inertia in the quasi-static phase (w_0 independent) and current sheet rigidity (w_0 dependent) in the dynamic phase. The presented pair plasma PIC simulations cannot answer the question, whether the observed FMR rates are independent from mechanisms that break the frozen-in condition, as is the case for an electron-proton plasma [Shay et al., 2001; Pritchett, 2001; Hesse & Kuznetsova, 2001]. This breaking might happen in the innermost inertial scale region d_0.
Finally, the size of the AR determines the acceleration time t_R, i.e. the energy gain in a single acceleration step. FMR regions in electron-proton plasma presumably extend about one electron inertial length d_0 [Hoshino et al., 2001] in width, whereas the AR in the quasi-static phase of the 3D simulation [Fig. 3.8(a)] is already $\sim 10\,d_0$ wide. With respect to the late-time evolution AR lifetimes are an issue. Ion inertia certainly will damp dynamic E_z-contributions, but stabilize ARs. However, even 2D PIC simulations on ion inertial length and time scales of the extend presented here for electron dynamic scales are beyond the power of contemporary high performance computing.

Comparison with Previous Results on 2D Scenarios

In Zenitani & Hoshino [2001] the system differs from the 2D configurations presented here : The simulation is 2D with overall periodic boundaries, therefore two antiparallel Harris sheets are neighboured in the simulation plane. Initial parameters are comparable, though the system size for each current sheet is less. The system is initialized in a way that reconnection X- and O-points alternate, which significantly increases current sheet stability and plasma inflow into the X-point. As a consequence, the quasi-static reconnection phase is pronounced, and in combination with the smaller total system extension the simulation ends before entering the highly dynamic late-time phases. The final PDF obtained in Zenitani & Hoshino [2001] is consistent with the results of run 2D_e at $t\,\omega_{c0} = 90$ [Fig. 3.6(d)]. At this time 2D_e is already in the dynamic phase. Apparently, particle acceleration in the static AR yields comparable net effects on the PDF as acceleration in the dynamic AR associated with a single plasmoid (Class 1+2). Both scenarios result in a high-energy bump structure before the cut-off, which is pronounced for a dominant quasi-static phase. Multiple accelerations associated with ARs of several X-points (Class 3) - which is the case in turbulent plasma with a stochastic distributions of current sheet filaments - smoothes the power-law tail in the PDF at late times (Fig. 3.6).

Concluding Remarks on Particle Acceleration in FMR

We have presented efficient particle acceleration in self-consistent PIC simulations of fast magnetic reconnection in relativistic pair plasma. Deviating from Zenitani & Hoshino [2001], we stress the highly dynamic late-time evolution of the current sheet, and in addition have studied the effect of the finite AR potential in a real 3D configuration, as well as the influence of current sheet instabilities effective perpendicular to the 2D simulation plane. The late-time evolution is of distinguished importance for particle acceleration, because single thin sheets in low-density background plasma exhibit rapid reconnection onset in several X-points, and dynamic $\mathbf{v} \times \mathbf{B}$-contributions are dominant for a collisionless pair plasma in which $\mathrm{c} \sim \mathrm{v}_{\mathrm{A0}}$ is always valid. In a parametric study of five 2D PIC simulations, a general time scheme has been observed, constituted by reconnection onset, dominant single X-point phase, and, finally coalescence of tearing islands. Within the single X-point phase the system evolves at $\mathrm{t} = \mathrm{t}_{\mathrm{sep}}$ from a quasi-static AR structure into a highly variable, dynamic AR configuration, in which $\mathbf{v} \times \mathbf{B}$-contributions dominate. The parametric study showed that the high-energy cut-off is most efficiently tuned with $\mathrm{c}/\mathrm{v}_{\mathrm{A0}}$, at late times furthermore by w_0. Most remarkable: The spectral index of the PDF power-law tails $\mathrm{s} \sim -3$ (within a single X-zone $\mathrm{s} \sim -1$), is independent of both parameter- as well as acceleration-scenario (quasi-static/dynamic ARs). The spectral index appears as characteristic of the reconnection process, preserved in the highly dynamic late-time evolution! Contributions from several ARs at late times even smooth the PDF power-law shape up to the high-energy cut-off ("wash-out" effect). A detailed analysis of the acceleration mechanism showed that, for a quasi-static AR, typical particle escape times are prolonged by relativistic mass gain ($\mathrm{v}_{\mathrm{esc}} \propto 1/\gamma$) (consistent with the argumentation in Zenitani & Hoshino [2001]), but decisive in the dynamic phase is that the particle deflection is parallel and comparable $\mathrm{c} \sim \mathrm{v}_{\mathrm{equ}}$ to AR motion. As a consequence, particles essentially perform some fraction of a gyro-orbit in a single acceleration step, which explains the preservation of the power-law shape. Three insights are obtained from the 3D configuration: First, due to plasma dynamics within the (x, y)-plane, the potential of a single AR is finite in 3D, i.e. $\Delta\Phi_{\mathrm{3D}} \sim 30\,\mathrm{MeV}$. Therefore most energetic Class 1 particles (from quasi-static as well as dynamic ARs) are an artefact of the 2D configuration. Only multiple acceleration scenarios (Class 2 and 3) are valid in 3D. Second, in 3D a RTSI/RDKI-type instability disrupts the current sheet contiguity in the (x, z)-plane. Consecutive particle acceleration is observed in the arising segments of parallel $\mathbf{E}_{\mathrm{z}}$ [Zenitani & Hoshino, 2003]. Third, if an initial perturbation (for instance plasma inflow perpendicular to the current sheet) is applied, particle acceleration is dominant in the contiguous AR zone. We finally note, that the RTSI/RDKI-type instability for thin 3D current layers should be important also with respect to reconnection onset. Furthermore, since the plasma inflow is of extreme importance for the AR lifetime/contiguity, we therefore expect significant changes in the acceleration efficiency if driven reconnection configurations are considered [Horiuchi & Sato, 1994; 1997].

3.4 Synchrotron Signatures of the Self-Consistent Model

The following section is published as

'Relativistic Kinetic Reconnection as the Possible Source Mechanism for High Variability and Flat Spectra in Extragalactic Radio Sources'

C.H. Jaroschek, H. Lesch, and R.A. Treumann
The Astrophysical Journal, 605, L09-L12, 2004

3.4.1 Abstract

We present the first synchrotron power spectra of a self-consistent kinetic reconnection scenario in the highly relativistic regime of a pair plasma. A fully electromagnetic relativistic Particle-In-Cell code is used to study the late-time evolution of kinetic magnetic reconnection at high resolution with a total ensemble of more than 10^8 particles. We show (i) the importance of the extremely dynamic late-time evolution of the reconnection region for the generation of non-thermal particles, (ii) the efficient synchrotron emission by the accelerated fraction of particles, and (iii) the application of the simulation results to pair-dominated AGN core regions - the presumable origin of 'light' jets. We conclude that collisionless kinetic reconnection in the relativistic regime is capable to explain the enormous power output of $\mathrm{P} \sim 10^{47}\,\mathrm{erg\,s^{-1}}$ in certain luminous intra-day variable quasars and the extremely hard observed radio spectra of Flat Spectrum Radio Quasars.

3.4.2 Introduction

Extragalactic radio sources like active galactic nuclei (AGN) exhibit various observational features that are a challenge for the theoretical understanding of the underlying microphysics (see Urri & Padovani [1995] for a recent review on radio-loud AGN). The extreme intra-day variability of certain luminous quasars [Wagner, 1998; Quirrenbach et al., 1992; Kellermann & Pauliny-Toth, 1981] places tight limits on the time and length scales of the emission process. High luminosities with energy dissipation of up to 10^{51} erg [Reeves et al., 2002; Protheroe, 2003] and remarkably hard spectra with spectral index $\mathrm{s} > -0.5$ in certain Flat Spectrum Radio Quasars (FSRQs) [Teräsranta et al., 2001] need to be powered by a violent process. A promising source mechanism is magnetic reconnection as a fundamental plasma process that dissipates magnetic energy and efficiently generates non-thermal particles [Di Matteo, 1998; Birk et al., 2001]. Collisionless reconnection in electron-ion plasma is suggested by observations from the earth's magnetotail [Nagai et al., 1998] and has been extensively studied in kinetic simulations [Drake, 2001; Pritchett, 2001]. These simulations revealed that collisionless reconnection proceeds 'fast' on electron inertial length scales, i.e. the reconnection outflow takes place at speeds comparable to the Alfvén velocity $\mathrm{v_{out}} \sim \mathrm{v_A}$. Since in a pair plasma kinetic reconnection efficiency is not limited by ion inertia, we furtheron use the term fast magnetic reconnection (FMR). In this Letter, we address the synchrotron power spectra generated within the late-time evolution of FMR in a relativistic pair plasma. There is convincing observational evidence for the existence of pair dominated 'light' jets [Wardle et al., 1998; Hirotani et al., 2000; Lobanov & Zensus, 2001]. Internal jet conditions do not allow for significant pair production, hence these 'light' jets probe the plasma conditions in certain AGN core regions. Zenitani & Hoshino [2001] first investigated the generation of non-thermal particles in FMR in the relativistic regime of a pair plasma in a 2D Particle-In-Cell (PIC) simulation. The simulations presented here are entirely self-consistent using a fully electromagnetic relativistic PIC code [Zeiler et al., 2002]. Their results are applied to environment parameters expectable for certain AGN core regions. We discuss the total synchrotron power output, spectral features within the reconnection X-zone especially with respect to the observed extremely flat radio spectra, and pitch angle distributions. We conclude that FMR in the relativistic regime is a promising mechanism to explain the extremely energetic processes underlying the fundamental plasma physics of 'light'-jet-dominated extragalactic radio sources as an alternative scenario to conventional shock-in-jet intrinsic models [Marscher, Gear & Travis, 1992].

3.4.3 Simulation Model

The pair plasma reconnection configuration is studied in $2\frac{1}{2}$D with a massively parallelized PIC code (see Birdsall & Langdon [2000] for details on the PIC model) for a total number of $1.5 \cdot 10^8$ particles. A 1D Harris configuration [Harris, 1962] is initialized in the magnetic field $\mathrm{B(y) = B_0 \tanh[(y - L_y/2)/w_0]}$ and density $\mathrm{n = n_0 \, sech^2[(y - L_y/2)/w_0]}$. $\mathrm{B_0}$ is the asymptotic magnetic field far away from the current sheet, and $\mathrm{n_0}$ the current sheet density without background contributions. The Harris sheet width is set to $\mathrm{w_0 = 1.85\, d_0}$. The simulation is performed in the xy-plane with total system size $\mathrm{L_x \times L_y = 816\, d_0 \times 102\, d_0}$. Length scales are normalized to the electron inertial length $\mathrm{d_0 = c/\omega_{p0}}$, with the plasma frequency $\mathrm{\omega_{p0} = (4\pi n_0 e^2/m)^{1/2}}$. Time steps are given in units of the inverse electron gyro-frequency $\mathrm{\omega_{c0}^{-1} = mc/eB_0}$. The index '0' indicates quantities evaluated at reference conditions $\mathrm{B_0}$ and $\mathrm{n_0}$. Dimensional values are calculated in section 3.4.4 for $\mathrm{B_0, n_0}$ of a typical astrophysical source environment. A fractional background of $0.77\,\%\ \mathrm{n_0}$ is added homogeneously over the entire simulation box. A high resolution grid mesh with $\mathrm{nx \times ny = 4096 \times 512}$ grid points is applied. $\mathrm{n_0}$ corresponds to 1168 pairs per grid cell. Initially, particles are inserted in phase space according to an isotropic relativistic Maxwell-Juettner distribution $\mathrm{f(p) \propto p^2 exp[\gamma(p) mc^2/kT_0]}$, where p is the particle momentum, c the speed of light, γ relativistic energy, m particle rest mass and $\mathrm{kT_0 = 100\, keV}$ the initial thermal energy. The Alfvén velocity $\mathrm{v_A}$ is comparable to c. The Debye length is resolved better than three times. The total energy E is conserved within $\mathrm{\Delta E/E(t = 0) \sim 10^{-4}}$ over the total simulation time of $\mathrm{t_{tot}\, \omega_{c0} = 280}$. Boundary conditions are periodic in x and z, the simulation is 3D in momentum space. The y-boundary is open for particles and fields [Birdsall & Langdon, 2000]. The system configuration is similar to Zenitani & Hoshino [2001], with three important modifications. First, the system size is prolonged by a factor of four in x- and by a factor of two in y-direction. This extends the total simulated time by more than a factor of three and allows to study the late-time evolution [Jaroschek et al., 2004] of the thin current sheet. Besides the initial reconnection X-point, several secondary X-points evolve. Particles are consecutively accelerated in various X-points, a phenomenon not observed by Zenitani & Hoshino [2001]. Second, the non-periodicity of the boundary condition in y allows to consider a single Harris sheet configuration, and hence to exclude the stabilizing effect of a neighbouring current sheet. This causes a much more violent, highly nonlinear late-time evolution of the system. Third, an initial particle drift towards the centered X-point is pronounced, since the large y-extension of the system serves as a background particle reservoir, optimizing the efficiency of the particle acceleration mechanism, since reconnection rates are essentially limited by the inflow of magnetic-flux carrying particles. Particle and field data at any given time step are used to calculate the synchrotron emission of the system. Contributions to the particle dynamics from radiative electric fields with frequencies beyond the grid mesh resolution are not an issue with respect to simulation self-consistency, since the typical synchrotron cooling time $\mathrm{t_{sc}}\,\omega_{\mathrm{c0}} = 10^{12}/\gamma(\mathrm{B_0}/1000\,\mathrm{G})^2\sin^2\alpha$ exceeds the total simulation time by a factor of $\mathrm{t_{sc}/t_{tot}} \sim 10^8$. γ denotes the accelerated particles' relativistic energy and α the pitch angle.

3.4.4 Numerical Results and Physical Picture

Non-thermal Particle Generation in the Late-time Evolution

Decisive for the efficiency of non-thermal particle generation is the reconnection rate, i.e. the inductive electric field $\mathrm{E_z}$, and the time a particle remains within the X-zone [Zenitani & Hoshino, 2001]. Figure 3.11 shows the accelerating $\mathrm{E_z}$ component and magnetic field line configuration for the late-time evolution at $\mathrm{t}\,\omega_{\mathrm{c0}} = 220$. The initial X-point is centered in the xy-plane. Several secondary X-points have evolved along the current sheet. In this extremely dynamic late stage, the current sheet filaments separated by the X-points tend to merge in ±x-direction, thereby generating additional accelerating $\mathrm{E_z}$-fields via $-\mathbf{v}_\mathrm{x} \times \mathbf{B}_\mathrm{y}$ [Jaroschek et al., 2004]. $\mathbf{v}_\mathrm{x}$ is the merging speed of an individual current sheet filament and $\mathbf{B}_\mathrm{y}$ the locally reconnected magnetic field strength. The dynamic contributions in the late-time evolution of the system superpose resonantly to $|\mathrm{E_z^{max}/B_0}| = 1.5$, compared to $|\mathrm{E_z^{max}/B_0}| = 0.33$ obtained by Zenitani & Hoshino [2001]. High $\mathrm{E_z}$-fields around X-points in close proximity make multiple acceleration in consecutive steps work efficiently [Jaroschek et al., 2004]. The generation of non-thermal particles after reconnection onset is shown in the time evolution (Figure 3.12a) of the normalized distribution function $\mathrm{f}(\gamma)\mathrm{d}\gamma$. Non-thermal contributions coincide with the formation of the initial X-point at $\mathrm{t}\,\omega_{\mathrm{c0}} = 60$. Zenitani & Hoshino [2001] found a power-law tail with high-energy cut-off at $\gamma \sim 27$. In Figure 3.12a, $\mathrm{f}(\gamma)\mathrm{d}\gamma$ reaches up to $\gamma \sim 68$ during the late-time evolution. The cut-off energy finally is decisive for the total synchrotron power output as well as the cut-off frequency of the emission spectrum. Though the system is highly dynamic and the geometry of individual X-zones is more complicated, $\mathrm{f}(\gamma)\,\mathrm{d}\gamma$ still exhibits a power-law shape.

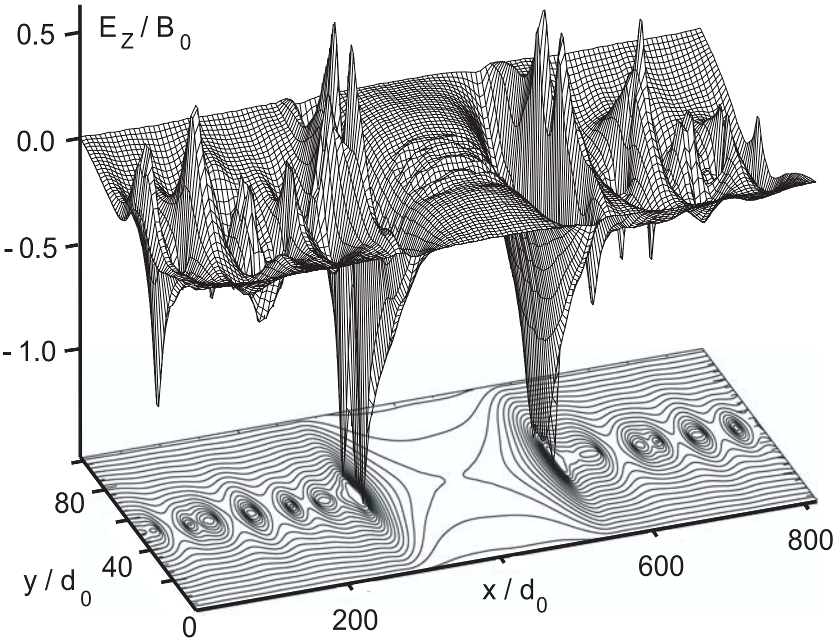

Fig. 3.11: Composite plot of the acceleration electric field E_z (meshed surface) and the magnetic field line contours in the xy-simulation plane at $t\,\omega_{c0} = 220$. The first reconnection X-point is in the center, several primary X-points evolve along the thin current sheet. Reconnection is responsible for $-E_z$ components. Superposed in the late time stages are significant $-\mathbf{v}_x \times \mathbf{B}_y$ contributions that result from the merging of current sheet filaments.

Synchrotron Emission

The time evolution of the total synchrotron power spectrum is shown in Figure 3.12b. Comparison with non-thermal particle generation in Figure 3.12a at $t\,\omega_{c0} = 60$ shows that reconnection onset and significant synchrotron power output dramatically coincide in time. From reconnection onset to the late evolution of the system the integrated total synchrotron power increases by a factor of $4.4 \cdot 10^4$. Thereby the cut-off frequency shifts by 2.5 powers of ten. Synchrotron pitch angles are dominated by particles moving perpendicular to the ambient field (Figure 3.13). For $t\,\omega_{c0} < 60$, pitch angles are expected to be isotropic, but only initial thermal particles with $\omega_{\mathrm{cut}} > 10^{-8}\,\omega_{\mathrm{cut,fin}}$ of the final spectral cut-off $\omega_{\mathrm{cut,fin}}$ can contribute. At intermediate times contributions from those particles appear which move just slightly oblique to $\mathbf{B}$. Certain luminous radio sources exhibit extreme intra-day variability, i.e. the radiative flux doubles within a time window of $t_{\mathrm{var}} \lesssim 10^5$ s. This restricts the spatial extension of the emission region to $R < 10^{16}$ cm. Total bolometric luminosities of $P_{\mathrm{tot}} \sim 10^{47}\,\mathrm{erg\,s^{-1}}$ are measured. The total dissipated energy during such flaring events integrates up to $E_{\mathrm{tot}} = 10^{51}$ erg. P_{tot} requires a $10^9\,M_\odot$ black hole accreting $\dot{M} \sim 4.5\,M_\odot/\mathrm{yr}$ at maximum Kerr efficiency close to the Eddington limit. Since we study pair-plasma reconnection, the results apply to

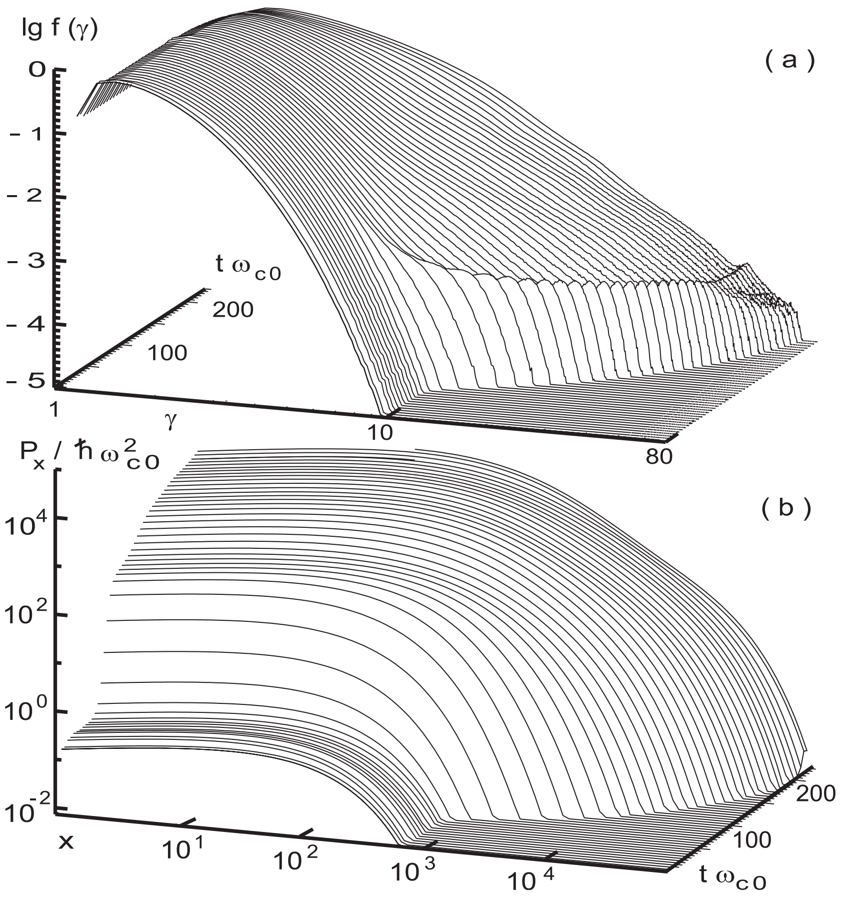

Fig. 3.12: Double logarithmic stack plots of the normalized particle distribution $\mathrm{f}(\gamma)$ as function of relativistic energy γ (a), and total spectral synchrotron power output $\mathrm{P(x)}$ as function of the dimensionless parameter $\mathrm{x} = \omega/\omega_{\mathrm{c0}}$ (b). Simulation time is on the third axis. Reconnection onset at $\mathrm{t}\,\omega_{\mathrm{c0}} = 60$ coincides with the generation of non-thermal particles and significant synchrotron emission. Remarkable is the stability of the power-law tail in (a) even in the highly dynamical late-time evolution of the system up to the cut-off at $\gamma \sim 68$. In (b) the cut-off frequency shifts by 2.5 powers of ten, the frequency integrated synchrotron power increases by a factor of $4.4 \cdot 10^4$.

pair-dominated AGN core regions, which presumably serve as the ’heads‘ of ’light‘ jets. Plasma theoretical arguments yield jet ’head‘ densities $\mathrm{n_0} = \dot{\mathrm{M}}/\pi\,\mathrm{R\,m\,v_{jet}} \sim 10^{10}\,\mathrm{cm^{-3}}$ [Lesch, Appl, & Camenzind, 1989] for jet velocities $\mathrm{v_{jet}} \sim \mathrm{c}$ [Lobanov & Zensus, 2001]. The magnetic confinement of AGN coronal regions has been discussed by Rees [1987], estimating the magnetic field strength to $\mathrm{B_0} \sim 0.4\,\mathrm{f}^{1/2}\,(\mathrm{P_{tot}}/10^{46}\mathrm{erg\,s^{-1}})^{1/2}(\mathrm{R}/10^{18}\mathrm{cm})^{-1}$ $\sim\ 1000\,\mathrm{G}$. $\mathrm{f} \sim 1$ is the fractional energy emitted by the central compact object as Poynting flux. The characteristic synchrotron cooling time $\mathrm{t_{sc}}$ is shorter than the dynamic time scales of the emission region. So a low-beta plasma is expected with plasma

$\beta = \mathrm{B}^2/8\pi \mathrm{n}_0 \mathrm{kT}_0 \approx 0.1 - 0.01$. A typical temperature $\mathrm{T}_0 \sim 10^9\,\mathrm{K}$ is the consequence. Recent X-ray [Reeves et al., 2002] and radio [Protheroe, 2003] data confirm the sub-equipartition argument as well as the values for n_0 and T_0. Under isotropic conditions the emission ratio of synchrotron (S) to inverse Compton (IC) power $\mathrm{P_S/P_{IC} = u_B/u_{ph}}$ in the Thomson limit is determined by the ratio of magnetic $\mathrm{u_B}$ to photon $\mathrm{u_{ph}}$ energy densities. Source luminosities $\mathrm{P_{tot}} \sim 10^{47}\,\mathrm{erg\,s^{-1}}$ imply $\mathrm{u_{ph}} \sim 10^3\,\mathrm{erg\,cm^{-3}}$ for isotropic emission out of core regions extending $\mathrm{R} \sim 10^{16}\,\mathrm{cm}$. Consequently, for sub-equipartitioned coronal plasma synchrotron emission $10^{2-3} \lesssim \mathrm{P_S/P_{IC}}$ dominates in the radio-optical regime. The corresponding time and length scales are $\mathrm{t}_0 = \omega_{\mathrm{c}0}^{-1} = 5.6 \cdot 10^{-11} (\mathrm{B}_0/1000\,\mathrm{G})^{-1}\,\mathrm{s}$ and $\mathrm{d}_0 = 1.1(\mathrm{T}_0/100\,\mathrm{keV})(\mathrm{B}_0/1000\,\mathrm{G})^{-1}(\beta/0.1)^{-1/2}\,\mathrm{cm}$, respectively. To relate the synchrotron power output of the microphysical plasma process with the synchrotron emission rate of a quasar, a stochastic distribution of reconnection zones over the entire coronal source region is assumed. Synchrotron self-absorption (SSA) and subsequent plasma 'thermalization' effects [Ghisellini, Haardt & Svensson, 1998] are neglegted. The dimensional scale height of the spectral synchrotron power is $\mathrm{P}_0 = 2.5 \cdot 10^{27} (\mathrm{R}/10^{16}\,\mathrm{d}_0)^3 (\mu/10^5)$ $\mathrm{erg\,s^{-1}\,Hz^{-1}}$. Spatial coherence limits of the emission region are constrained by $\mathrm{t_{var}}$, the further observational fact of constant radiative flux within a minimum time frame of $\mathrm{t_{min}} \sim 1\,\mathrm{ks}$ places a condition on the temporal coherence of the emission event, accounted for in the event multiplicity μ. For the parameters at hand, an individial re-

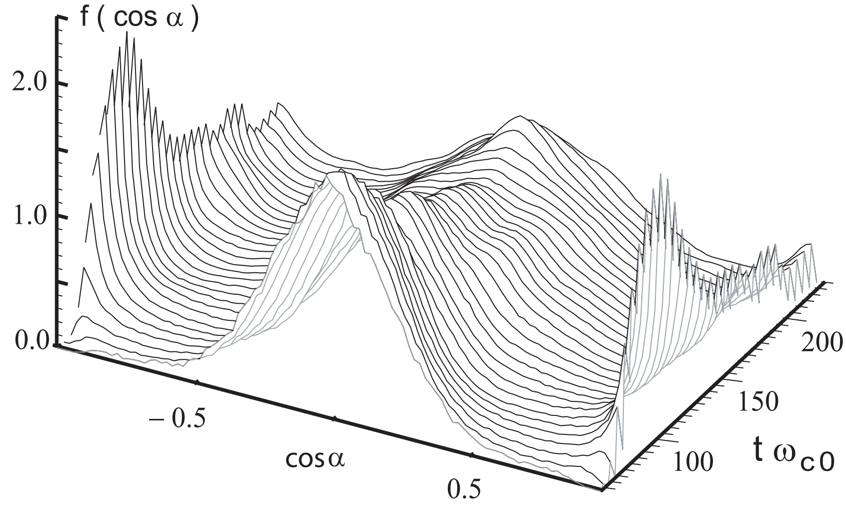

Fig. 3.13: Time evolution of the pitch angle distribution $\mathrm{f}(\cos\alpha)$ starting with reconnection onset at $\mathrm{t}\,\omega_{\mathrm{c}0} = 60$. Perpendicular pitch angles dominate over all times. During an intermediate time phase the first X-zone dominates and violent particle inflow at slightly oblique angles to the newly reconnected $\mathbf{B}_\mathrm{y}$ component gives contributions at very small and very large pitch angles.

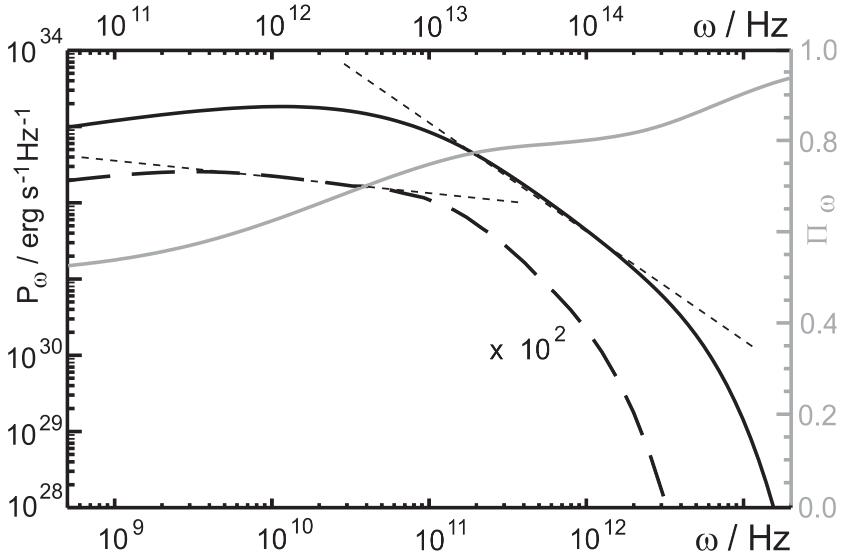

Fig. 3.14: Total spectral synchrotron power output $\mathrm{P}(\omega)$ as function of frequency ω for typical environment parameters of a luminous extragalactic radio source. $\mathrm{P}(\omega)$ for the complete simulation box at $\mathrm{t}\,\omega_{\mathrm{c0}} = 220$ is represented by the solid black line (upper frequency axis). The dotted asymptote of the power-law tail exhibits a spectral index $\mathrm{s} = -1.36$, the spectral cut-off reaches up into the optical. For the broken black line, spectral emission $\mathrm{P}(\omega)$ is spatially restricted to the first X-zone at $\mathrm{t}\,\omega_{\mathrm{c0}} = 135$. $\mathrm{P}(\omega)$ is magnified by a factor of 10^2 to fit into the ordinate range. The spectrum is extremely flat with $\mathrm{s} = -0.17$ in the frequency range $1\,\mathrm{GHz} < \nu < 100\,\mathrm{GHz}$. The emitted synchrotron emission (black solid line) is highly polarized, with spectral polarization $\Pi(\omega) > 75\%$ for $\omega > 10\,\mathrm{THz}$ (grey line, right axis).

connection event takes place within $\mathrm{t}_{\mathrm{tot}} \sim 10^{-8-7}\,\mathrm{s}$, which allows for a superposed cascade of $\sim 10^5$ events within 1 ks. This implies the very conservative assumption that the process, restoring the magnetic energy in the accretion disc corona, is 10^5 times slower than the respective dissipation process. In cooler environments ($\mathrm{T}_0 \sim 10\,\mathrm{keV}$) and higher magnetic fields the reconnection event gets even more confined, and the radiation output is even more violent. The typical synchrotron cooling time for such a source is $\mathrm{t}_{\mathrm{sc}} = 10^2/\gamma_0(\mathrm{B}_0/1000\,\mathrm{G})^2 \sim 0.1 - 10\,\mathrm{s}$. Hence, $\mathrm{t}_{\mathrm{tot}} \ll \mathrm{t}_{\mathrm{sc}} \ll \mathrm{t}_{\mathrm{var}}$ assures the self-consistency of the simulation. According to the pitch angle distributions (Figure 3.13) perpendicular emission dominates, i.e. is at maximum efficiency. Figure 3.14 shows the late time total synchrotron power spectrum at $\mathrm{t}\,\omega_{\mathrm{c0}} = 220$. With $\mathrm{B}_0 = 1000\,\mathrm{G}$, $\mathrm{T}_0 = 100\,\mathrm{keV}$, $\beta = 0.1$, the spectrum exhibits a power-law with spectral index $\mathrm{s} = -1.4$ well up to the cut-off frequency at $\omega_{\mathrm{cut}} \sim 10^{15}\,\mathrm{Hz}$. The frequency-integrated total power output is $\mathrm{P}_{\mathrm{tot}} = 3.5 \cdot 10^{46}\ \mathrm{erg\,s}^{-1}$. If we restrict the source region to an individual X-point, extremely hard spectra result with $\mathrm{s} = -0.17$ up to the cut-off frequency at $\nu_{\mathrm{cut}} \sim 100\,\mathrm{GHz}$. This intense synchrotron emission provides a plasma-theoretical foundation for recently observed extremely hard spectra from flat-spectrum radio sources with $\mathrm{s} > -0.5$ in the frequency band $1.4 < \nu < 4.85\,\mathrm{GHz}$ by Teräsranta et al. [2001]. We note that the hard radio spectra are independent of the time variability argument and hence are not restricted to AGN core regions. P_0 and ν_{cut} will vary according to B_0,n_0 present for instance in the jet, whereas the power-law index remains invariant. Lobanov & Zensus [2001] identified a complex magnetic field structure in the jet, suggesting that magnetic reconnection is present. The synchrotron emission is highly polarized with polarization degree $\Pi(\omega) > 75\,\%$ beyond $\omega \sim 10\,\mathrm{THz}$. We note that this is the theoretical polarization for an individual reconnection zone, and the polarization degree decreases for a stochastic distribution of reconnection regions. Nevertheless these results can in principle explain observed polarization degrees $\Pi(\omega = 3.67\,\mathrm{GHz}) = 60 - 70\,\%$ in jet components of BL Lac objects as well as $\Pi(\omega = 3.67\,\mathrm{GHz}) = 2 - 9\,\%$ [Gabuzda & Cawthorne, 2000] in the respective core regions.

3.4.5 Summary and Conclusions

We calculated synchrotron emission spectra from self-consistent PIC simulations of FMR in the relativistic regime of a pair plasma. The highly dynamic nonlinear late-time evolution of a thin current sheet serves as the fundamental plasma scenario to obtain synchrotron power spectra for environment parameters expected in certain pair-dominated AGN core regions. We assumed strong magnetic confinement and neglected SSA. Particle distributions are highly non-thermal, which results in a dominant synchrotron spectral component. This deviates from models of thermal synchrotron emission [Wardziński & Zdziarski, 2000]. Observations of dominant X/γ-ray emission via Comptonization exist [Reeves et al., 2002; Kubo et al., 1998]. A more sophisticated study should clarify the importance of SSA/IC upscattering of ambient photons as function of the density profile and isotropy deviations - especially with respect to blazar-type AGNs, in which synchrotron self-comptonization becomes significant [Kino, Takahara, & Kusunose, 2002]. In the FMR scenario the generation of non-thermal particles in an individual reconnection X-zone is confined to an extremely small volume of m^3 size and takes place on sub-μs timescales for typical source environment parameters. This results in optimized spatial and temporal coherence as a consequence of high event multiplicity. Typical synchrotron cooling times range on the order of seconds. Hence, simulation self-consistency is not limited by the grid mesh resolution. We conclude, that the synchrotron emission scenario presented here provides a satisfactory description of the energetics for the immense power output of $\mathrm{P}_{\mathrm{tot}} \sim 10^{47}\mathrm{erg\,s}^{-1}$ and intra-day radio variability within the constraints of an intrinsic AGN variability model. Hence, FMR is an alternative to shock-in-jet variability scenarios and is superior with respect to self-consistent generation of power-law spectra on the plasma kinetic level.

Chapter 4

Magnetic Fields in 3D Weibel Scenarios

4.1 Magnetic Fields in γ-Ray Burst Models - Generation, Topology and Lifetime

The Weibel mechanism is proclaimed responsible for the generation of magnetic fields on scales stretching from cosmic interrelations (e.g. intergalactic field topologies) over expanding supernova bubbles and filamentation in extragalactic jets to γ-ray bursts (GRBs) and pulsar winds.

Such ubiquity already forecloses the fundamental nature of the process. In fact, the Weibel mechanism is expected to play a key role in all originally unmagnetized plasma scenarios in which the free energy of the system is pervasively contained in the relative bulk motion of plasma shells. In the following we use the term 'shell' as abstract synonym for an entity of plasma particles whose individual motions are described by a finite center-of-mass (CMS) / bulk motion and a superposed individual motion, with the latter small compared to the respective bulk component. Counterstreaming plasma shells also represent the conditions realized in 3D kinetic collisionless shocks in the region trailing the immediate shock front.

In this chapter we focus on plasma shell collisions in the context of GRB scenarios. This is for manifold reasons: GRBs rank among the most violent radiation outbursts known and come along with certain unique features. Energetic constraints on the thermonuclear / accretional energy production rule out the isotropic emission of radiation. Hence, the GRB progenitors are assumed to evolve highly anisotropic to account for relativistic beaming effects. Conventional GRB emission models [Mészáros, 2002; Piran, 1999] advocate the conceptual picture of a compact central engine ejecting fireball shells (Fig. 4.1). Fireballs evolve in regions in which the γ-photon density reaches the opacity to sustain significant electron-positron-pair production. Fireballs radiatively cool down to pair plasma shells. Therein the plasma is highly density rarefied, and as a consequence thereof, optical thickness and particle-particle encounters become insignificant. Then pair annihilation and Coulomb collisions are negligible, i.e. the plasma is collisionless. Under such conditions the plasma dynamics is governed by the electrodynamic interaction of charged particles with collective plasma instabilities. Shell ejection from the central engine is supposed to show intermittency and variations in bulk motion provoking the collision of individual plasma shells. These events are referred to as GRB source internal collisions and are proclaimed to be responsible for GRB prompt emission events and early afterglow. Since internal shells descend from fireball ejecta the

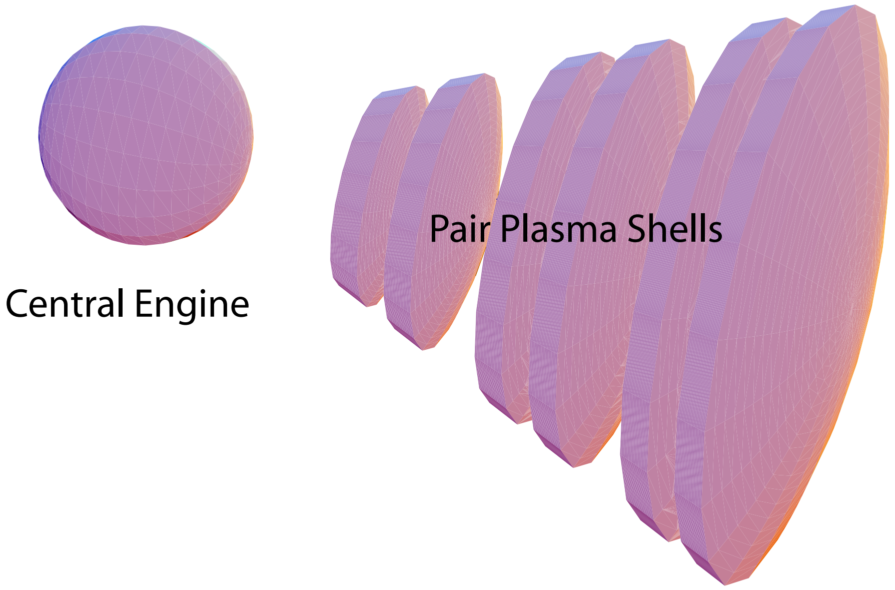

Fig. 4.1: Conceptual GRB fireball model: Anisotropic, relativistically coned ejection of pair plasma shells from a central engine [Piran, 1999].

plasma is predominantly populated by electron-positron pairs. This peculiarity of the GRB scenario in combination with the highly relativistic bulk motion is an ideal testbed for fundamental kinetic plasma simulations. The restriction to two oppositely charged species with equal mass implies that only a single temporal and spatial scale is involved, i.e. processes evolve on electron inertial times $\omega_{\mathrm{p}}^{-1} = (\mathrm{m}/4\pi \mathrm{ne}^2)^{1/2}$ and lengths $\mathrm{c}/\omega_{\mathrm{p}}$. A thorough discussion on the problems arising in the effort to represent a physical many-body system in a numerical model can be found in Appendix A. One major purpose of the simulations is to gain insight into the highly non-linear saturated plasma state at late times. In the relativistic regime this allegation is computationally progressively demanding, since velocities get very close to the speed of light and diminish the number of significant digits in the position integration step (cf. chapter 2 for details on the numerical algorithm). Furthermore the gyro motions typically scale $\propto \gamma$, and inertial motions $\propto \gamma^{1/2}$ with relativistic energy. To summarize these arguments in a concise statement: Even massively parallelized simulations on contemporary supercomputing facilities are incapable to explore the ultra-relativistic regime, if more than one space-time scale is involved. As always such a statement becomes less strict, if further assumptions are introduced and the demand of complete self-consistency is relaxed. An outlook on such options is included in sections 4.2.6, 4.3.5 of this chapter.

GRBs further qualify as a paradigmatic scenario for fundamental studies with respect to the observed emission spectra. Band et al. [1993] introduced an excellent phenomenological fit at the GRB spectrum. It is essentially characterized by two power-laws joined smoothly at some break energy. In addition there is observational evidence that the radiation released during prompt emission and early afterglow is highly polarized [Coburn & Boggs, 2003]. Consequently, in combination with the power-law shaped spectrum a synchrotron emission mechanism is the favored source process. However, a self-consistent motivation of a power-law spectrum emanating out of an initially thermal particle distribution or monoenergetic beam remains a challenging enterprise for the theorist. The foundations of the synchrotron model root in the highly non-thermal particle distribution and magnetic field configuration of the plasma state prevalent in colliding plasma shells. The self-consistent modelling of such plasma states is entirely in the domain of kinetic simulations.

In this chapter we address several of the most critical questions posed by the synchrotron emission scenario. In plasma shell collisions as proposed by generic GRB fireball models the preeminent plasma mode is the Electromagnetic Counterstreaming Instability (EMCSI) or - as synonymous reference - the Coupled Two-Stream-Weibel (CTW) mode. A thorough treatment of the EMCSI/CTW begins with a rigorous linear analysis of the expected instability modes and afterwards continues with the simulation of the highly non-linear saturated plasma state. The linear analysis provides essential insight into the physical mechanism underlying the instability and the typical length and time scales involved. Linear instability modes are directly verifiable during the linear simulation regime. Corresponding growth rates are an important checkpoint for the quality of the simulation. Linear dispersion relations serve to identify the respective plasma modes. Finally the linear theory always provides a strong interpretative background for the non-linear regime at late times, like expectable instability time and length scales as function of initial simulation parameters (cf. section 4.2.4).

During the linear phase the EMCSI evolves in 2D and the linear analysis maps the three spacetime components $(\mathrm{t}, \mathrm{x}, \mathrm{z})$ into the corresponding Fourier space $(\omega, \mathrm{k_x}, \mathrm{k_z})$. To maintain readability we usually present dispersion relations in planes obtained by suitable cuts through this Fourier space. We derive the 2D EMCSI/CTW mode for the general case of an initial magnetic (guide) field $\mathrm{B_G}$ and arbitrary initial velocities of the counterstreaming shells and shell constituents. The linear analysis is performed within the constraints of the *zero temperature approximation* or *cold beam limit*, i.e. the thermal spread of the particle distribution in each shell's comoving frame is neglected. On a superficial glance such an assumption appears paradox, since the plasma state itself implies a certain thermal ionization energy. The line of thought gets transparent as soon as the term *cold beam limit* is reformulated more precisely as the limit, in which *the typical relativistic thermal energy* $\mathrm{E_{th}}$ *is negligible compared to the relativistic energy of the bulk motion* $\mathrm{E_0} = \gamma_0 \mathrm{mc}^2$. It is important to note that in the relativistic regime the bulk motion $\gamma_0 = (1 - \mathrm{v}_0^2)^{-1/2}$ and thermal spread are not (!) independent, but are connected through the relativistic energy-momentum tensor $\mathrm{T}^{\mu\nu}$. The definition of $\mathrm{T}^{\mu\nu}$ lies at the roots of the understanding of temperature in a highly non-thermal, anisotropic plasma state. Details on interpretation and numerical evaluation of $\mathrm{T}^{\mu\nu}$ are deferred to section 4.2.4. However, for small thermal spread $\mathrm{E_{th}} \simeq \gamma_0 \mathrm{m v_{th}^2}$ is approximately valid. Consequently, for the GRB scenario the cold beam condition is easily met, if one considers that the typical binding energy for positronium (hydrogen) is $\mathrm{E_B} = 6.7\,\mathrm{eV}$ $(13.5\,\mathrm{eV})$, respectively, and typical thermal spreads range around $\mathrm{E_{th}} \sim 10^{-2} - 10^{2}\,\mathrm{keV}$ counterpoised to collision energies around $\mathrm{E_0} \sim 5 - 50\,\mathrm{MeV}$. Then the term cold beam limit refers to the case $\mathrm{E_B} \lesssim \mathrm{E_{th}} \ll \mathrm{E_0}$. In principle, for an adiabatically cooled, collisionless plasma shell even $\mathrm{E_{th}} \lesssim \mathrm{E_B}$ is possible. In all simulations the z-direction is identified as direction of reference, i.e. direction of parallel propagation and initial zero order vector quantities, consequently x is perpendicular. The initially upward (in +z) moving shell corresponds to $\mathrm{s} = 1$. Each shell is quasi-neutral itself, i.e. consists of electrons (index e) and positrons (index p). The basic set of equations in the linear theory is given by Maxwell's equations, continuity and Lorentz force. Though the ideas behind the linear analysis are plain and conventional, the algebra involved in intermediate steps can get quite tedious and the corresponding expressions easily become page-filling. Therefore we defer the derivation of the 2D EMCSI/CTW mode to Appendix B. There we also present the basic assumptions of the cold beam limit, the nomenclature for the formal substitutions, and the most important intermediate results. With a skillful choice of the substitutions the final determinant and the dispersion relation appear in a formal and concise fashion. The symmetric structure of contributing terms in the determinant and the combination of these terms (each descending from 1D modes) to the intertwined 2D mode becomes apparent.

For the GRB scenario we consider the case of negligible initial magnetic field $\mathrm{B_G} \rightarrow 0$. This assumption is motivated by the fact that almost nothing is known about the GRB central engine and shell collisions occur at distances at which only an extremely strong central dipolar field would still have significant strength. The modifications introduced by an initial guide field are investigated in chapter 5. It will be shown that the presence of a non-zero $\mathrm{B_G}$ has profound consequences on the physical nature of the instability. Harnessing the results from Appendix B we obtain the general dispersion relation D

$$\mathrm{D} = \mathrm{LM} \cdot \mathrm{CTW},$$

as combination of the purely real light mode LM (cf. Appendix B for nomenclature)

$$\mathrm{LM} = \omega^2 - (\mathrm{k_x^2} + \mathrm{k_z^2}) - \sum_{\mathrm{s}} \left(\frac{\mathrm{n_{0ps}}}{\gamma_{\mathrm{0ps}}} + \frac{\mathrm{n_{0es}}}{\gamma_{\mathrm{0es}}}\right) = \omega^2 - (\mathrm{k_x^2} + \mathrm{k_z^2}) - 4\omega_{\mathrm{p}}^{2\prime}$$

and the 2D CTW composed of the 1D Two-Stream (TSI) and 1D Weibel (WBI) modes

$$\begin{aligned} \mathrm{CTW} &= \mathrm{TSI} \cdot \mathrm{CT} + \mathrm{WBI} \\ &= (1 - \Omega_2^{-2}) \cdot \mathrm{CT} + \mathrm{k_x^2}[(1 + \Omega_4^{-2})(1 - \Omega_1^{-2}) + \Omega_3^{-4}] \end{aligned}$$

with the formal identifications

$$\mathrm{CT} = \mathrm{k}_\mathrm{z}^2(1+\Omega_4^{-2}) - \omega^2(1-\Omega_1^{-2}) - 2\omega \mathrm{k}_\mathrm{z}\Omega_3^{-2}$$

$$\begin{aligned}
\Omega_1^{-2} &= \Omega_{1\mathrm{p}}^{-2} + \Omega_{1\mathrm{e}}^{-2} \\
&= \sum_\mathrm{s} \left(\frac{\mathrm{n}_{0\mathrm{ps}}}{\gamma_{0\mathrm{ps}}\bar{\omega}_\mathrm{ps}^2} + \frac{\mathrm{n}_{0\mathrm{es}}}{\gamma_{0\mathrm{es}}\bar{\omega}_\mathrm{es}^2} \right) \\
\Omega_2^{-2} &= \Omega_{2\mathrm{p}}^{-2} + \Omega_{2\mathrm{e}}^{-2} \\
&= \sum_\mathrm{s} \left(\frac{\mathrm{n}_{0\mathrm{ps}}}{\gamma_{0\mathrm{ps}}^3\bar{\omega}_\mathrm{ps}^2} + \frac{\mathrm{n}_{0\mathrm{es}}}{\gamma_{0\mathrm{es}}^3\bar{\omega}_\mathrm{es}^2} \right)
\end{aligned}
\qquad
\begin{aligned}
\Omega_3^{-2} &= \Omega_{3\mathrm{p}}^{-2} + \Omega_{3\mathrm{e}}^{-2} \\
&= \sum_\mathrm{s} \left(\frac{\mathrm{n}_{0\mathrm{ps}}\mathrm{v}_{0\mathrm{ps}}}{\gamma_{0\mathrm{ps}}\bar{\omega}_\mathrm{ps}^2} + \frac{\mathrm{n}_{0\mathrm{es}}\mathrm{v}_{0\mathrm{es}}}{\gamma_{0\mathrm{es}}\bar{\omega}_\mathrm{es}^2} \right) \\
\Omega_4^{-2} &= \Omega_{4\mathrm{p}}^{-2} + \Omega_{4\mathrm{e}}^{-2} \\
&= \sum_\mathrm{s} \left(\frac{\mathrm{n}_{0\mathrm{ps}}\mathrm{v}_{0\mathrm{ps}}^2}{\gamma_{0\mathrm{ps}}\bar{\omega}_\mathrm{ps}^2} + \frac{\mathrm{n}_{0\mathrm{es}}\mathrm{v}_{0\mathrm{es}}^2}{\gamma_{0\mathrm{es}}\bar{\omega}_\mathrm{es}^2} \right) .
\end{aligned}$$

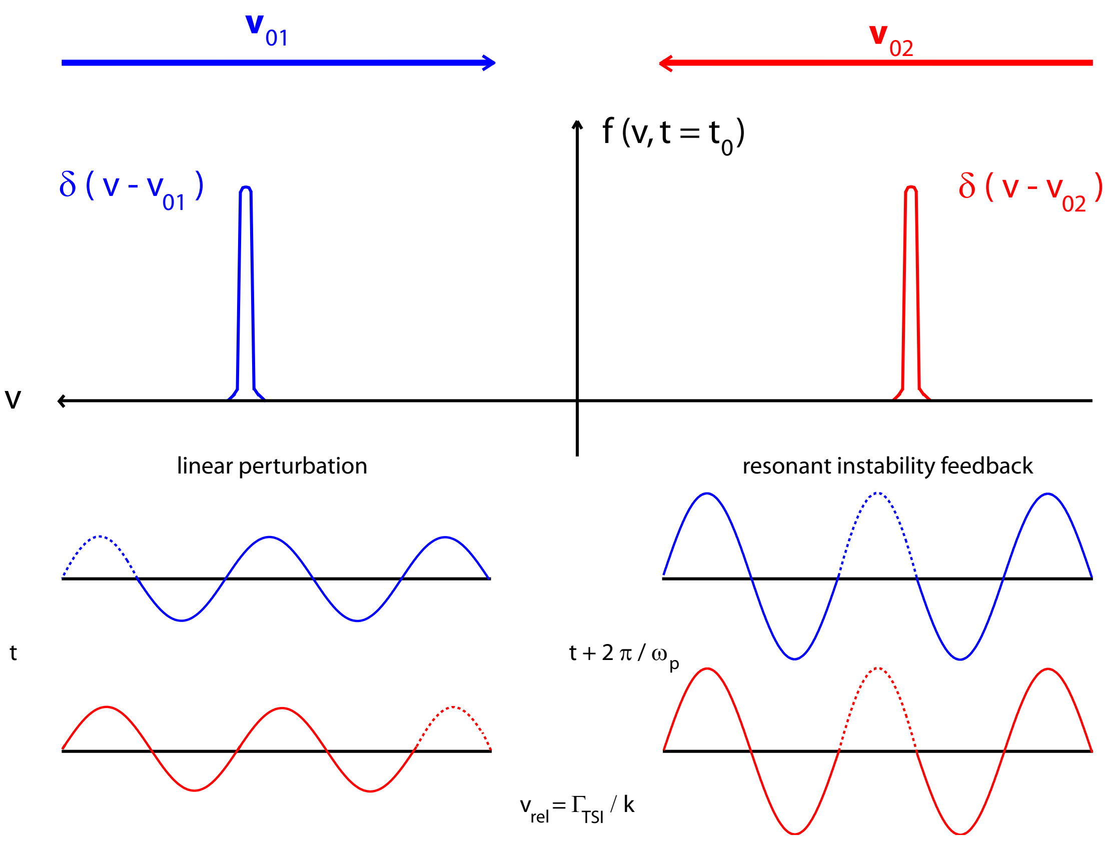

Fig. 4.2: On the physical mechanism of the 1D TSI mode: Linear (sinusoidal) perturbations (e.g. density, parallel electric field) of wavenumber k superpose resonantly for shells counterstreaming with $\mathrm{v}_\mathrm{rel} \simeq \Gamma_\mathrm{TSI}/\mathrm{k}$. Γ_TSI is the typical instability growth rate.

The 2D CTW mode as the linear progenitor of the plasma states evolving in 3D scenarios is subject to intense discussion in the subsequent sections. To obtain a consistent impression about the physical nature of the instability, we pause to take a closer look at the 1D constituents:
The TSI mode is the purely parallel and electrostatic constituent. The physical mechanism of the instability is quite simple. Plasma shells represent entities which are counterstreaming and clearly separated in velocity/momentum space (Fig. 4.2), but homogeneously interpenetrated in configuration space. Linear perturbations in the plasma configuration (within the constraints of linear theory assumed as harmonic/plane wave deviations from equilibrium state) can superpose resonantly, if the perturbations approach about one wavelength $\lambda = 2\pi/\mathrm{k}$ during the typical time of instability growth $\tau \sim 2\pi/\Gamma_{\mathrm{TSI}}$. With the relative velocity of the respective shells in the center-of-mass (cms) frame $\mathrm{v}_{\mathrm{rel}}$ and the typical growth rate Γ_{TSI} the criterion for instability is estimated to $\mathrm{v}_{\mathrm{rel}} \simeq \Gamma_{\mathrm{TSI}}/\mathrm{k}$. This relation has some predictive power on the behaviour of instability growth in the highly relativistic regime. For $\gamma \gg 1$ the approximation $\mathrm{v}_{\mathrm{rel}} \sim \mathrm{c}$ is valid, in the cms frame the wavelength appears Lorentz contracted to λ/γ, and the plasma frequency as the basic timescale of the instability is reduced according to $\omega_{\mathrm{p}} \propto \gamma^{-1/2}$. Consequently the TSI growth is expected to receive a relativistic damping like $\Gamma_{\mathrm{TSI}} \propto \gamma^{-3/2}$.
In this way the mechanism and behaviour of the TSI are motivated by intuitive arguments. Certainly such arguments are to be confirmed by a rigorous mathematical analysis of the dispersion relation. In the simulation GRB shell collisions are studied in a Cartesian slab configuration. The simulation (= lab) inertial frame is the cms frame of pair plasma shells which are homogeneous in density $\mathrm{n}_{0\mathrm{ps}} = \mathrm{n}_{0\mathrm{es}} = \mathrm{n}_0$ and counterstreaming with $\mathbf{v}_{01} = -\mathbf{v}_{02}$ and $\mathrm{v}_{\mathrm{z0ps}} = \mathrm{v}_{\mathrm{z0es}} = \mathrm{v}_0$. Under such conditions the dispersion relation for the TSI takes the form

$$1 - \Omega_2^{-2} = \omega^4 - 4\omega_{\mathrm{p}}^2\omega^2 + 2\omega^2\mathrm{k}_{\mathrm{z}}^2\mathrm{v}_0^2 - 4\omega_{\mathrm{p}}^2\mathrm{k}_{\mathrm{z}}^2\mathrm{v}_0^2 + \mathrm{k}_{\mathrm{z}}^4\mathrm{v}_0^4,$$

which is a biquadratic equation in ω as well as $\mathrm{k}_{\mathrm{z}}\mathrm{v}_0$. The solutions of this equation are plotted for the exemplaric case $\mathrm{v}_0 = 0.5$ in Fig. 4.3 a). The physical solution in ω is purely real and forms a hyperbolic curve in the $\omega(\mathrm{k}_{\mathrm{z}})$ diagram with vertex at the relativistically modified plasma frequency $\omega_{\mathrm{cut}}^{\mathrm{ES}} = 2\omega_{\mathrm{p}}' = 2\omega_{\mathrm{p0}}\gamma_0^{-3/2}$. The $\mathrm{k}_{\mathrm{z}} \to 0$ limit corresponds to stationary plasma (= Langmuir) oscillations. From this vertex plasma waves disperse with increasing k_{z} asymptotically towards comotion with the shell, i.e. the respective phase and group velocity tend asymptotically towards the shell velocity in the cms frame $\omega = \mathrm{k}_{\mathrm{z}}\mathrm{v}_0$. Upward and downward moving shells correspond to right and left branches of the dispersion relation. Consequently, plasma waves are interpreted straightforwardly as Doppler-boosted Langmuir oscillations. Since the second solution is again purely electrostatic, the shell velocity is employed as the separatrix to discriminate the high-frequency electrostatic (HF-ES) mode of the biquadatric ω solution and the further low-frequency electrostatic (LF-ES) mode contained in the biquadratic $\mathrm{k}_{\mathrm{z}}\mathrm{v}_0$ solution. The LF-ES mode is purely real from $\mathrm{k}_{\mathrm{z,cut}} = 2\omega_{\mathrm{p}}'/\mathrm{v}_0$ on and tends asymptotically towards the shell motion for $\mathrm{k}_{\mathrm{z}} \to \infty$. At sufficiently large wavelengths $\mathrm{k}_{\mathrm{z}} < \mathrm{k}_{\mathrm{z,cut}}$

the LF-ES mode is purely imaginary (broken blue line in Fig. 4.3a). This part is solely responsible for the spontaneous growth of the TSI. The growth rate Γ_{TSI} and the associated mode wavelength $\mathrm{k}_{\mathrm{z}}^{\mathrm{ES}}$ correspond to the maximum of the imaginary solution, since only the fastest growing mode asserts itself in the exponential growth during the linear phase. With the linear analysis of the TSI at hand, the critical question is how well the results reconcile with the PIC simulation.

To answer this question we create a simulation setup of counterstreaming homogeneous plasma shells, in which particle motion is restricted to one degree of freedom, i.e. to the longitudinal direction. Then only the TSI mode is excited and the perpendicular WBI mode is suppressed. Figure 4.3b shows the parallel electric field E_{z} associated with TSI in the fully evolved linear stage at $\mathrm{t}\omega_{\mathrm{p0}} = 12$. According to the time evolution in Fig. 4.3c the time point is selected shortly before non-linear saturation becomes important. The dominant wavenumber in the corresponding Fourier spectrum $\mathrm{E}_{\mathrm{z}}(\mathrm{k}_{\mathrm{z}})$ corresponds to the wavelength $\lambda = 3.17\,(\mathrm{c}/\omega_{\mathrm{p0}})$ and coincides precisely with the maximum (red cross in Fig. 4.3a) of the imaginary solution. The Fourier spectrum is broadened around $\mathrm{k}_{\mathrm{z}}^{\mathrm{ES}}$ due to the finite longitudinal system length. Further extended systems yield progressively sharper Fourier peaks. The growth rate is determined to $\Gamma_{\mathrm{TSI}}\,\omega_{\mathrm{p0}}^{-1} = 0.58$ (dotted line in Fig. 4.3c) which again exactly confirms the prediction of the linear theory. The linear analysis is merely a mathematical method rather than the description of a physical mechanism. Therefore it is instructive to observe how the individual linear modes as solutions of the dispersion relation manifest in the field data. For initially cold plasma $\mathrm{T} \rightarrow 0$ (Fig. 4.4a) the HF-ES solution is the solely excited mode. The analytically derived $(\omega, \mathrm{k}_{\mathrm{z}})$ dispersion is directly manifested in the parallel electric field E_{z}. The low-frequency cut-off and shell velocity asymptote are confirmed. The HF-ES mode is purely real and intrinsically not growing. However, it is obvious to see that the instability free energy is pumped into the HF-ES via the purely imaginary (=exponentially growing) mode at $\mathrm{k}_{\mathrm{z}}^{\mathrm{ES}} = 2.0\,(\omega_{\mathrm{p0}}/\mathrm{c})$. In conclusion, in the cold plasma limit the TSI remains completely electrostatic. The situation alters for hot plasma conditions. Certainly the HF-ES is excited again (Fig. 4.4b), though not exclusively in the ground state but furthermore in higher harmonics. Actually higher harmonics appear not as exact integer multiples, since the local plasma frequency ω_{p} as the fundamental frequency varies according to the density fluctuations. There is also an important qualitative difference, since the electromagnetic LM mode coexists besides the HF-ES (Fig. 4.4c). Then also $\omega_{\mathrm{cut}}^{\mathrm{EM}}$ and the light speed as small wavelengths asymptote are clearly identifiable. Electromagnetic and electrostatic signatures are comparable in power density because $\mathrm{v}_{\mathrm{A0}} = \mathrm{c}$ is valid. In the hot plasma case low-frequency density fluctuations become more prominent (Fig. 4.4d), though it is hard to identify the LF-ES mode, since there is strong background of non-linear electro-acoustic modes.

The second 1D constituent of the CTW mode is the Weibel instability (WBI). The WBI is inherently electromagnetic and in distinction to whistlers a so-called zero- or low-frequency mode. As the TSI the WBI is a kinetic instability, originally discovered by Weibel [Weibel, 1959] for the case of a Maxwellian plasma with temperature anisotropies. As elaborated in detail in section 4.2.4, beam or counterstreaming scenarios represent the non-thermal limit of extreme anisotropy and, hence, the WBI is certainly contained

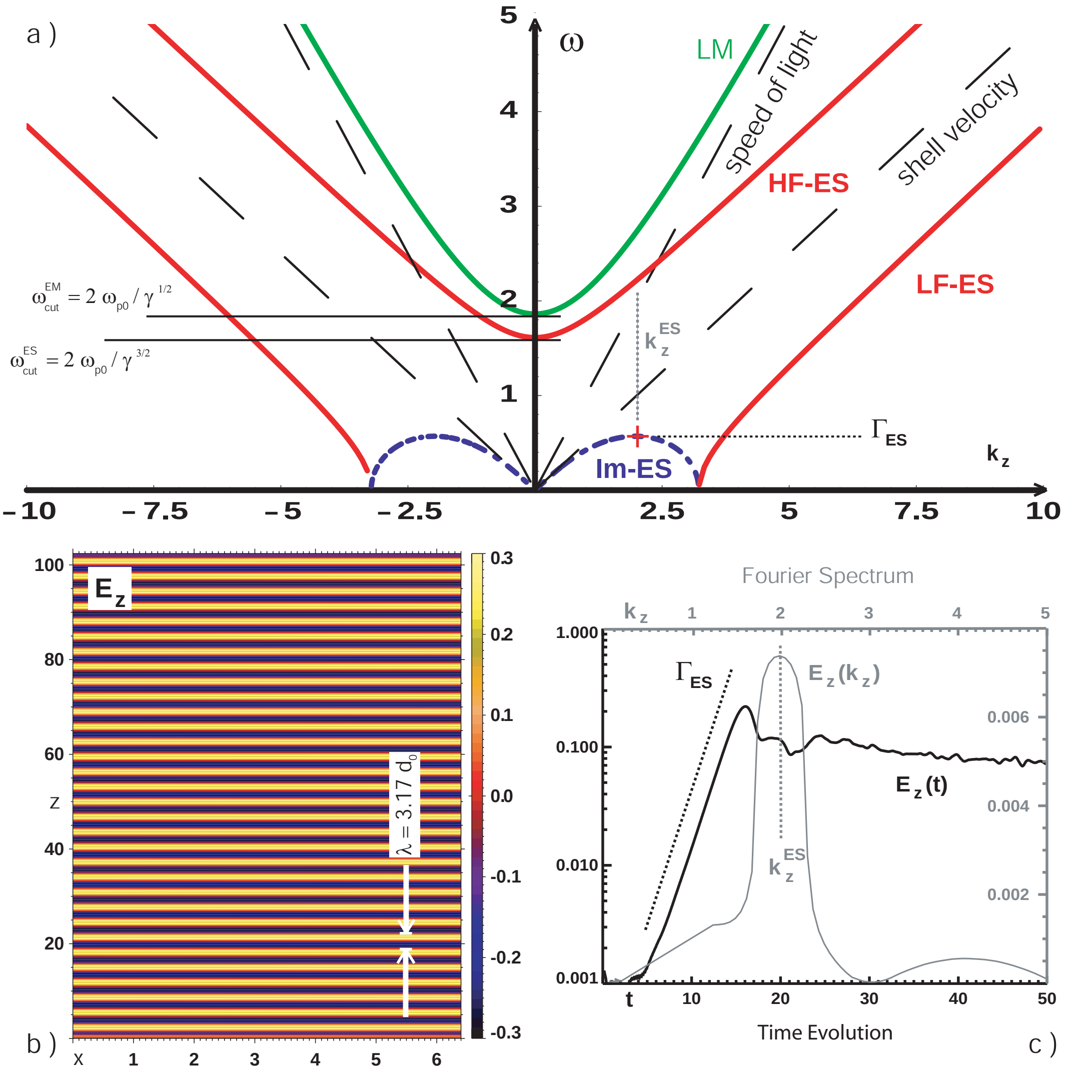

Fig. 4.3: Linear analysis of the TSI mode. $\omega(k_z)$ diagram of the LM mode and high-frequency (HF-ES) and low-frequency (LF-ES) electrostatic TSI solutions with shell velocity $v_0 = 0.5$ as separating asymptote (a). The red cross indicates the rate Γ_{TSI} and wavenumber k_z^{ES} of maximum linear TSI growth. Results of the linear analysis are directly identified in the PIC simulation: The excited parallel electric field E_z in configuration space at $t\,\omega_{p0} = 12$ (b) and the associated Fourier spectrum (c) reflect exactly the expected wavenumber k_z^{ES}. Further the time evolution of the electrostatic field E_z pinpoints the calculated value for Γ_{TSI}.

within the framework of the cold beam limit. Again the fundamental physical mechanism of the instability is motivated straightforwardly (Fig. 4.5). Positrons and electrons within one shell represent oppositely aligned currents. Parallel currents are mutually attractive and therefore particle species form likewise current filaments. The current creates a toroidal magnetic field around each filament. As filaments become spatially confined the self-generated magnetic field progressively gains in strength, thereby closing the instability feedback loop. For counterstreaming shells of different density, the self-pinching is balanced at some point by repulsive electrostatic forces. For equally dens shells as in the scenarios discussed in the present work, in the counterstreaming shell the likewise current is formed by the oppositely-charged specie. Therefore the current filaments remain quasi-neutral and self-pinching is finished during non-linear saturation by the growing finite thermal pressure of the plasma.

Again we dissect the dispersion relation of the 1D WBI, which follows in the limit $\mathrm{k_z} \to 0$ from the 2D CTW. Based on the analytic expression

$$\mathrm{WBI} = \omega^2(1-\Omega_1^{-2})(1-\Omega_2^{-2}) - \mathrm{k_x^2}[(1+\Omega_4^{-2})(1-\Omega_1^{-2}) + \Omega_3^{-4}]$$

an equivalent analysis as elaborated above for the TSI yields the ensemble of possible solutions plotted in Fig. 4.6a. In distinction from the results for the TSI two electromagnetic LM modes exist and only the high-frequency electrostatic ES mode is predicted. Further the ES appears non-dispersive $\omega(\mathrm{k_x}) = \omega_{\mathrm{cut}}^{\mathrm{ES}} = \mathrm{const}$ as entirely stationary Langmuir oscillations. This is understood intuitively, if one recalls the fact that the mode propagation in the forced limit is entirely parallel and as a consequence thereof decoupled from the parallel shell motion. Hence, the comotion of plasma oscillations is suppressed and no Doppler-boosting to plasma waves takes place. It is interesting to note that the low-frequency cut-offs of the EM and ES modes exhibit a relativistic scaling with γ which is exactly interchanged for the TSI and WBI, respectively. Further the separation of low-frequency cut-offs is a peculiarity of the relativistic regime. In the non-relativistic limit $\gamma \to 1$ the LM/EM and ES modes have a common intersection point at $\mathrm{k} = 0$. The single purely imaginary solution (dotted blue line in Fig. 4.6a) characterizes the growing Weibel mode, with the saturated value at $\mathrm{k_x} \to \infty$ predicting the instability rate of growth Γ_{WBI}. The ultimate test on the validity of theoretical statements is again the excitation of modes in the simulation. Therefore we design an initial setup in which plasma shell collisions are studied solely in the plane perpendicular to the shell motion. To allow comparison with TSI simulation the counterstreaming is again set to $\mathrm{v_0} = 0.5$. The WBI mode manifests equivalently prominent in the perpendicular magnetic fields $\mathrm{B_\perp}$ and parallel electric field $\mathrm{E_z}$. The growth rate $\Gamma_{\mathrm{WBI}}\,\omega_{\mathrm{p0}}^{-1} = 0.88$ (Fig. 4.6b) again exactly confirms the theoretical prediction. As soon as the system runs into non-linear saturation also the respective orthogonal quantities $(\mathrm{B_z}, \mathrm{E_\perp})$ gain in importance. From the evolution of the Fourier spectrum it is evident that the Weibel magnetic fields initially form at small scales and afterwards relax towards larger inherent structures, i.e. smaller wavenumbers. The details of this time-variant self-similar topologies are of extreme importance for GRB synchrotron signatures and are addressed in detail in section 4.4. The growing Weibel solution is itself a zero-frequency mode with prominent contributions to the $(\omega, \mathrm{k_x})$ dispersion (Fig. 4.6c). In the non-linear regime significant energy

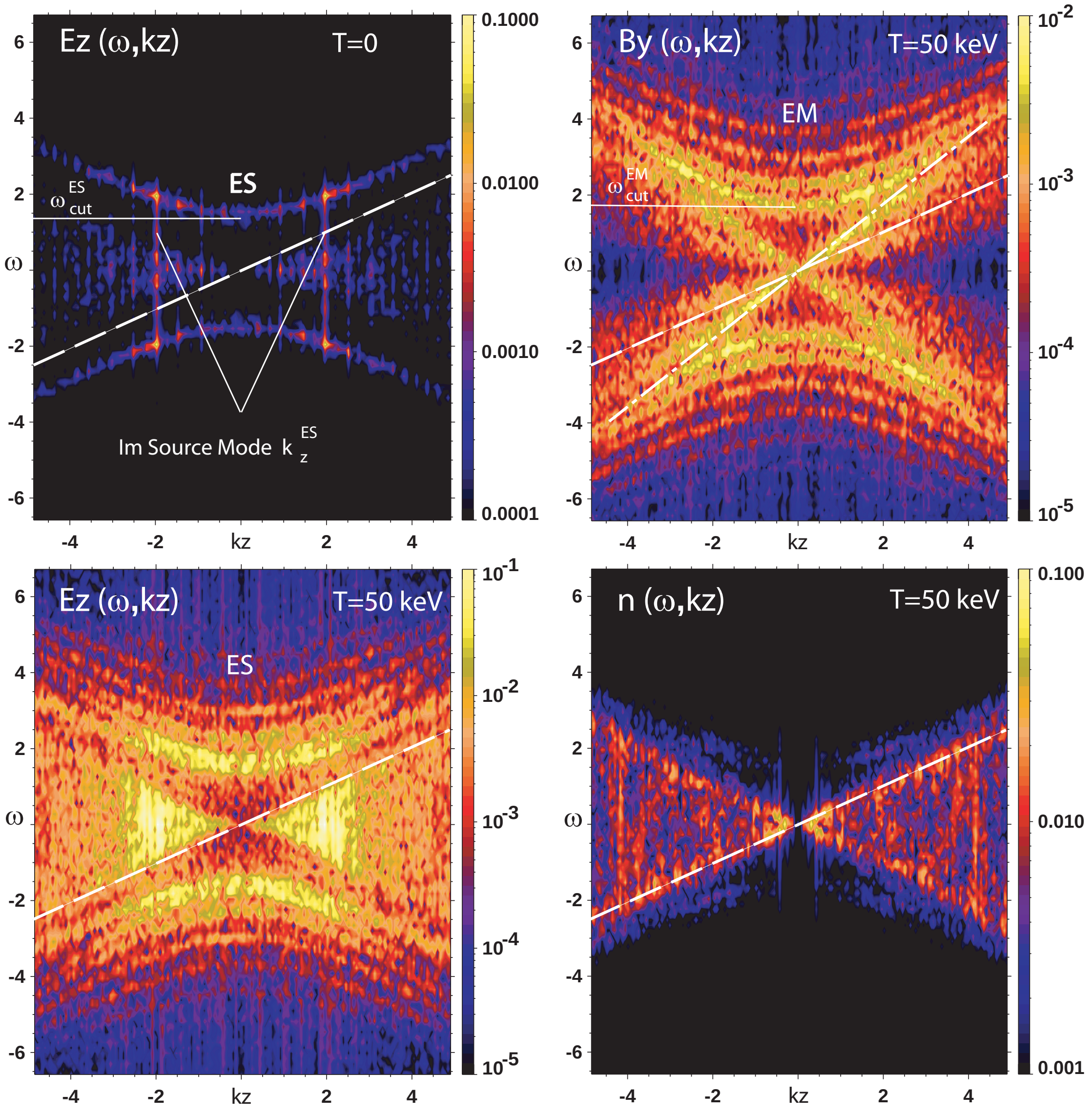

Fig. 4.4: Dispersion signatures of the 1D parallel counterstreaming scenario. For cold plasma conditions (a) the HF-ES is the solely excited real mode which is nourished by the imaginary mode at $\mathrm{k_z^{ES}} = 2.0\,(\omega_{\mathrm{p0}}/\mathrm{c})$. In the hot plasma limit higher order ES modes (b) and - as qualitative difference - the electromagnetic LM mode (c) are excited. At such conditions the density fluctuations become more prominent (d) and manifest in contributions of non-linear electro-acoustic modes. In all physical quantities the analytically determined asymptotic behaviour and low-frequency cut-offs are retained.

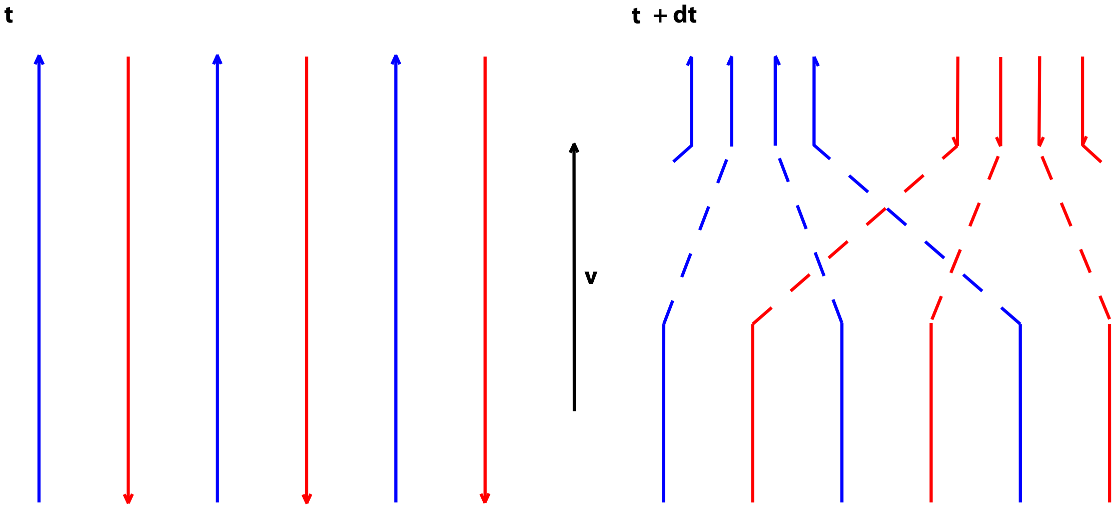

Fig. 4.5: On the physical mechanism of the 1D WBI mode: Positrons (blue) and electrons (red) propagate in parallel with velocity **v** forming counterpoised currents (arrows) at time t. Parallel currents are mutually attractive and coalesce. The configuration is unstable, since attraction and coalescence superpose resonantly, i.e. at t + dt the current filaments 'self-pinch'.

drains into the LM modes intriguingly at the wavenumber $\mathrm{k}_\mathrm{x}^\mathrm{EM}$ which dominates the Fourier spectrum at late times.

Up to this point we have presented the results of the linear theory for the 2D EM-CSI/CTW mode in the limit of zero initial magnetic guide component B_G. The 2D mode is a combination of an entirely parallel 1D TSI mode and perpendicular 1D WBI mode. We have understood the basic physical nature of the 1D constituents and how the instabilities manifest fingerprints in the data of self-consistent kinetic simulations. The coincidence of simulated data with linear theory is immaculate. We further keep in mind that an initially hot plasma exhibits behaviour deviating from the predictions of linear theory in the zero temperature approximation. Such extensions beyond the cold beam limit are referred to as 'thermal effects' which we will discuss in detail for specific problems. Due to the coupling term the features of the 2D instability are more complex than a simple superposition of the linear constituents - even during the linear phase. Basic characteristics of the 2D mode are discussed in conjunction with the simulation of real 3D scenarios in the following sections. In section 4.2 we investigate the CTW mode for the high to ultra-relativistic energies expectable in GRB fireball collisions. Linear theory provides the key ideas for the interpretation of the non-linear saturated steady state. During non-linear saturation the plasma modes evolve from the 2D case into a real 3D configuration. 3D contributions are an entirely non-linear effect not included in

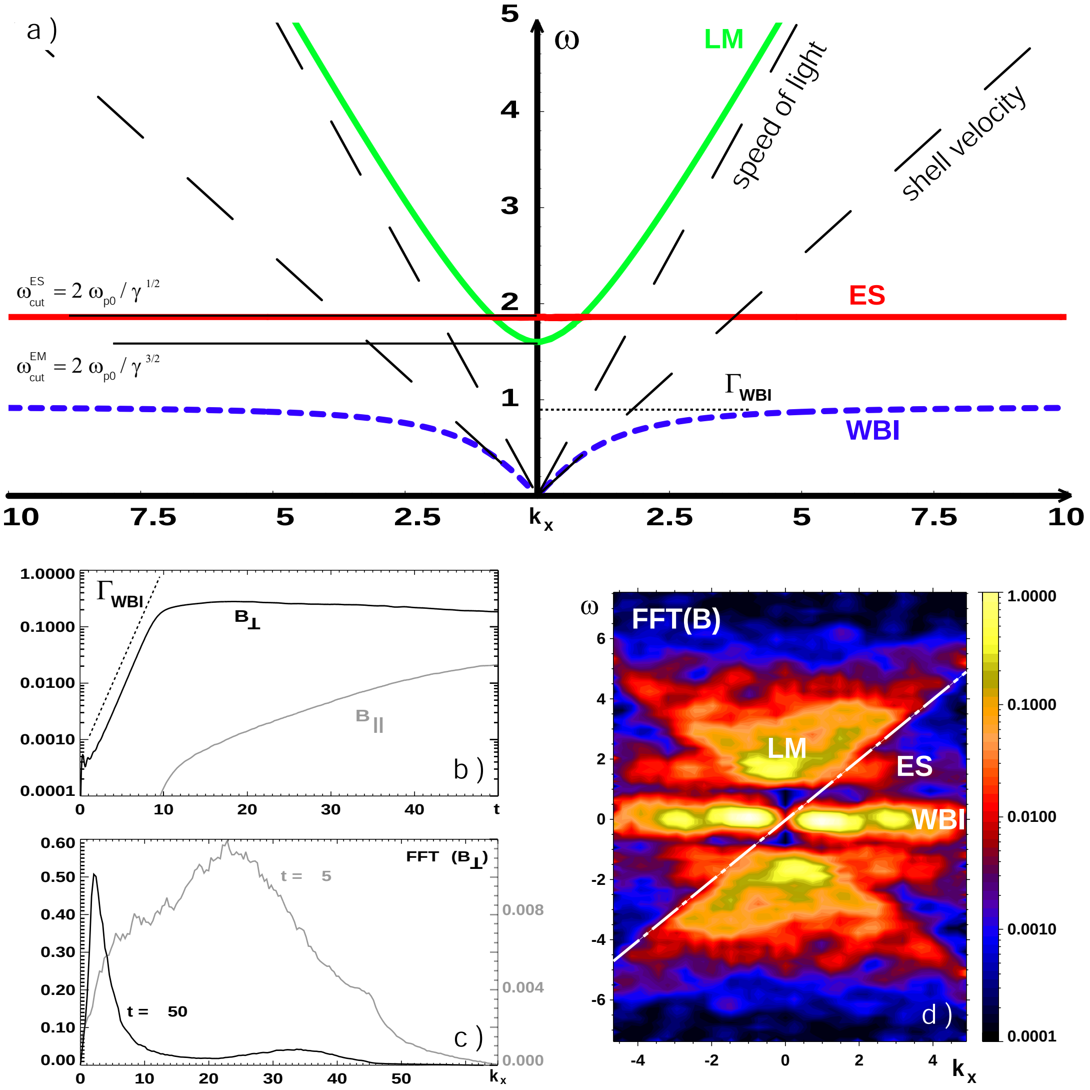

Fig. 4.6: Detailed analysis of the 1D WBI mode characteristics: Theoretical predictions illustrated in the $(\omega, \mathrm{k_x})$ dispersion diagram (a) are precisely validated in the PIC simulation (b,c). The Fourier spectrum shows the cascade from small to large scale magnetic structures and the time evolution confirms the expected linear growth $\Gamma_{\mathrm{WBI}}\,\omega_{\mathrm{p0}}^{-1} = 0.88$ (b). In (c) the WBI is identified in the magnetic field as zero-frequency mode which in the non-linear phase nourishes the excitation of LM modes.

the linear analysis. We further devote section 4.2.4 to a thorough discussion on the possible impact of thermal effects. Affirmed by the insights for the final 3D EMCSI/CTW configuration we continue with the tedious analysis of the microphysics pervasive in this final saturated 3D plasma state. Section 4.3 is devoted to the diffusion-limited stability of Weibel magnetic fields. Such lifetime limits are crucial for the validity of GRB synchrotron emission models. We note that the PIC simulation method is the only one capable to identify the diffusion mechanism and determine self-consistent diffusion coefficients. This is again due to the fact that one can trace individual particle trajectories and correlate them with the field data. The implications for the synchrotron spectra are then subject to section 4.4. We further give an outlook on the modifications introduced by a third heavier plasma specie, i.e. the influence of a second spacetime scale. Such effects are expected to be important for the external collision of fireballs with the interstellar medium and the filamentation of extragalactic jets.

We finally note that the simulation of such 3D scenarios is computationally extremely expensive and restricted to the domain of massively parallelized codes employing the upper edge of contemporary supercomputing performance.

4.2 Ultra-Relativistic Plasma Shell Collisions - The Magnetic Equipartition Ratio

The following section is published as

'Ultra-Relativistic Plasma Shell Collisions in Gamma-Ray Burst Sources: Dimensional Effects on the Final Steady-State Magnetic Field'

C.H. Jaroschek, H. Lesch, and R.A. Treumann

The Astrophysical Journal, 618, 822, 10 Jan 2005

4.2.1 Abstract

Ultra-relativistic electron-positron plasma shell collisions as an integral part of generic γ-ray burst (GRB) fireball models are studied in the framework of self-consistent 3D Particle-In-Cell (PIC) simulations. Compared are scenarios at moderate ($\gamma_0 \simeq 10$) and ultra-relativistic ($\gamma_0 \simeq 100$) energies which directly correspond to the regimes of internal and external shell collisions in GRB synchrotron emission models. Simulated systems are comprised by $5 \cdot 10^8$ particles, applying a relativistic, fully electromagnetic, massively parallelized code. It is found that Weibel-generated, steady-state magnetic equipartition ratios in external collisions reach up to $\epsilon_\mathrm{B} \sim 12\,\%$, exceeding the respective internal ratios by nearly one power of ten. Enhanced ϵ_B yields can be explained theoretically by the effective reduction of dimensionality in the ultra-relativistic limit, i.e. the energy dependent confinement of the 3D Weibel instability within quasi-2D plasma shell slices.

4.2.2 Introduction

Theoretical concepts on astrophysical phenomena like extragalactic jets, cosmical magnetic fields and γ-ray bursts (GRBs) rely on the thorough understanding of relativistic plasma beam instabilities in the highly non-linear regime. In generic GRB fireball models a compact central engine ejects electron-positron (e,p) plasma shells (for an extensive review on GRBs see Piran [1999]; Mészáros [2002]). To resolve the 'compactness problem' (i.e. the optical thickness against pair production at the observed extreme γ-ray luminosities) by relativistic beaming, the shells must be confined within a narrow opening angle around the source and move at highly relativistic speeds. Source variabilities cause internal plasma shell collisions at relativistic energies $\gamma_0^\mathrm{int} \sim 10$ which are claimed to be responsible for the γ-emission via Comptonized synchrotron radiation. GRB radio afterglows can be explained by direct synchrotron emission from the plasma shells with the external medium at significantly higher collision energies of $\gamma_0^\mathrm{ext} \sim 100$-300 [Panaitescu & Kumar, 2002].

Essential for all synchrotron emission models is the generation of magnetic fields close to equipartition during the shell collisions. Magnetic field enhancement via shock compression at the boundary of interpenetrating shells is one option proposed [Kazimura et al., 1998], though the rapid decay of the magnetic field strength behind the shock front represents a systematic weakness [Gruzinov, 2001] of the model. Extremely promising appears the approach by Medvedev & Loeb [1999] and Pruet, Abazajian, & Fuller [2001] of magnetic field generation via the Weibel instability [Weibel, 1959] which is effective in the counterstreaming plasmas of deeply interpenetrated colliding shells. We note that the term 'collision' refers to the interaction between rarefied plasmas of different bulk motion (=shells), within which the charged particles experience scattering at the collective fields of plasma instabilities [Sagdeev, 1966]. The validity of the Weibel approach with respect to magnetic field generation has been confirmed in Particle-In-Cell (PIC) simulations of colliding (e,p) plasma shells at weakly-to-moderately relativistic collision energies ${\gamma_0^1}^{(10)} = 1.17\,(10.05)$ [Silva et al., 2003] which applies to the regime of internal collisions. Therein, final steady-state equipartition ratios of the magnetic field energy $\epsilon_\mathrm{B} \sim 0.25\,\%\,(2.5\,\%)$ for ${\gamma_0^1}^{(10)}$ were obtained. The equipartition ratio ϵ is defined as the ratio of field-to-total particle relativistic energy.

In the present article we report 3D PIC simulation results on the magnetic field generation by the electromagnetic (EM) counterstreaming instability at external collision energies of $\gamma_0^{100} = 100.005$. In 3D scenarios the EM counterstreaming instability [Haruki & Sakai, 2003; Saito & Sakai, 2004] is a 2D Coupled Two-Stream-Weibel (CTW) mode. For comparison, we reproduce shell collisions at the moderate γ_0^{10} and can confirm the results of Silva et al. [2003]. We show that at external collision energies of γ_0^{100} even higher equipartition magnetic field ratios up to $\epsilon_\mathrm{B} \sim 12\,\%$ are obtained. In contrast to the internal case, magnetic fields in the saturation and final steady-state phases become comparable. In the present analysis we focus on the behaviour of the 2D CTW mode as function of collision relativistic energy. Therefore plasma shells are initially cold to avoid kinetic contributions of finite thermal spread within the linear regime. However, the Weibel mode is an inherently kinetic instability [Weibel, 1959] and the scenario of counterstreaming plasmas is nothing else than an extreme form of temperature anisotropy. Therefore we present a thorough discussion of the limits of the cold plasma approximation, effects of non-negligible thermal spread and define the characteristic quantities deciding upon the impact of kinetic modifications in the relativistic regime. Energy dependence of equipartition yields in the final steady-state configuration indicates that the non-linear coupling between the unstable Weibel and Two-Stream modes is sensitive to the transition from moderate ($\gamma_0^{10} \sim \gamma^{\mathrm{int}}$) to ultra-relativistic ($\gamma_0^{100} \sim \gamma^{\mathrm{ext}}$) collision energies. Linear stability theory provides good arguments for explaining the energy dependence of the coupled mode, which are subsequently validated in the non-linear regime at late times by means of the PIC simulations. The essential point is the progressive dominance of the Weibel over the Two-Stream contributions in the CTW mode at ultra-relativistic energies, causing an energy-dependent reduction of the dimensionality: For extreme collision energies the 3D Coupled Two-Stream-Weibel mode (CTW) propagates in quasi-2D shell slices transverse to the bulk motion. We finally conclude, that the reduced dimensionality in external shell collisions enhances the Weibel generated magnetic equipartition ratio by one order of magnitude.

Table 4.1: Simulation characteristic quantities.

Simulation	$\mathrm{L_x \times L_y \times L_z}$	$\mathrm{u_{z0,1}}$	$\mathrm{v^{cms}_{th,\perp}}$
1	25.6 × 25.6 × 12.8	10.00	$4.5 \cdot 10^{-5}$
2	25.6 × 25.6 × 12.8	10.00	$100.0 \cdot 10^{-5}$
3	25.6 × 25.6 × 12.8	100.00	$4.5 \cdot 10^{-5}$
4	51.6 × 3.2 × 51.6	100.00	$4.5 \cdot 10^{-5}$

4.2.3 Simulation Description

The simulations are performed with a massively parallelized, relativistic and fully electromagnetic PIC code. A detailed discussion of the PIC method is found in Birdsall & Langdon [2000]. The field quantities are represented on a highly refined grid mesh with resolution $\Delta_{\mathrm{x,y,z}} = 0.1\,(\mathrm{c}/\omega_{\mathrm{p0}})$ in each Cartesian direction. Times are normalized to the inverse plasma frequency $\omega_{\mathrm{p0}}^{-1} = (4\pi \mathrm{e}^2\mathrm{n}_0/\mathrm{m})^{-1}$, lengths to the plasma skin depth $(\mathrm{c}/\omega_{\mathrm{p0}})$ and, as a consequence thereof, velocities to the speed of light c. e and m are electronic charge and mass, respectively. We study the Weibel instability in 3D with a total ensemble up to $5 \cdot 10^8$ individual particles. In the initial configuration, particles are homogeneously distributed in configuration space and appendant to counterstreaming ensembles in velocity space: An upward moving pair plasma shell $\mathrm{v_{z0,1}} > 0$ with electron-/positron density $\mathrm{n_{p0}} = \mathrm{n_{e0}} = \mathrm{n_0}$ and an equally dense counterstreaming shell $\mathrm{v_{z0,2}} = -\mathrm{v_{z0,1}}$. The grid mesh frame is the Lorentzian laboratory and center of mass (cms) frame. Consequently the system is initially charge and current neutral. The initial setup corresponds to the situation of interpenetrating plasma shells studied in slab geometry, i.e. the conditions prevalent in 3D collisionless shocks in a cms frame comoving downstream of the shock front.

A selection of four simulations is presented, respectively two simulation runs at moderate-relativistic normalized bulk momentum $\mathrm{p_{z0}/mc} = \mathrm{u_{z0}} = \gamma_0^{10}\mathrm{v_{z0}} = 10.00$ and at ultra-relativistic $\gamma_0^{100}\mathrm{v_{z0}} = 100.00$. The different relativistic energies $\gamma_0^{10(100)}$ not only probe the regimes of internal and external collision energies by direct numerical simulation, they also provide insight into the energy dependence of the coupling term in the 2D Two-Stream-Weibel coupled instability for the highly non-linear evolution at late times. Table 4.1 summarizes the key quantities of the individual initial setups. Particles are inserted in momentum space according to an isotropic Maxwellian in the comoving frame of the shells. In the cms (=lab) frame the particle distributions appear Lorentz-boosted. The finite temperature of the respective Lorentz-boosted Maxwellian corresponds to a thermal velocity spread $\mathrm{v^{cms}_{th,\perp}}$ perpendicular to the bulk motion. We adopt the definition employed in Silva et al. [2003] and Medvedev & Loeb [1999] and define the initial bulk motion in +z as the parallel direction of reference. This is opposite to the convention used in Yoon & Davidson [1987a;b], Yang et al. [1993b], and Yang, Arons & Langdon

[1993a] where the 1D Weibel mode has been analyzed in the presence of a magnetic field providing the preferred direction of parallel propagation.

In all simulations that follow, the initialized plasma shells are cold, i.e. the initial perpendicular temperatures $\mathrm{T}_\perp$ reside in the eV-regime. This situation is fundamentally different from fast ignitor scenarios. The relativistic definition of temperature and kinetic modifications introduced in the case of significant thermal spread are discussed in section 4.2.4. For γ_0^{10} two scenarios are compared which differ by a factor ~ 500 in the initial $\mathrm{T}_\perp$ in order to put constraints on the validity of the cold beam assumption in the linear stability analysis in section 4.2.4. Though the plasma shells are cold at initialization and during the linear regime, a fully kinetic numerical plasma model is essential to include non-thermal heating / particle acceleration during late times. The two ultra-relativistic runs are performed in different geometries of the simulated volume for gaining insight into the effect of the finite size of the simulation box imposed by computational limitations. We note that the Coupled Two-Stream-Weibel (CTW) instability is an inherently 3D problem: Though the coupled plasma mode is 2D in the linear regime, in the phase of non-linear saturation only oppositely aligned current self-pinches are mutually neighboring in any 2D plane which includes the z-direction. A third dimension is required to allow for the coalescence of alike current filaments by circumventing the respective counter-currents, as was already recognized by Lee & Lampe [1973]. The late time evolution is studied in simulations 1, 2 and 3 which lasted for $\Delta \mathrm{t}\omega_{\mathrm{p}0} = 260$, requiring 5500 time steps for γ_0^{10} and 45000 time steps for γ_0^{100} in order to assure energy stability of 0.1 % and 1 %, respectively.

4.2.4 Dimensional Effects in Relativistic Plasma Shell Collisions

Linear Progenitors of the Preeminent Plasma Instability Modes

In 3D scenarios of counterstreaming plasma shells the conversion of collision-kinetic into electromagnetic energy is conducted by the 2D Coupled Two-Stream-Weibel instability (CTW). In the linear regime the system is degenerate in the transverse direction. As already noted, the configuration becomes 3D during non-linear saturation and coalescence of the current filaments. The CTW propagates at oblique angles as the coupled mode consisting of the purely 1D electromagnetic Weibel instability (WBI) which propagates exactly transversely and the 1D electrostatic Two-Stream instability (TSI) propagating longitudinally.

In all parameter regimes plasma shell collisions proceed in three successive phases: the linear growth phase, followed by the highly non-linear saturation phase of the individual modes, and the phase of formation of a final steady-state configuration. Though the linear phase evolves on time-scales/perturbation-scale heights irrelevant in the astrophysical context, all the preeminent dissipation channels of the system's free energy are excited. Hence, the linear analysis provides the essential interpretative insights into the energy dependence of the linear mode. It also has some predictive power for the processes vital during the two late-time phases, when the non-linear coupling and kinetic effects come into play.

In the initial setup the finite thermal spread of plasma shells is negligible. As is shown in section 4.2.4, the perpendicular temperatures remain in the sub-keV regime during the entire linear phase up to the time of non-linear mode saturation. Consequently, for the initial setups presented in this article the cold beam approximation is valid for the entire linear regime. The plasma dynamics of counterstreaming electron-positron (e,p) shells in the cold beam limit [Califano, Pegoraro, & Bulanov, 1997; Kazimura et al., 1998] is governed by the set of equations consisting of the Lorentz force equation

$$\partial \mathbf{p}_\mathrm{i}/\partial \mathrm{t} + \mathbf{v}_\mathrm{i} \cdot \nabla \mathbf{p}_\mathrm{i} = \pm(\mathbf{E} + \mathbf{v}_\mathrm{i} \times \mathbf{B}), \tag{4.1}$$

the dynamic Maxwell equations

$$\partial \mathbf{B}/\partial \mathrm{t} = -\nabla \times \mathbf{E} \tag{4.2}$$

$$\partial \mathbf{E}/\partial \mathrm{t} = \nabla \times \mathbf{B} - \sum_\mathrm{i} \mathbf{j}_\mathrm{i} \tag{4.3}$$

with the current in each individual shell i given by $\mathbf{j}_\mathrm{i} = \mathrm{n}_{\mathrm{p,i}}\mathbf{v}_{\mathrm{p,i}} - \mathrm{n}_{\mathrm{e,i}}\mathbf{v}_{\mathrm{e,i}}$, and the continuity equations

$$\partial \mathrm{n}_\mathrm{i}/\partial \mathrm{t} = -\nabla \cdot \mathbf{j}_\mathrm{i}. \tag{4.4}$$

Linearization yields the dispersion relation

$$\begin{aligned}(1 - 2\Omega_2^{-2})[\mathrm{k}_\mathrm{z}^2(1 + 2\Omega_4^{-2}) - \omega^2(1 - 2\Omega_1^{-2}) - 4\omega \mathrm{k}_\mathrm{z}\Omega_3^{-2}]&\\ +\mathrm{k}_\mathrm{x}^2[(1 - 2\Omega_1^{-2})(1 + 2\Omega_4^{-2}) + 4\Omega_3^{-4}] &= 0\end{aligned} \tag{4.5}$$

which contains the dimensionless expressions

$$\Omega_1^{-2} = \sum_\mathrm{i} \frac{\mathrm{n}_{0,\mathrm{i}}}{\gamma_{0,\mathrm{i}}\,\Omega_\mathrm{i}^{-2}} \qquad \Omega_2^{-2} = \sum_\mathrm{i} \frac{\mathrm{n}_{0,\mathrm{i}}}{\gamma_{0,\mathrm{i}}^3\,\Omega_\mathrm{i}^{-2}} \tag{4.6}$$

$$\Omega_3^{-2} = \sum_\mathrm{i} \frac{\mathrm{n}_{0,\mathrm{i}}\mathrm{v}_{0,\mathrm{i}}}{\gamma_{0,\mathrm{i}}\,\Omega_\mathrm{i}^{-2}} \qquad \Omega_4^{-2} = \sum_\mathrm{i} \frac{\mathrm{n}_{0,\mathrm{i}}\mathrm{v}_{0,\mathrm{i}}^2}{\gamma_{0,\mathrm{i}}\,\Omega_\mathrm{i}^{-2}}, \tag{4.7}$$

where the summation over (e, p) species has already been performed. Therein $\mathrm{i} = 1, 2$ indicate quantities of the respective shells, i.e. reduced frequency $\Omega_\mathrm{i} = \omega - \mathrm{k}_\mathrm{z}\mathrm{v}_{0,\mathrm{i}}$ and relativistic energy $\gamma_{0,\mathrm{i}} = (1 - \mathrm{v}_{0,\mathrm{i}}^2)^{-1/2}$. Equation (5) is the dispersion relation of the coupled 2D CTW mode, its lower dimensional constituents are retained in the limits $\mathrm{k}_{\mathrm{x,z}} \to 0$. In a formal way the dispersion relation is constituted by the Two-Stream (TSI) and Weibel (WBI) contributions which are connected via a coupling term (CT):

$$\mathrm{CTW} = \mathrm{TSI} \cdot \mathrm{CT} + \mathrm{WBI} \tag{4.8}$$

Figure 4.7 compares the essential information on the linear theory for the weakly relativistic $\gamma_0^1 = 1.17$ (grey) to the moderate and ultra-relativistic regime $\gamma_0^{10\,(100)} = 10.05$ (100.005) (dotted (solid)). The WBI mechanism relies on the fact that comoving particles of like charge in one shell as well as the respective pendant of opposite charge in the counterstreaming shell represent like currents mutually attracting each other. Incipient charge-neutral current filaments evolve, each sustaining a toroidal magnetic field that self-pinches its generating current and, hence, close the instability feedback loop. Self-pinching in colliding (e,p)-shells is limited only by the transverse oscillations of the particles in the Weibel magnetic fields (meandering motion as directly illustrated with an ensemble of trace particles in Fig. 4.12b). The central idea of 'dimensional effects' is based on the energy dependence of the 2D CTW mode in the highly relativistic regime (i.e. $\gamma_0 \geq 5$), which is understood as the superposition of its 1D constituents. In Fig. 4.7a the growth rates Γ_{WBI} of the purely transverse 1D WBI are shown. In the cold-beam limit the WBI has finite growth rate at all wavelengths of interest for the weakly-to-ultra relativistic regimes. At high relativistic energies Γ_{WBI} scales like $\propto \gamma_0^{-1/2}$ as function of collision energy.

Relativistic damping is much more severe for the 1D TSI mode as the purely longitudinal constituent. It evolves from Langmuir fluctuations driven by the relative motion of the shells. $\Gamma_{\mathrm{TSI}} \propto \gamma_0^{-3/2}$ directly images the behaviour of the maximum of the TSI growth rate as shown in Fig. 4.7b as well as the cut-off shift towards longer wavelengths. Γ_{TSI} drops by about a factor of $\sim 100^{\frac{3}{2}}$ from $\sim 0.63 \to\sim 7.1 \cdot 10^{-4}$ during the transition from $\gamma_0^1 \to \gamma_0^{100}$. Consequently, mode damping due to relativistic mass gain is much more severe for the direction parallel rather than perpendicular to the shells' bulk motion. The relativistic energy dependence is retained straightforwardly, if the momentum variations $\delta \mathrm{p}_\perp = \gamma_0 \delta \mathrm{v}_\perp$ (WBI) and $\delta \mathrm{p}_\| = \gamma_0^3 \delta \mathrm{v}_\|$ (TSI) in the respective directions are considered. Variations in the fields act via the Lorentz force (1) on the momentum variations, which then transfer to velocity variations according to the relativistic bulk motion as preferential, non-degenerate direction. Variations in velocity introduce variations in density/currents by continuity (4) closing the feedback loop to the fields (2,3). Besides the coupling term, the TSI and WBI contributions to the CTW are biquadratic, and hence, $\Gamma_{\mathrm{WBI}} \propto \gamma_0^{-1/2}$ and $\Gamma_{\mathrm{TSI}} \propto \gamma_0^{-3/2}$ are motivated.

The behaviour of the 2D CTW mode results from the superposition of its 1D components. Maximum growth of TSI and WBI are comparable in the non- and weakly relativistic regimes (Fig. 4.7a,b). Both modes show significant differences in energy scaling. As a consequence thereof, the relative weights of the respective contributions and total coupling strength in the 2D CTW exhibit a strong dependence on relativistic energy. The relative weight of each contribution is reflected in the propagation angle, which migrates to quasi-transversal for $\gamma_0 \to 100$ (Fig. 4.7c). The cut-off is retained from the TSI and is always present in the 2D mode (Fig. 4.7d). The cut-off in the $(\mathrm{k_x}, \mathrm{k_z})$-plane is sharp, while the growth rate is practically flat within the unstable region at $\Gamma_{\mathrm{CTW}}^{100}/\omega_{\mathrm{p0}} = 0.14$ and $\Gamma_{\mathrm{CTW}}^{10}/\omega_{\mathrm{p0}} = 0.51$ for $\gamma_0 = 100$ and 10, respectively. The dashed lines in Fig. 4.7d indicate the $(\mathrm{k_x}, \mathrm{k_z})$-space that is covered by the finite grid resolution/box extension in the PIC simulation as imposed by the computational limitations. The coupling strength weakens significantly, since Γ of the WBI becomes comparable to the CTW mode for $\gamma_0 \to 100$, and hence, decoupling sets on earlier in this limit.

In all modes, the source of free energy is the bulk kinetic energy of the shells. The propagation angle of the fastest growing 2D mode turns abruptly into quasi-perpendicular

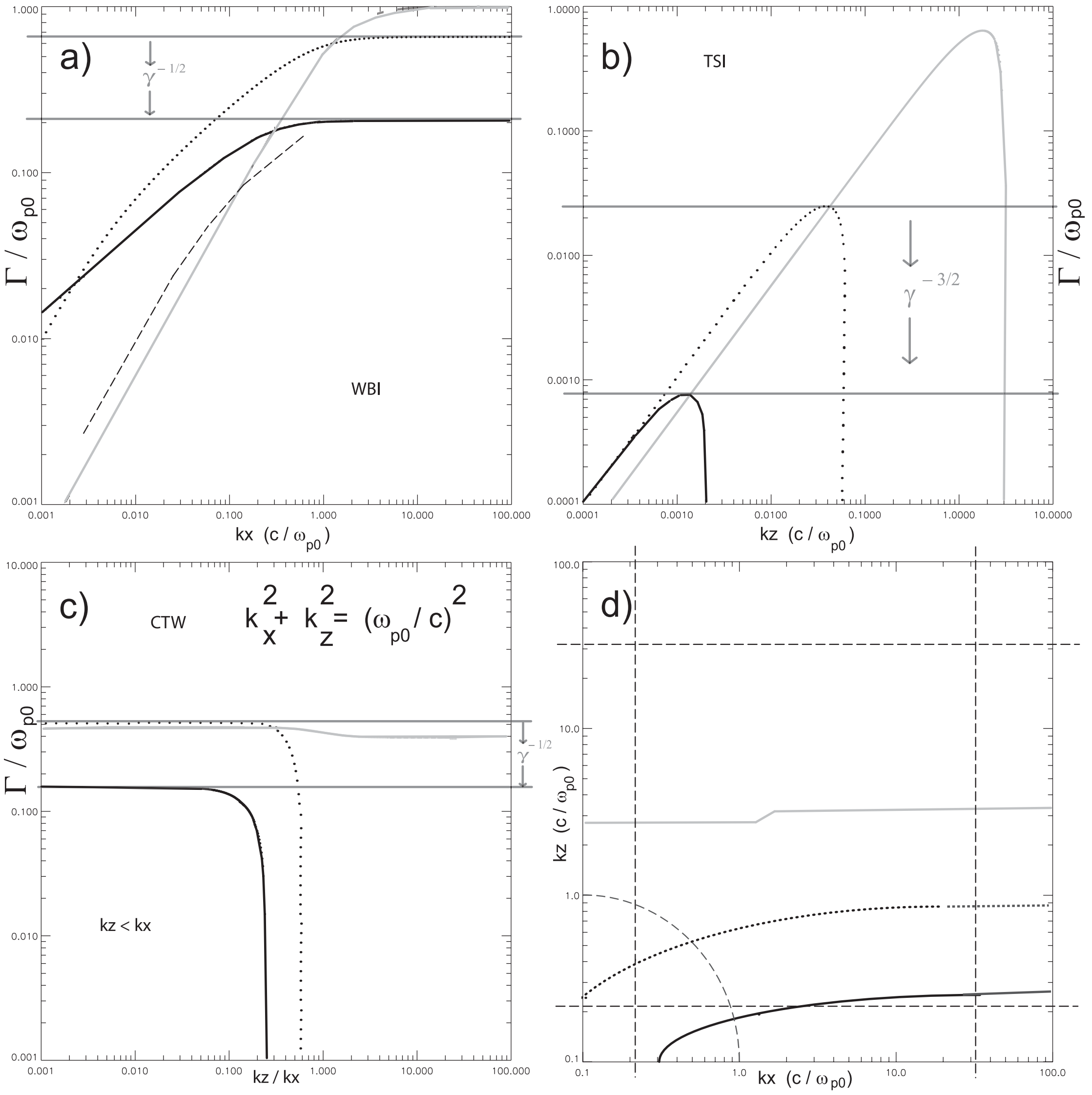

Fig. 4.7: Linear growth rates (a) $\Gamma(k_x)$ of the 1D WBI, (b) $\Gamma(k_z)$ of the 1D TSI , and (c) $\Gamma(k_z/k_x)$ of the 2D CTW mode (the latter taken on the dashed circle of constant k as indicated in panel (d)) for different collision energies $\gamma_0^{1,10,100}$ (grey, dotted, solid). For comparison, in (a) the Yang et al. (1993) growth rate for the 'double waterbag distribution' is given (dashed). From (a-c) it is obvious that in the ultra-relativistic regime the WBI contributions to the 2D CTW dominate over the respective TSI contributions. Consequently, the 2D CTW appears to propagate almost perpendicular $k_z/k_x \ll 1$. $\Gamma(k_z/k_x)$ is about constant at unstable angles and exhibits sharp angular cut-offs. (d) Cut-off wave vectors $k_{max}^{1,10,100}$ for the CTW in (k_x, k_z)-space. Dashed straight lines give the Fourier limits imposed by the grid resolution/box extension indicating that the unstable regions are well resolved numerically in all energy regimes.

direction, reflecting the dominance of the WBI over the TSI in the coupled mode. Conclusively, for relativistic collision energies beyond $\gamma_0 \sim 30$ the physics of an initially 3D shell configuration ultimately takes place within 2D plane-parallel shell slices (which in particular is valid in the linear regime), i.e. the transition to the ultra-relativistic regime implies an effective reduction in dimensionality. The validity and implications of this statement are investigated in section 4.2.5 in PIC simulations of the highly non-linear late-time evolution of the system.

Effects of a Finite Thermal Spread: Kinetic Modifications

The Weibel instability is an inherently kinetic instability [Weibel, 1959; Yoon & Davidson, 1989] with the temperature anisotropy $\Delta_\mathrm{T} = \mathrm{T}_{\|}/\mathrm{T}_{\perp} - 1$ as the driving source of free energy. Each counterstreaming plasma shell represents an intense plasma beam. A plasma beam of finite thermal spread is the limiting case of strong T-anisotropy. In the relativistic regime temperatures $\mathrm{T}_{\|}$ parallel and $\mathrm{T}_{\perp}$ perpendicular to the bulk motion $\mathrm{v}_0\,\mathbf{e}_\mathrm{z}$ are coupled via the relativistic $\gamma_0 = (1 - \mathrm{v}_0^2)^{-1/2}$ in the energy-momentum tensor $\mathrm{T}^{\sigma\sigma}$ [Groot, Leeuwen, & Weert, 1980]. The spatial components in covariant form $\mathrm{T}^\mathrm{mn}/\mathrm{mc}^2 = \int \mathrm{d}^3\mathrm{p}\,\mathrm{u}^\mathrm{m}\mathrm{v}^\mathrm{n}\mathrm{f}(\mathbf{p})$ $(\mathrm{m}, \mathrm{n} = 1, 2, 3)$ constitute the temperature tensor in the most general formulation as the second moment of the normalized distribution function $\mathrm{f}(\mathbf{p})$. Assuming that the anomalous resistivity is negligible during the linear regime and accounting for a symmetric degeneracy in the perpendicular direction, T^mn reduces to the diagonal elements

$$\mathrm{T}_{\perp}/\mathrm{mc}^2 = \frac{1}{2}\int \mathrm{d}^3\mathrm{p}\,\mathrm{u}_{\perp}\mathrm{v}_{\perp}\mathrm{f}(\mathrm{p}_{\perp}, \mathrm{p}_{\|}) \tag{4.9}$$

and

$$\mathrm{T}_{\|}/\mathrm{mc}^2 = \int \mathrm{d}^3\mathrm{p}\,\mathrm{u}_{\|}\mathrm{v}_{\|}\mathrm{f}(\mathrm{p}_{\perp}, \mathrm{p}_{\|}). \tag{4.10}$$

Consequently, for given perpendicular thermal spread $\mathrm{v}_{\mathrm{th},\perp}$ the relativistic collision energy γ_0 decides about the significance of thermal effects. Two questions arise in the present study: (i) Which thermal effects are predicted by linear kinetic theory and in which parameter regime of the critical quantities $\gamma_0, \Delta_\mathrm{T}$ will such effects become important? (ii) What consequences result for the argumentation given in section 4.2.4?

The purely transverse relativistic Weibel instability has been studied kinetically in the context of ‘waterbag’ models [Yoon & Davidson, 1987a;b; Yang et al., 1993b; Yang, Arons & Langdon, 1993a; Silva et al., 2002]. The property of such models is to approximate the finite thermal spread by a step-functioned particle distribution

$$\mathrm{F}(\mathbf{p}, \mathbf{p}_\mathrm{th}) = \theta(\mathbf{p}_\mathrm{th}^2 - \mathbf{p}^2) \tag{4.11}$$

in order to simplify the linear kinetic analysis. [We note that in the 1D studies by Yoon & Davidson [1987a;b]; Yang et al. [1993b]; Yang, Arons & Langdon [1993a] the Weibel instability defines the direction of parallel propagation.] Since the Weibel mode propagates transverse to the bulk motion, the definitions of parallel and perpendicular are exactly interchanged compared to the ones used in this article and by Medvedev & Loeb [1999] and Silva et al. [2002; 2003]. Yoon & Davidson [1987b] and Silva et al. [2003] considered a single waterbag distribution to investigate the effect of a finite $\mathrm{T}_\perp$, i.e. a finite thermal spread in the direction of Weibel propagation. By assuming a ring distribution in the plane of momentum space normal with respect to the waterbag Yoon & Davidson [1987b] introduced a large initial anisotropy. Within this plane the absolute momenta are sharply δ-confined and zero bulk momentum is ensured by the circular symmetry. Linear stability analysis then shows that in the relativistic regime kinetic effects produce an upper cut-off for the unstable wavenumbers, i.e. short scale Weibel fields are inhibited and the Weibel instability can develop only on sufficiently large spatial scales retaining the $\Gamma_{\mathrm{WBI}} \propto \gamma_0^{-1/2}$ behaviour.

However, the constraints on spatial scales and growth rate depend critically on the T-anisotropy Δ_{T}. For Δ_{T} sufficiently large, every criterion for an upshift in the wave number cut-off is met. For instance, an initial $\Delta_{\mathrm{T}} \geq 10$ guarantees mode growth within the constraints of our simulation box even for γ_0^{100}. Silva et al. [2002] substituted a particle beam for the ring in momentum space. As in Yoon & Davidson [1987b] the instability is carried by electrons within an immobile charge-neutralizing background. Silva et al. [2002] further introduce an ensemble of background electrons imposing some constraints on the relative beam strength $\chi = \mathrm{n}_0/\mathrm{n}_{\mathrm{bgd}}$. In the ultra-relativistic regime this scenario is close to the configuration of counterstreaming shells. The essentials of the analysis by Silva et al. [2002] are the threshold conditions for Weibel growth in χ and $\mathrm{T}_\perp$. Since the initial beam spread $\sigma_{\mathrm{sp}} \lesssim 10^{-8}$ and the Two-Stream limit $\chi \sim 1$ are valid, the threshold condition $\chi \geq \gamma_0 \mathrm{v}_{\mathrm{th}}^2/\mathrm{v}_0^2 = \sigma_{\mathrm{sp}}$ is fulfilled in all our simulations with no restriction.

Severe damping of Weibel growth in the strong beam limit is observed for $\mathrm{T}_\perp \geq 50\,\mathrm{keV}$. Such limiting constraints on Weibel growth are important for the fast ignitor scenarios in which the beam is usually density-rarefied, and in plasma-shell collisions in which the thermal spread amounts to at least $\sim 1\,\%$ of the bulk momentum. Moreover, Yang et al. [1993b] extend the sharp plasma beam to a second waterbag distribution $\mathrm{G}(\mathrm{p}_\|) = \theta(\mathrm{p}_0^2 - \mathrm{p}_\|^2)$ with $\mathrm{p}_0/\mathrm{mc} = (\gamma_0^2 - 1)^{1/2}$ in order to investigate the effects of a parallel close-to-thermal velocity spread. The analysis contains the effect of a magnetic field parallel to the direction of Weibel propagation. However, some central insights are retained in the limit of negligible magnetic field strength. In the regime of dominant $\mathrm{T}_\|$ (which is always the case in shell collisions with dominant bulk motion) the stability properties are determined by the relative weight of the $\mathrm{T}_\perp$-contributions, i.e. by Δ_{T}. In the limit $\mathrm{T}_\perp \to 0, \Delta_{\mathrm{T}} \to \infty$ [see dashed line in Figure 2a of Yang et al., 1993b] the WBI mode is purely growing over a broad range of wave numbers. The quantitative growth rate is consistent with Γ_{WBI} computed for a cold plasma beam (see Fig. 4.7a dashed line for comparison). Consequently, for an extreme Δ_{T} the ‘waterbag’- and ‘beam’-models become indistinguishable. As observed by Silva et al. [2002] for the beam distribution, the extension to finite $\mathrm{T}_\perp$ causes an upper cut-off in the wave number region of Weibel growth for the model distribution as well used by Yang et al. [1993b]. The cut-off scales like

$$\mathrm{k_{cut}}(\mathrm{c}/\omega_{\mathrm{p0}}) = (2\pi/3\gamma_0)^{\frac{1}{2}}\Delta_{\mathrm{T}}, \tag{4.12}$$

which implies that for sufficiently high Δ_{T} the growth of Weibel modes extends into the range of short wavelengths. To be more precise, the above threshold value was derived by Yang et al. [1993b] using a Nyquist analysis of a so-called 'smooth' distribution function which had been designed to model a power-law distribution at high energies. Differences between 'smooth' and 'waterbag' distributions become insignificant at large Δ_{T}.

Thus the critical quantities ruling the importance of kinetic effects in relativistic plasma-shell collisions are the collision energy γ_0 and the temperature anisotropy Δ_{T}. Figures 4.8a-c show the time evolution of $\mathrm{T}_\perp, \mathrm{T}_\parallel$ and Δ_{T} as computed in the fully self-consistent PIC simulations. The initial $\mathrm{T}_\parallel$ is given by the relativistic collision energy γ_0. For the cold initial perpendicular temperatures at hand the Maxwellian velocity spread as shown in Tab. 4.1 per definitionem corresponds to $\mathrm{T}_\perp/\mathrm{mc}^2 = \mathrm{v}_{\mathrm{th},\perp}^{\mathrm{cms}\ 2}$. Such conditions are well modelled by the 'waterbag' distribution in equation (4.11), for which one obtains

$$\mathrm{T}_\parallel/\mathrm{mc}^2 = \gamma \mathrm{v}_0^2 \xi(\mathrm{v}_{\mathrm{th},\perp}^{\mathrm{cms}}) \tag{4.13}$$

and

$$\mathrm{T}_\perp/\mathrm{mc}^2 = \frac{1}{2}\gamma(1 - \xi(\mathrm{v}_{\mathrm{th},\perp}^{\mathrm{cms}}) + \mathrm{v}_{\mathrm{th},\perp}^{\mathrm{cms}\ 2}\xi(\mathrm{v}_{\mathrm{th},\perp}^{\mathrm{cms}})), \tag{4.14}$$

with $\xi(\mathrm{x}) = \frac{1}{2}\mathrm{x}\ \ln[(1+\mathrm{x})/(1-\mathrm{x})]$. In the limit of small thermal spread $\mathrm{v}_{\mathrm{th},\perp}^{\mathrm{cms}} \ll 1$ and $\xi(\mathrm{x}) \simeq 1 + \mathrm{x}^2/3 + ...$ one obtains

$$\hat{\mathrm{T}}_\parallel/\mathrm{mc}^2 = \gamma_0, \qquad \hat{\mathrm{T}}_\perp/\mathrm{mc}^2 = \frac{1}{3}\gamma_0 \mathrm{v}_{\mathrm{th},\perp}^{\mathrm{cms}\ 2} \tag{4.15}$$

For the simulations 1,3,4 the values $\hat{\mathrm{T}}_\perp/\mathrm{mc}^2 = 6.8 \cdot 10^{-8}$ are close to the Maxwellian $\mathrm{T}_\perp/\mathrm{mc}^2 = 2.0 \cdot 10^{-7}$. Comparison with the time evolution of the equipartition ratios in Fig. 4.8d shows that at the respective collision energies γ_0^{10},γ_0^{100} throughout the linear instability regime the perpendicular temperatures are in the sub-keV domain, and the corresponding anisotropy ranges well above $\Delta_{\mathrm{T}} \geq 10^4$. Consequently, the transversal cut-offs caused by finite $\mathrm{T}_\perp$ are expected to occur at $\mathrm{k_{x/y,cut}}(\mathrm{c}/\omega_{\mathrm{p0}}) \sim 10^4$. Such values are far beyond the smallest spatial scales of interest in the astrophysical context, since anyway in the non-linear regime the instability migrates towards larger scales.

We note that the estimates of the kinetic contributions are based on 1D linear analysis. However, the idea is to point out in which parameter regime modifications due to kinetic effects could be expected, of what kind these modifications are, and by which critical quantities they are controlled. The values of $\mathrm{T}_\parallel$ and Δ_{T} obtained from the PIC data indicated that the assumption of negligible thermal spread for the linear analysis in section 4.2.4 is well justified in our simulations.

To provide additional evidence that the above estimates can be transferred to the 2D CTW case, additional simulations are performed with energies γ_0^{10} and γ_0^{100} (Tab. 4.1). At γ_0^{10} simulation 1 and 2 differ by a factor of ~ 500 in the initial $\mathrm{T}_\perp$ and Δ_{T}. Since the limit $\Delta_{\mathrm{T}} \rightarrow \infty$ applies to both runs, the time evolution in Figs. 4.8a-c and Fig. 4.9a is comparable. Furthermore, the difference in initial $\mathrm{T}_\perp$ and Δ_{T} is negligible even beyond

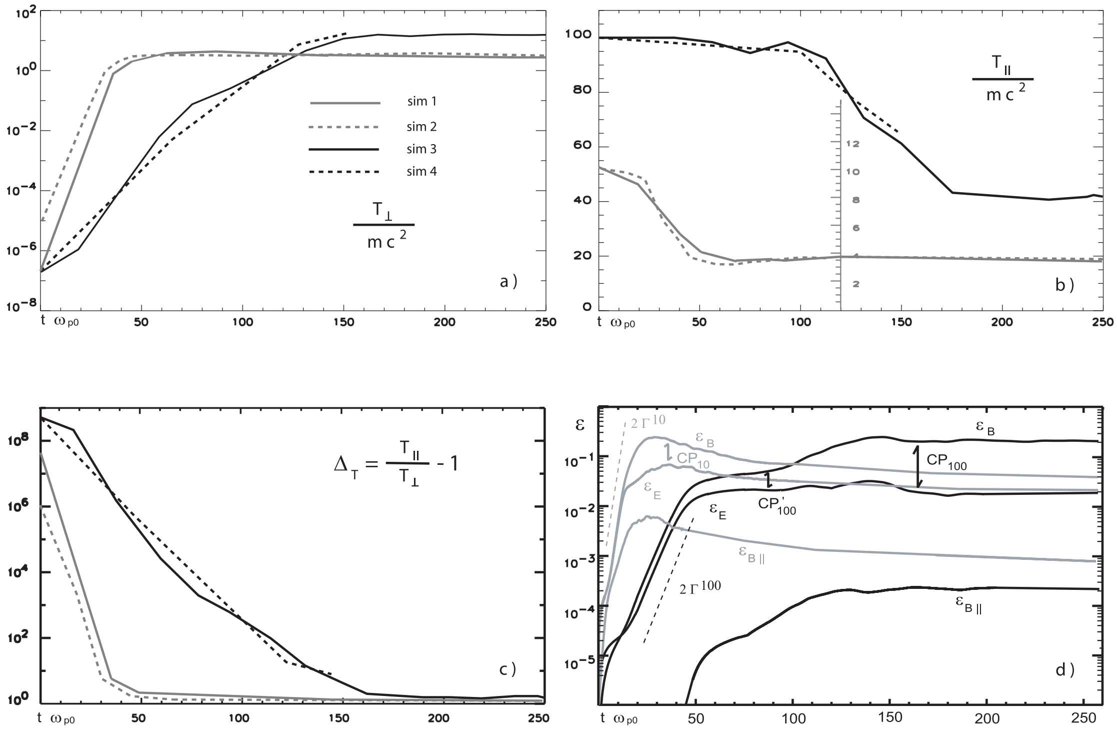

Fig. 4.8: Time evolution of perpendicular temperature $T_\perp$ (a) for γ_0^{10} (grey) and γ_0^{100} (black). During linear mode growth (cf. panel (d)), $T_\perp < 1\,\mathrm{keV}$. Thus, for all simulations (see simulation 2, dotted grey) variations in $T_\perp$ are insignificant and the cold beam limit applies. The final state is as well independent on the initial thermal spread for the cold initialization at hand. Panel (b) shows the time evolution of $T_\parallel$ (line coding as in (a); note the expanded scale for the run with γ_0^{10}!). In the linear regime $T_\parallel$ is dominated by the bulk motion, therefore 'waterbag' and 'beam' distributions yield comparable results. At late times significant beam energy is deposited in Weibel electromagnetic fields and particle heating. The resulting temperature anisotropies of $\Delta_T \geq 10^4$ (c) for the respective runs during the linear regime clearly indicate that thermal mode damping or restrictions to the range of unstable wavenumbers are negligible. Remarkably, a finite residual anisotropy $\Delta_T \sim$ 2-3 remains. The time evolution of equipartition ratios is given in (d) for $\gamma_0^{10(100)}$ (grey(black)) with linear growth up to $t_1\omega_{p0} = 13(42)$, saturation at $t_2\omega_{p0} = 27(145)$, and final steady state at $t_3\omega_{p0} > 130(190)$. The coupling strength in the 2D CTW mode weakens from γ_0^{10} toward γ_0^{100}, i.e. $CP_{10} > CP_{100}$. The contributions of $B_\parallel$ are persistently negligible. In general, longitudinal modifications to the total field configuration - attributed to the TSI - are prominent only at γ_0^{10}.

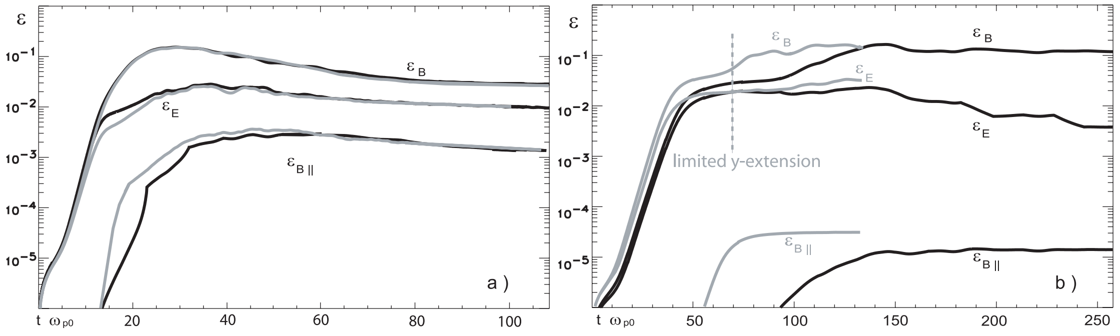

Fig. 4.9: Comparison of the equipartition ratios (a) for simulations 1 and 2 (grey), which differ solely in initial $T_\perp$. Results are comparable in all essential quantities. In the linear regime the growth rates are obtained as expected from the linear analysis in the cold beam limit. Saturated field values scale like $\propto 1/(1 - v_{th,\perp}^{cms})$ [Silva et al., 2003] and, hence, thermal effects are insignificant also during non-linear saturation. In (b) ϵ evolutions are shown for simulations 3 and 4. Within the linear regime results are again comparable, clearly indicating that dimensional effects are not modified by the finite size of the computational domain. Then the final steady-state is reached earlier in simulation 4 (grey) in coincidence with the transversal growth of the current self-pinches reaching the reduced y-extension of the system.

the linear regime up to the phases of non-linear saturation and the final steady-state. In the γ_0^{100} (simulations 3 and 4) cases transverse and longitudinal extensions of the simulation box have been varied in order to investigate any possible effects of the finite size of the computational domain on linear mode growth. This has been done for the higher energy, because limitations in the range of unstable wave numbers are then expected to be more severe keeping in mind the results of the linear kinetic analysis discussed above. Figures 4.8a-c and 4.9b as well as the analysis of the late-time non-linear evolution in section 4.2.5 demonstrate that no such restrictions apply to our simulations.

Even more convincing that thermal effects play no role in the present study is the comparison of the analytic growth rates with the growth rate determined from the PIC results in the linear regime. Linear growth rates (section 4.2.4) for the 2D coupled CTW mode of $\Gamma_{CTW}^{100}/\omega_{p0} = 0.51$ and $\Gamma_{CTW}^{10}/\omega_{p0} = 0.14$ are obtained for the respective energies within the constraints of the zero temperature limit. From the simulated time evolution of the equipartition ratios ϵ plotted in Fig. 4.8d these growth rates are well reproduced (ϵ contains the squared field quantities).

In conclusion, in the present study the cold plasma limit holds for all the simulations. $T_\perp$ remains in the sub-keV range for the entire linear regime. Significant thermal modifications, i.e. mode damping and narrowing of the bandwidth of unstable wave numbers, is expected for less pronounced Δ_T only, which is the case if $T_\perp$ reaches at least %-partitions of the collision bulk momentum. In contrast to fast ignitor conditions, X-ray observations of early afterglows indicate rather moderate thermal cut-offs around

$\sim 5\,\mathrm{keV}$. So the initial scenario of cold plasma shells appears sensible. However, kinetic effects might become important for colliding shells of extremely unbalanced density ratios, i.e. for afterglow scenarios with a strong beam passing a rarefied interstellar cavity. Such scenarios are possible subjects for future studies.

4.2.5 The Saturated and Steady-State Final Magnetic Fields

The maximum possible equipartition ratio ϵ_{B} generated by the Weibel instability as the microphysical source process is an essential input quantity for global GRB synchrotron models. In the previous sections the analysis was restricted to the linear regime that is the first of three consecutive stages in the evolution of the instability. During the linear phase ($\mathrm{t} = \mathrm{t}_1$ in Figs. 4.10, 4.11) incipient current filaments evolve and a magnetic field structure of complex topology ensues from the superposition of toroidal magnetic fields. Magnetic field topologies are complex though not completely random. It is possible to identify self-similar structures which allow for a certain degree of regularization as is discussed in detail in section 4.4. The linear regime is followed by the intermediate stage of non-linear saturation of the Weibel-generated magnetic fields in the maximum self-pinched state of current filamentation ($\mathrm{t} = \mathrm{t}_2$ in Figs. 4.10, 4.11). As soon as the pair plasma self-pinching is counterbalanced by the progressive thermal pressure within each current filament, the system enters the final third phase ($\mathrm{t} = \mathrm{t}_3$) of the proposed time scheme. Therein self-pinches coalesce and form a steady-state configuration after all immediately neighboured filaments of aligned currents have merged. On astrophysical (=synchrotron loss) time scales this last stage is the only one that is relevant, since the system passes through the former two phases within less than $\sim 100\,\omega_{\mathrm{p0}}^{-1}$, i.e. on astrophysical measures in an instant. The Weibel mechanism is an inherently kinetic process and the highly non-linear saturation is the pervasive state in the astrophysical context. Consequently, kinetic simulations are the method of choice to obtain reliable values for the steady-state ϵ_{B} rates.

Figure 4.8d shows the time evolution of the transverse

$$\epsilon_{\mathrm{B}\perp} = \mathrm{V}^{-1}\int \mathrm{dV}(\mathrm{B}_{\mathrm{x}}^2 + \mathrm{B}_{\mathrm{y}}^2)/8\pi\mu_{\mathrm{kin}} \tag{4.16}$$

and longitudinal

$$\epsilon_{\mathrm{B}\|} = \mathrm{V}^{-1}\int \mathrm{dVB}_{\mathrm{z}}^2/8\pi\mu_{\mathrm{kin}} \tag{4.17}$$

magnetic WBI-fields. Since $\epsilon_{\mathrm{B}\|}$ ratios (i.e. 3D magnetic topologies) are negligible, transverse magnetic fields are pervasive and $\epsilon_{\mathrm{B}\perp} \simeq \epsilon_{\mathrm{B}}$ follows. With respect to electric fields, $\mathrm{E}_{\|} = \mathrm{E}_{\mathrm{z}}$ and $\mathrm{E}_{\perp}$ contribute about equal shares to the corresponding equipartition ratio

$$\epsilon_{\mathrm{E}} = \mathrm{V}^{-1}\int \mathrm{dV}(\mathrm{E}_{\|}^2 + \mathrm{E}_{\perp}^2)/8\pi\mu_{\mathrm{kin}}. \tag{4.18}$$

Here $\mu_{\mathrm{kin}} = 4(\gamma_0 - 1)\mathrm{n}_0\mathrm{mc}^2$ is the initial kinetic energy density of the system applying the convention to define the reference density n_0 on the base of one specie of each individual shell. During the linear regime the time evolutions of ϵ_{B} and ϵ_{E} proceed in

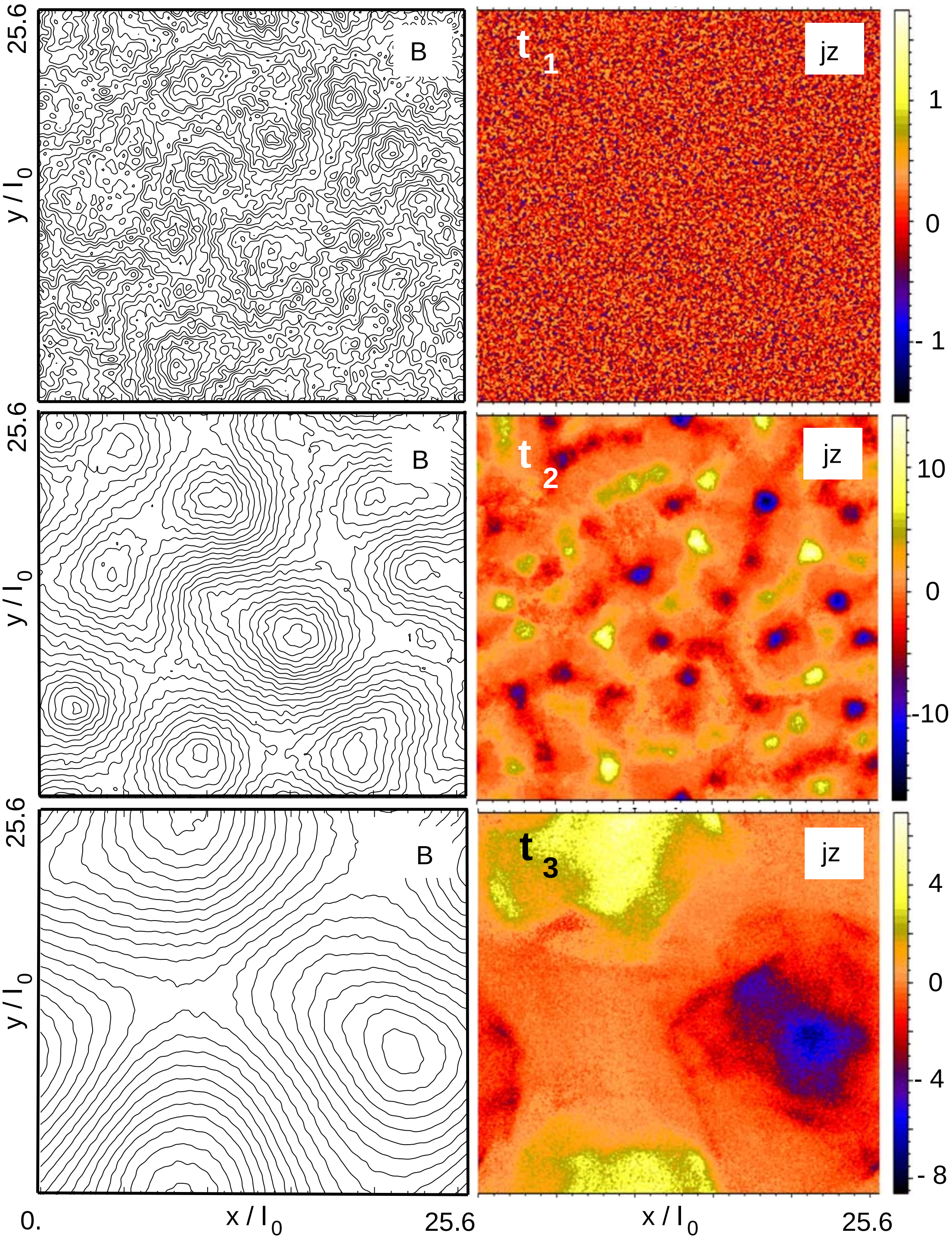

Fig. 4.10: Magnetic field lines and j_z current filaments during the linear phase ($t = t_1$), in the maximum self-pinched state ($t = t_2$) and the final coalesced configuration ($t = t_3$) in the (x, y)-plane through the simulation box center. Current filaments generate the magnetic field, which further pinches the filaments thereby enhancing itself (instability feedback loop). Coalescence ceases as soon as only oppositely aligned currents neighbour each other.

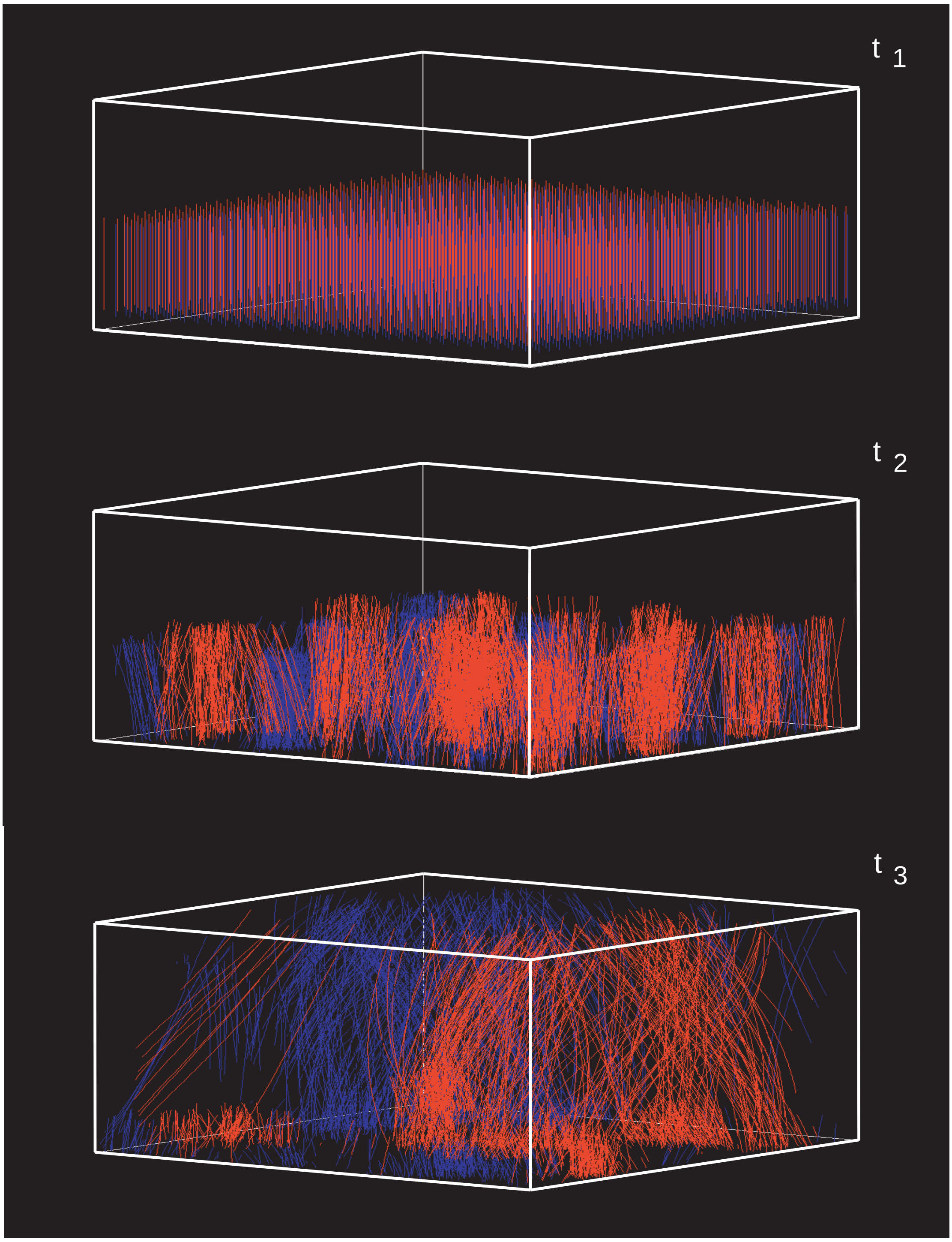

Fig. 4.11: Initially homogeneously distributed ($t = t_1$) trace electrons (red) and positrons (blue) appendant to the in $+z$ moving shell, which then self-pinch due to the WBI ($t = t_2$). The formed current filaments finally coalesce ($t = t_3$) until only oppositely aligned currents are neighboured. Self-consistent particle trajectories are a feature which is found uniquely in the PIC method.

close proximity. Consequently the coupling of 1D TSI/WBI constituents in the combined 2D CTW mode is strong. The corresponding growth rates scale $\propto \gamma_0^{-1/2}$ and are quantitatively in very good agreement with the linear theory as has been confirmed in section 4.2.4. As soon as the evolving filaments reach the maximum self-pinched state the system runs into non-linear saturation. In this phase the mode coupling weakens and the energy-dependent relative strengths of the 1D constituents is reflected in the different electric and magnetic saturated equipartition ratios. Figure 4.12a illustrates the closest-packed current self-pinches at the saturation point for γ_0^{10}. For the weakly relativistic cases, the current response on the self-pinching by the toroidal magnetic field is channeled into a velocity response $\delta\mathbf{j} \sim \mathrm{n}_0 \delta\mathbf{v}$. Beyond $\gamma_0 \sim 5$ this transforms into a density response $\delta\mathbf{j} \sim \delta \mathrm{n}\mathbf{c}$, i.e. the density fluctuations increase towards higher collision energies, reaching up to $12\,\mathrm{n}_0$ for γ_0^{100}. Each self-pinch consists of a void in the magnetic field enclosed by toroidal field walls. Particles initially moving in ±z perform a meandering motion within each pinch, being reflected by the fields with inverted directions at opposite walls as seen in Fig. 4.12c (for better visibility particle trajectories are shown here for a later phase). The saturated field values scale like $\mathrm{B_{sat}} \propto (\mathrm{n}\gamma_0)^{1/2}/(1-\mathrm{v_{th}})$ with saturation taking place when the meandering frequency $\omega_\mathrm{m} \propto \mathrm{B}\gamma_0^{-1}$ equals the CTW growth rate $\Gamma_\mathrm{CTW} \propto (\mathrm{n}/\gamma_0)^{1/2}$. Obviously thermal corrections to the saturated field $\mathrm{B_{sat}} \propto (1-\mathrm{v_{th}^{cms}})$ [Silva et al., 2003] become insignificant for sufficiently cold plasma shells.

Silva et al. [2003] set the initial thermal spread to $\mathrm{v_{th,\perp}^{cms}} = 0.01$ for γ_0^{10}. The saturated field values obtained by them are in agreement with the respective values obtained in simulations 1 and 2 confirming that the cold beam approximation holds for all these simulations and thermal corrections are negligible. Differences in the equipartition ratios are the sole result of energy-dependent 'dimensional effects' on which we focus in the present study. In contrast to the linear regime where thermal corrections become more restrictive for higher collision energy (cf. section 4.2.4), the behaviour of the CTW is modified during non-linear saturation. In this phase thermal corrections are introduced via the velocity response, but since in the ultra-relativistic limit the density response $\delta\mathrm{n}$ dominates during pinching, thermal corrections become increasingly less important.

In the simulations 1 and 3 (Fig. 4.8)d, the saturated $\epsilon_\mathrm{B}^\mathrm{sat}$-values are equal for both cases γ_0^{10} and γ^{100}. What differs are the coupling strength and the relative weight of the contributions from the TSI ($=\epsilon_{\mathrm{E}\|}$) and WBI ($=\epsilon_{\mathrm{B}\perp}$) mode in the non-linear regime at late times: In the final phase the current self-pinches coalesce. The magnetic fields around each self-pinched filament are practically at equipartition. The 'filling factor' of the volume with self-pinches decides upon the final steady-state ϵ_B. The TSI imposes a complex 3D structure on the current filaments for γ_0^{10} (Fig. 4.12b), thereby reducing the 'filling factor'. Field energy is re-converted into disordered particle kinetic energy causing particle heating. In Fig. 4.8d, $\epsilon^{10}_{\mathrm{B}\perp\,(\mathrm{E}\|)}$ drops by one magnitude from the saturated to the final state.

In contrast, for γ_0^{100} 3D modifications of the final current/field configuration by the TSI are marginal only (Fig. 4.12d), whereas WBI contributions dominate. The reconversion process of energy is practically absent and $\epsilon_{\mathrm{B}\perp}^\mathrm{sat} \sim \epsilon_{\mathrm{B}\perp}^\mathrm{final}$. The reconversion of (latent) field

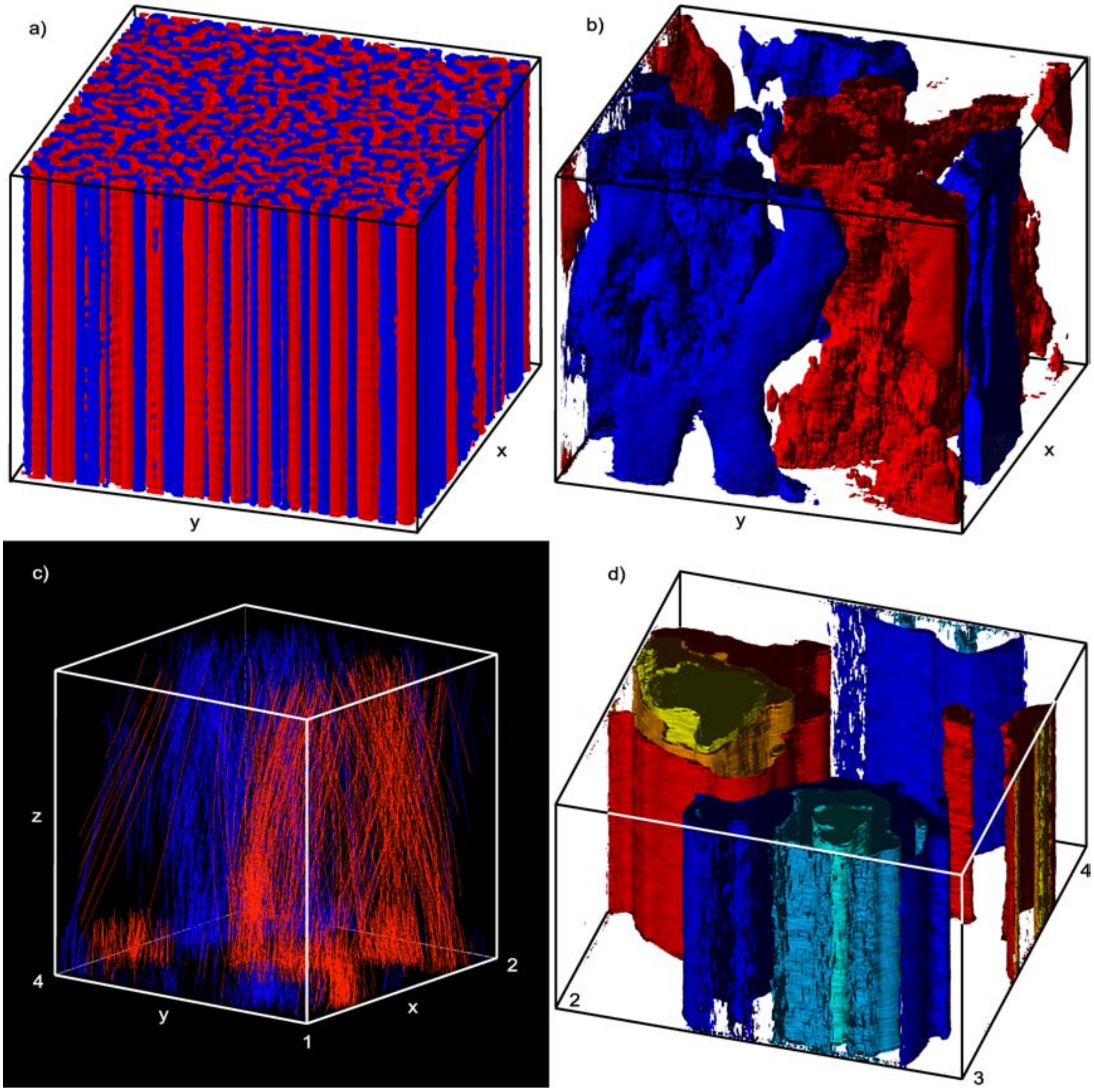

Fig. 4.12: Iso-contours of the current density in the saturated self-pinched state at $t\omega_{\mathrm{p0}} = 27$ ($j_z = \pm 0.75$) (a) and the final coalesced state $t\omega_{\mathrm{p0}} = 250$ ($j_z = \pm 1.5$) (b) for γ_0^{10}, +z-directed currents in blue. Individual traces of 2048 selected positrons (blue) and electrons appendant to the in +z-moving shell are shown in (c) for γ_0^{100} at $t\omega_{\mathrm{p0}} = 250$. Particles perform a meandering motion in the magnetic void of each current filament. Directly corresponding are the respective current iso-contours for $j_z = 4.5, 2.5, 1.5$ (yellow, orange, red) and $j_z = -4.5, -2.5, -1.5$ (turquoise, blue, dark blue) in (d). Relativistic dimensional reduction from 3D to 2D is obvious in the comparison of (b) and (d).

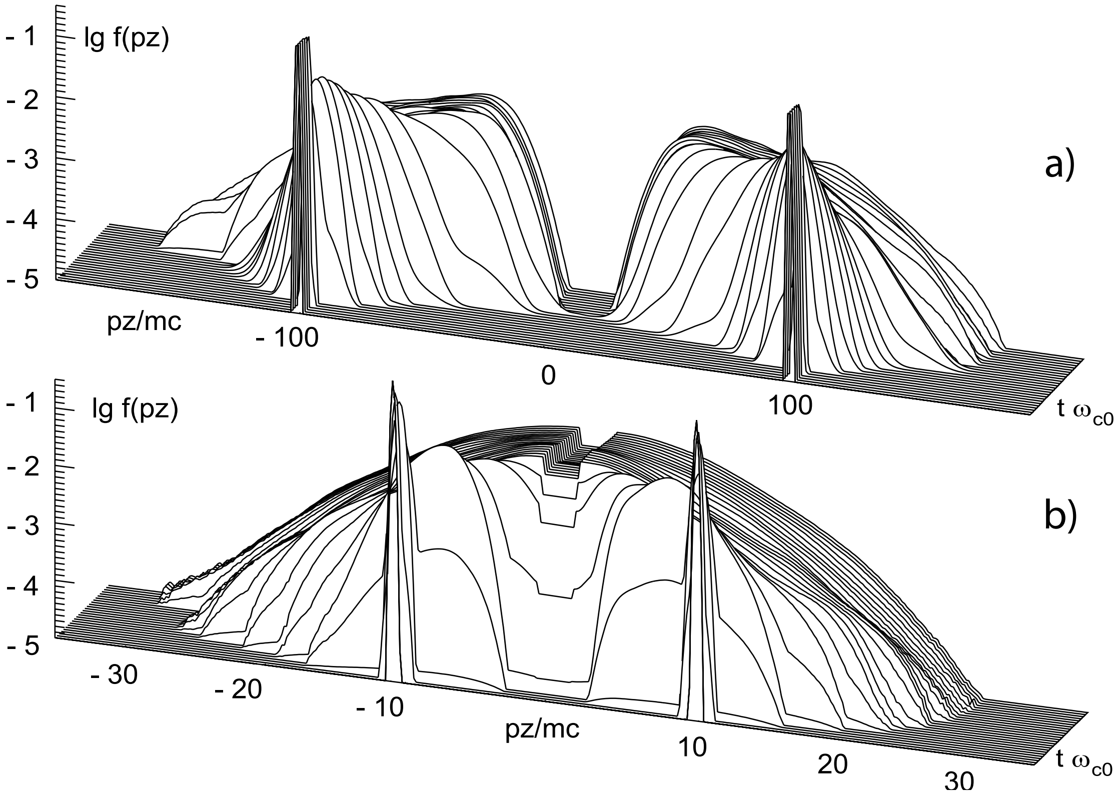

Fig. 4.13: Time evolution of the normalized particle distributions $\mathrm{f(p_z)}$ as function of the $\mathrm{p_z}$ momentum for γ_0^{100} (a) and γ_0^{10} (b). Parallel electric fields $\mathrm{E}_\parallel$ attributable to the electrostatic TSI contributions are more pronounced for lower energies. Consequently particle acceleration is more prominent in (b) for γ_0^{10}, where $\mathrm{p_z/mc} \sim \gamma$ reaches up to 3.5 times the initial bulk momentum/relativistic energy γ_0.

into (thermal) particle energy during the transition from non-linear saturation to final coalesced steady-state is directly observable in the particle distribution functions shown in Fig. 4.13. The comparative electrostatic energy excess for γ_0^{10} at decoupling time ($\epsilon_{\mathrm{E}\parallel}^{10} \sim 10\,\epsilon_{\mathrm{E}\parallel}^{100}$) is reconverted into particle kinetic energy as seen from Fig. 4.13b. Particles are accelerated in this case by the TSI up to 3.5 times the initial collision energy. For γ_0^{100} particle heating/TSI are both suppressed, in return WBI contributions/particle cooling are more pronounced (Fig. 4.13a). In conclusion, dimensional reduction in the ultra-relativistic regime comes along with an optimized conversion of particle free energy into magnetic field energy, i.e. with optimized magnetic equipartition ratios.

A critical final question is whether the observed ‘dimensional effects’ are modified by the finite size of the computational domain. In view of this effect we varied the geometry of the simulation box between simulation 3 and 4, extending the parallel and one perpendicular dimension by a factor of 4 (Tab. 4.1). For the regimes of linear growth

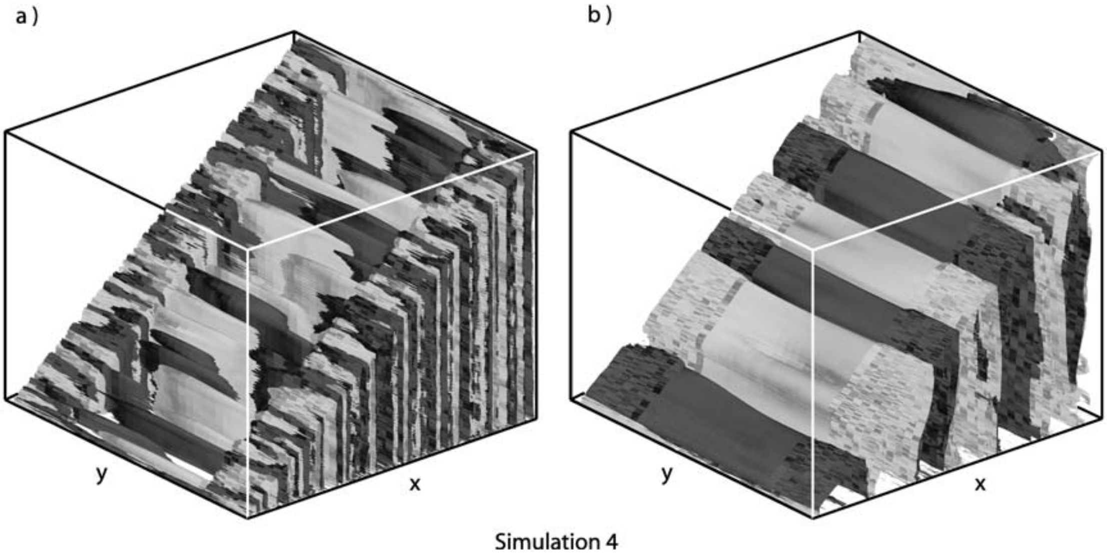

Fig. 4.14: Iso-contours of the current ($j > 0$ black) in the phase of non-linear saturation (a) at $t\,\omega_{p0} = 48$ and after extending beyond the y-extension (b) of the system at $t\,\omega_{p0} = 100$, which in simulation 4 is reduced to $L_y = 3.2\,(c/\omega_{p0})$. In (b) the configuration is reduced to quasi-2D, artificially stretched ad infinitum in y. Consequences on the field structure are comparable to the coalescence of current self-pinches at late times. Therefore the time evolution is shifted and the final steady-state equipartitions are comparable, but precipitate relative to simulation 3 as shown in Fig. 4.9b.

and non-linear saturation both simulations yield exactly the same results: According to Fig. 4.9b linear growth rates Γ_{CTW}, the relations between $\epsilon_B, \epsilon_{B\|}, \epsilon_E$ (i.e. the relative weight of TSI and WBI contributions to the 2D coupled mode), and the times when non-linear saturation is reached (i.e. coupling strengths) are exactly in accord. Furthermore, direct correspondence is seen in the time evolution of temperatures and anisotropies (Fig. 4.8a-c). The saturated and final steady-state equipartition ratios are comparable, though the final configuration is reached earlier in simulation 4. Due to computational limitations the extension of the (x, z)-plane in simulation 4 enforces a respective reduction in y down to $L_y = 3.2\,(c/\omega_{p0})$. In the linear regime the coupled CTW mode is 2D and the y-extension is insignificant. Hence, the correspondence of results between simulations 3 and 4 proves that the 'dimensional effects' under study have not been affected by the limitations of the computational domain. The simulations are comparable as long as the cross sections of the toroidal current self-pinches fit into the (x, y) plane (Fig. 4.14a) of the simulation. Coalescence of self-pinches to the final steady-state in simulation 4 precipitates the respective phase in simulation 3 as soon as the self-pinch diameter becomes comparable to L_y and the system is confined to be quasi-2D within the (x, z)-plane (Fig. 4.14b). The equipartition ratios are determined by the 'filling factor' of the volume by current filaments. The equipartition ratios of simulations 3 and 4 are quantitatively comparable (Figs. 4.8d, and 4.9b), and so are the shapes of the current filaments in z as seen in Figs. 4.12d, and 4.14b. Disruption of filaments in z as taking place for γ_0^{10} (Fig. 4.12b) are absent independent of the finite extension of the simulation box. The comparison of simulations 3 and 4 serves in the first place the proof that in the present simulations the contributions of the longitudinal TSI are not suppressed by the finite box extension in z. Such a result is intuitive, since the argumentation in section 4.2.4 is based on relativistic damping of growth rates (=time scales, not wave number cut-offs). Furthermore, system variations in the transverse extension are uncritical, since the cross sections of the coalesced current filaments in the final steady-state configuration are primarily determined by $T_\perp$. Since the temperatures/anisotropies Δ_T (Fig. 4.8c) in all simulations saturate before spatial restrictions come into play, the final equipartition ratios obtained are independent of the finite box extensions.

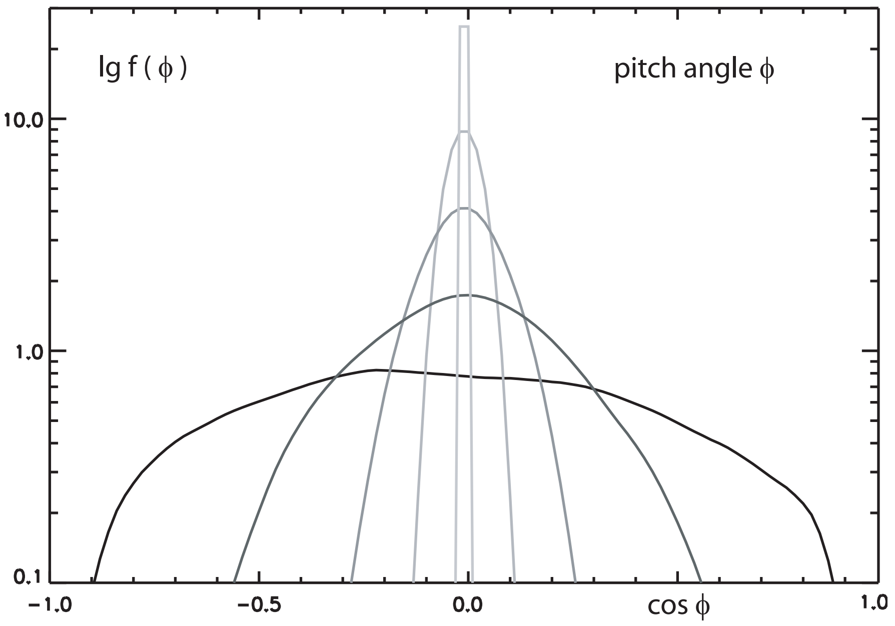

Fig. 4.15: Isotropization of synchrotron pitch angles for simulation 3 as time cascade $t\omega_{p0} = 5, 75, 94, 112, 245$ (darkening from bright grey to black). Apparently isotropization is pervasive in the non-linear regime and taking place most efficiently after equipartitions are at maximum (i.e. for γ_0^{100} after $t\omega_{p0} \sim 100$). Within the total simulated time, i.e. on a time scale negligible with respect to typical synchrotron loss times, practically complete isotropy is reached.

According to Fig. 4.8c some finite $\Delta_T \sim 2 - 3$ remains in the final steady-state configuration [Yang et al., 1993b; Yang, Arons & Langdon, 1993a]. This residual anisotropy is slightly higher in the ultra-relativistic regime. This fact sustains the essential statement of 'dimensional effects', in which WBI contributions / filamentation become gradually pronounced at higher relativistic energies. The current filaments have a preferential direction, modifications in z-structure are reduced and, as a consequence, residual anisotropies remain.

In view of the emission of synchrotron radiation an interesting question is the time evolution of the pitch angles $\cos\phi = \mathbf{B} \cdot \mathbf{p}/\mathrm{Bp}$ of the particles involved. Figure 4.15 shows that pitch angle isotropization takes place most efficiently in the regime after non-linear saturation during the final coalescence of self-pinches. Due to inertial effects on the particles the pitch angles isotropize later for higher than for lower energies γ_0. However, even for the external high collision energies between the shells the pitch angle isotropization takes place and is complete on time scales which are short compared with typical synchrotron loss times.

4.2.6 Summary and Perspectives

We have presented self-consistent, fully electromagnetic 3D PIC simulations of electron-positron-plasma shell collisions at moderate to ultra-relativistic collision energies $\gamma_0^{10\,(100)}$ with total particle ensembles of $\sim 5 \cdot 10^8$. For the first time the generation of magnetic fields by the Weibel instability has been investigated for external collision energies of $\gamma_0 \sim 100$. As a peculiarity of this energy regime we find that 3D modifications by the TSI mode become progressively insignificant. As a consequence the conversion of particle kinetic energy into magnetic fields by the Weibel mechanism takes place with optimized efficiency in quasi-2D shell slices. We provided evidence that such 'dimensional effects' are introduced in the ultra-relativistic regime by damping of TSI contributions to the 2D Coupled Two-Stream-Weibel mode and are not influenced by variations of the computational domain. We provided arguments from linear theory for this transition which turn out to hold in the highly non-linear late-time evolution covered by the PIC simulations. From the reduction of dimensionality, final steady-state equipartition ratios of $\epsilon_\mathrm{B} \sim 12.5\%$ result for external collision energies, exceeding the respective values achieved in internal collisions by a factor of five. The linear analysis was performed within the constraints of the cold beam limit (zero temperature approximation). This assumption is valid as long as the thermal spread of plasma shells is less then 1% of the bulk collision energy. In this respect the scenario under study is fundamentally different from fast ignitor scenarios. We have demonstrated that 'dimensional effects' are introduced as new physical behaviour in the ultra-relativistic regime. For the cold initial temperatures at hand, such a behavior is not affected by kinetic effects as far as the linear kinetic analysis is concerned. The phenomenon of dimensional reduction was not included in previous studies of the highly non-linear late-time evolution, which are either lower dimensional or different in the energy regime.

We note that for the external collision of GRB fireball ejecta with the surrounding medium contributions from electron-proton plasma [Nishikawa et al., 2003] are as well involved. As had been noted by Silva et al. [2003], the fundamental instability process/ϵ_B-values will remain unchanged in this case, merely the time and length scales are upscaled by the proton-to-electron mass ratio $(\mathrm{m_p}/\mathrm{m})^{1/2} \sim 43$. The critical question is, however, the lifetime of the final steady-state magnetic fields in this case, since typical synchrotron loss times range in the order of 10^5 times the total simulated time. The dominant process responsible for the decay of the magnetic fields in this case is collisionless diffusion. Typical decay rates and diffusion coefficients obtained from self-consistent PIC simulations will be presented elsewhere [Jaroschek, Lesch & Treumann, 2004c].

4.3 Topology and Lifetime - A Critical Test for Synchrotron Emission Models

The following section is published as

'Self-Consistent Diffusive Lifetimes of Weibel Magnetic Fields in Gamma-Ray Bursts'

C.H. Jaroschek, H. Lesch, and R.A. Treumann
The Astrophysical Journal, 1 Dec 2004, 616, 1065

4.3.1 Abstract

Weibel filamentation in relativistic plasma shell collisions has been demonstrated as an efficient and fast mechanism for the generation of near-equipartition magnetic fields in self-consistent Particle-In-Cell (PIC) simulations. In generic γ-ray burst (GRB) models with kinetically dominated plasma outflow sufficient strength and lifetime of magnetic fields is essential to validate synchrotron emission as the source of radiative outbursts. In this article we report on self-consistent PIC simulations of pair-plasma shell collisions in the highly relativistic regime with particle ensembles up to $5 \cdot 10^8$. Energy dependence of magnetic field generation in the Weibel process is discussed and for the first time the diffusion-limited lifetime of magnetic fields is investigated self-consistently. In three different ways of analysis the diffusion coefficient is determined self-consistently from the microphysical particle data. Cross-field diffusion is identified as 'Bohm'-type by direct confirmation of the characteristic T/B-behaviour. With the stability-limiting process pinned down, the lifetime of Weibel magnetic fields in plasma shell collisions subsumes to $\tau\, \omega_{\rm p0} \sim 10^9$ (with $\omega_{\rm p0}$ the plasma inertial time scale as characteristic of any system). In the context of typical synchrotron cooling times we conclude that the Weibel fields are sufficiently long-lived for GRB prompt emission as well as afterglows, especially in view of the likely 'baryonic' pollution of pair-plasma shells.

4.3.2 Introduction

The generation and stability of magnetic fields in γ-ray bursts (GRBs) remains a central problem of all theoretical concepts to explain the enormous radiation deposition in such phenomena. In principle two plasma physical mechanisms qualify to generate magnetic fields of sufficient strength for synchrotron emission models to work: Magnetic field amplification via shock compression [Kazimura et al., 1998] and Weibel filamentation [Medvedev & Loeb, 1999] in plasma shell collisions. Both processes rely on the interaction of counterstreaming plasmas.

Conceptual GRB emission models (for an extensive review on GRBs see Piran [1999]; Mészáros [2002]) propose a central source ejecting plasma shells at variable bulk speeds and intermittencies. Differences in bulk speed cause individual plasma shells to collide at some distance from the central object. In close similarity to the so-called corotating interaction regions (CIR) in the solar wind, high Mach number shock fronts are triggered at the face of the interaction regions. However, albeit shock compression provides magnetic field strengths close to equipartition, Gruzinov [2001] presented arguments that the shock-amplified fields decay rapidly in the zone downstream of the shock front. Direct numerical simulations indicate short magnetic field lifetimes on the order of a few tens of plasma dynamic scales ω_{p}^{-1}, whereas generic synchrotron emission scenarios take place on longer time scales, ranging from 10^5-$10^{10}\,\omega_{\mathrm{p}}^{-1}$.

The alternative approach of Weibel-induced magnetic fields refers to the counterstreaming motion of deeply interpenetrating plasma shells: Shock compression is spatially confined within the narrow zone of the shock front propagating as the wake of plasma interaction into the colliding shells. Counterstreaming develops downstream as a consequence of the progressive interchange of the shells' bulk momentum and downstream advection of electromagnetic fields and, hence, characterizes merely the late evolution of shock scenarios [Frederiksen et al., 2004]. We note that for typical source environments the plasma is strongly rarefied in density. Consequently, the term 'collision' refers to particle scattering effective in the collective potentials of plasma instabilities [Sagdeev, 1966] rather than to Coulomb interaction between nearest neighbours.

The Weibel mechanism [Weibel, 1959] relies on the free energy stored in a particle distribution which is anisotropic in velocity space. Counterstreaming plasma shells represent an extreme case of velocity anisotropy. Each moving charge represents a current. Parallel currents are mutually attractive. Small initial perturbations cause likewise currents to merge and form small incipient current filaments. Therefore the Weibel instability is also called filamentation instability. We present a scenario of counterstreaming pair-plasma shells with equal density and equal absolute bulk momentum. As a consequence thereof the configuration is initially charge and current neutral in the center of mass frame (i.e. simulation/lab frame). Current filaments consist of equal charges moving parallel in one shell and respectively opposite charges moving anti-parallel as constituents of the counterstreaming shell. Filaments remain quasi-neutral and sustain a toroidal magnetic field. The toroidal field self-pinches its generating current, thereby amplifying the current and closing the instability feedback loop. Separation of self-pinches is determined by the fastest growing Weibel mode. The toroidal magnetic fields of individual filaments superpose to complex field structures predominantly oriented transverse to the respective currents. Particles perform a meandering motion in the toroidal field confinement. The instability saturates as soon as the bounce frequency associated with the meandering becomes comparable to the instability growth [Silva et al., 2003]. Self-consistent Particle-In-Cell (PIC) simulations of the Weibel instability in electron-positron $(\mathrm{e}^-, \mathrm{e}^+)$ shell collisions [Silva et al., 2003] proved its capacity to generate near-equipartition magnetic fields. Since sufficient strength of the newly generated fields is granted, the critical question to be answered concerns the stability of the Weibel magnetic fields.

In this article we investigate the finite lifetime of Weibel-generated magnetic fields in relativistic plasma shell collisions. The highly non-linear late-time evolution of plasma instabilities is the condition prevalent on astrophysical time scales, and direct numerical simulation is one possible approach to explore this regime. The PIC method allows to simulate the Weibel instability on the plasma kinetic level and to trace the individual trajectories of particles self-consistently involved in the generation of the fields. These are essential differences with respect to test particle approaches. Since the process is manifestly collisionless, the destruction of the magnetic fields can only take place by scattering of the current-carrying particles in the field inhomogeneities and by intrinsic instabilities. This should lead to diffusive losses of particles from the current filaments and thus to destruction of the current-field configuration. In order to determine the importance and time scales of this kind of diffusion, we harness the data of individual particle orbits to analyze the mechanism of magnetic cross-field diffusion. We further note that contributions to cross-field decay can also arise from flute instabilities of the Kelvin-Helmholtz-, sausage-, kink-, or pinch-type. Such instabilities modify the current-field configuration on length scales which require global scenarios and thus are beyond the feasability of self-consistent kinetic simulations. We focus here on the microphysics to investigate the fundamental mechanism of cross-field transport and the time scales involved.

It is essential to simulate 3D configurations due to two constraints: First, up to moderately relativistic collision energies $\gamma_0 \sim 10$ assumed in internal shell collision scenarios the current filaments exhibit an intrinsic 3D structure [Silva et al., 2003]. 3D elements arise from the energy-dependent coupling between the Weibel mode (effective perpendicular to the collision-aligned direction) and the parallel two-stream instability mode. For external shell-collision energies with Lorentz factors inferred from GRB light curves around $\gamma_0 \sim 100$ [Panaitescu & Kumar, 2002], the coupling strength between both instability modes softens. The Weibel contributions prevail instead, and the current filament/magnetic field structure becomes quasi-2D [Jaroschek, Lesch & Treumann, 2005]. However, the particle trajectories maintain a distinctively complex 3D pattern. Second, even in entirely 2D magnetic field configurations it is a fundamental insight that perpendicular transport requires a 3D configuration [Jokipii, Kóta & Giacalone, 1993].

Details upon the PIC simulation setup are described in section 4.3.3. In the consecutive section we show that the lifetime of the final steady-state magnetic fields generated in the Weibel process is limited by magnetic cross-field diffusion. Meticulous analysis of individual self-consistent particle trajectories allows (i) the concise determination of the diffusion coefficient and (ii) the identification of the diffusion mechanism as of 'Bohm'-type and, hence, qualifying it as the conservative upper limit of particle transport. The diffusion coefficient obtained in the self-consistent PIC simulation renders feasable magnetic field lifetimes of $\sim 10^9\,\omega_{\mathrm{p}}^{-1}$ in ultra-relativistic plasma shell collisions. This credences the validity of Weibel-generated magnetic fields in the context of conceptual GRB synchrotron emission models.

4.3.3 Simulation Description

The PIC simulations serving as foundation for the present study are similar to the ones described in Jaroschek, Lesch & Treumann [2005]. For completeness we summarize the simulation setup: The simulations are performed with a massively parallelized, relativistic, fully electromagnetic PIC code on a high resolution mesh with $256 \times 256 \times 128$ grid points representing a 3D system of extension $\mathrm{L_x} \times \mathrm{L_y} \times \mathrm{L_z} = 25.6 \times 25.6 \times 12.8\,(\mathrm{c}/\omega_{\mathrm{p0}})^3$.

The total number of particles subsumes to $5 \cdot 10^8$, homogeneously distributed in configuration space and divided in phase space into two equal subensembles initially moving in ±z with $\mathrm{v}_{z0,1} = -\mathrm{v}_{z0,2}$. Each subensemble represents a quasi-neutral $(\mathrm{e}^+, \mathrm{e}^-)$ shell of

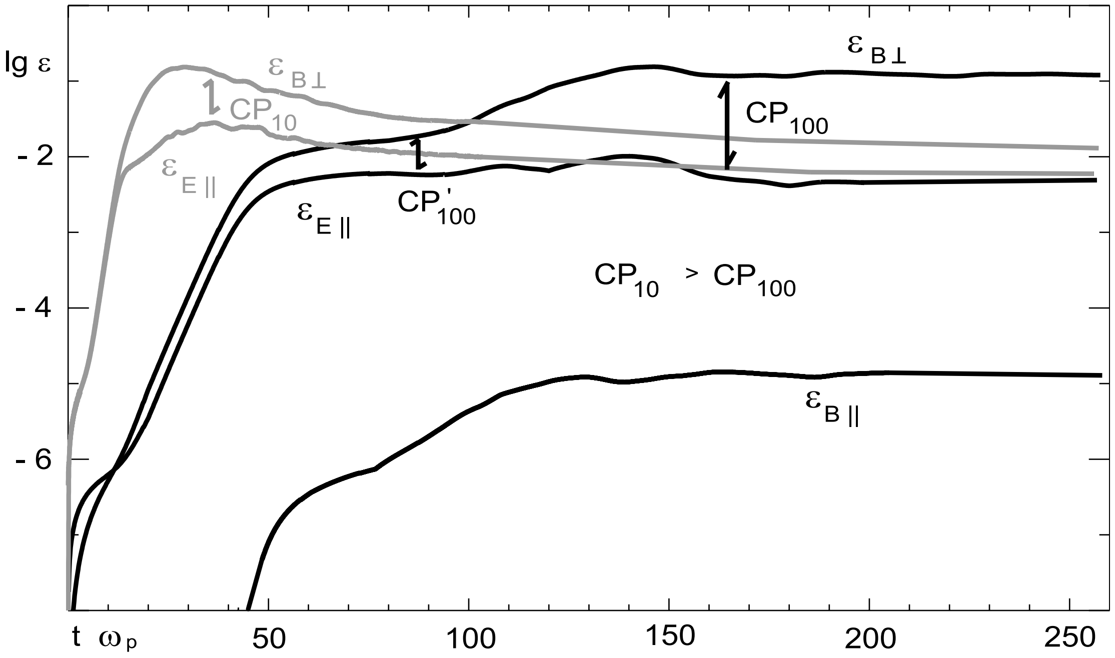

Fig. 4.16: Time evolution of equipartition ratios for $\gamma_0^{10(100)}$ (grey(black)) with linear growth until decoupling at $\mathrm{t}_1\omega_{\mathrm{p0}} = 13(42)$, saturation at $\mathrm{t}_2\omega_{\mathrm{p0}} = 27(140)$, and final steady-state for $\mathrm{t}_2\omega_{\mathrm{p0}} > 130(190)$. The coupling strength in the 2D TSI-WBI mode weakens from γ_0^{10} to γ_0^{100}, i.e $\mathrm{CP}_{10} > \mathrm{CP}_{100}$. Longitudinal $\mathrm{B}_{\|}$ contributions are always negligible. As final equipartition ratios result $\epsilon_{\mathrm{B}}^{10} \sim 2.5\,\%$ and $\epsilon_{\mathrm{B}}^{10} \sim 12\,\%$.

density $\mathrm{n}_0^+ = \mathrm{n}_0^- = \mathrm{n}_0$. Times are normalized to the inverse plasma frequency $\omega_{\mathrm{p0}}^{-1} = (4\pi \mathrm{e}^2\ \mathrm{n}_0/\mathrm{m})^{-1/2}$, lengths to the skin depth $(\mathrm{c}/\omega_{\mathrm{p0}})$ and, as a consequence thereof, velocities to the speed of light c. n_0 is the initial density of one specie within a particular shell, e and m are electron charge and mass, respectively. Initial bulk motions correspond to $\gamma_0^{10}\mathrm{v}_{z0} = 10.00$ and $\gamma_0^{100}\mathrm{v}_{z,0} = 100.00$. The transverse thermal spread in the shells' comoving frame is $\mathrm{v}_{\mathrm{th},0} = 10^{-4}$, corresponding to $\mathrm{v}_{\mathrm{th},0}^{10} = 10^{-5}$ and $\mathrm{v}_{\mathrm{th},0}^{100} = 10^{-6}$ in lab (=grid mesh) frame. Simulations endured for $\Delta \mathrm{t}\omega_{\mathrm{p0}} = 260$, requiring 5500 timesteps for γ_0^{10} and 45000 timesteps for γ_0^{100} to assure energy stabilities of 0.1 % and 1 %, respectively.

The efficiency of magnetic field generation in the Weibel process is quantified in the

equipartition ratio $\epsilon_\mathrm{B} = \mathrm{V}^{-1} \int \mathrm{dV}\,(\mathrm{B}^2/8\pi)/\mu_\mathrm{kin}$, i.e. the energy density on average converted into magnetic field B from an initial particle kinetic reservoir $\mu_\mathrm{kin} = 4(\gamma_0 - 1)\mathrm{n}_0$ mc^2. Figure 4.16 shows the time evolution of $\epsilon_\mathrm{B}^{10,100}$ for moderate γ_{10} and ultra-relativistic γ_0^{100} collision energy. $\epsilon_\mathrm{B}^{10}(\mathrm{t})$ is precisely consistent with results of Silva et al. [2003] and corresponds to the regime of internal (prompt emission) GRB shell collisions. $\epsilon_\mathrm{B}^{100}(\mathrm{t})$ first probes the regime of external (afterglow) collisions. In general the plasma instability is a coupled mode propagating at skewed angle with a Two-Stream (TSI) and Weibel (WBI) constituent, each effective exactly parallel and perpendicular to the bulk motion, respectively.
As reported in detail in Jaroschek, Lesch & Treumann [2005], WBI contributions responsible for the conversion of particle-kinetic into magnetic-field energy progressively dominate the TSI contributions for higher collision energies, the latter associated with parallel electric fields and plasma heating. As a direct consequence, the final steady-state magnetic field strength is higher in the ultra-relativistic limit (cf. Fig. 4.16). In plasma-physical terms, the propagation angle of the coupled TSI-WBI-mode becomes quasi-perpendicular, while the current filament/magnetic structure becomes quasi-2D (Fig. 4.17). We note in passing that the coupled TSI-WBI-mode in any energy regime remains a real 3D problem at late times, when filaments of like currents tend to merge and require the third dimension to circumnavigate their respective counter-currents, the latter are essential to ensure the system's time-invariant overall current neutrality [Lee & Lampe, 1973].

4.3.4 Diffusion Limited Lifetime of Magnetic Fields

Diffusion Coefficients Obtained by the PIC Simulation

In the final steady-state configuration only oppositely aligned current filaments neighbour each other being confined within the voids of their self-generated toroidal magnetic fields (Fig. 4.17) and forming something like a quasi-stable lattice. Consequently, the magnetic field gradient / particle density exhibit minima in the magnetic walls separating the current filaments. This differs fundamentally from the situation of Harris-type cross-field diffusion scenarios [Jaroschek, Lesch, & Treumann, 2004a]. In the following we concentrate on the case $\gamma_0 = 100$ because magnetic field topology then is essentially quasi-2D, and discuss 3D modifications for less energetic collisions in the end. Stability / lifetime limits of this configuration are imposed by cross-field diffusion between the Weibel current filaments. Perpendicular transport requires some perturbation along the particle's gyro orbit to break its 'force-free' appendence to a specific field line. Since Coulomb collisions are absent, 'anomalous' transport is retained by particles scattering off collective electromagnetic fluctuations. Electrostatic 'convective cells' in thermalized plasma were identified as the origin of collisionless perpendicular diffusion within the framework of a guiding center $\mathbf{E} \times \mathbf{B}/\mathrm{B}^2$ drift (zero frequency) limit by Taylor & McNamara [1971] and were then generalized to cover a broad spectral range of fluctuations by Dawson, Okuda & Carlile [1971]. In the Weibel scenario, the dominant contributions to cross-field transport are expected to arise from density/magnetic field gradients. Self-

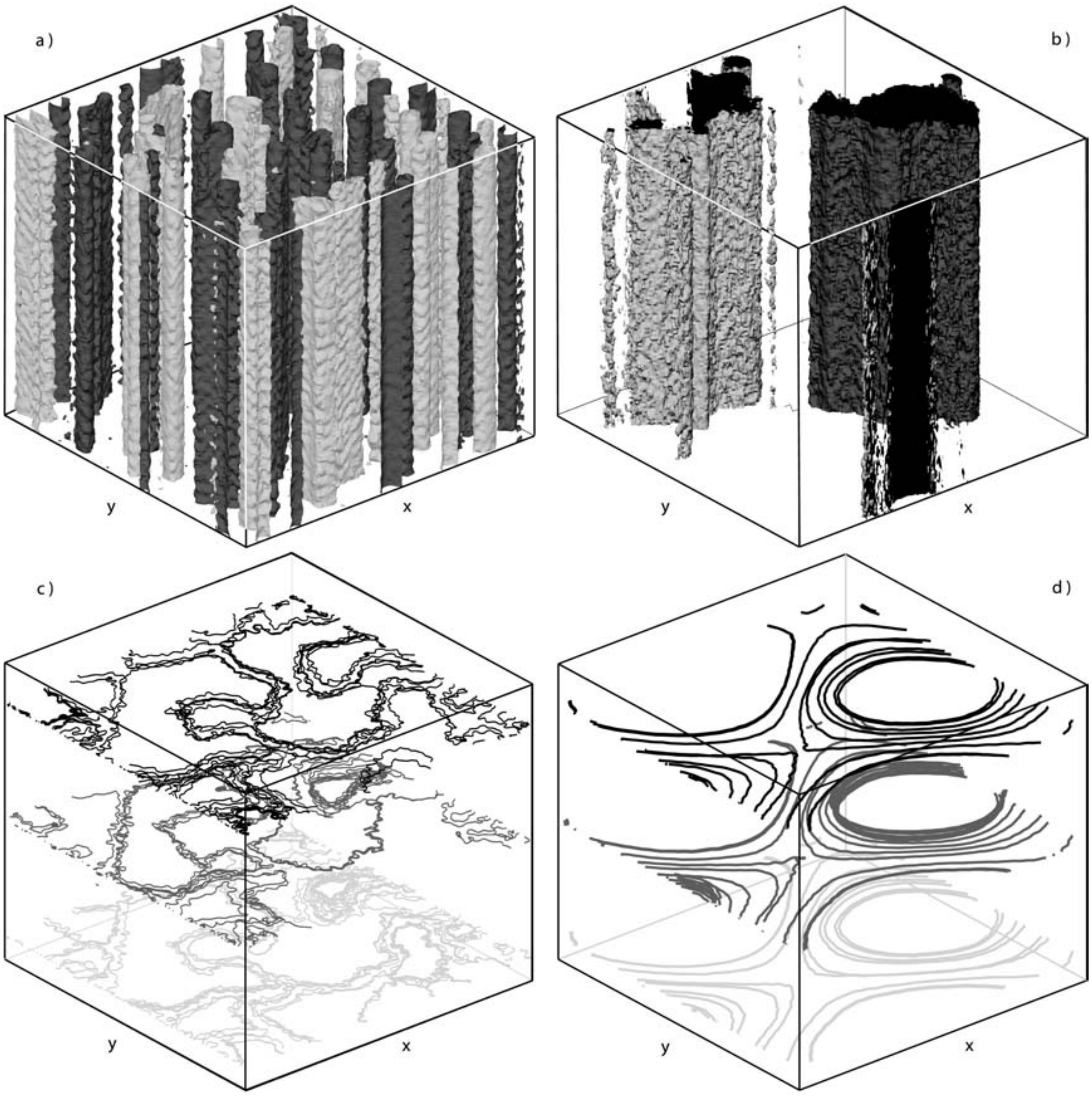

Fig. 4.17: Isocontours of the current density for γ_0^{100} in the maximum self-pinched state at $t\omega_{p0} = 140$ (a). Coalescence of self-pinches ceases as soon as only oppositely aligned currents ($j_z > 0$ dark, $j_z < 0$ bright) neighbour each other and the final steady-state configuration is reached for $t\omega_{p0}^{-1} > 190$ (b). The corresponding magnetic field configurations are visualized in c) and d), respectively. Spatial agglomeration of the field lines reflects the magnetic energy distribution. Filaments are confined within the self-generated quasi-2D toroidal magnetic fields (for clarity only shown in three staggered planes). Around each filament magnetic fields are close to equipartition. The typical correlation scale of the current-field configuration evolves exponentially in time from large to small wavenumbers k (cf. Fig. 4.19).

consistent PIC simulations allow for the determination of a net diffusion coefficient $\mathrm{D_{PIC}}$ as gross yield of individual transport processes directly from the analysis of the particle data.

On the microphysical level the diffusion coefficient is defined for each individual particle $\mathrm{D^*_{PIC}} = (\Delta\,\mathrm{x})^2/\Delta\mathrm{t}$ as temporal path variance $(\Delta\,\mathrm{x})^2(\mathrm{t})$ across the magnetic field. Figure 4.18a shows $(\Delta\,\mathrm{x})^2(\mathrm{t})$ for a selected individual particle. Significant path variations set on around $\mathrm{t}\,\omega_{\mathrm{p0}} \sim 130$ in coincidence with non-linear magnetic field saturation (cf. Fig. 4.16). $(\Delta\,\mathrm{x})^2$ clearly represents the superposition of an oscillatory motion and a distinct cross-field drift. The oscillation describes the meandering of the particle within the magnetic voids each current filament is embedded in. The toroidal magnetic field confines the particle, i.e. escaping current carriers are diverted reversely into the filament. The oscillation time scale is short compared to the cross field drift, but is straightforwardly removed in a linear regression line fit. The resulting slope of the fit corresponds to the cross field diffusion $\mathrm{D^*_{PIC}} = 3.2 \cdot 10^{-5}\,(\mathrm{c}^2/\omega_{\mathrm{p0}})$ of the individual particle.

We determined $\mathrm{D^*_{PIC}}$ for a sample of 32768 individual trajectories. The sample consists of two distinct classes: 20472 particles constitute a first class, characterized by $\mathrm{D^*_{PIC}} < 0$, which corresponds to a particle ensemble being cooled and progressively confined within the magnetic voids. The second class contains all particles with $\mathrm{D^*_{PIC}} > 0$ exhibiting cross-field diffusion with average diffusion coefficient $\mathrm{D_{PIC}} = 9.6 \cdot 10^{-6}\,(\mathrm{c}^2/\omega_{\mathrm{p0}})$. The critical question in this analysis is whether the two classes are distinctly separated, i.e. whether the average diffusion coefficient is sharply defined. Figure 4.18b shows the normalized distribution of the class 2 particles around $\mathrm{D_{PIC}}$. Intriguingly, the rate of cross-field diffusion is reflected in a concise and unambiguous fashion in the self-consistent particle transport data.

In Figure 4.17 b),d) a steady-state configuration is reached in which only oppositely aligned currents are neighboured. Cross-field diffusion describes the tendency of mutual annihilation of opposite currents, i.e. ohmic dissipation of the free energy stored in the currents by an ‘anomalous’ resistivity $\overline{\eta}$. In a second line of argumentation, $\overline{\eta}$ serves as a cross-check for perpendicular transport: The dissipative ohmic power-loss as average over the simulated volume subsumes to

$$\Pi_{\mathrm{Ohm}} = -\mathrm{V}^{-1}\int \mathrm{dV}(\overline{\eta}\cdot\mathbf{j})_{\perp}\cdot\mathbf{j} = -\mathrm{V}^{-1}\int \mathrm{dV}\tilde{\mathbf{E}}_{\perp}\cdot\tilde{\mathbf{j}}.$$

Therein the local current density $\tilde{\mathbf{j}} = \sum_{\mathrm{ppg}} \mathrm{q_i}\mathbf{v}_{\mathrm{i}}$ is an ensemble quantity defined for each individual grid cell. The grid cell level is the most refined entity in configuration space. $\tilde{\mathbf{E}} = \sum \mathbf{E}_{\mathrm{i}}/\mathrm{ppg}$ is the corresponding ensemble-averaged local electric field as superposition of values $\mathbf{E}_{\mathrm{i}}$ interpolated to the respective positions of ppg particles per individual grid cell. PIC simulations are systematically ‘noisy’ with respect to electric field fluctuations. Such fluctuations are artificially introduced by the quasi-particle/field-grid representation [Birdsall & Langdon, 2000]. The number of quasi-particles per grid cell (qpc) is the critical quantity with respect to the fluctuation level. We tested qpc-variations in the simulation setup to ensure that the model-inherent resistivity $\overline{\eta}_{\mathbf{qpc}} \ll \eta$ is not blending the results. The initial kinetic energy of the configuration is determined by the shells’ bulk motion $\mu_{\mathrm{kin}} = 4(\gamma_0 - 1)\mathrm{n_0 mc^2}$ since the initial thermal spread is negligible.

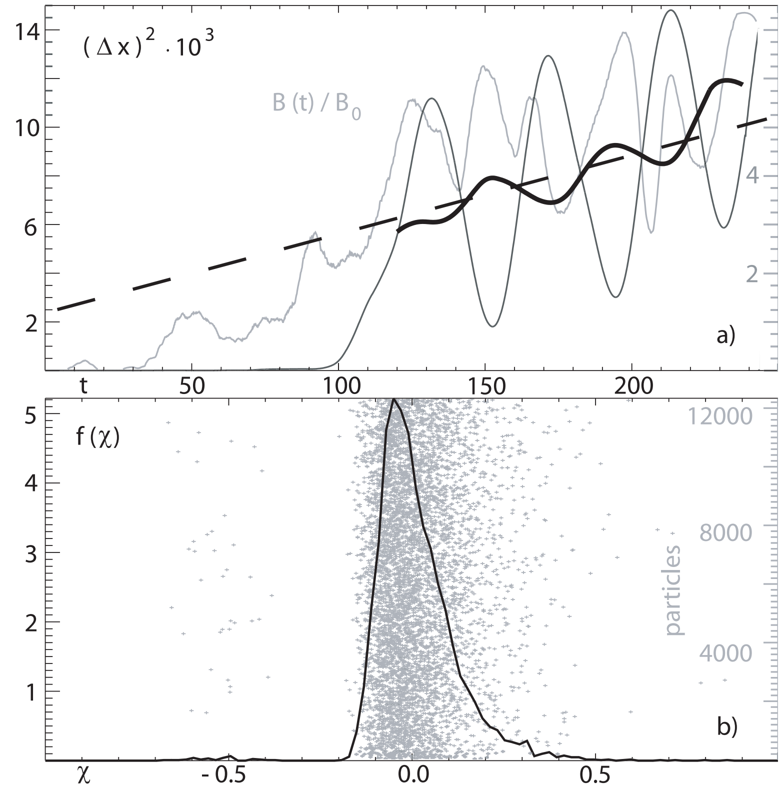

Fig. 4.18: Path variance $(\Delta \mathrm{x})^2\,(\mathrm{t})$ as function of time for an individual particle (a). For significant Weibel magnetic fields at the particle position (grey), the trajectory is constituted by the superposition of the meandering motion within the magnetic confinement and a distinct cross-field drift. In order to subtract meandering, particle motion is smoothed (thick line) and the slope of the respective regression line fit indicates a microphysical diffusion coefficient $\mathrm{D}^*_{\mathrm{PIC}} = 3.2 \cdot 10^{-5}\,(\mathrm{c}^2/\omega_{\mathrm{p0}})$. 37.5 % of a subensemble of 32768 trace particles shows cross-field diffusion with $\chi = \lg\,(\mathrm{D}^*_{\mathrm{PIC}}/\mathrm{D}_{\mathrm{PIC}})/\lg \mathrm{D}_{\mathrm{PIC}} = 0$ corresponding to an statistical average $\mathrm{D}_{\mathrm{PIC}} = 9.6 \cdot 10^{-6}\,(\mathrm{c}^2/\omega_{\mathrm{p0}})$ (b). Diffusing particles form a distinct class as seen from the sharp normalized distribution $\mathrm{f}(\chi)$ around $\mathrm{D}_{\mathrm{PIC}}$.

Anomalous dissipative losses define a 'thermalization'-decay time scale of the magnetic fields $\tau_\eta = -\mu_{\mathrm{kin}}/\Pi_{\mathrm{Ohm}}$. Since the decay time $\tau_\eta \gg \mathrm{t}_{\mathrm{tot}} \gg \delta\mathrm{t}$ is large compared to the total simulated time $\mathrm{t}_{\mathrm{tot}}$ and the timestep $\delta\mathrm{t}$, we can study the time evolution of $\tau_\eta(\mathrm{t})$ during the simulation. Most interesting is the direct correspondence to the time evolution of magnetic field structures as shown in Fig. 4.19. When Weibel filamentation sets on, the magnetic field is topologically characterized by large wavenumbers k (=small scales) and comparatively weak strengths. With consecutive coalescence of current fila-

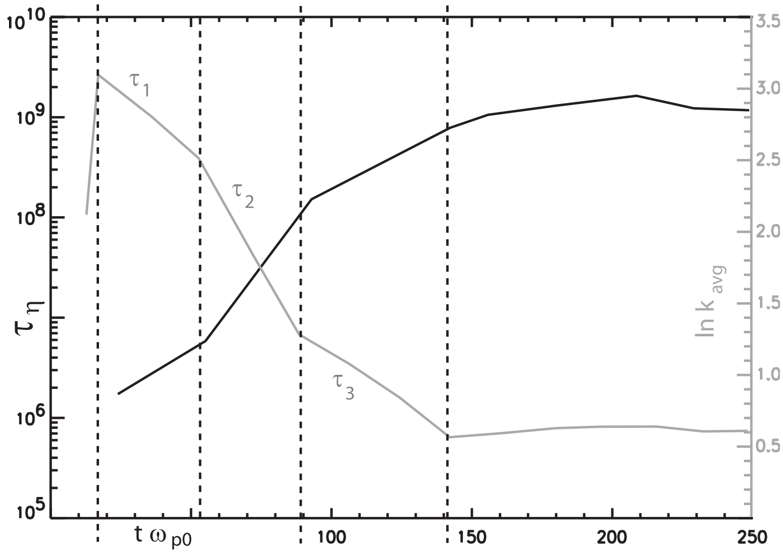

Fig. 4.19: 'Thermalization' time scale $\tau_\eta \omega_{\mathrm{p0}}\,(\mathrm{t})$ for ohmic dissipation of the initial kinetic energy by 'anomalous' particle transport and the time evolution of the average wavenumber $\mathrm{k_{avg}(t)\,c}/\omega_{\mathrm{p0}}$ (grey) in the magnetic field Fourier spectrum. Short field correlation scales (large $\mathrm{k_{avg}}$) directly correspond to strong cross-field diffusion (short τ_η). Typical correlation scale e-folding times for the regime of linear growth / current self-pinching $\tau_1\omega_{\mathrm{p0}} \sim 60$ and self-pinch coalescence $\tau_3\omega_{\mathrm{p0}} \sim 75$ result from the typical particle gyro times (meandering) $\mathrm{t_c}\omega_{\mathrm{p0}} = (2\epsilon_{\mathrm{B}})^{-1/2}$ in the self-generated field. In the intermediate phase $\tau_2\omega_{\mathrm{p0}} \sim 25$ the time evolution is progressive, because incipient current self-pinches are weakly shielded by their own toroidal field and oppositely aligned filaments can cross each other. τ_η saturates at a point in time prior to the start of the analysis of the individual particle data in Fig. 4.18.

ments, structures migrate to smaller k, separative field strengths grow, and cross-field diffusion / anomalous resistivity weakens. The final (on simulation times) steady-state configuration stabilizes at typical decay times around $\tau_\eta(\mathrm{t_{fin}})\,\omega_{\mathrm{p0}} \sim 10^9$.
Intriguingly, this value is consistent with the cross-field diffusion $\mathrm{D_{PIC}}$ obtained from the microphysical analysis of self-consistent particle motion. Since filaments are roughly separated by $\mathrm{L} \sim 10^2\,(\mathrm{c}/\omega_{\mathrm{p0}})$ in the final state, typical diffusion-limited lifetimes of $\tau_{\mathrm{DL}} = \mathrm{L}^2/\mathrm{D_{PIC}} \sim 10^4\,(\mathrm{c}/\omega_{\mathrm{p0}})^2/9.6 \cdot 10^{-6}(\mathrm{c}^2/\omega_{\mathrm{p0}}) \sim 10^9\,\omega_{\mathrm{p0}}^{-1}$ result.
For the lower collision energy γ_0^{10} the current filament / magnetic field topology is much more complex, because the parallel TSI mode contributes significantly. Filaments then show time-dependent 3D modifications, structures saturate at smaller k and typical separation distances decrease [Jaroschek, Lesch & Treumann, 2005]. The corresponding diffusion-limited lifetimes decay down to $\tau_{\mathrm{DL}}^{10}\,\omega_{\mathrm{p0}} \sim 10^7$ suggesting that under certain conditions (cf. section 4.3.5) magnetic field lifetimes become insufficient to warrant synchrotron emission. This result is in accordance with the analysis of certain time-resolved

GRB prompt emission spectra [Ghirlanda, Celotti, & Ghisellini, 2003]. Therein the comparison of observational data with the spectral shapes as expected from non-thermal emission models is unsatisfactory indicating that internal magnetic fields live on a time scale which is short compared to synchrotron loss.

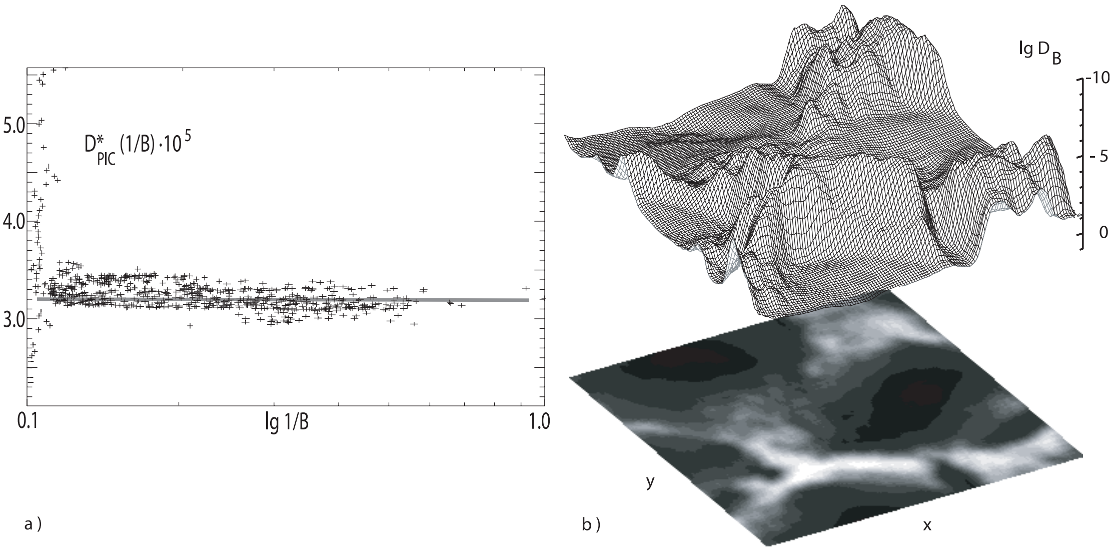

Fig. 4.20: Microphysical diffusion coefficient $D^*_{PIC}(1/B)$ as function of 1/B for the individual particle already analyzed in Fig. 4.18(a). The straight line indicates 'Bohm'-type 1/B behaviour derived from the line fit in Fig. 4.18(a) (which corresponds to the time average). The high fluctuations at small 1/B reflect the relation $\delta B/B \sim 1$ for the fluctuation scale height. Scattering around the straight line represents contributions from the meandering motion. The surface contours in (b) show the z-averaged Bohm diffusion coefficient $D_B = \alpha c T_\perp / eB$ derived from the perpendicular temperature ($T_\perp$ as the statistical quantity of the total ensemble of $5 \cdot 10^8$ simulated particles, $\alpha = 1$ assumed). $D_B \sim 10^{-5}\,(c^2/\omega_{p0})$ indicates $\alpha \sim 1 - 1/10$ in fine agreement with the 'Maxwellian' $\alpha = 1/16$.

Diffusion is Identified as 'Bohm'-type

Collisionless cross-field diffusion was identifed as 'Bohm'-type in test-particle simulations of high temperature (T) plasma in the limit of strong magnetic fields (B). Motivated as pervasive in fusion devices such conditions imply Debye lengths to be larger than typical particle gyro radii $\lambda_D > \rho$. In this limit Dawson, Okuda & Carlile [1971] associated 'Bohm'-type behaviour with anomalous particle collisions with electrostatic 'convective cells'. Chu, Chu & Ohkawa [1978] further identified contributions of a magnetostatic mode to retain $\propto$ T-diffusion and Lin, Dawson & Okuda [1978] proved electrostatic fluctuations to be the dominant source of scattering. Diffusion is understood as 'Bohm'-type if it exhibits the characteristic $\mathrm{D_B} \propto \mathrm{T/B}$-behaviour. Bohm diffusion provides the most efficient cross-field transport possible, far more efficient than expected from a simple extrapolation of the 'classical', collision-imposed $1/\mathrm{B}^2$-dependence.

The Weibel instability is of interest in GRB scenarios in which the plasma outflow is kinetically dominated, i.e. $\lambda_\mathrm{D} < \rho$ is valid. A fundamental question is then, whether Weibel generated magnetic fields do also exhibit 'Bohm'-type diffusion. Figure 4.20 a) shows the diffusion rate $(\Delta \mathrm{x})^2/\Delta \mathrm{t}\,(1/\mathrm{B})$ plotted as function of the inverse magnetic field at the respective particle position. The straight horizontal line is significant and clearly indicates 'Bohm'-type $\mathrm{D_B} \propto 1/\mathrm{B}$-dependence - again directly obtained from the particle data. The ordinate value $(\Delta \mathrm{x})^2/\Delta \mathrm{t} = 3.2 \cdot 10^{-5}\, \mathrm{c}^2/\omega_\mathrm{p0}$ coincides with the slope of the line fit obtained for the same particle in Fig. 4.18 a). With this insight obtained, we look for the ratio of $\mathrm{D_B} = \alpha\, \mathrm{c T_\perp/eB}$ as characteristic of the Bohm diffusion and α representing only an insignificant dimensionless correction factor. Setting $\alpha = 1$ and calculating the perpendicular temperature $\mathrm{T_\perp} = \int \mathrm{d}\mathbf{p}\mathrm{p_\perp v_\perp f}(\mathbf{p})$ as defined in the relativistic energy-momentum tensor, $\mathrm{D_B}$ surface contours are shown in Fig. 4.20 b). As a third and absolutely consistent constraint on the cross-field diffusion $\mathrm{D_B} \sim 10^{-6}\, (\mathrm{c}^2/\omega_\mathrm{p0})$ is reached as maximum (=time-limiting) value located in the walls of magnetic confinement (cf. Fig. 4.17).

As a provocative conjecture, one could infer a general mechanism of 'minimum action' governing the complete scenario: Ab initio the system contains its free energy in the directed motion of plasma shells. The final objective is the maximum enthalpy gain via thermalization. Two plasma instability channels are possible: (i) The TSI mode with parallel electric fields broadens the initially sharply defined bulk motion. (ii) The WBI mode introduces magnetic fields responsible for isotropization. The coupling of the two modes is energy-dependent. For progressively higher energies WBI contributions dominate resulting in the magnetically confined (quasi-) steady-state configuration which is final on time scales feasible in PIC simulations. Nevertheless 'Bohm'-type transport is accomplished as the most efficient 'anomalous' thermalization process.

4.3.5 Consequences for Synchrotron Emission

As the net effect of all microphysical diffusion processes the lifetime of Weibel magnetic fields is limited to $\tau_\mathrm{DL}\, \omega_\mathrm{p0} \sim 10^9$. Albeit the presented simulations refer to $(\mathrm{e}^+, \mathrm{e}^-)$ shell collisions, the results directly transfer to the case of 'baryonic' contributions: Frederiksen et al. [2004] investigated the Weibel instability for relativistic collisions of electron-proton (e, p) shells. Though applying an artificial mass ratio of just $\mathrm{m_p/m_e} = 16$, magnetic field generation / plasma heating via the WBI-TSI mode is spatially and temporally decoupled by a relative factor of $\mathrm{f_r} = (\mathrm{m_p/m_e})^{1/2}$, and lower hybrid contributions appear to be negligible. Simulation of the real mass ratio in 3D scenarios is beyond the scope of contemporary supercomputers, but the decoupling is expected to be even more pronounced for higher mass ratios. Comparable bulk energies γ_0 yield equivalent equipartition ratios

$\epsilon_{\mathrm{B,e}} \sim \epsilon_{\mathrm{B,p}}$ for each of the species. Consequently, protons give dominant ($\propto \mathrm{f_r}$) contributions to the Weibel magnetic field / current filament structure. Electrons are strongly thermalized, modify the field structure in the sub-%-regime, and merely serve as the charge/current neutralizing element. However, electrons further represent the dominant source of synchrotron emission in the proton-sustained Weibel fields.

With the Weibel mechanism as the connection between plasma kinetic quantities ($\mathrm{n_0}, \gamma_0$) and the generated magnetic field ($\epsilon_\mathrm{B}, \mathrm{B_0}$), typical synchrotron cooling times can be formulated in units of plasma inertial time scales

$$\tau_{\mathrm{sc}}\,\omega_{\mathrm{p0}} = 3.5 \cdot 10^{17}\,\gamma_0^{-1}(\gamma_0 - 1)^{-1}\,(\mathrm{n/1\,cm^3})^{-1/2}\,\epsilon_\mathrm{B}^{-1/2}\,(\mathrm{m/m_e})^{-3/2}.$$

According to Fig. 4.16, $\epsilon_\mathrm{B}^{10} \sim 2.5\,\%$ and $\epsilon_\mathrm{B}^{100} \sim 10\,\%$ result as final steady-state conditions in the highly non-linear regime. Apparently the mass ratio $\mathrm{m/m_e}$ is important. Being unity for ($\mathrm{e^+, e^-}$) shells, it represents the fact that in the case of baryonic contributions magnetic field generation and diffusive decay take place on ion scales, while radiative cooling is appendant to lepton scales. Distinguishing between GRB prompt emission as the result of internal collisions associated with plasma densities $\mathrm{n_0^{int}} \sim 10^{10}\text{-}10^{16}\,\mathrm{cm^{-3}}$ and afterglow in external collisions with the ambient medium in the regime $\mathrm{n_0^{ext}} \sim 10^{0}\text{-}10^{2}\,\mathrm{cm^{-3}}$, typical observed time scales $\tau_{\mathrm{int}} = 10^{-3}\text{-}10^{-1}\,\mathrm{s}$, $\tau_{\mathrm{ext}} = 10^{1}\text{-}10^{4}\,\mathrm{s}$ correspond to typical plasma inertial scales $\tau_{\mathrm{int}}\,\omega_{\mathrm{p0}} \approx \tau_{\mathrm{ext}}\,\omega_{\mathrm{p0}} \sim 10^{5}\text{-}10^{10}$. In the general scheme, internal collisions are associated with ($\mathrm{e^+, e^-}$) fireball ejecta [Piran, 1999], external collisions in the 'standard' afterglow model [Panaitescu & Kumar, 2002] with the ($\mathrm{e, p}$) plasma of the ambient medium. Beloborodov [2002] argues convincingly that (i) internal ($\mathrm{e^+, e^-}$) plasma should contain a 'baryonic' pollution because otherwise the observational fact of comparable energy deposition for prompt emission and afterglow is unbalanced towards early times, (ii) external ($\mathrm{e, p}$) plasma should possess a 'leptonic' pollution due to the impact of the prompt γ-ray blast on the ambient medium, a facet not covered in the 'standard' afterglow model.

Employing the PIC simulation's self-consistent equipartition ratios, typical synchrotron cooling times are calculated to

$$\begin{array}{rcl|rcl}
\tau_{\mathrm{sc},10}^{\mathrm{int}}\,\omega_{\mathrm{p0}} & = & 10^{8} - 10^{11} & \tau_{\mathrm{sc},10}^{\mathrm{ext}}\,\omega_{\mathrm{p0}} & = & 10^{15} - 10^{16} \\
\tau_{\mathrm{sc},100}^{\mathrm{int}}\,\omega_{\mathrm{p0}} & = & 10^{6} - 10^{9} & \tau_{\mathrm{sc},100}^{\mathrm{ext}}\,\omega_{\mathrm{p0}} & = & 10^{13} - 10^{14} \\
\tau_{\mathrm{sc},10}^{\mathrm{int}}\,\omega_{\mathrm{p0}} & = & 10^{3} - 10^{6} & \tau_{\mathrm{sc},10}^{\mathrm{ext}}\,\omega_{\mathrm{p0}} & = & 10^{10} - 10^{11} \\
\tau_{\mathrm{sc},100}^{\mathrm{int}}\,\omega_{\mathrm{p0}} & = & 10^{1} - 10^{4} & \tau_{\mathrm{sc},100}^{\mathrm{ext}}\,\omega_{\mathrm{p0}} & = & 10^{8} - 10^{9}
\end{array}$$

for $\gamma_0 = 10$, (100), respectively. As soon as baryonic contributions are significant, the mass ratio becomes important ($\tau_{\rm sc}$ values in grey). The corresponding synchrotron cut-offs in the collision frame

$$\omega_{\rm cut}/\omega_{\rm p0} = 3\sqrt{2}(\gamma_0 - 1)^{1/2}\gamma_0^2\epsilon_{\rm B}^{1/2}$$

range around $\omega_{\rm cut,100}^{\rm int} \sim 10^{14}$-$10^{18}$ Hz and $\omega_{\rm cut,100}^{\rm ext} \sim 10^{10}$-$10^{11}$ Hz. Cut-off frequencies are less sensitive to density variations / baryonic contributions and suggest an energy range $\gamma_0 \sim 10^2$ for both internal and external collisions, thereby giving credit to conjectures that variabilities in the shells' bulk momentum range around the respective absolute momentum $\Delta\gamma/\gamma_0 \sim 1$.
The important result is that typical synchrotron cooling times $\tau_{\rm sc}\,\omega_{\rm p0} \lesssim 10^9 \sim \tau_{\rm DL}$ are shorter than the diffusion-limited lifetimes of Weibel fields at sufficiently high collision energies $\gamma_0 \sim 10^2$. The energetic constraint relaxes for higher densities and 'baryonic' contributions, the latter appear most likely. Furthermore, the generation of Weibel fields up to the steady-state configuration takes place within $\tau\,\omega_{\rm p0} \lesssim 10^2$, i.e is instantly fast with respect to diffusive decay / synchrotron emission. Plasma shells in a real GRB scenario are expected to be far more extended in the direction of bulk motion, which relates to a simulation setup which is continuously pumped by an injected plasma beam (cf. Frederiksen et al. [2004], especially Fig. 5 therein). In an open, beam-powered system diffusive losses are readily compensated, extending the diffusion limit by the respective beam lifetime.

In conclusion, PIC simulations serve to identify the stability of Weibel scenarios by self-consistent analysis of magnetic cross-field diffusion. The diffusion process is identified as 'Bohm'-type, which is the fastest diffusive decay mechanism possible. Hence, the typical diffusion-limited lifetime of the Weibel fields in plasma shell collisions represents a merely conservative limit around $\tau_{\rm DL}\,\omega_{\rm p0} \sim 10^9$. Such a stability appears sufficient to validate synchrotron emission scenarios for GRB prompt emission as well as afterglow, especially in view of likely 'baryonic' contributions to the pair-plasma and plasma shells which are much more extended in the parallel direction than imposed by the computational limits of the PIC simulations.

4.4 Self-Consistent Synchrotron Cascades

In the previous sections we presented the results of self-consistent PIC simulations for 3D relativistic plasma shell collisions. All the tedious details and meticulous analysis of the plasma configuration essentially served to provide evidence for two fundamental statements:

1. The magnetic field strengths generated via the Weibel mechanism (ϵ_B) are sufficient to make synchrotron emission processes potentially important.
2. The diffusion-limited lifetime of the final saturated plasma state is long compared to typical synchrotron cooling times, i.e. the magnetic fields survive for a sufficiently long time to allow for synchrotron emission!

In the introductory section 4.1 to this chapter we noted that GRB spectra are phenomenologically fitted by power-laws. Then unavoidably we run into a critical question for the theorist:
Can the self-consistently created synchrotron spectra assume power-law shapes? And if so, is there a synchrotron spectral index characteristic for the source process as it appears to be valid for the reconnection mechanism?
The solution to such questions is much tougher than one might think at the first glance. Certainly synchrotron power-law spectra are obtained if one starts with a particle distribution which is initially already power-law shaped in energy - this is a standard textbook result. Turbulent magnetic field structures as observed during Weibel filamentation rapidly enforce pitch angle isotropization (cf. Fig. 4.15). The spectral synchrotron power per unit angle $\mathrm{P}(\omega)$ is derived from the single particle motion by evaluating the Lienard-Wiechart retarded potentials. Due to the effect of relativistic beaming the charged particle is not just emitting at the frequency of angular motion (cyclotron radiation), but the electromagnetic fields are confined to a radiation pulse. Pulses are formed by the superposition of wavetrains covering an extended frequency range and in the limit of highly relativistic particle energies the frequency spectrum is described by modified Bessel functions $\mathrm{P}(\omega)\,\mathrm{d}\omega = \mathrm{C}\,\omega_\mathrm{crit}\mathrm{F}(\mathrm{x})$, with $\mathrm{F}(\mathrm{x}) = \mathrm{x}\int_\mathrm{x}^\infty \mathrm{K}_{5/3}(\lambda)\,\mathrm{d}\lambda$. C is just the dimensional correction and normalization in energy, x the dimensionless parameter $\mathrm{x} = \omega/\omega_\mathrm{crit}$. Bessel functions K_ν are involved because the gyro motion has cylindrical symmetry. They form a space of orthonormal functions and the process of synchrotron radiation can be understood as the respective mapping of charged particle motion from configuration space. Most important is the fact, that the qualitative synchrotron spectral shape $\mathrm{F}(\mathrm{x})$ is independent (!) of particle energy γ. γ only determines the absolute value of the cut-off frequency $\omega_\mathrm{crit} = 3\gamma^2\mathrm{qB}\sin\alpha/2\mathrm{mc} = \gamma^2\hat{\mathrm{B}}\omega_\mathrm{c0}^{-1}\sin\alpha$. ω_crit essentially marks the upper end of the spectrum in frequency. Test-particle simulations start with a power-law particle distribution (PDF) $f(\gamma)\gamma \propto \gamma^{-p}d\gamma$ as an ad-hoc assumption and then total synchrotron power-laws ensue as the result of direct mapping into the modified Bessel function space:

$$\mathrm{P}_\mathrm{tot}(\omega) \propto \int_{\gamma_\mathrm{min}}^{\gamma_\mathrm{max}} \mathrm{P}(\omega)\mathrm{f}(\gamma)\gamma^\mathrm{p}\,\mathrm{d}\gamma \propto \omega^{-(\mathrm{p}-1)/2} \int_{\gamma_\mathrm{min}}^{\gamma_\mathrm{max}} \mathrm{F}(\mathrm{x})\mathrm{x}^{(\mathrm{p}-3)/2}\,\mathrm{dx}$$

For the class of power-laws which are sufficiently extended in energy the integral is just a quasi-constant numerical factor, and the power-law PDF transfers to a synchrotron power-law $\mathrm{P_{tot}} \propto \omega^{\mathrm{n}} \mathrm{d}\omega$ with spectral index $\mathrm{n} = -(\mathrm{p}-1)/2$. When other radiative processes are included, which unlike pure synchrotron emission introduce energy dependent modifications to the spectral shape (like Comptonization/Synchrotron-Self-Comptonization), then the power-law spectral index is varied upon modifications of the upper/lower energy cut-off $\gamma_{\mathrm{max}}/\gamma_{\mathrm{min}}$ in the PDF. Simulations of this kind provide just a description of the radiative process, not a self-consistent explanation of the physics involved.

Therefore we come to the crucial point: Which kind of synchrotron spectra can result from an entirely self-consistent simulation starting with a monoenergetic beam at initialization time? The magnetic field is the mediator for any reconfiguration of the PDF in energy/momentum space. Consequently the first step is to consider the time evolution of magnetic field structures in relativistic plasma shell collisions. As a result from the previous sections we know that the magnetic field is dominated by the components perpendicular to the shell bulk motion. Figure 4.21 shows the spectrum of perpendicular magnetic field energy density $\mathrm{B}_{\perp}^2(\mathrm{k}_{\perp})$ for $\gamma_0 = 100$ (a) and $\gamma_0 = 10$ (c), respectively. In the linear regime the magnetic field is highly filamented and the corresponding energy density $\mathrm{B}_{\perp}^2 \propto \mathrm{k}_{\perp}^{\mathrm{s}}$ is power-law shaped with spectral index $\mathrm{s} = 2/3$. The linear Weibel mode is purely growing for all $\mathrm{k}_{\perp}$ (cf. Fig. 4.5) with γ_0-dependent growth rates. Consequently differences in (a) and (c) occur in the absolute time scale but the spectral index s is equivalent throughout the linear regime.

The maximum spectral cut-off is determined by the limited resolution of the simulation grid. The resolution limits imposed by computational resources are the inherent problem of all simulations which involve spectral cascades. The limited range of scales is independent of the applied simulation method, i.e. is present in kinetic as well as magneto-/hydrodynamic approaches. A dimensionless quantification of the range of scales covered is the Reynolds number (Re), which is inherited from fluid simulations. On contemporary supercomputing systems $\mathrm{Re} \sim \mathrm{O}(10^3)$ is reached for 3D configurations which essentially is the ratio of the largest to smallest resolved scale length. The linear regime also exhibits clear features of self-similar structures and regularization in fractal dimensional ordering (d). During the subsequent intermediate phases of non-linear saturation and coalescence of current self-pinches the power-law appears broken and deformed. In the final saturated plasma state the power-law shape is reestablished though the spectral index has opposite sign. The time evolution (b) shows the inversion of the spectral cascade, i.e. the spectral dominance migrates from small scale to large scale structures.

The remarkable fact is that the final spectra of magnetic energy density exhibit stable power-laws and show distinct similarities to the respective spectra obtained in simulations of 3D magnetohydrodynamic (MHD) turbulence. The 'inverse cascade' in the spectral time evolution proceeds on time and length scales too tiny to be resolved in the MHD approaches. However, the final saturated configuration is stable on diffusive (= long !) time scales and therefore should provide the connection to results of MHD turbulence.

For the first time we are thus in the position to study 3D turbulence on the kinetic level

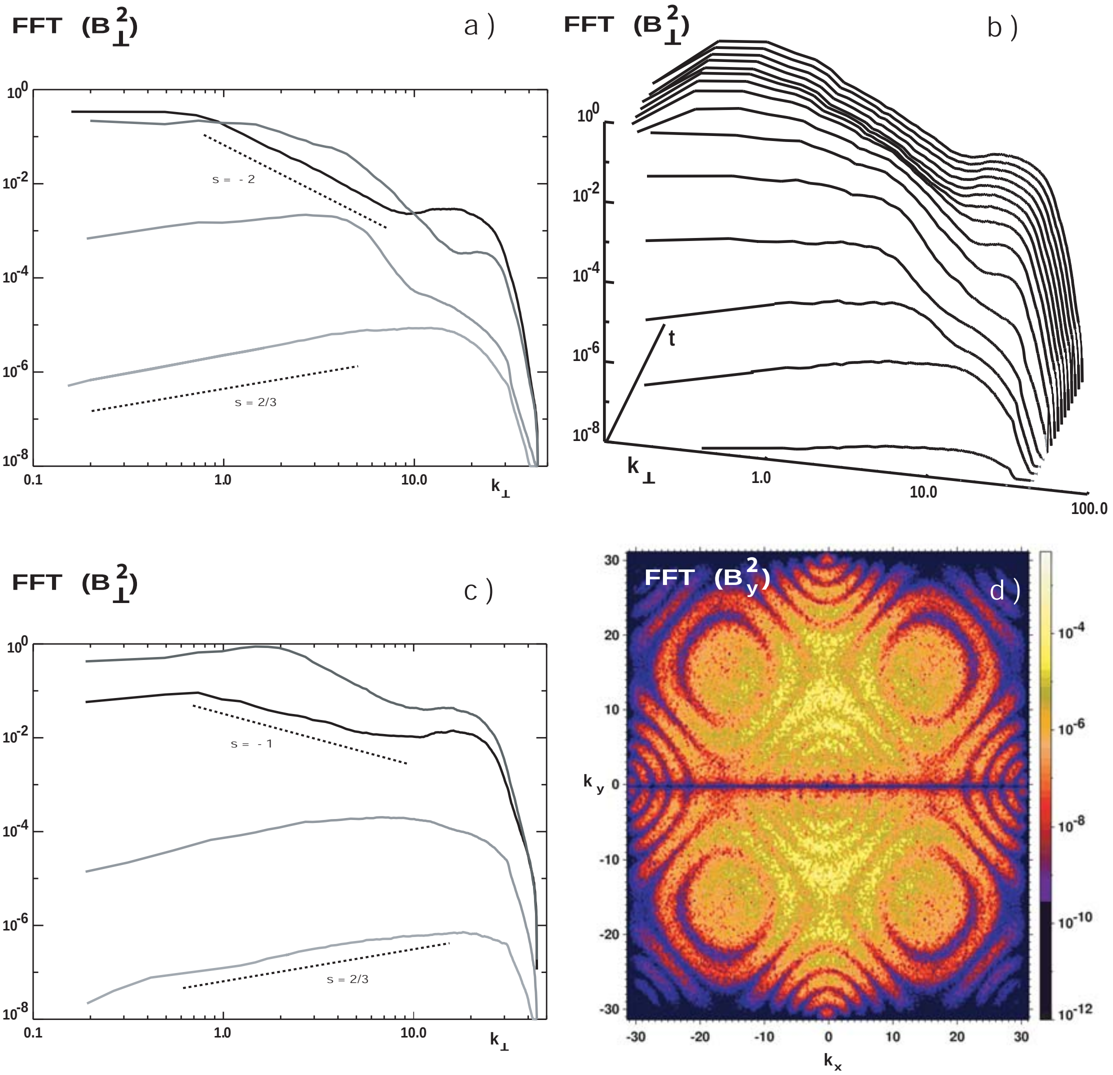

Fig. 4.21: Fourier spectra of transverse magnetic energy density FFT($B_\perp^2$) for shell collision energy $\gamma_0 = 100$ (a,b) and $\gamma_0 = 10$ (c), respectively. The selected time points (a,c) correspond to linear phase, non-linear saturation, coalescence of self-pinches and final saturated state (with respective colors from bright grey to black). The time evolution shows an 'inverse cascade', i.e. the transformation from an initial power-law with positive slope over short timed intermediate stages to a final power-law with negative slope. Final slopes reflect γ_0-dependent dimensional effects. During the linear phase magnetic fields are regularized by self-similar structures (d).

and obtain insight into the connection between the particle and the fluid picture of the plasma:

The final turbulent spectrum for the collision energy $\gamma_0 = 10$ (d) exhibits a spectral index $\mathrm{s} = -1$. Consequently the spectrum is significantly shallower than predicted from Kolmogorov turbulence. Kolmogorov [Kolmogorov, 1941] obtained a scaling law in the framework of incompressible non-magnetized hydrodynamics by constituting a relation $\mathrm{v_l} \propto \mathrm{l}^{1/3}$ between the relative velocity of fluid elements $\mathrm{v_l}$ and their relative separation l. Parsefal's power theorem connects the turbulent spectral energy W and kinetic energy like $\mathrm{kW(k)} \propto \mathrm{v_l^2}$ with the typical wavenumber of the fluctuations $\mathrm{k} \sim 1/\mathrm{l}$. As a consequence thereof the Kolmogorov spectrum scales $\mathrm{W(k)} \propto \mathrm{k}^{-5/3}$. For sub-Alfvénic turbulence the Alfvén, slow and fast wave modes contribute to the MHD spectrum. (The literature on MHD turbulence is vast. A detailed compendium on the field is found in [Biskamp, 2003]. In the following we concentrate on Cho & Lazarian [2003] for results which reflect the actual status of contemporary research). The Kolmogorov $\mathrm{k}^{-5/3}$ scaling provides a good description of the Alfvèn and slow mode turbulent spectra, whereas the fast modes show Kraichnan type $\mathrm{k}^{-3/2}$ power-laws. Interesting for the comparison with the kinetic simulation is regime of scales in which the (magneto-)hydrodynamic scaling laws begin to break down. It is known that the viscosity sets a minimum scale on hydrodynamic turbulence, below which the hydrodynamic mode cascade is exponentially damped. In the simulations by Cho & Lazarian [2003] (cf. Figure 9 therein) the magnetic energy density cascade extends far beyond the hydrodynamic minimum and shows power-law behaviour with spectral index k^{-1}. Conclusively, in the viscosity damped regime the MHD turbulent spectrum is equivalent to the turbulent spectrum of magnetic fields generated in kinetic plasma shell collisions. For ultra-relativistic collision energies $\gamma_0 = 100$ the $\mathrm{B}_\perp^2(\mathrm{k}_\perp)$ spectrum steepens towards $\mathrm{s} = -2$. This result is intuitively understood if one considers that the fundamental scale size of $\mathrm{B}_\perp$ structures is determined by the particle 'bounce motion' (cf. Fig. 4.12c for details on the particle motion). The relativistic mass gain broadens current filaments in the saturated state towards larger scales, i.e. shifts the spectral energy towards smaller wavenumbers. Furthermore the spectral index $\mathrm{s} = -2$ is indicative for shock physics, since the plasma discontinuity of the shock front transfers to a k^{-2} cascade in Fourier space. The effects of this shock discontinuity are more pronounced for the $\gamma_0 = 100$ case, since the mode propagates quasi-perpendicular and 3D modifications are diminished.

With the magnetic field structures identified as characteristic for 3D kinetic turbulence, the consecutive step is to investigate the effect of power-law magnetic cascades on the PDF. Therefore we need to understand whether resonant scattering of particles takes place, and if so, in which way the PDF is modified. The magnetic field structures are generated by the current filaments. As a direct consequence the transverse extension of the filaments and the typical structures of $\mathrm{B}_\perp$ evolve on a common length scale. Efficient scattering sets in when the particle 'sees' the field fluctuations, i.e. if the particle motion also proceeds on comparable spatial scales. Since the particles perform a meandering motion in the current filaments the resonant coupling to the field structures is ensured and collisionless scattering is expected to take place.

What is the impact on the PDF? Resonant particle scattering on power-law shaped magnetic field spectra has been discussed in the context of cosmic ray generation in the interstellar medium and particle reacceleration in radio sources [Kardashev, 1962; Kaplan & Tsytovich, 1973; Melrose, 1971; Eilek & Henriksen, 1984]. In such scenarios Alfvén wave turbulence is assumed to generate the magnetic field structures. Alfvén waves have the convenient characteristic not to suffer Landau damping if the respective Alfvén velocity exceeds the speed of sound. Then the initial power-law spectral shape $W_A \propto k^m$ is maintained. The interaction of an arbitrary initial PDF with such 3D turbulent magnetic fields is discussed in the framework of a diffusive approach [Lacombe, 1979].

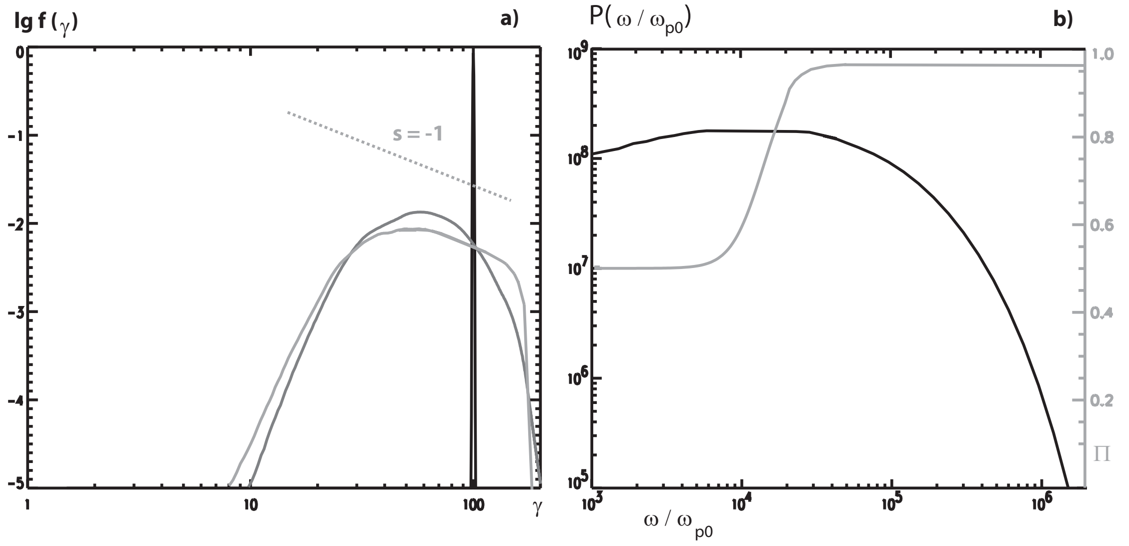

Fig. 4.22: Time evolution of the PDF $f(\gamma)d\gamma$ (a). The PDF is initialized as monoenergetic beam $\gamma_0 = 100$ ($t = t_0$), then thermalizes over a broad energy range ($t = t_{th}$)and gains non-thermal features up to the final simulated time ($t = t_{fin}$)(black to bright grey). The synchrotron spectrum at t_{fin} exhibits incipient power-law contributions and at the upper frequency range a high degree of polarization Π (b).

Therein the time evolution of the PDF is studied in energy/momentum space with a modified diffusion coefficient containing the characteristics of the turbulent spectrum. The details are quite cumbersome, but in general there exist two classes of solutions. Time-independent stationary solutions in which the final state of the PDF critically depends on the initial conditions [Kardashev, 1962] and so called self-similar solutions. Self-similar solutions describe the PDF for a system which has forgotten all initial conditions, the solutions are independent from the specific choice of spatial and temporal scales and are obtained as asymptotic solutions for a characteristic set of boundary conditions. The rate of change in relativistic energy which results from the diffusive approach for the power-law magnetic spectrum has been derived as $\mathrm{d}\gamma/\mathrm{dt} \propto \gamma^{-(\mathrm{m}+1)}$ in Kaplan & Tsytovich [1973]. Corresponding self-similar solutions are calculated in [Melrose, 1969; 1971; Lacombe, 1979; Eilek & Henriksen, 1984]. Therein the underlying theoretical scenario consists of an arbitrary initial PDF getting scattered off propagating Alfvén waves. For the peculiar boundary condition of a constant flux of zero-energy particles the self-similar solution is $\mathrm{f}(\gamma) \propto \gamma^{1+\mathrm{m}}$ which is also stationary in time. The scenario realized in plasma shell collisions is equivalent, just the inertial frame is exchanged. Magnetic field structures are at rest in the cms frame. However, seen from the inertial frame of a plasma shell which encounters the fields produced in the collision of a preceding shell generation, the shell particles represent the constant flux of zero-energy particles and the field structures are approaching. Consequently from the magnetic field spectra shown in Fig. 4.21 the self-similar solutions predict power-law shaped PDFs with spectral index $\mathrm{p} = 0$ for $\gamma = 10$ and $\mathrm{p} = -1$ for $\gamma = 100$, respectively.

Finally, how well do the PIC simulation results reconcile with these predictions? For a correct interpretation one has to recall the four time scales which are involved in the current discussion. The PIC simulations cover a very limited time interval with respect to astrophysical time scales. The simulations end with the final saturated plasma configuration at $\mathrm{t} = \mathrm{t}_{\mathrm{fin}}$. $\mathrm{t}_{\mathrm{fin}}$ characterizes the time necessary to generate the field structures and naturally this time is small compared to typical time $\mathrm{t}_{\mathrm{psc}}$ necessary to produce self-similar PDFs out of particle scattering. Both of these time scales are negligible compared to typical synchrotron cooling times t_{sc} which are evidently below or on the order of the typical diffusive lifetimes $\mathrm{t}_{\mathrm{dif}}$ of the respective fields. Consequently $\mathrm{t}_{\mathrm{fin}} \ll \mathrm{t}_{\mathrm{psc}} \lll \mathrm{t}_{\mathrm{sc}} \lesssim \mathrm{t}_{\mathrm{dif}}$ is the given time frame. Obviously on the current level the simulation can only provide insight into the beginning of PDF scattering on the fields. The time evolution of the PDF in Fig. 4.22a shows the transition from a monoenergetic beam over a thermalized PDF with significant bulk motion to the formation of non-thermal contributions. Remarkably the non-thermal features at the final simulated time exhibit the predicted power-law shape with spectral index $\mathrm{p} = -1$. The associated synchrotron spectrum in (b) as calculated explicitely from the particle data then shows a narrow range of the predicted $\mathrm{n} = (\mathrm{p} - 1)/2 = 0$ plateau. A thorough investigation of the resonant particle scattering is in principle possible with implicit simulation techniques and is an interesting subject for futures studies.

Chapter 5

The Weibel-Two-Stream Connection

5.1 The Electromagnetic Counterstreaming Instability with Magnetic Guide Field

The Electromagnetic Counterstreaming Instability (EMCSI/CTW) is of utmost importance in relativistic collisionless plasmas. According to the analysis in the previous chapter the EMCSI is expected to be the dominant plasma mode in all scenarios which involve significant counterstreaming motion. The reasons are obvious. Thermal background fluctuations unspecifically excite all possible plasma modes. During the linear regime all modes exhibit exponential growth and, hence, only the fastest growing mode succeeds in the competition. The free energy of the configuration is efficiently channeled into the fasted growing mode, and the contributions from slower modes are of negligible influence. The EMCSI has an electrostatic (TSI) and electromagnetic (WBI) constituent. Due to their physical nature electrostatic (ES) modes evolve faster in any regime than electromagnetic non-radiative (EMNR) modes. We refer here to EM but non-radiative modes to distinguish from EM light modes. The WBI is a paradigm for an EMNR zero-frequency and, as a consequence thereof, non-radiative instability. ES instabilities couple resonantly to the particle motion on timescales determined essentially by the speed of light. In the EMNR case resonant instability feedback is mediated by velocities close to Alfvénic. Consequently EMNR instability growth strongly depends on the plasma parameters. In pair plasma environments which are in addition collisionless (i.e. highly rarefied in density) the Alfvén velocity gets close to the speed of light. Then ES and EMNR instabilities proceed on comparable timescales.

In 3D scenarios the EMCSI/CTW is a coupled 2D mode with ES and EM/EMNR contributions. Conclusively, the conditions pervasive in collisionless pair plasmas deploy the EMCSI as the dominant instability mode for configurations in which the velocity/temperature anisotropies are the source of free energy. In a formal line of thought the TSI and WBI contributions have somewhat competing effects on the plasma configuration: The TSI and associated parallel electric fields conduct plasma heating and phase space isotropization. After non-linear saturation the WBI sustains current filaments embedded and stabilized in magnetic voids. Whereas the TSI ultimately consumes all the free energy of phase space anisotropy, the WBI retains a finite residual anisotropy in the system (see Fig. 4.8). These characteristics (abundantly elaborated in chapter 4) have profound implications in the context of plasma transport processes on astrophysical time and length scales.

Plasma transport is an ubiquitous phenomenon in astrophysical sites, so we only mention two examples: In extragalactic jets the radiative signatures of relativistic particles exhibit strong localized inhomogeneities. Relativistic particles travel several hundreds of kiloparsec (kpc) in dynamic equilibrium between synchrotron loss and continuous in situ reacceleration. At some disjunct points the particle transport changes spatially on sub-kpc scales and the radiative energy deposition increases tremendously. In such 'hot spots' the magnetic field / plasma configuration apparently experiences significant modifications. Another example deploying completely different plasma parameters and characteristic scales in the kilometer range is the pulsar magnetosphere. In this scenario the dipolar magnetic field around the central neutron star is the dominant physical quantity. The dipolar approximation allows to determine emission heights for the emerging radio pulses. Radio pulses and corresponding emission heights are reproduceable events. This suggests that the respective plasma source process does not proceed randomly but immediately as soon as the environment conditions allow for it. In both examples plasma is transported almost unperturbedly over certain distances, then environment parameters change and the bulk kinetic energy (phase space anisotropy) is dissipated on distances which are small compared to the previously passed. Formally we associate the characteristics of the nonlinear WBI and TSI with 'transport' and 'dissipation', respectively. In order to explain the described variabilities of plasma transport, we need to identify a constraint which separates the coupled 2D CTW mode into the 1D constituents and further distinctively characterizes one of the 1D modes as dominant. In section 4.2 we discussed the influence of variabilities in the initial collision energy γ_0 on the relative weight of the TSI and WBI characteristics within the 2D CTW. Essential point of the argumentation in this context are the differences in relativistic damping, since in the linear analysis (see section 4.2) $\Gamma_{\mathrm{WBI}} \propto \gamma_0^{-1/2}$ and $\Gamma_{\mathrm{TSI}} \propto \gamma_0^{-3/2}$ are observed. However, the energy constraint does not offer the key to split the 2D CTW into the 1D constituents and empower one mode to dominate over the other.

The solution to the problem relies on the introduction of a magnetic guide field $\mathbf{B}_{\mathrm{G}}$. This statement does not originate as some sort of 'educated guess', but rather from some more abstract considerations: First, $\mathbf{B}_{\mathrm{G}}$ introduces an anisotropy into the system. In general anisotropies eliminate degeneracies in a physical system. If $\mathbf{B}_{\mathrm{G}}$ is chosen parallel to the bulk motion, the 2D CTW as coupled mode with oblique propagation is suppressed, whereas the separation into 1D TSI and 1D WBI as purely parallel and perpendicular modes, respectively, is pronounced. Second and even more intuitive, the 1D TSI is a completely electrostatic mode, i.e. it remains unaffected by the introduction and variation of $\mathbf{B}_{\mathrm{G}}$. The 1D WBI on the contrary is significantly modified by $\mathbf{B}_{\mathrm{G}}$, because filamentation and coalescence require particle motions perpendicular to the magnetic field. As a preliminary conclusion we therefore already infer that the introduction of $\mathbf{B}_{\mathrm{G}}$ splits the CTW into TSI and WBI. Furthermore, beyond a critical magnitude of

$\mathbf{B}_\mathrm{G}$ the TSI is expected to prevail in the presence of the WBI. Of course such intuitive argumentation needs to be validated in the mathematical analysis of the linear modes. In accordance with chapter 4 we study the evolution of the EMCSI in the context of relativistic plasma shell collisions. Again the collision scenario is transferred to a local event set up in slab geometry. Such an abstraction is always a decent simplification in PIC simulations since we restrict to the local microphysics, and the boundary conditions towards a global MHD picture are on weak theoretical grounds. We consider arbitrary collision energies and shell densities, but in extension to chapter 4 introduce a magnetic guide component $\mathbf{B}_\mathrm{G}$ parallel to the shell motion. Due to the excessive length the general derivation of the EMCSI in the presence of a magnetic guide field $\mathbf{B}_\mathrm{G}$ is deferred to Appendix B and we directly move towards a discussion of the solution. After somewhat cumbersome calculations the dispersion relation D finally ensues to

$$\mathrm{D} = \mathrm{LM} \cdot \mathrm{CTW} + \mathrm{CGD},$$

constituted by the Coupled-Two-Stream-Weibel (CTW) mode

$$\mathrm{CTW} = (1-\Omega_2^{-2})[\omega^2(1-\Omega_1^{-2}) - \mathrm{k}_\mathrm{z}^2(1+\Omega_4^{-2}) + 2\omega \mathrm{k}_\mathrm{z}\Omega_3^{-2}] - \mathrm{k}_\mathrm{x}^2[(1+\Omega_4^{-2})(1-\Omega_1^{-2}) + \Omega_3^{-4}],$$

a radiative Light mode (LM)

$$\mathrm{LM} = \omega^2(1-\Omega_1^{-2}) - \mathrm{k}_\mathrm{z}^2(1+\Omega_4^{-2}) + 2\omega \mathrm{k}_\mathrm{z}\Omega_3^{-2} - \mathrm{k}_\mathrm{x}^2,$$

and a class of objects referred to as Coupled-Gyration-Dominated (CGD) modes

$$\mathrm{CGD} = \Omega_\mathrm{G}^2\omega \mathrm{k}_\mathrm{z}\,[\,(1-\Omega_1^{-2})(\mathrm{a}\omega - \mathrm{b}\mathrm{k}_\mathrm{z})^2 - \mathrm{k}_\mathrm{x}^2(\mathrm{a}^2(1+\Omega_4^{-2}) - 2\mathrm{ab}\Omega_3^{-2} - \mathrm{b}^2(1-\Omega_1^{-2}))\,].$$

To preserve clarity we introduced the formal identifications (see Appendix B)

$$\begin{aligned} \Omega_1^{-2} &= \sum_{\mathrm{s,i}} \frac{\mathrm{n}_{0\mathrm{is}}\gamma_{0\mathrm{is}}}{\gamma_{0\mathrm{is}}^2\bar{\omega}_\mathrm{is}^2 - \Omega_\mathrm{G}^2} \\ \Omega_2^{-2} &= \sum_{\mathrm{s,i}} \frac{\mathrm{n}_{0\mathrm{is}}}{\gamma_{0\mathrm{is}}^3\bar{\omega}_\mathrm{is}^2} \end{aligned} \qquad \Bigg| \qquad \begin{aligned} \Omega_3^{-2} &= \sum_{\mathrm{s,i}} \frac{\mathrm{n}_{0\mathrm{is}}\mathrm{v}_{0\mathrm{is}}\gamma_{0\mathrm{is}}}{\gamma_{0\mathrm{is}}^2\bar{\omega}_\mathrm{is}^2 - \Omega_\mathrm{G}^2} \\ \Omega_4^{-2} &= \sum_{\mathrm{s,i}} \frac{\mathrm{n}_{0\mathrm{is}}\mathrm{v}_{0\mathrm{is}}^2\gamma_{0\mathrm{is}}}{\gamma_{0\mathrm{is}}^2\bar{\omega}_\mathrm{is}^2 - \Omega_\mathrm{G}^2} \end{aligned}$$

$$\begin{aligned} \mathrm{a} &= \sum_\mathrm{s} \left(\frac{\mathrm{n}_{0\mathrm{ps}}}{\gamma_{0\mathrm{ps}}^2\bar{\omega}_\mathrm{ps}^2 - \Omega_\mathrm{G}^2} - \frac{\mathrm{n}_{0\mathrm{es}}}{\gamma_{0\mathrm{es}}^2\bar{\omega}_\mathrm{es}^2 - \Omega_\mathrm{G}^2} \right) \\ \mathrm{b} &= \sum_\mathrm{s} \left(\frac{\mathrm{n}_{0\mathrm{ps}}\mathrm{v}_{0\mathrm{ps}}}{\gamma_{0\mathrm{ps}}^2\bar{\omega}_\mathrm{ps}^2 - \Omega_\mathrm{G}^2} - \frac{\mathrm{n}_{0\mathrm{es}}\mathrm{v}_{0\mathrm{es}}}{\gamma_{0\mathrm{es}}^2\bar{\omega}_\mathrm{es}^2 - \Omega_\mathrm{G}^2} \right). \end{aligned}$$

In the first place we are interested in the physics of the TSI and WBI contributions. This is formally expressed in the relation

$$\mathrm{CTW} = \mathrm{TSI} \cdot \mathrm{CT} + \mathrm{WBI},$$

in which the CTW is a combination of the 1D modes in conjunction with a coupling term CT. The relation is superficially equivalent to the situation discussed in sections 4.1, 4.2, though one should be prepared that the presence of a guide component $\mathrm{B_G}$ (i.e. the introduction of a gyration Ω_G) has profound consequences on the mode characteristics. The radiative light mode LM has only real solutions and is itself not growing. This mode is of interest in the context of mode conversion and radiation emission as discussed in section 5.2. The CGD modes are introduced by the magnetic guide field in case of a violation of the initial current neutrality. However, the CGD influence on the instability growth rates is negligible. We further tend to preserve overall current neutrality and therefore choose equal shell densities for both species. Consequently $\mathrm{a, b} \rightarrow 0$ is valid and CGD modes do not contribute.
As already mentioned the

$$\mathrm{TSI} = 1 - \Omega_2^{-2}$$

remains unaffected by the magnetic field. This statement is reflected by the fact that Ω_2^{-2} is independent of Ω_G. Complementarily, the

$$\mathrm{WBI} = -\mathrm{k_x^2}[(1 + \Omega_4^{-2})(1 - \Omega_1^{-2}) + \Omega_3^{-4}]$$

and

$$\mathrm{CT} = \omega^2(1 - \Omega_1^{-2}) - \mathrm{k_z^2}(1 + \Omega_4^{-2}) + 2\omega \mathrm{k_z} \Omega_3^{-2}$$

modes are EM and directly influenced by Ω_G. In order to understand the guide field modifications we choose a collision energy ($\mathrm{v_{z01}} = -\mathrm{v_{z02}} = 0.5,\ \gamma_0 = 1.17$) and study the CTW growth rates as function of $\mathrm{B_G}$. CTW growth rates are determined by the maximum purely imaginary root of the full CTW dispersion relation. The CTW dispersion relation is an irreducible equation of sixth order in ω and therefore can only be evaluated numerically. The CTW is a 2D mode with oblique propagation angle in the $(\mathrm{k_x, k_z})$ plane. Figure 5.1 shows the evolution of the CTW growth in the $(\mathrm{k_x, k_z})$ solution space for progressive $\mathrm{B_G}$ influence. Without magnetic guidance (a) the CTW is a coupled fully degenerate mode. Minor $\mathrm{B_G}$ contributions (b) weakly modify the propagation angle (determined by the respective maximum in the $(\mathrm{k_x, k_z})$ plane) towards parallel (i.e. $\mathrm{k_z}$) propagation. At some threshold guide field value $\mathrm{B_G} = \mathrm{B_G^{ths}}$ (c) the CTW mode degeneracy is suspended and the contributing 1D constituents TSI, WBI and CT emerge distinctively. The exact value of $\mathrm{B_G^{ths}}$ is a characteristic of the relativistic collision energy γ_0. In case of further increased guide field $\mathrm{B_G} > \mathrm{B_G^{ths}}$ (d) the WBI and CT modes are damped. The TSI as purely ES mode remains unaffected by $\mathrm{B_G}$

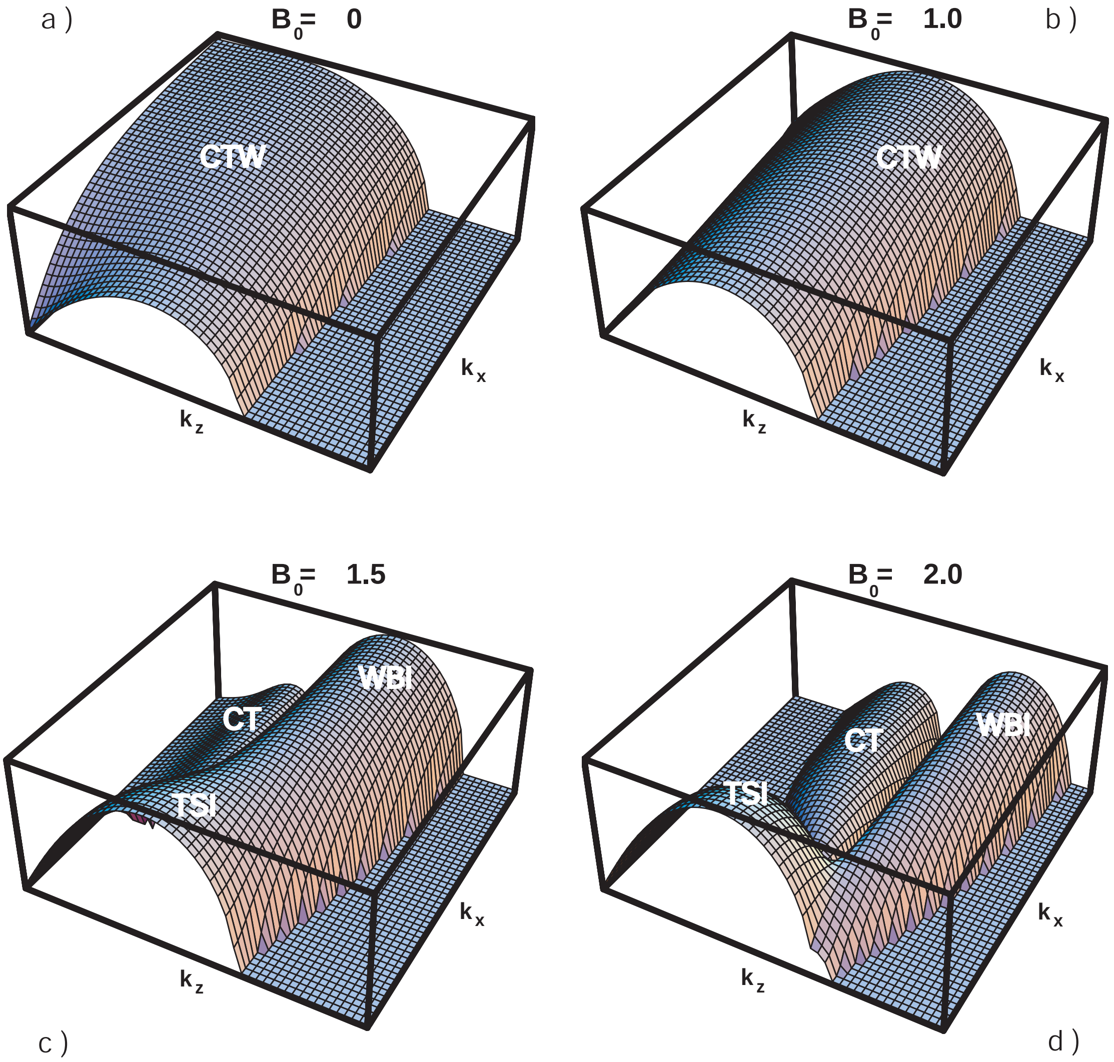

Fig. 5.1: Response of CTW growth (i.e. maximum purely imaginary root of the dispersion relation in each point of the (k_x, k_z) plane) on an increasing magnetic guide component for mildly relativistic colliding shells $v_{z01} = -v_{z02} = 0.5$. For zero guidance the CTW is fully degenerate and obliquely propagating (a). As B_G gains influence (b,c) the CTW distinctively separates into the 1D constituents TSI, WBI and CT. Beyond a certain threshold field $B_G > B_G^{ths}$ the TSI is the dominant mode (d). B_G^{ths} is solely determined by the collision energy and is a characteristic of the system.

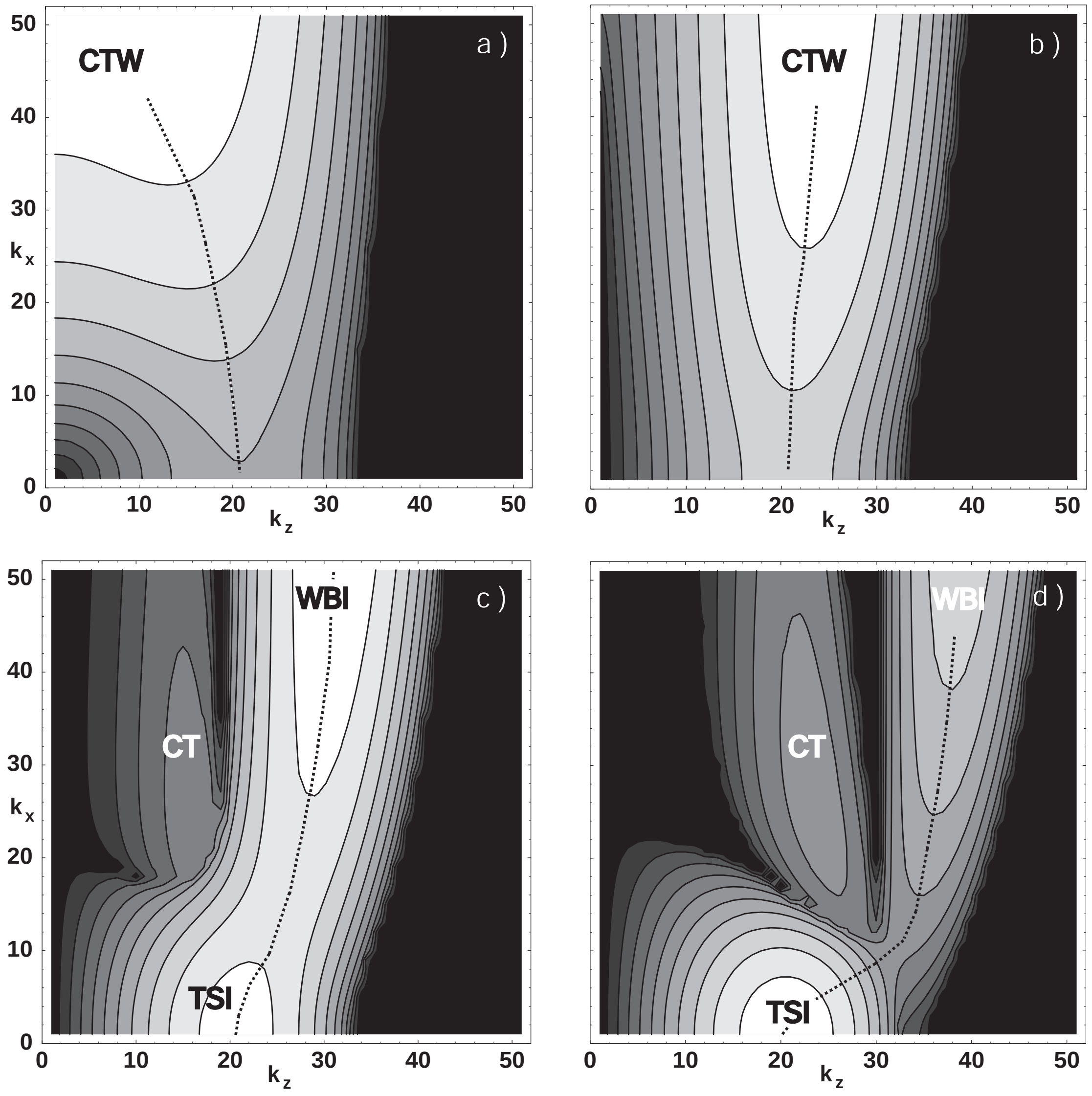

Fig. 5.2: Contours of CTW growth projected into the (k_x, k_z)-plane for the data shown in Fig. 5.1. The dotted black line in each plot indicates the location of maximum growth as function of $k_x = k_\perp$. In the following this line is generally referred to as 'diretissima'. The diretissima evolves smoothly upon B_G variations (a-d). At $B_G = B_G^{ths}$ (c) the CTW is distinctively separated into TSI and WBI along the diretissima. Then the associated growth rates are comparable $\Gamma_{TSI} \sim \Gamma_{WBI}$.

and is pronounced in the relative competition. Within the (k_x, k_z) plane we can define a line which represents the location of maximum CTW growth as function of perpendicular wavenumber k_x. In the following we refer to this line as ‘diretissima’ (Fig. 5.2). The maximum in the diretissima determines the growth rate and propagation angle. The diretissima exhibits monotonous k_x behavior as long as the degenerated CTW is the solely involved mode. As apparent from Fig. 5.3 the diretissima is qualitatively modified around $B_G^{ths}\,\omega_{c0}^{-1} = \Omega_G^{ths}\,\omega_{c0}^{-1} = 1.5$. Then two distinct maxima are formed by the TSI at small k_x and by the WBI at large k_x. In excess of the guide field threshold value $B_G > B_G^{ths}$ the TSI mode prevails. Then the physical nature of the instability has completely changed from 2D EM with oblique propagation (CTW) to 1D ES with parallel (k_z) propagation.

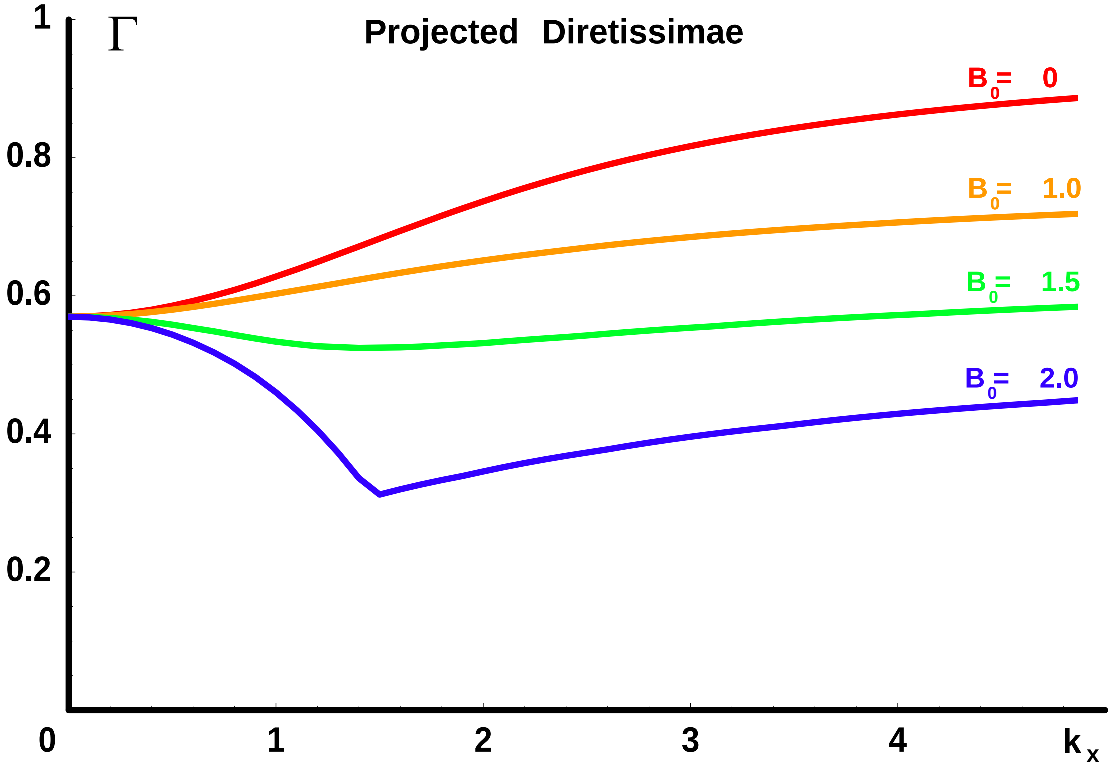

Fig. 5.3: Diretissimae of Fig. 5.2 projected on the perpendicular wavenumber. For negligible B_G only a single distinguished maximum associated with Γ_{CTW} exists. With increasing guidance the mode degeneracy is relinquished and two relative maxima ($\Gamma_{TSI}, \Gamma_{WBI}$) are formed. For $B_G = 2.0 > B_G^{ths}$ the TSI prevails and the instability evolves quasi-parallel $k_x \to 0$.

Since the value of B_G^{ths} is characteristic for the collision γ_0 the critical question focuses on the functional dependence $\mathrm{B_G^{ths}}(\gamma_0)$. Therefore we have to repeat the procedure elaborated before according to Figs. 5.1-5.3 for various γ_0. As often experienced previously, the numerical effort increases dramatically if one pushes towards the ultra-relativistic regime. To obtain the results presented for $\gamma_0 = 1.17$ it is sufficient to evaluate the CTW dispersion relation on a 2500×2500 grid within the $(\mathrm{k_x}, \mathrm{k_z})$ plane. Towards higher collision energies both EM modes become more confined in $(\mathrm{k_x}, \mathrm{k_z})$ space and generally tend towards larger wavenumbers. Consequently the resolution as well as total extension of the $(\mathrm{k_x}, \mathrm{k_z})$ space need to be extended and for $\gamma_0 = 3.5$ the evaluation on a 20000×20000 grid is gradually sufficient. The evolution of $\mathrm{B_G^{ths}}(\gamma_0)$ is shown in Fig. 5.4. The magnetic threshold $\mathrm{B_G^{ths}}$ necessary to suppress EM Weibel contributions and pronounce ES TSI behavior increases dramatically with shell collision energy. The best fitting results are obtained with the relation $\mathrm{B_G^{ths}} = 0.012\,\mathrm{Exp}(2.8\,\gamma_0) + 1.2$. It is a hard job to motivate such an energy dependence from first principles and we therefore just take it for granted. It is important to note that for the observed tremendous increase of $\mathrm{B_G^{ths}}$ the zero temperature approximation within the linear analysis contains a systematic weakness. The particle gyro radius scales like $\mathrm{r_L} \propto \gamma_0/\mathrm{B_G^{ths}}$. As soon as the gyration is confined to scales comparable to the Debye length $\Lambda_\mathrm{D} \propto \sqrt{\mathrm{T}}$ thermal effects become dominant. Qualitatively finite temperature effects are expected to compensate the exponential $\mathrm{B_G^{ths}}$ growth. Then a saturated magnetic threshold $\mathrm{B_G^{ths,sat}}$ exists for ultra-relativistic collisions solely determined by the perpendicular temperature $\mathrm{T}_\perp$. For higher $\mathrm{T}_\perp$ thermal modifications set in for respectively lower γ_0.

Nevertheless the presented results have profound implications for astrophysical scenarios. The deductions on the Weibel-Two-Stream connection permit a most fundamental conclusion: EM Weibel contributions (i.e. filamentation and finite phase space anisotropy) are pervasive in the relativistic regime because the magnetic guide fields required for an efficient suppression of this mode are only realized in very special scenarios.

Applied to plasma transport in extragalactic jets the Weibel-Two-Stream characteristics draft the following (very general) picture. Jets are composite objects in phase space with a low-energy, isotropic und roughly thermalized component and a high-energy, anisotropic and highly non-thermal component. Depending on the relative weight of both components and the local magnetic field structure, the coupled 2D CTW or one of the 1D modes (TSI/WBI) shapes the plasma configuration. For a strongly relativistic non-thermal particle distribution the Weibel filamentation is ubiquitous. Magnetic fields on extragalactic scales are not competitive in suppressing the filamentation. A finite residual anisotropy and associated plasma transport over vast distances prevail. At certain points the jet/magnetic field structure is deformed by macroscopic instabilities and interactions with the intergalactic medium. Then the low-energy component can take over and TSI contributions become pronounced. At such locations dissipative processes prevail and the mentioned ‘hot spots’ are formed.

The pulsar magnetosphere is one of the rare examples in which the magnetic guide field is sufficiently strong to suppress Weibel filamentation at highly relativistic energies. As is derived in the next section, the assumption of a specific emission mechanism for pulsar radio bursts is sufficient to estimate plasma shell collision energies of $\gamma_0 \sim 10$. Employing the best fit result of Fig. 5.4 the threshold value for the magnetic Weibel suppression

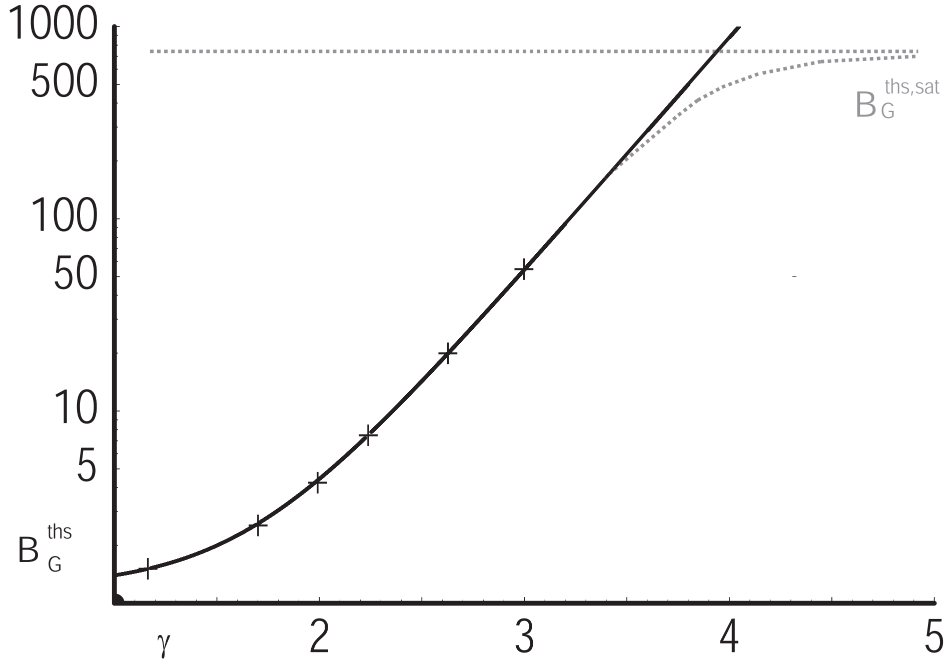

Fig. 5.4: B_G^{ths} is a characteristic for shell collisions at relativistic energy γ_0. Within the constraints of the cold beam limit the guidance threshold scales like $B_G^{ths} = 0.012\,\mathrm{Exp}(2.8\,\gamma_0) + 1.2$ as best fit result to the calculated values (crosses). The exponential growth of B_G^{ths} is not-recoverable and certainly an artefact of the zero temperature approximation. Thermal effects (indicated qualitatively by the dotted extrapolation) are expected to introduce significant compensation of B_G^{ths} growth and asymptotic saturation towards $B_G^{ths,sat}$. For progressively higher T the compensation sets in for comparatively lower γ_0 and associated saturation occurs at lower $B_G^{ths,sat}$.

is estimated to $B_G^{ths,sat} \sim 10^8$ G. Observations indicate that pulsar emission heights are reproducible and stable [Kijak & Gil, 1997; 1998]. Again in anticipation of the next section we state that the magnetic field at typical emission heights subsumes to $\sim 10^8$ G. Therefore we can close our discussion on the Weibel-Two-Stream connection with a somewhat provocative conjecture: Presumably pulsar emission heights are determined by the magnetic threshold for Weibel suppression. Plasma shell collisions in the pulsar magnetosphere proceed via the interaction of different generations of pair cascades. If relative bulk velocities are not too high, a finite time interval is necessary for the interpenetration of shells (for typical emission heights measured for the Crab pulsar the corresponding time intervals would range around milliseconds). Efficient emission can only take place as long as the energy dissipation conducted by the TSI is prominent (upper limit of heights) and counterstreaming is sufficient (lower limit of heights). Stable emission heights result as the logical consequence.

5.2 The Connection to Pulsar Physics - Stimulation of Collisionless Bremsstrahlung

Essential results of the following section are published in

'Ultra-Relativistic Plasma Shell Collisions
in Pulsar Magnetospheres and Gamma-Ray Bursts'

C.H. Jaroschek, C. Nodes, R. Schopper, H. Ruhl, and H. Lesch
High Performance Computing in Science and Engineering, Munich, 2004,
New York: Springer, 419

The appearance of the TSI as individual conformalized 1D mode is restricted to astrophysical scenarios with preeminent magnetic guide field. This remarkable insight is obtained from the previous discussion of the Weibel-Two-Stream connection. The foremost paradigm for such plasma configurations is the magnetosphere of a pulsar. The magnetosphere is defined as the plasma environment governed by the magnetic field around the central neutron star. The magnetic field is of dipolar structure up to a reasonable degree of approximation. Extreme field strengths up to 10^{13} G are reached close to the neutron star surface. The eponymous features of pulsar emission are the stationary pulse profiles which result in the superposition of a large number of individually non-stationary emission events. The pulse features characterize the radio (= low energy) pulsar emission. Several theoretical concepts of pulsar emission are under controversial discussion: Curvature radiation which has aged to become somewhat like the 'standard emission model', maser mechanisms and collisionless Bremsstrahlung stimulated in the turbulent electric fields of the non-linear TSI. Curvature radiation is synchrotron emission of the high energy particles traveling outwards along the magnetic field. Particle motion is strictly confined parallel to the magnetic field lines, since any perpendicular motion is gyro-magnetically damped. Synchrotron damping of perpendicular motion takes place on timescales which are extremely short compared to any timescale adherent to the neutron star dynamics or magnetospheric plasma physics. The parallel motion forced along the dipolar curvature is unstable to synchrotron emission.
All emission mechanisms have the potential to explain certain observed features of pulsar emission. This is essentially due to the fact that there exists only a very rough picture of the pulsar magnetosphere and the lack of a detailed global description is usually overcompensated by the arbitrariness in the plasma conditions. There are quite a few models of the pulsar magnetosphere (see [Michel, 1982; 1991] for an overview), however, none of these concepts leaves without a significant number of open questions - not to say inconsistencies. In such situations the usual scientific procedure is falsification, i.e. formulate the question: Are there extreme observed features placing critical constraints on the emission process to rule out competing mechanisms? At this point the observations of the Crab pulsar radio bursts by Hankins et al. [2003] assume an outstanding quality. These observations show three distinct characteristics: First, the radio bursts exhibit substructures evolving on nanosecond (ns) timescale ($\Delta t = 2\,ns$),

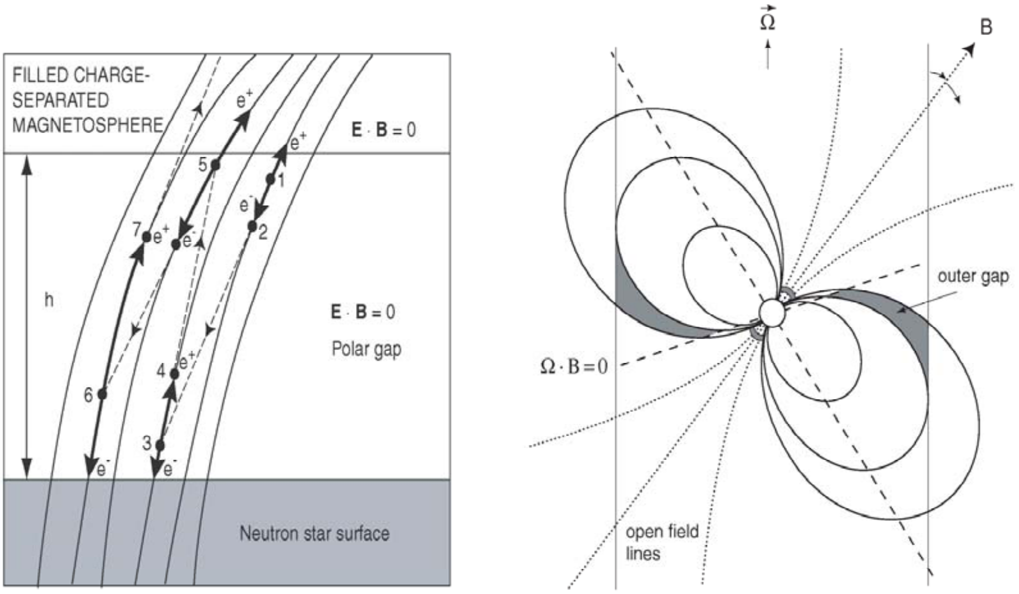

Fig. 5.5: Colliding plasma shells in the pulsar magnetosphere: Particle acceleration zones in the 'polar cap' regions [Sturrock, 1971; Ruderman & Sutherland, 1975] trigger cascades of secondary lepton pairs (left). Cascades are localized non-stationary events. Different plasma generations (i.e. shells) collide on the way out towards the light cylinder [Usov, 1987]. Critical for the validity of the emission is the cascade multiplicity M [Melrose & Gedalin, 1999]. A competing model for the stimulation of shell collisions is the 'outer gap' scenario (right) [Cheng, Ho & Ruderman, 1986a;b]. The polar cap approach is potentially superior for the description of nanosecond radio bursts since it creates pencil-shaped beams. In the outer gap model plasma beams spread to fan-shape which sets the foundation to explain a composition of several pulses as observed in the high energy γ-ray emission of some pulsars.

i.e. the location of radiation emission observes extreme local confinement. Dipolar fields have a finite curvature and multipole extensions decrease rapidly in strength. Consequently curvature radiation fails to explain emission timescales below $\sim 10\,\mu\mathrm{s}$ [Benford, 1977]. Second, the observed emission spectrum is broad $\Delta\nu_{\mathrm{obs}} \sim 500\,\mathrm{MHz}$ which is a systematic problem in maser mechanism approaches. And finally, the extreme radiative flux intensity of $\mathrm{S} = 1000\,\mathrm{Jy}$ associated with the observed radio spikes implies brightness temperatures $\mathrm{T_B} = \mathrm{Sd}^2/2\mathrm{k}(\nu_{\mathrm{obs}}\Delta\mathrm{t})^2 = 10^{37}\,\mathrm{K}$ (employing the Crab's distance $\mathrm{d} = 2\,\mathrm{kpc} = 6.5 \cdot 10^3\,\mathrm{Ly}$, isotropic emission assumed). Such extreme brightness temperatures clearly indicate a coherent emission mechanism. Just one single mechanism fulfills all the above criteria: The coherent radiation emission of relativistic particles stimulated in the collective parallel electric fields of the non-linear TSI.

Before we study the emission mechanism in detail, it is necessary to elaborate on the concept of plasma shell collisions in the context of global magnetospheric models and motivate the plasma conditions pervasive in the emission region. Pulsar emission is rotation-powered, i.e. the intense spin of the central neutron star is the ultimate power supply. The Crab pulsar PSR 0531+21 is with only 943 years of activity the youngest of all presently known radio pulsars. Consequently rapid rotation with $\mathrm{T_{rot}} = 33\,\mathrm{ms}$ periodicity is observed. Applying the MHD force free condition, rotation-induced $\mathbf{E} = -\mathbf{v}_{\mathrm{rot}} \times \mathbf{B}$ electric fields arise in the magnetosphere. At some distance from the neutron star surface along the extension of the magnetic poles the field lines are sufficiently curved to account for a significant parallel electric field component $\mathrm{E}_{\|} = \mathbf{E} \cdot \mathbf{B}/\mathrm{B} \neq 0$. In such 'polar caps' particles are accelerated to extreme energies which then in turn trigger cascades of secondary pairs (Fig. 5.5). The pair creation multiplicity M is a critical quantity. Melrose & Gedalin [1999] argue that $\mathrm{M} \lesssim 50$ should not be significantly exceeded, otherwise TSI stimulated emission ranges above the radio regime. Pair cascades are highly non-stationary and randomly localized events. Each cascade represents a plasma shell moving at relativistic speeds outwards along the field lines. Due to differences in the respective bulk velocities, different shell generations collide at some distance from the neutron star.

Are there reasonable estimates for the plasma parameters present in such shell collisions? Strict physical reasoning is tedious because consistent magnetospheric models are not at hand. We therefore propose a basic concept which is intriguing just due to its simplicity: We employ the frequency $\nu_{\mathrm{obs}} = 5.5\,\mathrm{GHz}$ observed by Hankins et al. [2003] and introduce the connection to the local plasma shell conditions (bulk energy γ, plasma frequency ω_{p}) via the assumption for the emission mechanism. In a second line of reasoning we apply the timescale estimate for the spatial restriction of the emission zone ($\mathrm{c}\Delta\mathrm{t} = 60\,\mathrm{cm}$) and provide the second constraint on the plasma conditions:

Emission Frequency + Emission Mechanism		Emission Timescale + Elementary Radiation Event
$2\pi\,\nu_{\mathrm{obs}} = \gamma^2\,\omega_{\mathrm{p}}$ $2\pi\,\nu_{\mathrm{obs}} = \gamma^2\,(4\pi \mathrm{e}^2 \mathrm{n}/\gamma \mathrm{m})^{1/2}$		$\mathrm{c}\,\Delta\mathrm{t} = \mathrm{c}/\omega_{\mathrm{p}}$ $\mathrm{c}\,\Delta\mathrm{t} = \gamma^{1/2}(\mathrm{mc}^2/4\pi \mathrm{ne}^2)^{1/2}$
intrinsically relativistic plasma (see Melrose & Gedalin [1999])		
$\mathrm{n} = \mathrm{m}/(4\pi\mathrm{e}^2)\,(2\pi\nu_{\mathrm{obs}}/\Delta\mathrm{t}^3)^{1/2}$	$\longleftarrow$	$\gamma^{3/2} = (4\pi\mathrm{ne}^2\Delta\mathrm{t}^2/\mathrm{m})^{3/2}$
		$\gamma = (4\pi\mathrm{ne}^2/\mathrm{m})\,\Delta\mathrm{t}^2$
$\underline{\mathbf{n = 6.5 \cdot 10^8}\,\mathrm{cm}^{-3}}$	$\longrightarrow$	$\underline{\gamma = \mathbf{8.3}}$

From the relations further follows the scaling $\mathrm{n} \propto \Delta \mathrm{t}^{-3/2}$ and $\gamma \propto \Delta \mathrm{t}^{1/2}$. If we further restrict to the Goldreich-Julian case [Goldreich & Julian, 1969] of the aligned rotator, the derived density

$$\mathrm{n} = \mathrm{n}_{\mathrm{GJ}} = \frac{\mathrm{B}}{\mathrm{ecPx}^3} = 6.3 \cdot 10^{12} \mathrm{cm}^{-3} \left(\frac{\mathrm{B}}{3 \cdot 10^{12}\,\mathrm{G}} \right) \left(\frac{\mathrm{P}}{33\,\mathrm{ms}} \right)$$

corresponds to a guide field strength $\mathrm{B}_{\mathrm{G}} = 3.1 \cdot 10^8$ G and an associated emission height of $\mathrm{x} = \mathrm{R}_{\mathrm{em}}/\mathrm{R}_{\mathrm{NS}} \simeq 21$. We note that the result for x is in fine agreement with observationally motivated emission heights [Kijak & Gil, 1997; 1998]. For the estimated bulk energies $\gamma \lesssim 10$ contemporary supercomputers are sufficiently powerful to simulate the non-linear TSI and resolve explicitely the associated stimulation of collisionless Bremsstrahlung.
The PIC simulations are again performed in slab geometry (Figs. 5.6-5.9). Deviating from the GRB scenario we study shell collisions not in the cms frame, but rather in the frame comoving with one plasma shell. The collision with a successive shell generation of higher bulk motion is then translated into the injection of a relativistic plasma beam (Fig. 5.6). A magnetic guide field B_{G} of extreme strength confines the trajectories of plasma particles into a 1D entirely parallel motion. The magnetic guidance is $\mathrm{B}_{\mathrm{G}}/\mathrm{B}_0 = 10^7$ times the equipartition field strength. According to the discussion of the Weibel-Two-Stream connection in section 5.2, we are clearly in the regime in which Weibel contributions are efficiently suppressed. With the purely electrostatic TSI as the preeminent instability mode of the system, the density fluctuations structure the beam during interpenetration of the background shell (Fig. 5.6a-c). Via the Poisson equation density fluctuations immediately translate into electric field variations. As we introduced the physical nature of the TSI in section 4.1, we already discussed the correlation between density fluctuations and parallel electric fields in detail. Collective parallel electric fields generated by the Langmuir-TSI cause significant variations in the electric potential. During the non-linear evolution of the TSI density variations up to $\Delta \mathrm{n}/\mathrm{n}_0 = 20$ are reached for sufficiently high bulk energies (see Fig. 5.12a). Relativistic beam particles then see extreme potential drops/gains and as a consequence thereof receive considerable momentum changes. Particles suffering non-stationary acceleration rates emit electromagnetic radiation. Radiation emission is stimulated by the Langmuir-TSI fields. The free energy stored in the non-thermal distribution of beam particles is equivalent to 'inverse occupation' of quantized though quasi-continuous Fermi levels in solid material. Since Langmuir fields are extended in configuration space an entire ensemble of beam particles emits phase-coupled, i.e. stimulated emission is coherently amplified. All these characteristics expose the similarity to the semiconductor laser. Therefore the concept of stimulated emission observed from an electron beam was introduced by Hasegawa [1978] as the 'Free Electron Laser' (FEL).
Melrose [1978] then recognized the potential of the FEL mechanism to explain nonthermal emission features of radio pulsars. Further features and implications of this process in the context of astrophysical scenarios are elaborated by Weatherall [1988] and Weatherall & Benford [1991]. Therein the FEL mechanism is renamed to collisionless Bremsstrahlung. Originally Bremsstrahlung takes place via Coulomb scattering of charged particles and therefore requires the interaction of species with different mass,

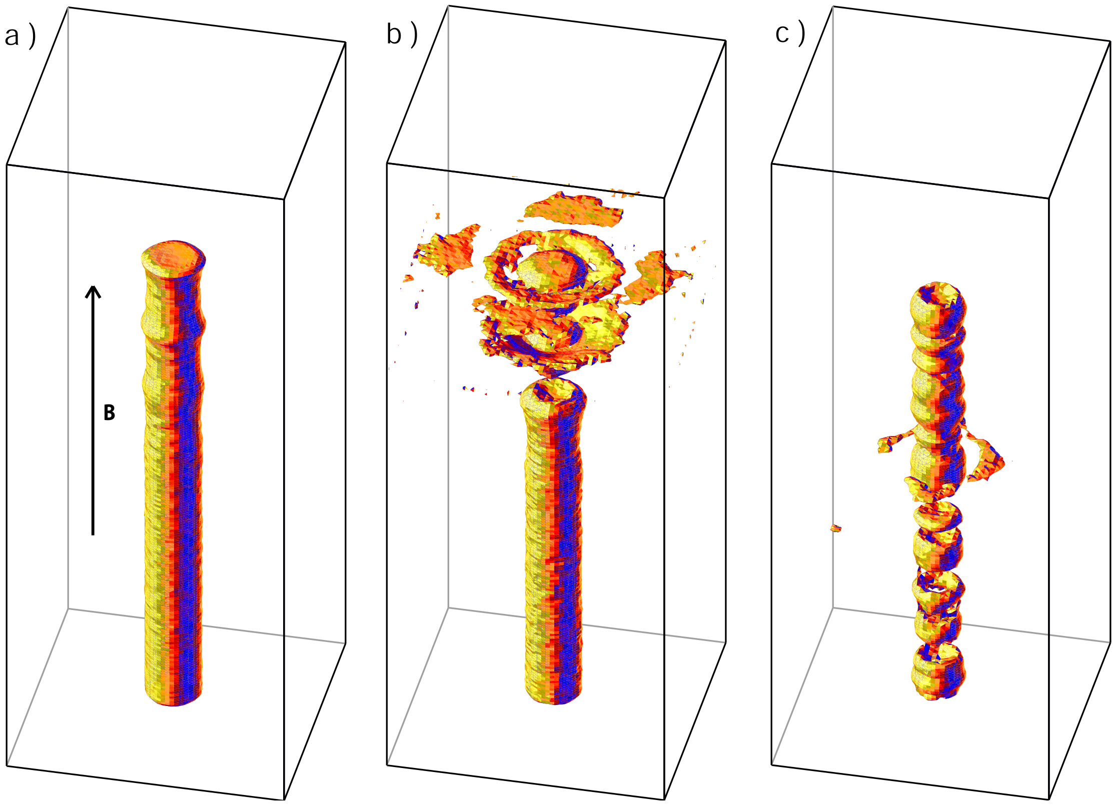

Fig. 5.6: Equidensity surfaces for the electrons at $t_1 = 20.47\,\mathrm{ns}$ (a), $t_2 = 30.17\,\mathrm{ns}$ (b), and $t_3 = 40.31\,\mathrm{ns}$ (c). The plasma beam is injected at the lower boundary and propagates parallel to the magnetic guide field **B**. The instability sets on at the uppermost beam extension (i.e. after maximum interaction time) and continues downwards. Surfaces correspond to electron densities $n^-/n_0 = 2$ in (a,b). The plasma beam gradually enters the non-linear Two-Stream regime (t_1) and couples radiatively to the background shell electrons (t_2) during non-linear saturation. At late times (t_3) the system evolves towards a saturated state which is highly structured in density over the entire beam extension (equidensity surfaces for $n^-/n_0 = 4.5$).

i.e. the Bethe-Heitler cross section approaches zero in the pair plasma limit. As noted several times in the previous chapters Coulomb scattering between nearest neighbours is in general negligible in the low density plasmas pervasive in astrophysical sites. However, Coulomb scattering takes place efficiently in the collective fields of the TSI. Since the plasma is collisionless and the mass composition of plasma species is irrelevant the process is then called Coherent Collisionless Bremsstrahlung (CCB) in order to discriminate from the inherited meaning. A third denomination of still the same mechanism is inverse Compton upscattering of Langmuir wave packets. The FEL can be understood as the upscattering of Langmuir wave packets off a relativistic electron distribution to-

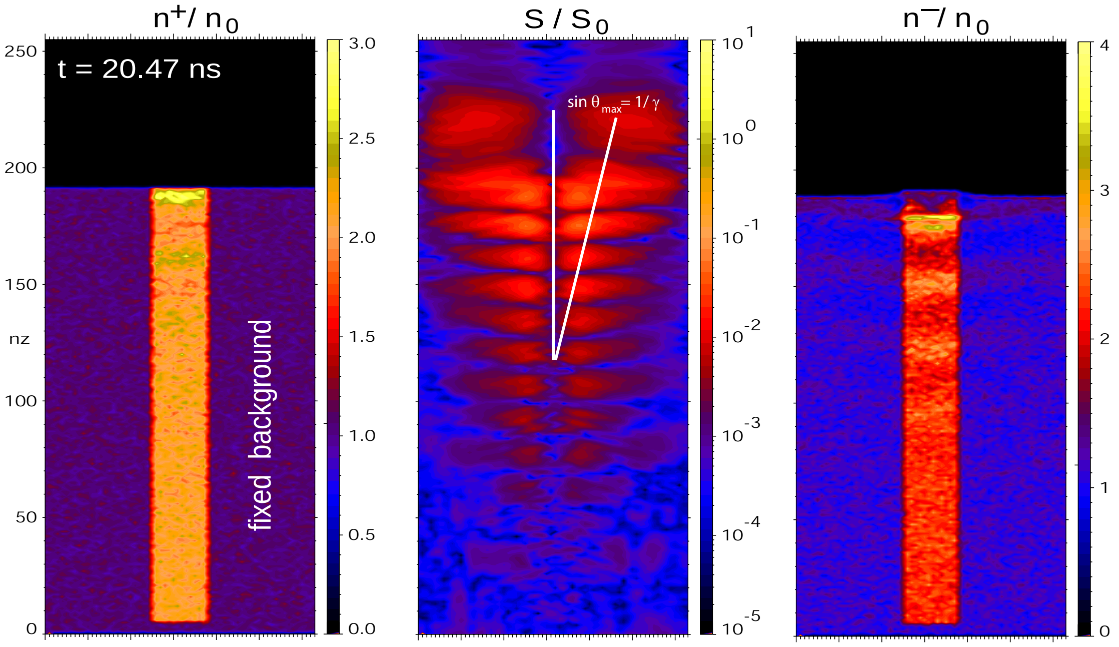

Fig. 5.7: (x, z)-cuts through the simulation box center for the configuration corresponding to Fig. 5.6a. The TSI gradually evolves towards the non-linear regime. Density fluctuations in positrons (n^+) and electrons (n^-) introduce parallel Langmuir electric fields (cf. Fig. 4.3). Relativistic particles are accelerated in the collective Langmuir-TSI fields and radiate. The radiation emission is relativistically beamed with maximum Poynting flux diverted to an angle $\sin\theta_{\max} \simeq 1/\gamma$ towards the bulk motion.

wards high frequencies [Schopper, 2002]. The nice characteristic of this interpretation is that energy proportions directly refer to the original process of Compton scattering ($1{:}\gamma{:}\gamma^2$), since quasi-stationary Langmuir fields scatter off a beam of relativistic energy γ and emit radiation of energy $\sim \gamma^2$. The drawback in this interpretation is that the Compton scenario incorporates the momentum exchange between photons and electrons and it is hard job to define the momentum for the low-frequency dispersed Langmuir wavepackets. Since the Bremsstrahlungs-approach has its footing on the energy balance of the process we can start on save grounds with the frequency as obtained from the linear Langmuir dispersion relation. Therefore we convene to proceed with the denomination Coherent Collisionless Bremsstrahlung (CCB).

Previous to the interpretation of simulation results we expose the theoretical foundations of the CCB process. The plasma beam is injected with relativistic energy $\gamma = (1 - \mathrm{v}^2)^{-1/2}$ and triggers the TSI. The 1D TSI dispersion was analyzed in section 4.1. Therein the linear TSI growth Γ_{TSI} associated with certain wavenumber $\mathrm{k}_{\max}$ has been identified. In the non-linear regime such linear results are transformed to $\Gamma^{\mathrm{nl}}_{\mathrm{TSI}}$

and $k_{\max}^{\rm nl}$ and reliable values are accessible only in the direct numerical simulation. The non-linear TSI evolves in the background plasma. Relativistic beam particles scatter off the Lorentz transformed Langmuir-TSI electric fields.

In the following we again make efficient use of the dimensionless representation (cf. Appendix A for details). In all derivations and all PIC simulations we choose $c = v_{A0}$. Consequently dimensionless frequencies ω refer to the normalized plasma frequency of the system ω_{p0}, velocities to the speed of light, and wavenumbers k to the inverse skin depth ω_{p0}/c, i.e. we employ an electromagnetic gauge. If we define the 4-wavevector $k_\mu = (\omega, \mathbf{k})$ the quantity $k_\mu x^\mu = \mathbf{kx} - \omega t$ forms a Lorentz invariant with any arbitrary 4-vector x^μ. Then the Lorentz transformed $(K \to K', K' \to K)$ wavevectors result as components of $k_\sigma = \Lambda_\sigma^\nu k_\nu$ straightforwardly to

$$\begin{array}{rcl|rcl} \omega' &=& \gamma(\omega - v k_{||}) & \omega &=& \gamma(\omega' + v k'_{||}) \\ k'_{||} &=& \gamma(k_{||} - v\omega) & k_{||} &=& \gamma(k'_{||} + v\omega') \\ \mathbf{k}'_\perp &=& \mathbf{k}_\perp & \mathbf{k}_\perp &=& \mathbf{k}'_\perp. \end{array}$$

Electron-positron pairs interact in the beam system K' with Langmuir wavepackets of frequency

$$\omega'_{\rm TSI} = \gamma(\Gamma_{\rm TSI}^{\rm nl} - v k_{\max}^{\rm nl}),$$

which is the fundamental frequency of the stimulated electromagnetic radiation $k'_{\rm EM} = \omega'_{\rm EM} = \omega'_{\rm TSI}$. The wavenumber $k_{\rm EM}$ received by an observer in the laboratory frame K then simply ensues as the Doppler-boosted quantity

$$k_{\rm EM} = k'_{\rm EM}\gamma(1 + v\cos\theta'),$$

with θ' the angle of emission in K' respective to the bulk motion. Conclusively, the stimulated collisionless Bremsstrahlung is observed with wavenumber

$$k_{\rm EM} = \gamma^2\left(\Gamma_{\rm TSI}^{\rm nl} - v\, k_{\max}^{\rm nl}\right)\left(1 + v\frac{\cos\theta - v}{1 - v\cos\theta}\right).$$

In the last step we used the 'light aberration' in the transition $K \to K'$

$$\cos\theta' = \left(\frac{\cos\theta - v}{1 - v\cos\theta}\right)$$

which directly ensues from the Lorentz transformation of parallel velocity u

$$u'\cos\theta' = u'_{||} = \left(\frac{u\cos\theta - v}{1 - v\, u\cos\theta}\right)$$

in the light speed limit $u, u' \to 1$. The essential insight obtained from these considerations is that the frequency of CCB scales as function of collision energy like $\omega_{\rm EM} \simeq \gamma^2\Gamma_{\rm TSI}^{\rm nl}$.

The next deliberate question concentrates on the received angular power $\mathrm{dP/d\Omega}$ in the lab frame K (which in the relativistic regime due to the effect of beaming and time dilation is clearly distinguished from the emitted angular power in K'). According to Rybicki & Lightman [1979] the emitted angular power in the instantaneous rest frame K' results as function of parallel acceleration $\mathrm{a}'_{||}$ as

$$\mathrm{dP}'_{\mathrm{e}}/\mathrm{d\Omega}' = \frac{\mathrm{e}^2}{4\pi \mathrm{c}^3}\,\mathrm{a}^{2\prime}_{||}\,\sin^2\theta'.$$

In analogous argumentation as above for the parallel light aberration we infer the perpendicular aberration $\sin^2\theta'$, further calculate $\mathrm{a}'_{||} = \gamma^3 \mathrm{a}_{||}$ and finally derive the received angular power in the simulation lab frame

$$\begin{aligned}
\mathrm{dP/d\Omega} &= \mathrm{dW/dtd\Omega} \\
&= \frac{1}{\gamma(1-\mathrm{v}\,\cos\theta)}\,\frac{1}{\gamma^2(1-\mathrm{v}\,\cos\theta)^2}\,\frac{1}{\gamma(1-\mathrm{v}\,\cos\theta)}\,\frac{\mathrm{e}^2\gamma^6\mathrm{a}_{||}^2}{4\pi\mathrm{c}^3}\,\frac{\sin^2\theta}{\gamma^2(1-\mathrm{v}\,\cos\theta)^2} \\
&= \frac{\mathrm{e}^2\mathrm{a}_{||}^2}{4\pi\mathrm{c}^3}\,\frac{\sin^2\theta}{(1-\mathrm{v}\cos\theta)^6}
\end{aligned}$$

with individual contributions of time dilation for the *received power*

$$\mathrm{dt} = \gamma(1-\mathrm{v}\,\cos\theta)\mathrm{dt}',$$

relativistic beaming ('lighthouse effect')

$$\begin{aligned}
\mathrm{d\Omega} &= \gamma^2(1-\mathrm{v}\,\cos\theta)^2\mathrm{d\Omega}' \\
\sin^2\theta' &= \frac{\sin^2\theta}{\gamma^2(1-\mathrm{v}\,\cos\theta)^2}
\end{aligned}$$

and Lorentz boosting

$$\mathrm{dW} = \gamma^{-1}(1-\mathrm{v}\,\cos\theta)^{-1}\mathrm{dW}'.$$

In the non-relativistic limit $\gamma \to 1$ the radiation emission takes place pervasively transverse to the bulk motion (Fig. 5.8). In the relativistic regime the lighthouse effect confines the spatial angle towards a cone around the particle trajectory in which the power deposition is highly boosted. For high bulk energies $\gamma \gg 1$ the Doppler factor is well approximated by $(1-\mathrm{v}\cos\theta) \simeq (1+(\theta\gamma)^2)/2\gamma^2$ and the angular power by

$$\mathrm{dP/d\Omega} \simeq \frac{16\mathrm{e}^2\mathrm{a}_{||}^2}{\pi\mathrm{c}^3}\,\gamma^{10}\,\frac{\gamma^2\theta^2}{(1+\gamma\theta)^6},$$

respectively. Obviously maximum emission occurs at $\sin\theta_{\mathrm{max}} \simeq 1/\gamma$ and within a progressively sharply confined azimuthal spread around θ_{max} the power is Lorentz boosted by the factor γ^{10}. The lighthouse effect is retained in the PIC simulations in the relativistic beaming of the Poynting flux (Fig. 5.7). During the late time evolution of the system the density fluctuations and associated radiation characteristics evolve into turbulent structures (Fig. 5.9). Background and beam plasma are withdrawn from the simulation box at $\mathrm{l_z} = 3/4\,\mathrm{L_z}$ to discriminate the radiative light modes from the EM modes which require the pair plasma as carrier medium.

The plasma processes presented in Figs. 5.6-5.9 take place at a shell collision energy $\gamma = \sqrt{5} \simeq 2.23$. With the previous estimate on the plasma conditions expectable during shell collisions in the pulsar magnetosphere, the projected target energy is $\gamma \sim 8.3$. As

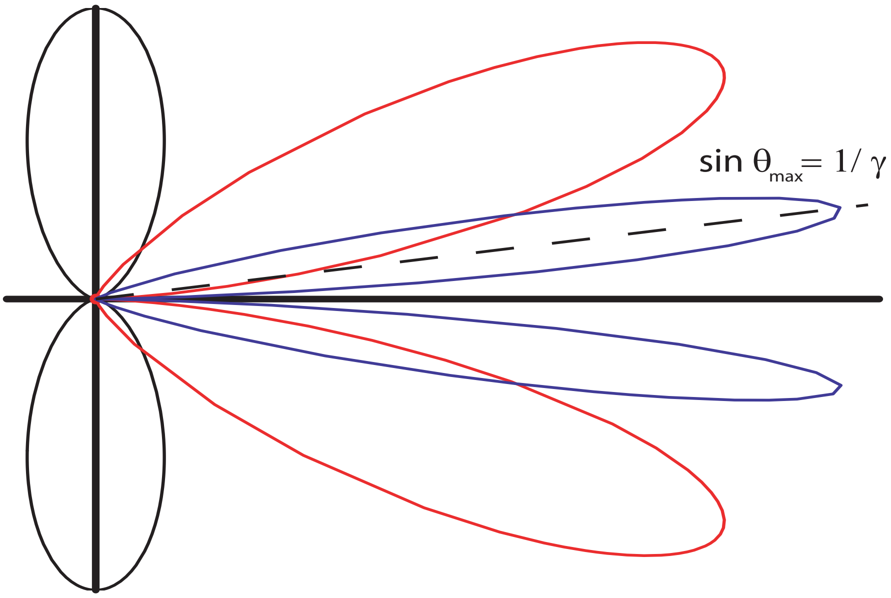

Fig. 5.8: Polar diagram of the normalized angular power $\gamma^{-10}\,\mathrm{dP/d\Omega}$ for bulk motions $\gamma = 1, 2.23, 6.2$ (black,red,blue) directed towards the positive z-direction. The lighthouse effect confines the radiative power progressively into a cone around the particle trajectory with opening angle $\sin\theta_{\mathrm{max}} = 1/\gamma$ $(\Delta\theta/\theta_{\mathrm{max}} \ll 1)$. Relativistic effects further tremendously increase the angular power around θ_{max} and therefore the polar diagrams are normalized by the factor $\gamma^{-10} = 1, 1/3125, 1/9160$ for the respective energies.

experienced so often before the numerics get complicated as one pushes towards highly relativistic energies. The computational effort ϵ_{PIC} for 3D PIC simulations of the CCB process scales like

$$\epsilon_{\mathrm{PIC}} \propto \gamma^{2\cdot 3} \cdot \gamma^{2} \cdot \gamma^{3/2} \cdot \gamma^{3/2} = \gamma^{11}$$

with relativistic energy. Due to the fact that in the CCB mechanism the EM radiation is generated with a frequency $\propto \gamma^2$ the respective spatial resolution in 3D and the time resolution have to be adapted accordingly. Further the TSI growth is relativistically damped by a factor $\gamma^{3/2}$ (see section 4.1) and takes place at wavelengths roughly extended by an additional factor of $\gamma^{3/2}$. The immediate consequence thereof are correspondingly longer simulation times and prolonged system extensions.

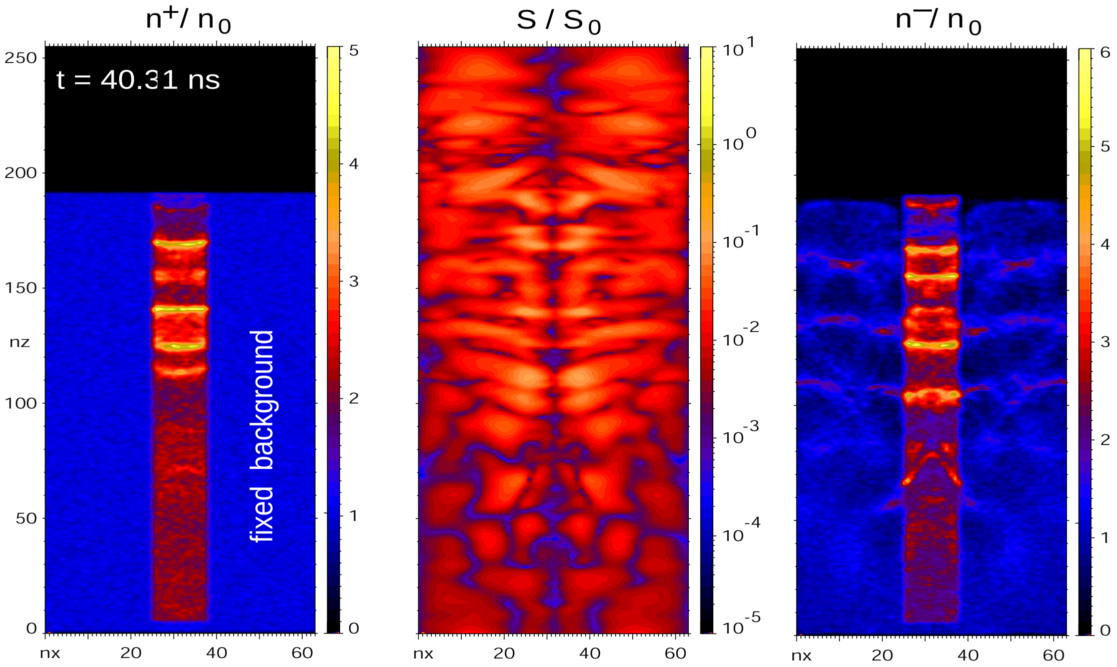

Fig. 5.9: At late times the configuration evolves into a dynamic equilibrium between beam injection and radiation emission. Local density fluctuations are highly non-stationary and the conditions are generally referred to as strong Langmuir turbulence.

Towards higher energies density fluctuations and associated stimulated CCB get even more pronounced. Figure 5.10 shows the configuration during the saturated state of Langmuir turbulence for collision energy $\gamma = 4.46$. For this energy the total system extension is already increased to a length of $L_z = 80.96\,(c/\omega_{p0})$ represented on 4096 grid points. (For comparison with Figs. 5.6-5.9: Shell collisions with $\gamma = 2.23$ are sufficiently resolved on extensions of $L_z = 40.48\,(c/\omega_{p0})$ with 256 grid points.) At this energy the radiative pressure of the stimulated Poynting flux is already sufficient to drive the feedback on the plasma density. The interaction between Poynting flux bursts and density fluctuations is studied along a cut through the (x, z) plane in Fig. 5.11. At a certain point in time $t = t_1$ extreme density fluctuations trigger burst-like stimulation of CCB. The Poynting flux evolves into solitonic structure and proceeds in parallel direction. The snapshot at $t = t_2$ shows that the Poynting flux S soliton provides feedback to the plasma in driving a fluctuation in plasma density n. A trailing Poynting flux burst is generated by the plasma density response and, hence, closing the instability feedback loop. The process is denominated as 'light surfing' since it reminds of the shock surfing mechanism. Shock surfing efficiently generates non-thermal particles as the plasma response of the potential variations proceeding at the front of 2D or 3D collisionless shocks.

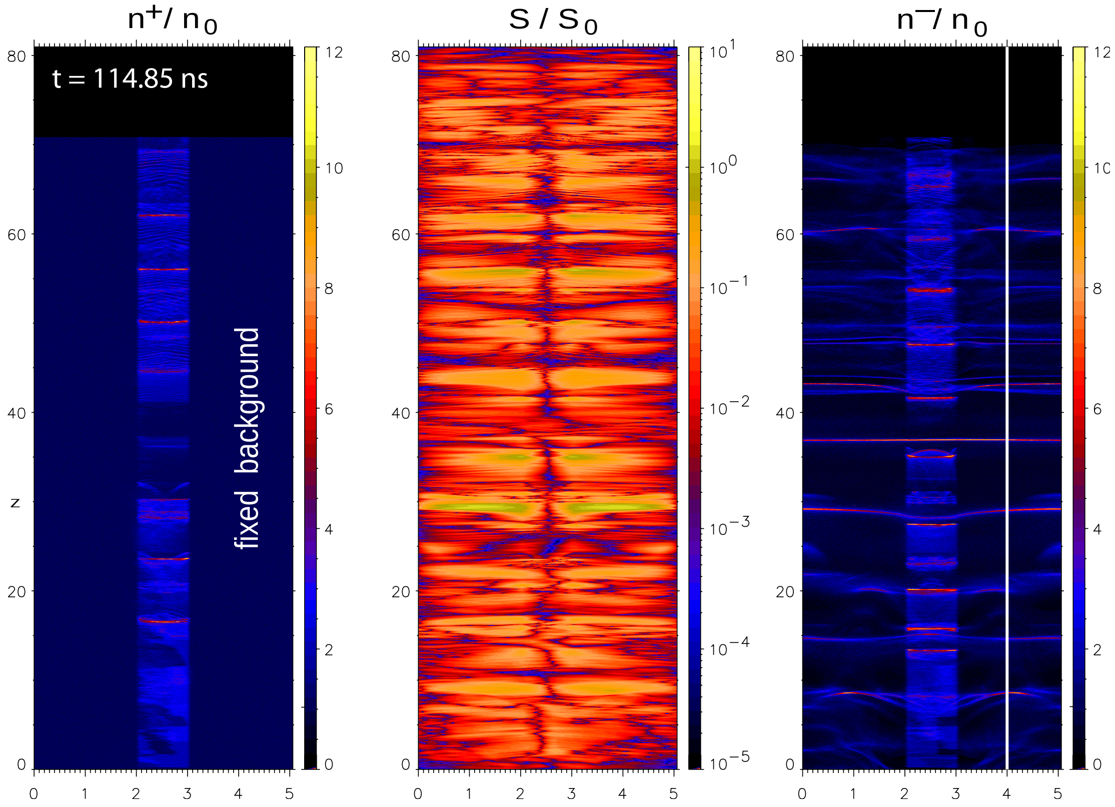

Fig. 5.10: Late time evolution of the configuration for $\gamma_0 = 4.46$. Density fluctuations become progressively violent and 'Poynting-Flux'-driven. The white line serves as cut for the analysis exposed in Fig. 5.11.

The previous analysis has validated the concept of CCB stimulated in strong Langmuir turbulence as efficient source of pulsar radio emission. Two critical points remain in the effort to explain the extreme radiation fluxes on nanosecond timescales as reported by Hankins et al. [2003]: First, under the assumption of CCB as emission mechanism, what is the minimum amount of plasma turbulent energy density w_{turb} necessary to explain the observed power P_{obs}? To predict a lower limit, optimum coherence is assumed, i.e. all particles sharing the maximum coherence volume $\mathrm{V_{coh}}$ accessible by a process beamed into spatial angle $\Delta\Omega \sim 1/\gamma^2$ radiate coherently. Then the minimum necessary turbulent energy density $\mathrm{w_{turb}}$ ensues to:

- Coherent emission: $\mathrm{P_{coh} = N^2 P_s}$ $\qquad \mathrm{V_{coh}} = (\mathrm{c}\Delta\mathrm{t})^3/\Delta\Omega\,(\Delta\omega/\omega)$
  (Melrose 1992)
- Individual emitters: $(\Delta\omega/\omega) \sim 1, \quad \Delta\Omega \sim 1/\gamma^2 \quad \longrightarrow \mathrm{N} = \gamma^2 \mathrm{n}(\mathrm{c}\Delta\mathrm{t})^3$
- Emissivity: $\mathrm{P_s} = \sigma_\mathrm{T}\,\gamma^2\,\mathrm{c}\,\mathrm{w_{turb}}$ (Benford & Weatherall 1991)
- Power balance : $\mathrm{P_{obs}} = 2 \cdot 10^{28}\,\mathrm{ergs\,s^{-1}}$ (Hankins et al. 2003)
  $\mathrm{P_{obs} = P_{coh}}$

$$\longrightarrow \underline{\mathrm{w_{turb}} \sim 10^8\,\mathrm{ergs\,cm^{-3}}}$$

Second, with the necessary amount of turbulent energy estimated, what is the amount of turbulent energy sustainable by the plasma beam? Therefore we anticipate a saturated dynamic equilibrium at late times and balance the beam intensity and the turbulent energy density flux transported by the Langmuir wavepackets:

- Beam intensity: $\mathrm{v_{beam}}\Delta\mathrm{w_{beam}} \sim (\gamma - 1)\,\mathrm{n\,m\,c^3}$
- Group velocity of strong Langmuir wave packets:
  $\mathrm{v_g = v_{th}^2/c = k_B T/mc}$ (Galeev et al. 1977)
  $\mathrm{T} \leq 172\,\mathrm{eV}$ (Tennant et al. 2001)
- Dynamic equilibrium of beam and turbulence intensities:
  $\mathrm{v_{beam}}\Delta\mathrm{w_{beam}} = \mathrm{v_g w^*_{turb}}$
  $\longrightarrow \mathrm{w^*_{turb}} \geq (\gamma - 1)\,\mathrm{n\,m\,c^2}\,(\mathrm{mc^2/k_B T})$ $\qquad \longrightarrow \underline{\mathrm{c/v_g} \sim 3000}$
  $\longrightarrow \mathrm{w^*_{turb}} \geq 1.2 \cdot 10^7 \mathrm{ergs/cm^3}$
- $\underline{\mathrm{w^*_{turb}} \sim 10^8\,\mathrm{ergs/cm^3}} \longrightarrow \mathrm{w_{turb}} \sim \mathrm{w^*_{turb}}$

Apparently the theoretical estimate predicts that the beam driven turbulence $\mathrm{w^*_{turb}}$ is (under optimum conditions) sufficient. The crucial quantities in the above considerations are the quality of coherence and the ratio of the speed of light to the Langmuir group velocity $\mathrm{c/v_g}$. The quality of coherence is determined by the effective coherence volume $\mathrm{V^{eff}_{coh}} \lesssim \mathrm{V_{coh}}$ which in reality is reduced due to a significant thermal spread (i.e. γ variation) of the non-linear beam distribution. Furtheron coherence is usually impured as the result of incomplete phase-coupling, i.e. $\mathrm{P_{coh} = N^\alpha P_s}$ with $1 \leq \alpha \leq 2$. In the dynamic equilibrium the Langmuir turbulent energy $\mathrm{w_{turb}}$ is nourished by the beam. Beam energy is pumped into the system with a flux essentially determined by the beam velocity, i.e. the speed of light. Langmuir wavepackets transport turbulent energy out of

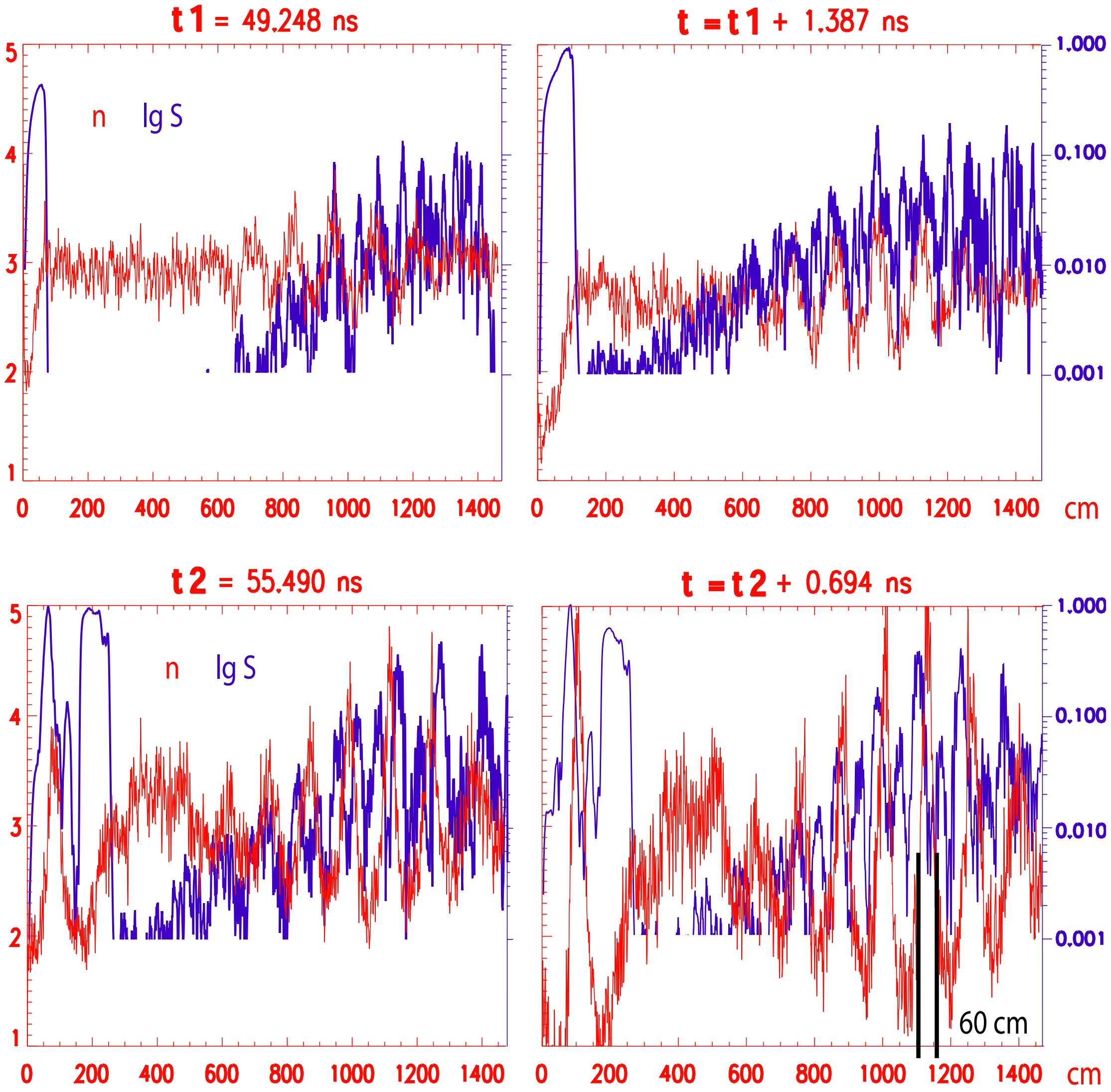

Fig. 5.11: 'Light surfing' mechanism: An incipient density perturbation n at $t = t_1$ couples to the electric field and triggers a radiative burst-like event in Poynting flux S. At $t = t_2$ the solitonic structure in S drives the density fluctuation off the front side. Further a second trailing soliton in S is gradually in formation. The denomination 'light surfing' is based on a similar process called 'shock surfing' which takes place parallel to a collisionless shock front.

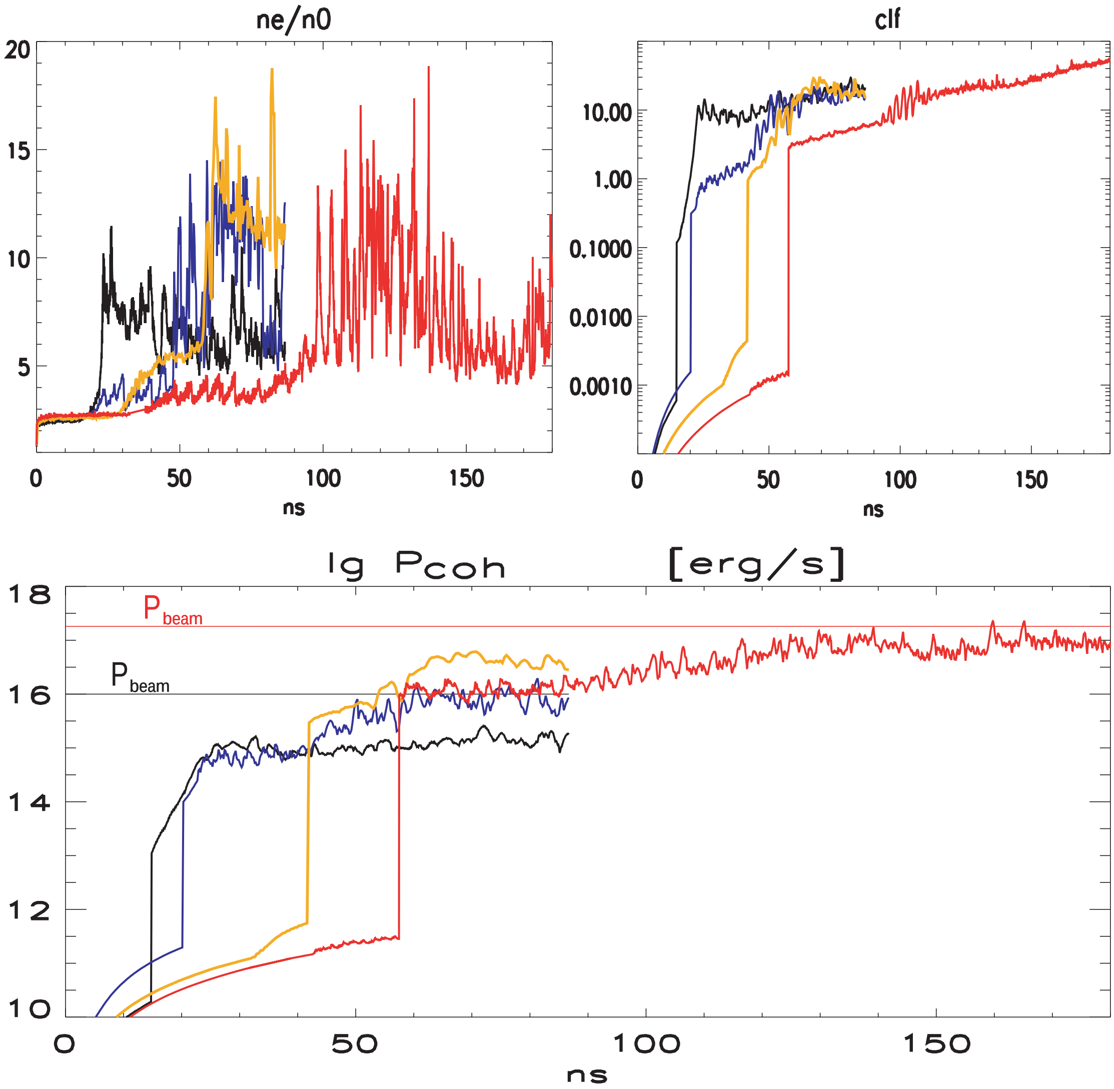

Fig. 5.12: Electron density fluctuations n_e/n_0, 'collision load factor clf', and coherent power emission P_{coh} for different collision energies $\gamma = 2.23, 3.35, 4, 46, 6.20$ (black,blue,orange,red) as function of time. For the highest collision energy the density fluctuations reach peak values $n_e/n_0 \sim 20$ and load factors clf ~ 50. The most remarkable qualitative difference is apparent from the emitted power P_{coh}, since only for the highest energy the radiation supersedes in burst-like 'spikes' the continuous beam power (straight lines).

the coherence volume with group velocity v_g. Consequently the system is energetically enriched by the 'collision load factor' clf $= c/v_g$. The Langmuir group velocity is essentially determined by the local temperature $c/v_g = mc^2/kT$. For the above considerations the temperature $T \leq 172\,eV$ inferred from the Crab's unpulsed thermal X-ray emission is used which is merely the surface temperature of the cooling neutron star. We have adopted this T value due to the lack of alternatives - every temperature estimate relying on a non-thermal emission process (non-thermal emission is the predominant radiation emission of the Crab) is liable only if the radiative mechanism is thoroughly understood. Right now we suffer a hard time to understand the basic features of CCB as non-thermal emission mechanism.

To cut the story short, strong plasma heating is definitely effective as long as the non-linear TSI governs the plasma dynamics. Parallel temperatures as calculated from the energy momentum tensor evolve towards the relativistic regime in the PIC simulations. Consequently the collision load factor is decreased. In the effort to reconcile the theoretical predictions with the PIC simulations the critical quantities are plotted in Fig. 5.12. Towards higher shell bulk momenta the energy balance factors increase up to clf ~ 50 - so the principle idea of energy overloading works fine. The PIC simulation at the highest collision energy $\gamma = 6.2$ exhibits the qualitatively outstanding characteristic, that for short time intervals the coherently emitted CCB power P_{coh} supersedes the continuous beam power. Though the coherently emitted power is extremely intense it is still magnitudes below the observed P_{obs}. Reviewed from the current status of research this is due to two reasons. First, the power calculated from the observations reported by Hankins et al. [2003] includes certain assumptions (geometry of emission etc.) and has to be confirmed by additional observations. Second, for the entire analysis the PIC simulation frame is considered as the local rest frame, i.e. only the relative bulk momenta between colliding shells have been of interest. If the PIC simulation frame is itself relativistically moving with γ'' then the lighthouse effect again comes into play. The beaming corrections imply $dP/d\Omega \propto \gamma''^4 dP_{coh}/d\Omega''$ and the theoretical approach of strong Langmuir turbulence is back on the winning team.

Utmostly intriguing is the qualitative concept of energy overloading, since the mechanism of CCB obeys an inherent maximum efficiency not be increased ad infinitum. Therefore the most promising focus in future studies is to confine the radiative energy release within progressively shorter and distinguished time intervals, i.e. to intensify and pronounce the 'power spiking'.

Chapter 6

Final Remarks

6.1 Achievements

Owing to the progress in observational techniques the emission features of astrophysical objects are resolved to unprecedented detail. Frequently the emission process is deeply connected to the physics of relativistic collisionless pair plasma. Paradigms are the ‘synchrotron wisps’ and radio outbursts of the Crab pulsar in particular as well as transport processes in relativistic jets and magnetic field generation in GRBs in general. The observations obtain an outstanding quality as the involved dynamic and spatial scales really probe the microphysics in the emission region. The explanation of such phenomena is beyond the scope of traditional MHD-based concepts of plasma astrophysics. New theoretical approaches invoke self-consistent kinetic plasma models taking into account the complete particle distribution function.

The selection of dominant instabilities in a given plasma environment is strictly competitive. The fastest growing plasma mode is the one which exclusively prevails. Reviewing the kinetic plasma phenomena of potential importance in astrophysical scenarios sets the focus on three processes: Fast Magnetic Reconnection (FMR) associated with magnetic boundary layers, the Coupled Two-Stream-Weibel (CTW) mode associated with collisionless shocks, and the impact of an exterior magnetic guide field on CTW mode degeneracy. On the most fundamental level the free energy in any plasma configuration is stored either in the magnetic field topology or in the particle bulk motion (i.e. phase space anisotropies). Focal points of the energy release are the boundary layers between different plasma entities. The three processes are ubiquitous in collisionless plasmas because they establish the most efficient mechanism of energy conversion. The respective mechanism is dominant because it is associated with the fastest growth rate. Owing to these characteristics we regard FMR and the Weibel-Two-Stream connection as *critical* for the understanding of relativistic plasma dynamics in astrophysical sites. However, though the importance of these processes is generally acknowledged by the astrophysical community, the rigorous kinetic treatment in the highly non-linear regime is still in its infancy. The main reason is that kinetic plasma modelling is computationally utmostly expensive and time consuming. The presented work is based on numerical simulations in the framework of the Particle-In-Cell (PIC) model. The simulations are performed with a 3D, fully electromagnetic and relativistic code and are completely self-consistent. Typical 3D scenarios are comprised by more than 10^9 particles. The simulation of such particle ensembles employs roughly 150 Gigabyte of random access memory and up to 50000 CPUhs computing time. The challenging hardware requirements are completely in the realm of massively parallelized supercomputer architectures. The simulations have been performed on the IBM p690 REGATTA system of the Rechenzentrum of the Max-Planck-Society in Garching and the HITACHI SR8000-F1 supercomputer of the Leibniz Computing Center in Munich.

Astrophysical timescales are generally long compared to plasma-kinetic timescales. Consequently the non-linear saturation is the prevalent plasma state in astrophysical sites. High performance computing has just reached the potential to engage the critical problems of relativistic plasma astrophysics in the highly dynamic late time evolution. In the presented work we study for the first time the critical processes in 3D PIC simulations. In the following we provide a final summary of the pioneering results and insights:

Fast Magnetic Reconnection

We focus on the particle acceleration mechanism in relativistic pair plasma reconnection. The acceleration efficiency is determined by the reconnection rate and the current sheet topology. We show that reconnection rates are appendant to the regime of fast magnetic reconnection, i.e. the X-zone inflow remains Alfvénic and is independent from the scale size of lepton demagnetization. The reconnection rate is directly reflected in the acceleration electric field $\mathrm{E_{acc}}$. Field strengths associated with resistive diffusion are limited to $\mathrm{E_{acc}/B_0} < 1$ in quasi-stationary X-zone configurations with asymptotic magnetic field $\mathrm{B_0}$. The highly dynamic evolution of the current sheet at late times is of crucial importance: Current filaments associated with the collisionless tearing instability move with a significant fraction of $\mathrm{v_A}$. The Alfvén velocity is of the order of the speed of light $\mathrm{v_A} \sim \mathrm{c}$ as peculiar feature of relativistic pair plasma. Therefore dynamic electric fields $\mathbf{E}'_{\mathrm{acc}} = -\mathbf{v}/\mathrm{c} \times \mathbf{B}$ significantly contribute to the acceleration process. The resulting acceleration field $(\mathrm{E_{acc}} + \mathrm{E}'_{\mathrm{acc}})/\mathrm{B_0} > 1$ exceeds unity. This is essential because it represents a qualitative difference to the reconnection rates obtained in quasi-stationary reconnection zones.

The results for pair plasma reconnection are the first for 3D scenarios. The late-time 3D current sheet topology is determined by the collisionless tearing and the relativistic drift kink mode. These competing modes cast the size of the particle acceleration regions. The size in combination with the reconnection rate determines the efficiency of particle acceleration. The different mechanisms of particle acceleration are identified with trace particles. We show that the acceleration process is modified in the relativistic regime, because the gyro radius grows proportional to the particle relativistic energy γ and inhibits the deflection of particles out of the acceleration regions. As further qualitative insight, we show that the upper limits for the energy gain are determined by the finite size of the acceleration zone. The size is imposed by the current sheet instabilities. This provides substantial evidence that only 3D scenarios can give the definite answer on the problem of particle acceleration in magnetic reconnection.

Finally, the most remarkable result: Though the current sheet evolution becomes highly dynamic at late times the particle distribution functions (PDFs) remain smooth and stable power-laws. Indifferent to respective variations in the initial conditions we obtain $\mathrm{s} = -1$ for the PDF spectral index within the X-zone and $\mathrm{s} = -3$ for the complete scenario. Parameter variations affect only the inherent timescales and the absolute magnitude of the high energy cut-off. The spectral shape is identified as a characteristic for the process of fast magnetic reconnection in pair plasmas. Consequently the correlation between source process / power-law index appears to be of universal nature.

Synchrotron signatures of kinetic reconnection

Kinetic reconnection scenarios result in highly turbulent electromagnetic field structures. The crucial question in the astrophysical context is whether the stability of the power-law particle distributions is reflected in the radiative signatures of the reconnection sites. We calculate the first synchrotron emission features from self-consistent PIC simulations. We show that the pitch angles are distributed quasi-isotropically on typical synchrotron cooling timescales. The PDF power-laws of $\mathrm{s} = -1$ within the X-zone and of $\mathrm{s} = -3$ transfer to synchrotron spectral indices of $\mathrm{s_{sc}} = -0.17$ and $\mathrm{s_{sc}} = -1.36$, respectively. The associated polarizations reach beyond 75 %. The stability of the power-law shape in combination with pitch-angle isotropy allows to scale the dimensionless results to the plasma conditions expectable in core regions of extragalactic radio sources. We show that the synchrotron emission features of the late-time FMR scenario provides a valid description for the observed high variability, hard and highly polarized spectra, and the extreme power output even of the most exceptionally luminous sources, so-called Flat-Spectrum-Radio-Quasars.

Weibel magnetic fields in γ-ray bursts

The generation of magnetic fields in collisionless shocks is the essential constituent of γ-ray burst (GRB) synchrotron emission models. On a conceptual level the GRB central engine generates a relativistically collimated power outflow. Source 'compactness' and time variabilities generate spatially confined electron-positron ($\mathrm{e}^-, \mathrm{e}^+$) fireball shells. Internal shocks arise from colliding fireball shells because of relative differences in the bulk flow. External shocks stem from fireballs running into the ambient interstellar medium. GRB prompt emission is associated with internal collisions, optical transients and radio afterglow with external collisions, respectively. The transformation of the shell-collision free energy into electromagnetic fields is established by the Weibel mechanism, i.e. the Coupled Two-Stream-Weibel (CTW) or Electromagnetic Counterstreaming Instability (EMCSI). The CTW is assembled by an electrostatic Two-Stream (TSI) component with bulk-parallel propagation, and an electromagnetic Weibel (WBI) component with strictly perpendicular propagation. We provide a thorough linear analysis of the CTW with emphasis on the critical energy dependence. Central point of the argumentation is that the TSI growth is damped $\propto \gamma^{-3/2}$ with relativistic energy, whereas the WBI behaves like $\propto \gamma^{-1/2}$. Consequently the CTW is expected to be progressively Weibel-dominated for increasing collision energies. This has profound implications for the magnetic equipartition ratio ϵ_{B}, the 3D structure of the magnetic field and the diffusion-limited lifetimes of the non-linearly saturated configuration. ϵ_{B} describes the efficiency of magnetic field generation and is the decisive input quantity for synchrotron emission models.

Based on the linear theory we predict a qualitative difference in the characteristics between GRB internal and external shocks. Internal collision energies range around $\gamma \sim 10$, typical external energies are $\gamma \sim 100$. We investigate the critical energy dependence of the CTW mode evolution in 3D PIC simulations. The comparisons of magnetic field topologies/ϵ_B-ratios in the highly non-linear regime of ultra-relativistic plasma shell collisions are unprecedented. Within the phase of linear mode growth the PIC simulations exactly coincide with the predictions of the linear theory. The final state is given by the non-linearly saturated CTW mode. This regime is the only one relevant on astrophysical timescales and completely in the realm of direct numerical simulations. The basic findings further validate the predictions of the linear analysis:

For internal collision energies the combination of TSI and WBI contributions yields a turbulent 3D electromagnetic field topology. The TSI imposes almost complete phase space isotropization and intense particle heating. This limits the final magnetization to $\epsilon_{\mathrm{B}} \sim 1\text{-}2\,\%$. The situation is different in the regime of external collisions. The WBI influence becomes dominant and the CTW proceeds pervasively transverse to the bulk in quasi-2D shell slices. The dimensional reduction stabilizes the magnetic field configuration. The associated equipartition yields profit substantially reaching up to $\epsilon_{\mathrm{B}} \sim 12\,\%$. Furthermore a finite residual momentum anisotropy persists throughout the final state. This has profound implications for the particle transport in saturated Weibel configurations and diffusion-limited magnetization lifetimes.

Self-consistent diffusive lifetimes of Weibel fields

3D PIC simulations of ultra-relativistic plasma shell collisions show beyond any reasonable doubt that the Weibel concept has the potential to generate magnetic fields of sufficient strength to validate synchrotron emission models. The critical question remaining is whether the Weibel magnetic fields are also sufficiently stable on typical synchrotron cooling times. To provide a definite answer in the framework of self-consistent kinetic simulations is a non-trivial task, since the involved timescales span over many orders of magnitude. Employing the plasma inertial timescale $\omega_{\mathrm{p0}}^{-1}$ as a characteristic of the system, the CTW mode typically proceeds within $\tau_{\mathrm{m}}\omega_{\mathrm{p0}} \sim 10^2$ towards the final state of non-linear saturation. Constrained by the power of contemporary supercomputers the analysis of the final stationary state is restricted to the successive time interval of roughly $\Delta\tau_{\mathrm{m}}\omega_{\mathrm{p0}} \sim 10^2$. The typical synchrotron cooling times associated with Weibel magnetic fields are $\tau_{\mathrm{sc}}\omega_{\mathrm{p0}} \sim 10^5\text{-}10^{10}$ depending on the individual assumptions for the plasma scenario. The crucial point is that kinetic plasma dynamics and radiative synchrotron cooling are appendant to completely different time regimes. Consequently reliable estimates on the lifetime of Weibel fields require some innovative concepts of simulation diagnostics. In this work we present the first stability analysis of self-consistent magnetic fields in plasma shell collisions. We identify magnetic cross-field diffusion as the dominant microphysical (i.e. kinetic) process of magnetic field decay. In the final state of 3D Weibel scenarios filaments of oppositely aligned currents are confined within magnetic walls. Magnetic confinement is established by the self-generated toroidal fields of the respective filaments.

We deduce the rate of cross-field diffusion in three independent ways: (i) The trajectories of more than $3 \cdot 10^4$ trace particles are locally cross-correlated with the magnetic field data. For a subensemble of particles the meandering motion within the current filaments is superposed by a distinct magnetic cross-field drift. The associated numerical values are sharply distributed around the ensemble average of cross-field diffusion. (ii) Cross-field diffusion can be understood as particles scattered off electrostatic convective cells, i.e. anomalous resistivity introduced by electrostatic fluctuations. The presence of anomalous resistivity is measured as dissipative ohmic power loss. Power loss and initial kinetic energy render the typical lifetime of the Weibel magnetic fields. We further identify an inverse correspondence between the average wavenumber logarithm of the magnetic field structures and the diffusion rates. Larger field extensions / e-folding times involve reduced cross-field diffusion. (iii) We prove that the diffusion coefficient shows distinctive $\propto 1/\mathrm{B}$-behaviour. This is the characteristic of Bohm diffusion. Employing the temperature definition from the relativistic energy-momentum tensor, we obtain a third independent estimate on the diffusion coefficient.

Intriguingly all three methods yield $\mathrm{D} = 10^{-6}\,(\mathrm{c}^2/\omega_{\mathrm{p0}})$ for the diffusion coefficient as consistent result. This corresponds to a diffusion-limited lifetime estimate of $\tau\omega_{\mathrm{p0}} \sim 10^9$ for Weibel magnetic fields in GRB shell collisions. The important point is that we employ an explicite simulation model which includes the complete variety of diffusive mechanisms. Therefore the approach is self-consistent. The diffusion process is identified as of Bohm-type, i.e. is in the fastest regime of cross-field diffusion. Consequently the obtained lifetimes represent a conservative lower limit. In conclusion, we herewith established the first convincing evidence that Weibel magnetic fields are stable on synchrotron cooling times.

Finally, with the synchrotron scenario verified, we address the problem of the resulting spectral emission features. Therefore we discuss the consequences of the magnetic field topology on the particle distribution function. Weibel magnetic fields in plasma shell collisions self-consistently form a power-law spectrum $\mathrm{B}_\perp(\mathrm{k}) \propto \mathrm{k}^{\mathrm{s}}$ in wavenumbers k. Most remarkable: The time evolution shows an ‘inverse cascade’, i.e. the spectral index turns from positive $\mathrm{s} = 2/3$ on entering the non-linear regime to negative s in the final state of non-linear saturation. $\mathrm{s} = -1$ for internal and $\mathrm{s} = -2$ for external collisions reflects the dimensional effects imposed by the energy dependence. These results represent the first step towards the kinetic treatment of magnetic turbulence. The spectral features are consistent with the so-called ‘viscosity-damped’ regime of 3D MHD turbulence. In this regime of small spatial scales the MHD description breaks down and only the self-consistent kinetic treatment provides further insights. Power-law shaped magnetic topologies imply power-laws in the PDF as can be inferred from self-similar solutions of particle diffusion.

Weibel-Two-Stream connection and coherent pulsar emission

The EMCSI / CTW instability is a coupled mode with degenerate characteristics of the TSI and WBI constituents. In an abstract formulation the TSI is associated with dissipation of bulk kinetic energy and strong phase space mixing. Somewhat complementary, magnetic confinement in current self-pinches and efficient particle transport are attributed to the WBI. The CTW mode is the critical plasma process in all 3D plasma scenarios with significant bulk flow. The balance of TSI and WBI contributions determines the distinct features of the CTW in the specific plasma environment. We show that the presence of an ambient magnetic guide field $\mathrm{B_G}$ removes the degeneracy of the CTW. For small guide fields the WBI component prevails. Above a threshold value $\mathrm{B_G^{ths}}$ the TSI becomes dominant. Our calculations show that $\mathrm{B_G^{ths}}$ exhibits an extreme energy dependence. For bulk relativistic energies exceeding $\gamma \sim 5$ the suppression of Weibel growth requires immense threshold strengths $\mathrm{B_G^{ths}} > 1000\,\mathrm{G}$. We note that the Weibel-Two-Stream connection is discussed within the framework of the 'cold beam approximation' and might be significantly modified by thermal effects.
We discuss the strong energy dependence of $\mathrm{B_G^{ths}}$ in the context of particle transport in relativistic jets and strong TSI-Langmuir turbulence in pulsars. In the jet scenario particle transport is established in self-collimated flows of current filaments. If the magnetic topology imposes significant guide contributions the TSI gains in importance, and bulk kinetic energy is dissipated in 'hot spots'. In the pulsar scenario the extremely strong guide field of the central neutron star suppresses Weibel contributions up to the typical radio emission heights. The TSI is the dominant instability mode which triggers strong Langmuir turbulence in the highly non-linear regime. Langmuir turbulence is associated with extreme densities and phase-coupled acceleration of particle bunches. The coherent particle acceleration in Langmuir fields is the basic principle of Coherent Collisionless Bremsstrahlung (CCB).
We explore the CCB mechanism in self-consistent PIC simulations of plasma shell collisions with strong magnetic guide field. The collision energy is the critical quantity which determines the density fluctuations and the 'collision load factor' (clf). The clf-factor arises from the difference between the collision bulk velocity (i.e. the energy source flux) and the group velocity of Langmuir wave packets (i.e. the potential emissivity). Self-consistent simulations of CCB at relativistic collision energies γ are a challenge to high performance computing, since the numerical effort increases $\propto \gamma^{11}$. We simulated for the first time collision energies up to $\gamma \simeq 6.2$ reaching load factors as high as clf ~ 50 and coherent power outbursts beyond $\mathrm{P_{coh}} = 10^{18}$ erg/s. These simulations are the first self-consistent approach to explain the giant radio pulses (GRPs) of the Crab pulsar. GRPs are power outbursts in the pulsar magnetosphere on nano-second timescales which are detected on earth with extreme intensities up to 1000 Jy. The crucial point is that the CCB mechanism is the only emission scenario which works down to nano-second timescales and has the potential to explain such extreme emissivities. Furthermore, the CCB process is the only pulsar emission concept ever validated in self-consistent simulations.

Certainly this is not the end of the story. As commensurable for a conservative study we should close with a final outlook on future perspectives.

6.2 Perspectives

The present work is dedicated to the study of critical kinetic plasma processes. Though the variety of problems under consideration is prolific and the applications to astrophysical scenarios are diverse, the study of these processes is inspired by some very simple and fundamental motivations. The physics of collisionless magnetic reconnection and collisionless shocks has been a subject of controversial discussion for decades. Certainly we do not claim to provide a definite answer to these issues within the framework of this work. We merely accomplished to shape some details in a puzzle consisting of an uncounted number of pieces. We can not even guarantee that our results are correct. This is beyond the scope of any theoretical concept. We can only assure that our results are consistent. Finally, we use the freedom of these closing sentences to speculate on the place our results assume in the general picture and render some points of future research:

- FMR as well as the EMCSI associated with collisionless shocks saturate in a highly turbulent configuration of electromagnetic fields. Turbulence prevails throughout the non-linear state being the only relevant regime on astrophysical timescales. Though the field structures are complex in configuration space, FMR and EMCSI show the remarkable characteristic to self-consistently generate stable power-laws. FMR is associated with a PDF spectral index of $\mathrm{s} \simeq -1$ on kinetic timescales, the Weibel magnetic fields associated with the EMCSI generate a PDF spectral index of $\mathrm{s} \simeq -2$ as self-similar solution on diffusive timescales. The connection between PDF and synchrotron spectral index is well established. Consequently, if the universal nature of the correspondence between plasma process and PDF spectral index is confirmed in future studies, observational spectra are directly indicative for the plasma processes active in the specific astrophysical site.

- Under realistic conditions for astrophysical sources the magnetic field topologies are expected to be much more complex than for certain model problems. Then reconnection and shock activities proceed in parallel. The paradigm is the Crab pulsar wind and its final termination shock. The corresponding simulation model would invoke a configuration of several anti-parallel Harris sheets and transverse plasma inflow as the trigger mechanism for reconnection onset. An alternative approach is the scenario of 3D quasi-perpendicular shocks. In this case the transverse ambient magnetic fields divert the Weibel current field filaments and reconnection activity substitutes cross-field diffusion. The qualitative change in particle transport should have tremendous consequences for the lifetime of Weibel magnetic fields.

- The EMCSI/Weibel filamentation provides a microphysical description for self-consistent plasma flow collimation. The concept is essential for GRB and jet scenarios. We investigated the EMCSI for relativistic pair plasma environments. Baryonic contributions introduce larger time and length scales. Existing simulations for artifically low electron-ion mass ratios give evidence that the coupling of electron and ion physics is inefficient. Therefore significant baryonic contributions are expected to preserve the qualitative shape of the magnetic field power spectra, though extending those spectra towards much larger wavenumbers. Since the spectral bandwidth of turbulence is essential for the evolution of diffusive processes, an investigation of baryonic mass contributions should provide precious theoretical insights.

However, speculations are nothing more than shadow and dust as long as they are not formulated within the framework of concise theoretical concepts. Therefore we take the chance to close and leave the loose ends to future studies.

- THE END -

Appendix A

Dimensionless Representation of Physical Quantities

Within a numerical algorithm physical quantities χ are represented by dimensionless numbers $\hat{\chi}$. The physical dimension and characteristic scale size are retained in a respective reference quantity χ_0 defined by the relation $\chi = \hat{\chi}\chi_0$.

The dimensionless representation offers two powerful advantages. First, a single dimensionless simulation describes an entire class of physical scenarios. This is due to the fact that any physical process involves a characteristic scale in space and time. Reference quantities χ_0 determine the absolute temporal and spatial scale of such a process. However, its physical nature is independent from absolute scales as long as the ratio between characteristic times and lengths is retained. The ratio is contained in the dimensionless representation and, hence, the simulation results apply to a variety of scenarios with typical absolute scales determined by the physical environment at hand. The covariance of simulated scenarios is valid under the restriction that only one fundamental force of interaction is present and retardation effects imposed by finite signal velocity are insignificant. Both restrictions are met in kinetic plasma simulation, since only electromagnetic interactions are involved and computational restrictions impose a local confinement within which signal spread is actually instantaneous. Second, on computer hardware numbers are represented with mantissa and exponent. Numerical performance is best for numbers which are comparable in size, because then the maximum mantissa length is accessible. A dimensionless representation adapted to the physical problem at hand ensures numbers close to unity.

In plasma physics natural choices for the time and length scale are ensued by the gyration period of cyclotron motion $\mathrm{T_0}/2\pi = \omega_{\mathrm{c0}}^{-1} = (\mathrm{eB_0/mc})^{-1}$ and the skin depth of inertial motion $\mathrm{d_0} = \mathrm{c}/\omega_{\mathrm{p0}} = \mathrm{c}(4\pi\mathrm{me^2/n_0})^{-1/2}$, respectively. m and e are the natural constants of electronic mass and charge. With respect to the covariance of physical scenarios as stated above, absolute values for time and length are fixed by the dimensional reference quantities for magnetic field $\mathrm{B_0}$ and density $\mathrm{n_0}$, respectively. The application to an individual physical environment fixes the time and length scale. However, the physics of the simulated process is equivalent for the entire class of environments in which the ratio of $\mathrm{B_0/n_0}$ is comparable, i.e. the relation of temporal and spatial scales is equivalent.

Consequently, the physics of the specific process simulated in dimensionless representation is characteristic for all environments with the same ratio of Alfvén to light velocity $\mathrm{c}/\mathrm{v}_{\mathrm{A0}} = (4\pi \mathrm{m} \mathrm{n}_0)^{1/2}\mathrm{c}/\mathrm{B}_0 := \hat{\mathrm{c}}$. $\hat{\mathrm{c}}$ is the essential input parameter of the simulation. On the most fundamental level kinetic plasma physics deals with Maxwell's equations for the evolution of electric and magnetic fields and the Lorentz force for the treatment of particle motion. Details on the numerical method are deferred to chapter 2. With the choices for time and length scales linked to fundamental plasma quantities the surjective mapping to the dimensionless representation follows straightforwardly:

$$
\begin{array}{lcl|lcl}
\mathbf{B} & \rightarrow & \hat{\mathbf{B}}\ \ \mathrm{B}_0 & \partial_{\mathrm{t}} & \rightarrow & \hat{\partial}_{\mathrm{t}}\ \omega_{\mathrm{c0}} \\
\mathrm{n} & \rightarrow & \hat{\mathrm{n}}\ \ \mathrm{n}_0 & \nabla & \rightarrow & \hat{\nabla}\ \omega_{\mathrm{p0}}/\mathrm{c} \\
\mathbf{E} & \rightarrow & \hat{\mathbf{E}}/\hat{\mathrm{c}}\,\mathrm{B}_0 & \mathbf{v} & \rightarrow & \hat{\mathbf{v}}\ \mathrm{v}_{\mathrm{A0}}
\end{array}
$$

The identification of the electric field in the simulation by $\hat{\mathrm{E}}/\hat{\mathrm{c}}$ follows not strictly. It is merely one possible *ad hoc* definition chosen in a way that the dimensionless expression of the Lorentz force ensues in the simplest possible form. This is sensible since the dominant computational effort is spent in the particle stepping. Then the fundamental set of equations transfers to the dimensionless representation:

	Gaussian—cgs	Dimensionless
Gauss	$\nabla \cdot \mathbf{D} = 4\pi\rho$	$\hat{\nabla} \cdot \hat{\mathbf{E}} = \hat{\mathrm{c}}^2 \hat{\mathrm{n}}$
Dirac	$\nabla \cdot \mathbf{B} = 0$	$\hat{\nabla} \cdot \hat{\mathbf{B}} = 0$
Faraday	$\mathrm{c}^{-1}\,\partial_t \mathbf{B} = -\nabla \times \mathbf{E}$	$\hat{\partial}_t \hat{\mathbf{B}} = -\hat{\nabla} \times \hat{\mathbf{E}}$
Ampere-Maxwell	$\mathrm{c}^{-1}\,\partial_t \mathbf{D} = \nabla \times \mathbf{H} - (4\pi/c)\,\mathbf{j}$	$\hat{\mathrm{c}}^{-2}\,\hat{\partial}_t \hat{\mathbf{E}} = \hat{\nabla} \times \hat{\mathbf{B}} - \hat{\mathbf{j}}$
Lorentz	$\mathrm{d}_{\mathrm{t}}(\gamma \mathrm{m} \mathbf{v}) = \mathrm{e}(\mathbf{E} + \mathbf{v}/\mathrm{c} \times \mathbf{B})$	$\hat{\mathrm{d}}_{\mathrm{t}}(\gamma \hat{\mathbf{v}}) = \hat{\mathbf{E}} + \hat{\mathbf{v}} \times \hat{\mathbf{B}}$

Since encountered frequently, furtheron the dimensionless expressions for conservation of charge and Poynting's theorem are derived in differential form from the above relations:

Continuity	$\mathrm{d_t}\rho = -\nabla\cdot\mathbf{j}$	$\hat{\mathrm{d}}_\mathrm{t}\hat{\mathrm{n}} = -\hat{\nabla}\cdot\hat{\mathbf{j}}$
PoyntingTheorem	$\mathrm{p_{Ohm}} + \partial_\mathrm{t}\mathcal{W}_\mathrm{EM} = -\nabla\cdot\mathbf{S}$	$\hat{\mathrm{p}}_\mathrm{Ohm} + \hat{\partial}_\mathrm{t}\hat{\mathcal{W}}_\mathrm{EM} = -\hat{\nabla}\cdot\hat{\mathbf{S}}$

with the following identities for Ohmic power density, EM energy density and EM energy flux (= Poynting flux vector), respectively,

Ohm	$\mathrm{p_{Ohm}} = \mathbf{j}\cdot\mathbf{E}$	$\hat{\mathrm{p}}_\mathrm{Ohm} = \hat{\mathbf{j}}\cdot\hat{\mathbf{E}}$
EM Energy	$\mathcal{W}_\mathrm{EM} = \frac{1}{8\pi}\,(\mathbf{E}\cdot\mathbf{D}+\mathbf{B}\cdot\mathbf{H})$	$\hat{\mathcal{W}}_{EM} = \frac{1}{2}\,((\hat{\mathrm{E}}/\hat{\mathrm{c}})^2+\hat{\mathrm{B}}^2)$
Poynting Vector	$\mathbf{S} = \frac{4\pi}{\mathrm{c}}\,(\mathbf{E}\times\mathbf{B})$	$\hat{\mathbf{S}} = \hat{\mathbf{E}}\times\hat{\mathbf{B}}$

The equations refer to the case of a pair plasma, i.e. only a single mass factor m is involved and conveniently set to unity. The extension to systems which include other species of various masses (for instance in the case of an electron-proton or electron-proton-ion plasma) is straightforward. Each mass factor implies a characteristic time ($\omega_{\mathrm{c0}} \propto \mathrm{m}^{-1}$) and length scale ($\mathrm{d_0} \propto \mathrm{m}^{1/2}$). Keeping in mind that numerical performance is best for quantities close to unity, one selects the specie / specific mass factor $\mathrm{m_r}$ as reference scale at which most of the physics is expected to take place. The scales introduced by the other species are then taken into account by a dimensionless relative mass $\mu_\mathrm{r} = \mathrm{m}/\mathrm{m_r}$ included in the particle momentum stepping:

Lorentz	$\mathrm{d_t}(\gamma\mathrm{m}\mathbf{v}) = \mathrm{e}(\mathbf{E}+\mathbf{v}/\mathrm{c}\times\mathbf{B})$	$\hat{\mathrm{d}}_\mathrm{t}(\gamma\mu_\mathrm{r}\hat{\mathbf{v}}) = \hat{\mathbf{E}}+\hat{\mathbf{v}}\times\hat{\mathbf{B}}$

Appendix B

Linear Theory of the 2D EM Counterstreaming Instability

In the most general scenario the electromagnetic counterstreaming instability (EMCSI) in a pair plasma implies two species of oppositely charged particles (electrons e and positrons p), two plasma entities of different bulk motion (= plasma shells) and an optional non-zero magnetic guide field $\mathbf{B}_{\mathrm{G}}$. Each plasma shell is identified by an index $\mathrm{s} = 1, 2$. In order to limit the obfuscation introduced by the sheer complexity of mathematical expressions, we restrain from utmost generality and introduce two further restrictions: First, we require the initial setup to be homogeneous in configuration space, i.e. the particle distribution function (PDF) at initialization time $\tilde{\mathrm{f}}(\mathbf{x}, \mathbf{p}, \mathrm{t} = \mathrm{t}_0) = \tilde{\mathrm{f}}_0(\mathbf{x}, \mathbf{p})$ is in lowest order defined as spatially invariant $\tilde{\mathrm{f}}_0(\mathbf{x}, \mathbf{p}) = \tilde{\mathrm{f}}_0(\mathbf{p})$. Second, we apply the zero temperature approximation or so called ‘cold beam limit’ $\mathrm{T}_0 \rightarrow 0$. In this limit the PDF is initially also sharply defined in momentum space $\tilde{\mathrm{f}}_0(\mathbf{p}) = \mathrm{f}_0 \delta^3(\mathbf{p} - \mathbf{p}_0) = \mathrm{n}_0$ around the respective bulk momentum $\mathbf{p}_0$, i.e. the plasma is assumed to be fluid-like. However in contrast to a purely magnetohydrodynamic approach the treatment is fully electromagnetic. Furthermore, as soon as the essential physical characteristics of the EMCSI are pointed out, we drop this second restriction and consider the kinetic modifications introduced by a finite initial thermal spread.

Within the linear regime the EMCSI evolves in 2D. 3D effects come into play after non-linear saturation which is explored in the PIC simulations. However, the analytic derivation presented in this Appendix remains within the constraints of the linear theory.

The plasma dynamics of the cold fluid system is completely described by the following set of equations:

Lorentz

$$\begin{aligned} \partial_{\mathrm{t}} \mathbf{p}_{\mathrm{ps}} + \mathbf{v}_{\mathrm{ps}} \cdot \nabla \mathbf{p}_{\mathbf{ps}} &= +(\mathbf{E} + \mathbf{v}_{\mathrm{ps}} \times \mathbf{B}) \qquad \text{(B.1)} \\ \partial_{\mathrm{t}} \mathbf{p}_{\mathrm{es}} + \mathbf{v}_{\mathrm{es}} \cdot \nabla \mathbf{p}_{\mathbf{es}} &= -(\mathbf{E} + \mathbf{v}_{\mathrm{es}} \times \mathbf{B}) \end{aligned}$$

Continuity

$$\begin{aligned} \partial_{\mathrm{t}} \rho_{\mathrm{ps}} + \nabla \cdot \mathbf{j}_{\mathrm{ps}} &= 0 \qquad \text{(B.2)} \\ \partial_{\mathrm{t}} \rho_{\mathrm{es}} + \nabla \cdot \mathbf{j}_{\mathrm{es}} &= 0 \end{aligned}$$

Gauss

$$\nabla \cdot \mathbf{E} = \sum_{\mathrm{s}} \rho_{\mathrm{s}} \qquad \text{(B.3)}$$

Faraday

$$\partial_{\mathrm{t}} \mathbf{B} = - \nabla \times \mathbf{E} \qquad \text{(B.4)}$$

Ampere-Maxwell

$$\partial_{\mathrm{t}} \mathbf{E} = \nabla \times \mathbf{B} - \sum_{\mathrm{s}} \mathbf{j}_{\mathrm{s}} \qquad \text{(B.5)}$$

Apparently the equations are dimensionless with $\hat{c}$ set to unity, which has to convenient implications. First, in the context of plasma shell collisions for magnetic field generation in γ-ray bursts no initial magnetic field is present. Then the reference magnetic field is defined simply by the initial density n_0 and the subsidiary constraint $\hat{c} = c/v_{A0} = 1$ which fixes the ratio B/n. Second, in the presented form of the equations lengths are normalized to the electron inertial length d_0 and times to the inverse electron plasma frequency ω_{p0} turning out to be a very sensible choice.

Bulk motion and parallel oriented magnetic guide field $\mathbf{B}_0$ introduce a symmetry breaking direction of reference into the system. We arbitrarily define this direction to point in $\mathbf{z}$, the $s=1$ shell moving towards +z with bulk velocity $\mathbf{v}_{01} = v_{z01}\mathbf{e}_z$. The counterstreaming plasma shell is aligned exactly anti-parallel. Each shell consists of quasi-neutral pair plasma with initial density $n_{0s} = n_{p0s} = n_{e0s}$ and relativistic momentum $\mathbf{p}_{0s} = \gamma_{0s}\mathbf{v}_{0s} = \mathbf{v}_{0s}/(1 - v_{0s}^2)^{1/2}$. The perpendicular direction is degenerate, so we furtheron convene that the 2D instability evolves within the (x, z)-plane.

Assuming plane wave solutions for linearly perturbed quantities the first order variations then appear in the fashion

$$\xi(\mathbf{x}, t) = \xi_0 + \xi\,\mathrm{Exp}[i(\mathbf{k}\cdot\mathbf{x} - \omega t)] \qquad \longrightarrow \qquad d\xi(\mathbf{x}, t) = \delta\xi \begin{pmatrix} ik_x\delta x - i\omega\delta t \\ 0 \\ ik_z\delta z - i\omega\delta t \end{pmatrix}$$

It is important to note that in the relativistic regime the momentum variation parallel and perpendicular to the direction of motion are different. This is understood straightforwardly, if one recalls that according to D'Alembert's method (i.e. the method of virtual displacement) the variation of a quantity is infinitely small and takes place instantaneously. As a consequence thereof, the k-norm of a vector quantity $\|\xi\|_k = (\sum_j (\xi_j)^k)^{1/k}$ is affected only by displacements $\delta\xi_j$ parallel to the respective vector, since just linear terms are considered. This general statement is certainly valid for the magnitude of a vector as the special case $k=2$-norm. In simple words, only velocity variations parallel to the initial bulk motion influence the relativistic energy γ_0 which solely depends on the magnitude of velocity:

$$\delta\mathbf{p}_s = \begin{pmatrix} \delta p_{\perp s} \\ \delta p_{\perp s} \\ \delta p_{\| s} \end{pmatrix} = \begin{pmatrix} \delta p_{xs} \\ \delta p_{ys} \\ \delta p_{zs} \end{pmatrix} = \begin{pmatrix} \gamma_{0s}\,\delta v_{xs} \\ \gamma_{0s}\,\delta v_{ys} \\ \gamma_{0s}^3\,\delta v_{zs} \end{pmatrix}$$

Then the perturbed system of equations (positrons/electrons ±) ensues to

(C.1′) :

$$-i\omega \begin{pmatrix} \delta p_{xs} \\ \delta p_{ys} \\ \delta p_{zs} \end{pmatrix} + \begin{pmatrix} \delta v_{xs} \\ \delta v_{ys} \\ \delta v_{zs} \end{pmatrix} \cdot \begin{pmatrix} ik_x\delta p_{xs} & 0 & ik_z\delta p_{xs} \\ ik_x\delta p_{ys} & 0 & ik_z\delta p_{ys} \\ ik_x\delta p_{zs} & 0 & ik_z\delta p_{zs} \end{pmatrix} = \pm \begin{pmatrix} \delta E_x + \delta v_{ys}B_G - v_{z0s}\delta B_y \\ \delta E_y + v_{z0s}\delta B_x - \delta v_{xs}B_G \\ \delta E_z \end{pmatrix}$$

(C.2′) :

$$\begin{aligned} \bar{\omega}_{ps}\delta n_{ps} - n_{0ps}(k_x\delta v_{xps} + k_z\delta v_{zps}) &= 0 \\ -\bar{\omega}_{es}\delta n_{es} + n_{0es}(k_x\delta v_{xes} + k_z\delta v_{zes}) &= 0 \end{aligned}$$

with the *reduced frequency* $\bar{\omega}_s = \omega - k_z v_{0s}$.

(C.3′) :

$$\omega \begin{pmatrix} \delta B_x \\ \delta B_y \\ \delta B_z \end{pmatrix} = \begin{pmatrix} -k_z\delta E_y \\ k_z\delta E_x - k_x\delta E_z \\ k_x\delta E_y \end{pmatrix}$$

(C.4′) :

$$-i\omega \begin{pmatrix} \delta E_x \\ \delta E_y \\ \delta E_z \end{pmatrix} = \begin{pmatrix} -ik_z\delta B_y \\ ik_z\delta B_x - ik_x\delta B_z \\ ik_x\delta B_y \end{pmatrix} - \sum_s \begin{pmatrix} n_{0ps}\delta v_{xps} - n_{0es}\delta v_{xes} \\ n_{0ps}\delta v_{yps} - n_{0es}\delta v_{yes} \\ \delta n_{ps}v_{z0ps} + n_{0ps}\delta v_{zps} - \delta n_{es}v_{z0es} - n_{0es}\delta v_{zes} \end{pmatrix}$$

(C.5′) :

$$ik_x\delta E_x + ik_z\delta E_z = \sum_s(\delta n_{ps} - \delta n_{es})$$

Actually equation (C.5′) is redundant since it just represents a linear combination of (C.2′) and (C.3′). However, the most efficient path to the final solution applies (C.5′) instead of (C.4c′).
The strategy is to eliminate the magnetic variations $\delta\mathbf{B}$ by means of (C.3′) to obtain the velocity and density variations in the form

(C.1″) :

$$\begin{aligned} \delta v_{xps} &= +i\frac{\gamma_{0ps}\bar{\omega}_{0ps}}{\gamma_{0ps}^2\bar{\omega}_{0ps}^2 - \Omega_G^2}\left(\frac{\bar{\omega}_{ps}}{\omega}\delta E_x + i\frac{\Omega_G}{\gamma_{0ps}\omega}\delta E_y + \frac{k_x v_{z0ps}}{\omega}\delta E_z\right) \\ \delta v_{xes} &= -i\frac{\gamma_{0es}\bar{\omega}_{0es}}{\gamma_{0es}^2\bar{\omega}_{0es}^2 - \Omega_G^2}\left(\frac{\bar{\omega}_{es}}{\omega}\delta E_x - i\frac{\Omega_G}{\gamma_{0es}\omega}\delta E_y + \frac{k_x v_{z0es}}{\omega}\delta E_z\right) \\ \delta v_{yps} &= +i\frac{\gamma_{0ps}\bar{\omega}_{0ps}}{\gamma_{0ps}^2\bar{\omega}_{0ps}^2 - \Omega_G^2}\left(-i\frac{\Omega_G}{\gamma_{0ps}\omega}\delta E_x + \frac{\bar{\omega}_{ps}}{\omega}\delta E_y - i\frac{\Omega_G}{\gamma_{0ps}\bar{\omega}_{ps}}\frac{k_x v_{z0ps}}{\omega}\delta E_z\right) \\ \delta v_{yes} &= -i\frac{\gamma_{0es}\bar{\omega}_{0es}}{\gamma_{0es}^2\bar{\omega}_{0es}^2 - \Omega_G^2}\left(+i\frac{\Omega_G}{\gamma_{0es}\omega}\delta E_x + \frac{\bar{\omega}_{es}}{\omega}\delta E_y + i\frac{\Omega_G}{\gamma_{0es}\omega_{es}}\frac{k_x v_{z0es}}{\omega}\delta E_z\right) \\ \delta v_{zps} &= +\frac{1}{\gamma_{0ps}^3\bar{\omega}_{ps}} \\ \delta v_{zes} &= -\frac{1}{\gamma_{0es}^3\bar{\omega}_{es}} \end{aligned}$$

and

$(\mathrm{C}.2'')$:

$$\begin{aligned}
\delta \mathrm{n_{ps}} &= + \left(\frac{\mathrm{n_{0ps}}}{\gamma_{\mathrm{0ps}}^2 \bar{\omega}_{\mathrm{ps}}^2 - \Omega_{\mathrm{G}}^2} \left(\frac{\mathrm{k_x} \bar{\omega}_{\mathrm{ps}} \gamma_{\mathrm{0ps}}}{\omega} \delta \mathrm{E_x} + \mathrm{i} \frac{\Omega_{\mathrm{G}} \mathrm{k_x}}{\omega} \delta \mathrm{E_y} + \frac{\mathrm{k_x^2} \gamma_{\mathrm{0ps}}}{\omega} \delta \mathrm{E_z} \right) + \frac{\mathrm{n_{0ps}}}{\gamma_{\mathrm{0ps}}^3 \bar{\omega}_{\mathrm{ps}}^2} \mathrm{k_z} \delta \mathrm{E_z} \right) \\
\delta \mathrm{n_{es}} &= - \left(\frac{\mathrm{n_{0es}}}{\gamma_{\mathrm{0es}}^2 \bar{\omega}_{\mathrm{es}}^2 - \Omega_{\mathrm{G}}^2} \left(\frac{\mathrm{k_x} \bar{\omega}_{\mathrm{es}} \gamma_{\mathrm{0es}}}{\omega} \delta \mathrm{E_x} - \mathrm{i} \frac{\Omega_{\mathrm{G}} \mathrm{k_x}}{\omega} \delta \mathrm{E_y} + \frac{\mathrm{k_x^2} \gamma_{\mathrm{0es}}}{\omega} \delta \mathrm{E_z} \right) + \frac{\mathrm{n_{0es}}}{\gamma_{\mathrm{0es}}^3 \bar{\omega}_{\mathrm{es}}^2} \mathrm{k_z} \delta \mathrm{E_z} \right)
\end{aligned}$$

Differences in sign between the positron and electron terms arise from the opposite charge and oppositely oriented gyro motions. The guide field contributions in dimensionless representation correspond to a gyro frequency $\Omega_{\mathrm{G}}\, \omega_{\mathrm{c0}}^{-1} = \mathrm{B_G}/\mathrm{B_0}$. Once more the choice $\hat{\mathrm{c}} = 1$ is advantageous, since $\omega_{\mathrm{c0}} = \omega_{\mathrm{p0}}$ follows at reference conditions and the coupling terms to the guide field $\mathrm{B_G}$ are as all other terms conveniently expressed as ratio to the reference plasma frequency of the system ω_{p0}.
Finally we insert $(\mathrm{C}.1''), (\mathrm{C}.2'')$ into $(\mathrm{C}.4'\mathrm{ab}), (\mathrm{C}.5')$ and again substitute $\delta \mathbf{B}$ variations with $(\mathrm{C}.3')$ to obtain the fully determined set of equations:

$$\begin{pmatrix}
\omega^2(1-\Omega_1^{-2})-\mathrm{k_z^2}(1+\Omega_4^{-2})+2\omega\mathrm{k_z}\Omega_3^{-2} & -\mathrm{i}\Omega_{\mathrm{G}}(\mathrm{a}\omega+\mathrm{k_z b}) & \mathrm{k_x k_z}(1+\Omega_4^{-2})-\omega\mathrm{k_x}\Omega_3^{-2} \\
\mathrm{i}\Omega_{\mathrm{G}}(\mathrm{a}\omega+\mathrm{k_z b}) & \omega^2(1-\Omega_1^{-2})-\mathrm{k_z^2}(1+\Omega_4^{-2})+2\omega\mathrm{k_z}\Omega_3^{-2}-\mathrm{k_x^2} & +\mathrm{i}\Omega_{\mathrm{G}}\mathrm{k_x b} \\
\omega\mathrm{k_x}(1-\Omega_1^{-2})+\mathrm{k_x k_z}\Omega_3^{-2} & -\mathrm{i}\Omega_{\mathrm{G}}\mathrm{k_x a} & \omega\mathrm{k_z}(1-\Omega_2^{-2})-\mathrm{k_x^2}\Omega_3^{-2}
\end{pmatrix} \delta\mathbf{E}=0$$

with the substitutions

$$\begin{aligned}
\Omega_1^{-2} &= \Omega_{1\mathrm{p}}^{-2} + \Omega_{1\mathrm{e}}^{-2} \\
&= \sum_{\mathrm{s}} \left(\frac{\mathrm{n_{0ps}} \gamma_{\mathrm{0ps}}}{\gamma_{\mathrm{0ps}}^2 \bar{\omega}_{\mathrm{ps}}^2 - \Omega_{\mathrm{G}}^2} + \frac{\mathrm{n_{0es}} \gamma_{\mathrm{0es}}}{\gamma_{\mathrm{0es}}^2 \bar{\omega}_{\mathrm{es}}^2 - \Omega_{\mathrm{G}}^2} \right) \\
\Omega_2^{-2} &= \Omega_{2\mathrm{p}}^{-2} + \Omega_{2\mathrm{e}}^{-2} \\
&= \sum_{\mathrm{s}} \left(\frac{\mathrm{n_{0ps}}}{\gamma_{\mathrm{0ps}}^3 \bar{\omega}_{\mathrm{ps}}^2} + \frac{\mathrm{n_{0es}}}{\gamma_{\mathrm{0es}}^3 \bar{\omega}_{\mathrm{es}}^2} \right) \\
\Omega_3^{-2} &= \Omega_{3\mathrm{p}}^{-2} + \Omega_{3\mathrm{e}}^{-2} \\
&= \sum_{\mathrm{s}} \left(\frac{\mathrm{n_{0ps}} \gamma_{\mathrm{0ps}} \mathrm{v_{0ps}}}{\gamma_{\mathrm{0ps}}^2 \bar{\omega}_{\mathrm{ps}}^2 - \Omega_{\mathrm{G}}^2} + \frac{\mathrm{n_{0es}} \gamma_{\mathrm{0es}} \mathrm{v_{0es}}}{\gamma_{\mathrm{0es}}^2 \bar{\omega}_{\mathrm{es}}^2 - \Omega_{\mathrm{G}}^2} \right) \\
\Omega_4^{-2} &= \Omega_{4\mathrm{p}}^{-2} + \Omega_{4\mathrm{e}}^{-2} \\
&= \sum_{\mathrm{s}} \left(\frac{\mathrm{n_{0ps}} \gamma_{\mathrm{0ps}} \mathrm{v_{0ps}^2}}{\gamma_{\mathrm{0ps}}^2 \bar{\omega}_{\mathrm{ps}}^2 - \Omega_{\mathrm{G}}^2} + \frac{\mathrm{n_{0es}} \gamma_{\mathrm{0es}} \mathrm{v_{0es}^2}}{\gamma_{\mathrm{0es}}^2 \bar{\omega}_{\mathrm{es}}^2 - \Omega_{\mathrm{G}}^2} \right)
\end{aligned}$$

and the entirely magnetically coupled contributions

$$\begin{aligned} a &= a_p - a_e \\ &= \sum_s \left(\frac{n_{0ps}}{\gamma_{0ps}^2 \bar{\omega}_{ps}^2 - \Omega_G^2} - \frac{n_{0es}}{\gamma_{0es}^2 \bar{\omega}_{es}^2 - \Omega_G^2} \right) \\ b &= b_p - b_e \\ &= \sum_s \left(\frac{n_{0ps} v_{0ps}}{\gamma_{0ps}^2 \bar{\omega}_{ps}^2 - \Omega_G^2} - \frac{n_{0es} v_{0es}}{\gamma_{0es}^2 \bar{\omega}_{es}^2 - \Omega_G^2} \right). \end{aligned}$$

The final determinant has the formal structure

$$\begin{vmatrix} \mathrm{CTW}_1 & -i\Omega_G \cdot \mathrm{CGD}_1 & \mathrm{CTW}_2 \\ +i\Omega_G \cdot \mathrm{CGD}_2 & \mathrm{LM} & -i\Omega_G \cdot \mathrm{CGD}_3 \\ \mathrm{CTW}_3 & +i\Omega_G \cdot \mathrm{CGD}_4 & \mathrm{CTW}_4 \end{vmatrix}$$

in which the denotations are indicative for the constituent terms of

the Coupled-Two-Stream-Weibel (CTW) mode

$$\mathrm{CTW} = (1 - \Omega_2^{-2})[\omega^2(1 - \Omega_1^{-2}) - k_z^2(1 + \Omega_4^{-2}) + 2\omega k_z \Omega_3^{-2}] - k_x^2[(1 + \Omega_4^{-2})(1 - \Omega_1^{-2}) + \Omega_3^{-4}],$$

the Light mode (LM)

$$\mathrm{LM} = \omega^2(1 - \Omega_1^{-2}) - k_z^2(1 + \Omega_4^{-2}) + 2\omega k_z \Omega_3^{-2} - k_x^2,$$

and the Coupled-Gyration-Dominated (CGD) modes

$$\mathrm{CGD} = \Omega_G^2 \omega k_z \left[(1 - \Omega_1^{-2})(a\omega - bk_z)^2 - k_x^2(a^2(1 + \Omega_4^{-2}) - 2ab\Omega_3^{-2} - b^2(1 - \Omega_1^{-2})) \right].$$

The final dispersion relation D then ensues to

$$D = \mathrm{LM} \cdot \mathrm{CTW} + \mathrm{CGD}.$$

The essential contributions with respect to plasma instability theory arise from the CTW mode. The constituents of this plasma mode, the physical characteristics in the context of different astrophysical scenarios, the highly non-linear saturation at late times and kinetic modifications are extensively studied in Chap. 4 and 5. In Chap. 4 the CTW mode serves as the instability pervasive in the collision of plasma shells in γ-ray bursts. The same instability develops very different characteristics in the presence of a strong guide field which is studied in Chap. 5 in the context of pulsar physics. The linear dispersion relation as derived here provides the foundations to understand the various characteristics of the CTW mode in a natural fashion by the response of the plasma mode on variations in the initial bulk kinetic energy γ_0 and the strength of the magnetic guide field Ω_{G}.

The LM mode is a possible solution in all scenarios. It describes the propagation of electromagnetic radiation with the plasma serving as the carrier medium. Within the dispersion relation the light mode is represented by roots without any imaginary contingents. As a consequence thereof the light mode is not inherently self-growing but nevertheless propagating in the plasma if triggered by a different source process. The simplest way to identify the nature of the LM mode is in the limit of negligible guide field $\Omega_{\mathrm{G}} \rightarrow 0$. Then the CGD modes vanish and furthermore the LM and CTW modes are completely decoupled. In this limit the expression for the LM mode simplifies to

$$\begin{aligned}
\mathrm{LM} &= \omega^2(1-\Omega_1^{-2}) - \mathrm{k}_{\mathrm{z}}^2(1+\Omega_4^{-2}) + 2\omega \mathrm{k}_{\mathrm{z}}\Omega_3^{-2} - \mathrm{k}_{\mathrm{x}}^2 \\
&= \omega^2 - (\mathrm{k}_{\mathrm{x}}^2 + \mathrm{k}_{\mathrm{z}}^2) - \sum_{\mathrm{s}} \Big(\frac{\mathrm{n}_{0\mathrm{ps}}\bar{\omega}_{\mathrm{ps}}}{\gamma_{0\mathrm{ps}}^2 \bar{\omega}_{\mathrm{ps}}^2 - \Omega_{\mathrm{G}}^2} + \frac{\mathrm{n}_{0\mathrm{ps}}\bar{\omega}_{\mathrm{ps}}}{\gamma_{0\mathrm{ps}}^2 \bar{\omega}_{\mathrm{ps}}^2 - \Omega_{\mathrm{G}}^2} \Big) \\
\Omega_{\mathrm{G}} \rightarrow 0 \quad &= \omega^2 - (\mathrm{k}_{\mathrm{x}}^2 + \mathrm{k}_{\mathrm{z}}^2) - \sum_{\mathrm{s}} \Big(\frac{\mathrm{n}_{0\mathrm{ps}}}{\gamma_{0\mathrm{ps}}} + \frac{\mathrm{n}_{0\mathrm{es}}}{\gamma_{0\mathrm{es}}} \Big) \\
&= \omega^2 - \mathrm{k}^2 - 4\omega_{\mathrm{p}}'^2 .
\end{aligned}$$

In the dimensionless representation the speed of light is set to unity and the sum over shell densities and relativistic bulk energies simply represent corrections to the plasma frequency $\omega_{\mathrm{p0}}^2 = 4\pi \mathrm{n}_0 \mathrm{e}^2/\mathrm{m}$ at reference conditions. Corrections define the local plasma frequency ω_{p}' Lorentz-boosted to the inertial frame of a specific scenario. Beyond the individual plasma frequency of a system the familiar vacuum dispersion of radiation is retained

$$\omega^2 \gg 4\omega_{\mathrm{p}}'^2 \qquad \longrightarrow \qquad \omega = \mathrm{kc}.$$

The CGD modes are dominated by the gyro motion of particles in the magnetic guide field. In the general case the purely imaginary roots of the CTW are polluted by small real contingents. This is understood straightforwardly since the magnetic field and couples propagating with unstable plasma modes. CGD modes are propagating electromagnetic plasma modes which are non-degenerate due to the symmetry break imposed by the magnetic field direction. However, the influence of the CGD modes on the physical evolution of the system is generally small and further decaying with growing bulk energy $\propto \gamma_0^{-1}$.

Bibliography

Aharonian, F.A. et al. 2004, Nature, 432, 75

Alfvén, H. 1954, *On the origin of the solar system* (Oxford: Oxford University Press)

Arons, J. 1983, *Electron-Positron Pairs in Astrophysics*, ed. M.L. Burns, A.K. Harding, & R. Ramaty (New York: AIP), 163

Artsimowitsch, L.A., & Sagdeev, R.S. 1983, *Plasmaphysik für Physiker* (Stuttgart: Teubner)

Baum, P.J. & Bratenahl, A. 1980, Adv. Electron. Electron Phys., 54, 1

Beloborodov, A.M. 2002, astro-ph/0201321

Benford, G. 1977, MNRAS, 179, 311

Benford, G. & Weatherall, J.C. 1991, ApJ, 378, 543

Bietenholz, M.F., Hester, J.J., Frail, D.A. & Bartel, N. 2004, ApJ, 615, 794

Birdsall, C.K., & Langdon, A.B. 1985, *Plasma Physics via Computer Simulation* (Bristol:IOP Publishing Ltd.)

Birk, G.T., Crusius-Wätzel, A.R., & Lesch, H. 2001, ApJ, 559, 96

Birn, J. et al. 2001, J. Geophys. Res., 106, 3715

Biskamp, D. 1986, Phys. Fluids, 29, 1520

Biskamp, D. & Bremer, U. 1993, Phys. Rev. Letters, 72, 3819

Biskamp, D., Schwarz, E. & Drake, J.F. 1997, Phys. Plasmas, 4, 1002

Biskamp, D. 2000, *Magnetic Reconnection in Plasmas* (Cambridge: Cambridge University Press)

Biskamp, D. 2003, *Magnetohydrodynamic Turbulence* (Cambridge: Cambridge University Press)

Blackman, E.G., & Field, G.B. 1994, Phys. Rev. Letters, 72, 494

Band, D.L. 1993, ApJ, 413, 281

Bogovalov, S.V. 1999, A&A, 371, 1017

Boris, J.P. 1970, in *Proceedings of Invited Papers, Conference on Numerical Simulation of Plasmas, Washington, 1970* (Washington, D.C.: Naval Research Laboratory), 3

Bulanov, S.V., Echkina, E.Y., Inovenkov, I.N., & Pegoraro, F. 2002, Phys. Plasmas, 9, 3835

Burkhart, G.R., Drake, J.F., & Chen, J. 1990, J. Geophys. Res., 95, 18833

Califano, F., Pegoraro, F., & Bulanov, S.V. 1997, Phys. Rev. E, 56, 963

Chandrasekhar, S. 1961, *Hydrodynamic and Hydromagnetic Stability* (New York: Dover Publications)

Cheng, K.S., Ho, C., & Ruderman, M.A. 1986, ApJ, 300, 500

Cheng, K.S., Ho, C., & Ruderman, M.A. 1986b, ApJ, 300, 522

Cho, J. & Lazarian, A. 2003, MNRAS, 345, 325

Chu, C., Chu, M., & Ohkawa, T. 1978, Phys. Rev. Letters, 41, 653

Coburn, W., & Boggs, S.E. 2003, Nature, 423, 415

Coroniti, F.V., & Eviatar, A. 1977, ApJ Suppl. Ser., 33, 189

Coroniti, F.V. 1990, ApJ, 349, 538

Daughton, W. 1998, J. Geophys. Res., 103, 29429

Daughton, W. 1999, Phys. Plasmas, 6, 1329

Dawson, J.M., Okuda, H., & Carlile, R.N. 1971, Phys. Rev. Letters, 27, 491

Di Matteo, T. 1998, MNRAS, 336, L56

Drake, J.F. 2001, Nature, 410, 525

Drake, J.F., Swisdak, M., Cattell, C., Shay, M.A., Rogers, B.N., & Zeiler, A. 2003, Science, 299, 873

Dungey, J.W 1988, Proceedings of an International Workshop in Space Plasma II [ESA Spec. Publ.], 285, 15

Eilek, J.A., & Henriksen, R.N. 1984, ApJ, 277, 820

Frederiksen, J.T., Hededal, C.B., Haugbolle, T., & Nordlund, A. 2004, ApJ, 608, L13

Gabuzda, D.C., & Cawthorne, T.V. 2000, MNRAS, 319, 1056

Galeev, A.A., Sagdeev, R.Z., Shapiro, V.D., & Shevchenko, V.I. 1977, Sov. Phys. JETP, 45, 266

Ghirlanda, G., Celotti, A., & Ghisellini, G. 2003, A&A, 406, 879

Ghisellini, G., Haardt, F., & Svensson, R. 1998, MNRAS, 297, 348

Goldreich, P., & Julian, W.H. 1969, ApJ, 157, 869

Goodman, J. 1986, ApJ, 308, L47

Greiner, J. et al. 2003, Nature, 426, 157

Groot, de S.G., Leeuwen, W.A., & Weert, van Ch.G. 1980, *Relativistic Kinetic Theory* (Amsterdam: North-Holland)

Gruzinov, A. 2001, ApJ, 563, L15

Gunn, J.E., & Ostriker, J.P. 1969, Nature, 221, 454

Hankins, T.H., Kern, J.S., Weatherall, J.C., & Eilek, J.A. 2003, Nature, 422, 141

Haruki, T., & Sakai, J.I. 2003, Phys. Plasmas, 10, 392

Harris, E.G. 1962, Nuovo Cimento, 23, 15

Hasegawa, A. 1978, The Bell Systems Technical Journal, 58, 3069

Hesse, M., Schindler, K., Birn, J., & Kuznetsowa, M. 1999, Phys. Plasmas, 6, 1781

Hesse, M., & Kuznetsova, M. 2001, J. Geophys. Res., 106, 29831

Hester, J.J. et al. 2002, ApJ, 577, L49

Hibschmann, J.A., & Arons, J. 2001, ApJ, 554, 624

Hirotani, K., Iguchi, S., Kimura, M., & Kiyoaki, W. 2000, ApJ, 545, 100

Hjorth, J. 2003, Nature, 423, 847

Hockney, R.W., & Eastwood, J.W. 1988,
Computer simulation using particles (Bristol: IOP Publishing Ltd.)

Horiuchi, R., & Sato, T., Phys. Plasmas 1994, 1, 3587

Horiuchi, R., & Sato, T. 1997, Phys. Plasmas, 4, 277

Hoshino, M., Mukai, T., Terasawa, T., & Shinohara, I. 2001, J. Geophys. Res., 106, 25979

Irion, R. 2002, Science, 297, 1979

Jaroschek, C.H., Treumann, R.A., Lesch, H., & Scholer, M. 2004, Phys. Plasmas, 11, 1151

Jaroschek, C.H., Lesch, H., & Treumann, R.A. 2004, ApJ, 605, L9

Jaroschek, C.H., Nodes, C., Schopper, R., Ruhl, H., & Lesch, H. 2004, in
High Performance Computing in Science and Engineering, Munich, 2004 (New York: Springer), 419

Jaroschek, C.H., Lesch, H., & Treumann, R.A. 2004, ApJ, 616, 1065

Jaroschek, C.H., Lesch, H., & Treumann, R.A. 2005, ApJ, 618, 822

Jokipii, J.R., Kóta, J., & Giacalone, J. 1993, Geophys. Res. Lett., 20, 1759

Jones, T. 1998, Nature, 395, 440

Jüttner, F. 1911, Ann. Phys., 34, 856

Jüttner, F. 1928, Z. Phys., 47, 542

Kaplan, S.A., & Tsytovich, V.N. 1973, *Plasma Astrophysics*, (Oxford: Pergamon Press)

Kardashev, N.S. 1962, Sov. Astron., 6, 317

Kazimura, Y., Sakai, J.I. Neubert, T., & Bulanov, S.V. 1998, ApJ, 498, L183

Kellermann, K.I., & Pauliny-Toth, I.K. 1981, ARA&A, 19, 373

Kennel, C.F., & Coroniti, F.V. 1984, ApJ, 283, 694

Kijak, J. & Gil, J. 1997, MNRAS, 288, 631

Kijak, J. & Gil, J. 1998, MNRAS, 299, 855

Kino, M., Takahara, F., & Kusunose, M. 2002, ApJ, 564, 97

Kippenhahn, R., & Möllenhoff, C. 1975, *Elementare Plasmaphysik* (Zürich: B.I.-Wissenschaftsverlag)

Kirk, J.G., & Skjæraasen, O. 2003, ApJ, 591, 366

Klebesadel, R.W., Strong, I.B., & Olson, R.A. 1973, ApJ, 182, L85

Kolmogorov, A. 1941, Dokl. Akad. Nauk SSSR, 31, 538

Krall, N.A., & Trivelpiece, A.W. 1986, *Principles of Plasma Physics* (San Francisco: San Francisco Press)

Kubo, H., Takahashi, T., Madejski, G., Tashiro, M., Makano, F., Inoue, S., & Takahara, F. 1998, ApJ, 504, 693

Kulkarni, S. et al. 1998, Nature, 393, 35

Lacombe, C. 1971, Astrophys. Space Sci., 10, 458

Landau, L.D., & Lifshitz, E.M. 1960, *Electrodynamics of Continuous Media* (New York: Pergamon)

Laval, G.R., Pellat, R., & Vuillemin, M. 1966, Plasma Phys. Controlled Nucl. Fusion Res., 2, 259

Lee, R., & Lampe, M. 1973, Phys. Rev. Letters, 31, 23

Lin, A.T., Dawson, J.M., & Okuda, H. 1978, Phys. Rev. Letters, 41, 753

Lesch, H. 1987, Dissertation, Rheinische Friedrich-Wilhelms-Universität Bonn

Lesch, H., Appl, S., & Camenzind, M. 1989, A&A, 225, 341

Lesch, H. & Reich, W. 1992, A&A, 264, 493

Lesch, H. & Birk, G.T. 1997, A&A, 324, 461

Lesch, H. & Birk, G.T. 1998, A&A, 499, 167

Lobanov, A.P., & Zensus, J.A. 2001, Science, 294, 128

Lyubarsky, Y., & Kirk, J.G. 2001, ApJ, 547, 437

Lyubarski, Y. & Eichler, D. 2001, ApJ, 562, 494

Lyubarski, Y. 2002, MNRAS, 329, L34

Lyubarski, Y. 2003, MNRAS, 339, 765

Marscher, A.P., Gear, W.K., & Travis, J.P. 1992, in *Variability of Blazars*, ed. E. Valtaoja & M. Valtonen (Cambridge: Cambridge Univ. Press), 85

McCormick, S.F. (ed.) 1988, *Theory, Applications, and Supercomputing* (New York: Marcel Dekker)

Medvedev, M.V., & Loeb, A. 1999, ApJ, 526, 697

Medvedev, M.V. 2000, ApJ, 540, 704

Meegan, C.A. et al. 1992, Nature, 355, 143

Melatos, A., & Melrose, D.B. 1969, MNRAS, 279, 1168

Melrose, D.B. 1969, Astrophys. Space Sci., 5, 131

Melrose, D.B. 1971, Astrophys. Space Sci., 10, 458

Melrose, D.B. 1978, ApJ, 225, 557

Melrose, D.B. 1992, in *Proceedings of IAU Colloq. 128.*, ed. T.H. Hankins, J.M. Rankin, & J.A. Gil (New York: Pedagogical Univ. Press), 306

Melrose, D.B. & Gedalin, M.A. 1999, ApJ, 521, 351

Mészáros, P., & Rees, M.J. 1993, ApJ, 415, 181

Mészáros, P. 2002, ARA&A, 40, 137

Mészáros, P. 2003, Nature, 423, 809

Metzger, M.R. et al. 1997, Nature, 387, 878

Michel, C. 1982, Rev. Mod. Phys., 54, 1

Michel, C. 1991, *Theory of Neutron Star Magnetospheres* (Chicago: University of Chicago Press)

Michel, F.C. 1994, ApJ, 431, 397

Mori, K., Burrows, D.N., Hester, J.J., Pavlov, G.G., Shibata, S., & Tsunemi, H. 2004, ApJ, 609, 186

Nagai, T. et al. 1998, J. Geophys. Res., 103, 4419

Nishikawa, K. & Wakatani, M. 1994, *Plasma Physics: Basic Theory with Fusion Applications* (Heidelberg: Springer-Verlag)

Nishikawa, K.-I., Hardee, P., Richardson, G., Preece, R., Sol, H., & Fishman, G.J. 2003, ApJ, 595, 555

Oieroset, M., Phan, T.D., Fujimoto, M., Lin, R.P., & Lepping, R.P. 2001, Nature, 412, 414

Paczyński, B. 1986, ApJ, 308, L43

Panaitescu, A., & Kumar, P. 2000, ApJ, 543, 66

Panaitescu, A., & Kumar, P. 2002, ApJ, 571, 779

Parker, E.N. 1957, J. Geophys. Res., 62, 509

Parker, E.N. 1979, *Spontaneous Current Sheets in Magnetic Fields* (New York: Oxford Univ. Press)

Petschek, H.E. 1964, AAS-NASA Symposium on Physics of Solar Flares [NASA Spec. Publ.], 50, 425

Piran, T. 1999, Phys. Rep., 314, 575

Piran, T. 2003, Nature, 422, 168

Price, P.A. et al. 2003, Nature, 423, 844

Priest, E.R. 2001, Earth Planets Space, 53, 483

Pritchett, P.L., Coroniti, F.V., & Decyk, V.K. 1996, J. Geophys. Res., 101, 27413

Pritchett, P.L. 2001, J. Geophys. Res., 106, 3783

Protheroe, R.J. 2003, MNRAS, 341, 230

Pruet, J., Abazajian, K., & Fuller, G. 2001, Phys. Rev. D, 64, 063002

Quirrenbach, A. et al. 1992, A&A, 258, 279

Rees, M.J., & Gunn, J.E. 1974, MNRAS, 167, 1

Rees, M.J. 1987, MNRAS, 228, 47P

Reeves, J.N., Wynn, G., O'Brien, P.T., & Pounds, K.A. 2002, MNRAS, 336, L56

Rogers, B.N., Denton, R.E., Drake, J.F., & Shay, M.A. 2001, Phys. Rev. Letters, 87, 195004

Romanova, M.M., & Lovelace, R.V. 1992, A&A, 262, 26

Ruderman, M.A., & Sutherland, P.G. 1975, ApJ, 196, 57

Rybicki, G., & Lightman, A. 1979, *Radiative Processes in Astrophysics* (New York: Wiley & Sons)

Sagdeev, R.Z. 1966, Rev. Plas. Phys., 4, 23

Sagdeev, R.Z. 1979, Rev. Mod. Phys., 51, 1

Sagdeev, R.Z. 1979, Rev. Mod. Phys., 51, 11

Saito, S., & Sakai, J.I. 2004, Phys. Plasmas, 11, 859

Sari, R., Narayan, R., & Piran, T. 1996, ApJ, 473, 204

Schaefer, B.E., King, J.R., & Deliyannis, C.P. 2000, ApJ, 529, 1026

Scholer, M., Sidorenko, I., Jaroschek, C.H., Treumann, R.A., & Zeiler, A. 2003, Phys. Plasmas, 10, 3521

Schopper, R. 2002, Dissertation, Ludwig-Maximilians-Universität München

Shay, M.A., & Drake, J.F. 1998, Geophys. Res. Lett., 25, 3759

Shay, M.A., Drake, J.F., Rogers, B.N., & Denton, R.E. 1999, Geophys. Res. Lett., 26, 2163

Shay, M.A., Drake, J.F., Rogers, B.N., & Denton, R.E. 2001, J. Geophys. Res., 106, 3759

Shibata, S., Tomatsuri, H., Shimanuki, M., Saito, K., Nakamura, Y. & Mori, K. 2003, MNRAS, 346, 841

Shinohara, I., Suzuki, H., Fujimoto, M., & Hoshino, M. 2001, Phys. Rev. Letters, 87, 095001

Shinohara, I., Suzuki, H., Fujimoto, M., & Hoshino, M. 2001, Phys. Rev. Letters, 87, 095001

Sikora, M., Blazejowski, M., & Moderski, R. 2002, ApJ, 577, 78

Silva, L.O. et al. 2002, Phys. Plasmas, 9, 2458

Silva, L.O., Fonseca, R.A., Tonge, J.W., Dawson, J.M., Mori, W.B., & Medvedev, M.V. 2003, ApJ, 596, L121

Slavin, J.A. et al. 2002, J. Geophys. Res., 107, 1106

Sonnerup, B.U.Ö. 1979, in *Solar System Plasma Physics III*, ed. L.J. Lanzerotti, C.F. Kennel, & E.N. Parker (New York: North Holland), 46

Stenzel, R.L. et al. 1982, J. Geophys. Res., 87, 111

Sturrock, P.A. 1971, ApJ, 164, 529

Sweet, P.A. 1958, in *Electromagnetic Phenomena in Cosmical Physics*, ed. B. Lehnert (New York: Cambridge Univ. Press), 123

Synge, J.L. 1956, *The Relativistic Gas* (New York: North Holland)

Synge, J.L. 1965, *Relativity: The Special Theory* (New York: North Holland)

Syrovatskii, S.I. 1971, Sov. Phys. JETP, 33, 933

Taylor, J.B., & McNamara, B. 1971, Phys. Fluids, 14, 1492

Tennant, A.F. et al. 2001, ApJ, 554, L173

Terasawa, T. 1983, Geophys. Res. Lett., 10, 475

Teräsranta, H., Urpo, S., Wiren, S., & Valtonen, M. 2001, A&A, 368, 431

Treumann, R.A. 2001, Earth Planets Space, 53, 453

Treumann, R.A., & Scholer, M. 2002, in *The Century of Space Science*, ed. J. Bleeker, J. Geis, & M.Huber (Dordrecht: Kluwer), 1495

Treumann, R.A., Jaroschek, C.H., & Scholer, M. 2004, Phys. Plasmas, 11, 1317

Treumann, R.A., Jaroschek, C.H., Constantinescu, O.D., Nakamura, R., Pokhotelov, O.A., & Georgescu, E. 2004, Non. Proc. Geophys., 11, 1607

Treumann, R.A., Jaroschek, C.H., Nakamura, R., Runov, A., & Scholer, M. 2005, Adv. Space Res., in press

Uemura, M. et al. 2003, Nature, 423, 843

Urri, C.M., & Padovani, P. 1995, PASP, 107, 803

Usov, V. V. 1987, ApJ, 320, 333

van Paradijs, J., Kouveliotou, C., & Wijers, R.A.M.J. 2000, ARA&A, 38, 379

Wagner, S. J. 1998, in *ASP Conf. Ser. 144*, ed. J.A. Zensus, G.B. Taylor, & J.M. Wrobel (San Francisco: ASP), 257

Wardle, J.F.C., Homan, D.C., Ojha, R., & Roberts, D.H. 1998, Nature, 395, 457

Wardziński, G., & Zdziarski, A.A. 2000, MNRAS, 314, 183

Waxman, E. 1997, ApJ, 485, L5

Weatherall, J.C. 1988, Phys. Rev. Letters, 60, 1302

Weatherall, J.C., & Benford, G. 1991, ApJ, 378, 543

Weatherall, J.C. 1998, ApJ, 506, 341

Weibel, E.S. 1959, Phys. Rev. Letters, 2, 83

Weisskopf, M.C. et al. 2000, ApJ, 536, L81

Yamada, M. et al. 1997, Phys. Rev. Letters, 78, 3117

Yang, T.-Y.B., Arons, J., & Langdon, A.B. 1993, Phys. Fluids B, 5, 3059

Yang, T.-Y.B., Gallant, Y., Arons, J., & Langdon, A.B. 1993, Phys. Fluids B, 5, 3369

Yoon, P.H., & Davidson, R.C. 1987, Phys. Rev. A, 35, 2619

Yoon, P.H., & Davidson, R.C. 1987, Phys. Rev. A, 35, 2718

Yoon, P.H., & Davidson, R.C. 1989, Phys. Fluids B, 1, 1336

Yoon, P.H., Lui, A.T.Y., & Sitnov, M.I. 2002, Phys. Plasmas, 9, 1526

Zeiler, A., Biskamp, D., Drake, J.F., Rogers, B.N., Shay, M.A., & Scholer, M. 2002, J. Geophys. Res., 107, 1230

Zenitani, S., & Hoshino, M. 2001, ApJ, 562, L63

Zenitani, S., & Hoshino, M. 2003, *private communication*

Zenitani, S., & Hoshino, M. 2005, ApJ, 618, L111

List of Publications

'Fast reconnection in relativistic pair plasmas: Analysis of particle acceleration in self-consistent full particle simulations'
C.H. Jaroschek, R.A. Treumann, H. Lesch, & M. Scholer
Physics of Plasmas, 11(3), 1151-1163, 2004

'Relativistic Kinetic Reconnection as the Possible Source Mechanism for High Variability and Flat Spectra in Extragalactic Radio Sources'
C.H. Jaroschek, H. Lesch, & R.A. Treumann,
The Astrophysical Journal, 605, L09-L12, 2004

'Ultra-Relativistic Plasma Shell Collisions in Pulsar Magnetospheres and Gamma-Ray Bursts'
C.H. Jaroschek, C. Nodes, R. Schopper, H. Ruhl, & H. Lesch
High Performance Computing in Science and Engineering, Munich (New York: Springer), 419-430, 2004

'Self-Consistent Diffusive Lifetimes of Weibel Magnetic Fields in Gamma-Ray Bursts'
C.H. Jaroschek, H. Lesch, & R.A. Treumann,
The Astrophysical Journal, 616, 1065-1071, 2004

'Ultra-Relativistic Plasma Shell Collisions in Gamma-Ray Burst Sources: Dimensional Effects on the Final Steady-State Magnetic Field'
C.H. Jaroschek, H. Lesch, & R.A. Treumann,
The Astrophysical Journal, 618, 822-831, 2005

'Onset of Collisionless Magnetic Reconnection in Thin Current Sheets: Three-Dimensional Particle Simulations'
M. Scholer, I. Sidorenko, C.H. Jaroschek, R.A. Treumann, & A. Zeiler
Physics of Plasmas, 10(9), 3521-3527, 2003

‘Stationary Plasma States Far From Equilibrium’
R.A. Treumann, C.H. Jaroschek, & M. Scholer
Physics of Plasmas, 11(4), 1317-1326, 2004

‘The Strange Physics of Low Frequency Mirror Mode Turbulence in the High Temperature Plasma of the Magnetosheath’
R.A. Treumann, C.H. Jaroschek, O.D. Constantinescu, R. Nakamura, O.A. Pokhotelov, & E. Georgescu
Nonlinear Processes in Geophysics, 11, 1607-1619, 2004

‘The Role of the Hall Effect in Collisionless Magnetic Reconnection’
R.A. Treumann, C.H. Jaroschek, R. Nakamura, A. Runov, & M. Scholer
Advances in Space Research, in press, 2005

Acknowledgements

Acknowledgements ... oder auf gut deutsch: Danksagung. Da es sich hierbei weniger um die Darstellung wissenschaftlicher Erkenntnis als vielmehr um die Aufarbeitung zwischenmenschlicher Kontakte handelt, erscheint mir die Wahl meiner Muttersprache angemessen und zwingend.

An vordringlichster Stelle gebührt mein aufrichtiger Dank natürlich meinen beiden Doktorvätern Prof. Dr. Harald Lesch und Prof. Dr. Rudolf Treumann. Das Werden und Gelingen der vorliegenden Arbeit gründet sich zweifelsfrei auf ihrer beständigen Initiative und ihrem sicheren Urteilsvermögen. Ich bin dankbar feststellen zu können, eine Betreuung über den rein wissenschaftlichen Aspekt hinaus erfahren zu haben. Eine wissenschaftliche Diskussion kann nur dadurch gewinnen, wenn sie in einer Atmosphäre von gegenseitigem Respekt verläuft. Es ist daher ganz entschieden der Ausgeglichenheit und Wohlbestimmtheit ihrer beider Charaktere zu verdanken, meine Bestrebungen in definierte Bahnen gelenkt zu haben.

Herzlich bedanken möchte ich mich weiterhin bei meiner Lebensgefährtin Martina und meinen Eltern Gerlinde und Günter. Der beständige gute Zuspruch, die aufbauenden Worte und tatkräftige Unterstützung, insgesamt die Gewissheit, mich uneingeschränkt auf Euch verlassen zu können, sind eine kontinuierliche Bestärkung.

Vielfacher Dank gilt natürlich auch meinen Freunden und Arbeitskollegen, insbesondere den ‘Ex-Sternwartlern’ Dr. Rüdiger Schopper, Dr. Christian Konz und Dr. Guido Birk, den ‘Max-Plancklern’ Dr. Klaus Hallatschek und Dr. Shuichi Matsukiyo, selbstverständlich meinen Promotionskommilitonen an der Universitäts-Sternwarte Tamara Repolust, Christoph Nodes, Stefan Lieb und Matthias Gritschneder, sowie den vielen anderen ‘Sternwartlern’ und ‘Max-Plancklern’, die mir freundschaftlich verbunden sind. Ich möchte mich bei allen für die gemeinsame Zeit bedanken und alles Gute für die Zukunft wünschen.

Curriculum Vitae

Name:	Claus H. Jaroschek
Geburtsdatum:	17.12.1976
Geburtsort:	Würzburg
Familienstand:	ledig

Werdegang:

Sep 1983 – Aug 1987	Grundschule Würzburg-Lengfeld
Sep 1987 – Jun 1996	Friedrich-König-Gymnasium Würzburg
Sep 1996 – Jun 1997	Grundwehrdienst
Nov 1997 – Jul 2000	Studium der Physik an der Julius-Maximilians-Universität Würzburg
Aug 2000 – Aug 2001	Studium der Physik an der State University of New York at Stony Brook
Sep 2001 – Apr 2004	Doktorand am Max-Planck-Institut für Extraterrestrische Physik
seit 01.05.2004	wissenschaftlicher Mitarbeiter am Institut für Astronomie und Astrophysik der Ludwigs-Maximilians-Universität München